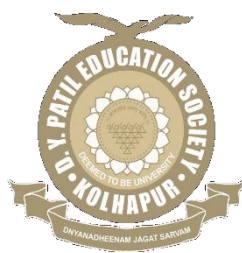


**CHEMICAL SYNTHESIS OF REDUCED GRAPHENE OXIDE/
DYSPROSIUM CHALCOGENIDE COMPOSITE ELECTRODES FOR
SUPERCAPACITOR AND SENSING APPLICATIONS**

**A THESIS SUBMITTED TO
D. Y. PATIL EDUCATION SOCIETY (DEEMED TO BE UNIVERSITY),
KOLHAPUR**



**FOR THE DEGREE OF
DOCTOR OF PHILOSOPHY
IN
PHYSICS
UNDER THE FACULTY OF
INTERDISCIPLINARY STUDIES**

**BY
MR. SAMBHAJI DINKAR KHOT**

M. Sc.

**UNDER THE SUPERVISION OF
PROF. CHANDRAKANT. D. LOKHANDE**

M. Sc., Ph. D.

**DEAN & RESEARCH DIRECTOR,
CENTRE FOR INTERDISCIPLINARY RESEARCH,
D. Y. PATIL EDUCATION SOCIETY (DEEMED TO BE UNIVERSITY), KOLHAPUR
416 006, MAHARASHTRA, (INDIA)**

2024

DECLARATION

I am **Sambhaji D. Khot**, hereby declare that the thesis entitled ***“CHEMICAL SYNTHESIS OF REDUCED GRAPHENE OXIDE/DYSPROSIUM CHALCOGENIDE COMPOSITE ELECTRODES FOR SUPERCAPACITOR AND SENSING APPLICATIONS”*** submitted for the degree of ***Doctor of Philosophy (Ph. D.) in Physics, Faculty of Interdisciplinary Studies, under the guidance of Prof. C. D. Lokhande, Centre for Interdisciplinary Research (CIR), D. Y. Patil Education Society (Deemed to be University), Kolhapur*** is completed and written by me, has not before made the basis for the award of any other higher education institute in India or any other country. To the best of my knowledge and belief the thesis contains no material previously published or written by another person except where due reference is made. Further, I declare that I have not violated any of the provisions under the copyright and piracy/cyber/IPR Act amended from time to time.

Research Student

Place: Kolhapur

Date: / /2024

Mr. Sambhaji Dinkar Khot

CERTIFICATE OF GUIDE

This is to certify that the thesis entitled *“CHEMICAL SYNTHESIS OF REDUCED GRAPHENE OXIDE/DYSPROSIUM CHALCOGENIDE COMPOSITE ELECTRODES FOR SUPERCAPACITOR AND SENSING APPLICATIONS”* which is being submitted herewith for the award of the Degree of *Doctor of Philosophy (Ph. D.) in Physics, Faculty of Interdisciplinary Studies*, under the guidance of *Prof. C. D. Lokhande*, Centre for Interdisciplinary Research (CIR), D. Y. Patil Education Society (Deemed to be University), Kolhapur, is the result of the original research work completed by *Mr. Sambhaji Dinkar Khot* under my supervision and guidance and to the best of my knowledge and belief the work embodied in this thesis has not formed earlier the basis for the award of any degree or similar title of this or any other university or examining body.

Research Guide

Place: Kolhapur

Date: / /2024

Prof. C. D. Lokhande
Dean and Research Director,
Centre for Interdisciplinary Research,
D. Y. Patil Education Society,
(Deemed to be University),
Kolhapur – 416 006.

ACKNOWLEDGEMENT

This journey has been a beautiful odyssey, an exploration of expanding the horizons of knowledge, uncovering strengths and weaknesses, and fostering mental and emotional resilience. The remarkable individuals I encountered along the path have greatly enhanced its beauty and richness. I would like to seize this moment to express my profound gratitude to those persons who enriched this journey with their presence.

*Upon completing my Ph.D. thesis, I extend my sincere gratitude to my mentor, **Prof. C. D. Lokhande**, Dean and Research Director, at the Centre for Interdisciplinary Research (CIR), D. Y. Patil Education Society (Deemed to be University), Kolhapur. Whose expertise was invaluable in formulating the research questions and methodology. I have learned a lot from his meticulous planning and implementation, dedication, and hard work. With his assistance, I was able to overcome personal and scientific obstacles in writing scientific papers, including this Ph.D. thesis. His insightful feedback pushed me to sharpen my thinking and brought my work to a higher level. My association with him for the past few years was a rewarding experience, which will be cherished by me all along. I am very thankful to him for choosing me as his PhD student, and I feel very fortunate to be part of the CDL group.*

*I extend my sincere thanks to President **Dr. Sanjay D. Patil Saheb**, Vice President **Mr. Satej D. Patil, Saheb**, Vice-Chancellor **Prof. R. K. Mudgal**, and Registrar **Dr. V. V. Bhosale** for their inspiration and support. I also express gratitude to **Dr. R. S. Patil, Dr. J. L. Gunjkar, Dr. U. M. Patil, Dr. V. M. Khot, Dr. S. B. Patil**, and **Dr. P. P. Pawar** for their assistance in analyzing the results with their empathy and cooperative mindset. Additionally, I acknowledge the contributions of **Dr. V. C. Lokhande (University of Newcastle, Australia)**, **Dr. A. C. Lokhande (Khalifa University, UAE)**, and **Dr. D. M. Malavekar (Chonnam University, Korea)** for providing important sample characterization data throughout my research endeavor.*

*In addition, I acknowledge the funding support from **Chatrapati Shahu Maharaj Research & Training Institute (SARTHI)**, Government of Maharashtra State, for the **Chhatrapati Shahu Maharaj Senior Research Fellowship (CSMSRF-2021)** sanctioned to me.*

*I would like to express sincere thanks to my M.Sc. and B.Sc. mentors, **Dr. S. T. Mane, Dr. D. P. Nade, Dr. S. P. Patil and Dr. S. M. Pawar** and my seniors, **Dr. P. P. Bagwde, Dr. S. B. Ubale, Dr. S. B. Jadhav, Dr. V. J. Mane, Dr. T. T. Ghogare, Dr. S. B. Kale, Dr. R. B. Shinde, Dr. P. K. Katkar, Dr. S. S. Pujari, Dr. S. A. Khalate, Dr. S. V. Sadavar, Dr. N. S. Padalkar, Dr. S. J. Marje, Mr. V. V. Magdum, Mr. Y. M. Chitare, and Ms. S. P. Kulkarni** for insightful guidance, scientific discussions, and valuable suggestions on the present work.*

*I would like to acknowledge my colleagues and juniors at the Centre for Interdisciplinary Research, **Ranjit Nikam, Sambhaji Kumbhar, Rushiraj Bhosale, Satish Phalke, Manohar Lad, Ketaki Kadam, Shraddha Bhosale, Dilip Patil, Ajinkya Bagde, Divya Pawar, Jyoti Thorat, Sohel Shaikh, Vinod Patil, Sumita Patil, Kuldeep Belekar, Rakesh Mohite, Prashant Sawant, Shweta Talekar, Shraddha Pawar, and Sagar Patil** for their wonderful collaboration. I want to thank them for their support and valuable suggestions during research work.*

*I am also thankful to all teaching and non-teaching staff, **Mr. Nirmale sir, Mr. Ramdas sir, Mrs. Namratha madam, Mr. Omkar, Mr. Shubham, and Mrs. Sarita mavshi** of the Centre for Interdisciplinary Research, for their cooperation.*

*My heartfelt appreciation goes out to my late father, **Dinkar Khot**, and my mother, a strong woman, **Gitanjali Khot**, whose strength has been an enduring source of inspiration. I would also like to thank my lovely elder brother, **Shivaji**, my elder sisters, **Shital** and **Swati**, all my family members and friends. Despite their hard times and struggles, they continuously supported and encouraged me to complete my research.*

~Sambhaji Khot

Place: Kolhapur

SUMMARY OF RESEARCH WORK

LIST OF PATENTS, PUBLICATIONS AND CONFERENCES ATTAINED

A) Patents: (Granted (05)/Published (03)):

- 1) Chemical synthesis of reduced graphene oxide-dysprosium selenide composite thin films for energy storage, Prof. C. D. Lokhande, **Mr. S. D. Khot**, Dr. D. B. Malavekar, Mr. R. P. Nikam, Dr. P. P. Bagwade, (Grant number: 433033).
- 2) Chemical synthesis of dysprosium sulphide coating for energy storage, Prof. C. D. Lokhande, **Mr. S. D. Khot**, Dr. V. C. Lokhande, (Grant number: 519511).
- 3) Electrochemical supercapacitor device. Prof. C. D. Lokhande, Dr. P. P. Bagwade, Dr. D. B. Malavekar, **Mr. S. D. Khot**, Mr. R. P. Nikam, (Grant number: 445967).
- 4) A method of synthesizing composite of reduced graphene oxide and nickel tungstate for energy storage, Prof. C. D. Lokhande, Mr. D. J. Patil, Dr. D. B. Malavekar, **Mr. S. D. Khot**, Mr. R. P. Nikam, (Grant number: 479403).
- 5) Chemical synthesis of cadmium selenide/reduced graphene oxide composite thin film and photoelectrochemical cell application. Prof. C. D. Lokhande, Mr. R. P. Nikam, **Mr. S. D. Khot**, Dr. P. P. Bagwade, Mr. D. J. Patil, (Grant number: 473475).
- 6) A chemical synthesis process for cobalt tungstate/reduced graphene oxide composite thin film and use as electrocatalyst thereof, Prof. C. D. Lokhande, Ms. P. P. Bagwade, **Mr. S. D. Khot**, Mr. R. P. Nikam, (Application No: 202221066956).
- 7) A method of synthesizing reduced graphene oxide-nickel cobalt oxide (rGO-NiCo₂O₄) composite coating, Prof. C. D. Lokhande, Mrs. J. P. Thorat, Mr. A. G. Bagde, Ms. D. C. Pawar, **Mr. S. D. Khot**, Dr. V. C. Lokhande, (Application No: 202321047985).
- 8) Method of synthesizing reduced graphene oxide/dysprosium sulfide composite coating for energy storage application thereof, Prof. C. D. Lokhande, **Mr. S. D. Khot**, A. G. Bagde, Ms. D. C. Pawar, Mr. S. B. Shaikh, Dr. V. C. Lokhande, (Application No: 202421063773).

B) Articles in International Journals: (Published 12):

- 1) SILAR synthesized dysprosium selenide (Dy_2Se_3) thin films for hybrid electrochemical capacitors, **S. D. Khot**, D. B. Malavekar, R. P. Nikam, S. B. Ubale, P. P. Bagwade, D. J. Patil, V. C. Lokhande, C. D. Lokhande, Synthetic metals, 287, (2022), 117075, (**I.F 4.0**).
- 2) Synthesis of reduced graphene oxide (rGO)/dysprosium selenide (Dy_2Se_3) composite electrode for energy storage; flexible asymmetric supercapacitor, **S. D. Khot**, D. B. Malavekar, P. P. Bagwade, R. P. Nikam, C. D. Lokhande, Journal of Physics and Chemistry of Solids, 179, (2023), 111419, (**I.F 4.3**).
- 3) Doping of rare earth elements: Towards enhancing the electrochemical performance of Pseudocapacitive materials, D. B. Malavekar, V. V. Magdum, **S. D. Khot**, J. H. Kim, C. D. Lokhande, Journal of Alloys and Compounds, 960, (2023), 170601, (**I.F: 5.8**).
- 4) Performance of solid-state symmetric supercapacitors based on Dy_2S_3 electrodes, P. P. Bagwade, R. P. Nikam, R. P. Bhosale, **S. D. Khot**, C. D. Lokhande, Applied Surface Science, 18, (2023), 100529, (**I.F: 7.5**).
- 5) Nanocrystalline cobalt tungstate thin films prepared by SILAR method for electrocatalytic oxygen evolution reaction, P. P. Bagwade D. B. Malavekar, V. V. Magdum, **S. D. Khot**, R. P. Nikam, D. J. Patil, U. M. Patil, C. D. Lokhande, International journal of hydrogen energy, 48, (2023), 8465, (**I.F: 8.1**).
- 6) Flexible solid-state asymmetric supercapacitor based on reduced graphene oxide (rGO)/ruthenium oxide (RuO_2) composite electrode, A. G. Bagde, D. B. Malavekar, A. C. Lokhande, S. D. Khot, C. D. Lokhande, Journal of Alloys and Compounds, 980, (2024), 173591, (**I.F: 5.8**).
- 7) Binder free synthesis of mesoporous nickel tungstate for Aqueous Asymmetric Supercapacitor Applications: Effect of film thickness, D. J. Patil, D. B. Malavekar, V. C. Lokhande, P. P. Bagwade, **S. D. Khot**, T. Ji, C. D. Lokhande, Energy Tecchnology, 10, (2022), 2200295, (**I.F: 3.8**).
- 8) Pseudocapacitive performance of amorphous ruthenium oxide deposited by successive ionic layer adsorption and reaction (SILAR): Effect of thickness, A. G. Bagde, D. B. Malavekar, D. C. Pawar, **S. D. Khot**, C. D. Lokhande, Journal of Physics and Chemistry of Solids, 179, (2023), 111386, (**I.F: 4.3**).
- 9) Performance of chemically synthesized polyaniline film based asymmetric supercapacitor: Effect of reaction bath temperature, D. C. Pawar, D. B. Malavekar, **S. D.**

Khot, A. G. Bagde, C. D. Lokhande, Materials Science and Engineering B, 292, (2023), 116432, (I.F: 3.9).

- 10) Chemical synthesis and photoelectrochemical study of CdS/rGO nanocomposite films, R. P. Nikam, A. C. Lokhande, **S. D. Khot**, V. J. Mane, C. D. Lokhande, Journal of Korean ceramic Society, 60, (2023), 238, (I.F: 2.7).
- 11) Effect of post annealing on chemisynthesized cadmium selenide (CdSe) thin films: physicochemical and photoelectrochemical properties, R. P. Nikam, V. C. Lokhande, **S. D. Khot**, P. P. Bagwade, J. L. Gunjkar, C. D. Lokhande, Journal of Materials Science: Materials in Electronics, 34, (2023), 1940, (I.F: 2.8).
- 12) Synthesis and characterization of crystalline cristobalite alpha low silicon dioxide nanoparticles: a cost-effective anode for lithium-ion battery, S. Thombare, R. Patil, R. Humane, B. Kale, R. Kalubarme, D. Malavekar, **S. Khot**, M. Phadatare, C. Lokhande, Journal of Materials Science: Materials in Electronics, 35, (2024), 1424, (I.F: 2.8).

C) Paper/Poster Presented at National/International Conferences (08)

- 1) **S. D. Khot**, C. D. Lokhande, Chemical synthesis of Dy₂Se₃ thin films for supercapacitor, 2nd Asian e-Conference on “Engineered Science” 2021 held online on 5th & 6th December 2021 organized by Prof. C. D. Lokhande Endowment Charitable Trust, and Engineered Science Publisher, USA.
- 2) **S. D. Khot**, C. D. Lokhande, Synthesis, characterization of dysprosium selenide (Dy₂Se₃) thin films by using simple successive ionic layer adsorption and reaction SILAR method, Fourth National Conference on “Recent Trends in Pure and Applied Sciences” held on 21st & 22nd January, 2022. Dr. Patangrao Kadam Mahavidyala, Sangli.
- 3) **S. D. Khot**, C. D. Lokhande, Chemical synthesis of dysprosium sulphide thin films for supercapacitor application, One Day International Conference on “Recent Trends in Science and Technology” held on 29th June 2022 at Willingdon College, Sangli.
- 4) **S. D. Khot**, C. D. Lokhande, Chemically synthesized dysprosium sulfide for supercapacitor, Two Day National Conference on “Emerging Trends in Chemical Sciences and Nanomaterials” (ETCSN-23) held on 24th & 25th February, 2023, Rajarshi Chhatrapati Shahu College, Kolhapur.
- 5) **S. D. Khot**, C. D. Lokhande, Chemical synthesis of dysprosium sulphide thin films for supercapacitor application, Two days National Seminar on “Recent Scenario in

Chemical Sciences and Material Sciences” held on 3rd & 4th March, 2023, Shri Vijaysinha Yadav College, Peth Vadgaon.

- 6) **S. D. Khot**, C. D. Lokhande, High performance flexible solid-state asymmetric supercapacitor device based on rGO-Dy₂Se₃ and MnO₂ electrodes, “Dnyanshodh-2023” organized by CIR, D. Y. Patil Education Society, (Deemed to be University), Kolhapur on 9th March 2023.
- 7) **S. D. Khot**, C. D. Lokhande, High performance flexible solid-state asymmetric supercapacitor device based on rGO/Dy₂Se₃ and MnO₂ electrodes, One Day International Conference on “Recent Trends in Fabrication of Nanomaterials and Their Applications (ICRTFNA-2023)” 15th March, 2023, Rajarshi Chhatrapati Shahu College, Kolhapur.
- 8) **S. D. Khot**, C. D. Lokhande, Synthesis of dysprosium selenide (Dy₂Se₃) thin films by successive ionic layer adsorption and reaction (SILAR) method for supercapacitor application, “Dnyanshodh-2024” organized by CIR, D. Y. Patil Education Society, (Deemed to be University), Kolhapur on 28th February 2024.

D) Participation in Conference/Seminar/Workshop/Science camp (10):

- 1) Participated in Workshop on “Good Laboratory Practices” organised by Department of Stem Cell and Regenerative Medicine and Department of Medical Physics, CIR, D. Y. Patil Education Society, (Deemed to be University), Kolhapur on 6th February 2021.
- 2) Participated in Workshop & hands-on training on XRD organised by SAIF-CFC, Shivaji University, Kolhapur held during 11th & 12th Nov, 2021.
- 3) Participated in “Dnyanshodh-2022” organized by CIR, D. Y. Patil Education Society, (Deemed to be University), Kolhapur on 28th February 2022.
- 4) Participated in the National Level One Day Online Workshop on “Intellectual Property Rights” under National IPR Awareness Mission organized by Research Committee, IPR Cell in Association with IQAC, D. P. Bhosale College, Koregaon, Dist- Satara and Collaboration with Office of Controller General of Patents & Design Office, Mumbai, Govt. of India on 12-08-2022.
- 5) Participated in International Conference on “Emerging Trends in Material Science” dated 9th & 10th November, 2022 jointly organized by Department of Physics & Chemistry in association with IQAC, D. P. Bhosale College, Koregaon, Satara, Maharashtra.

- 6) Volunteer in the Three “IN-YAS Science Camp-2021, 2022 & 2024” organised by CIR, D. Y. Patil Education Society, (Deemed to be University), Kolhapur, Indian National Young Academy of Science (IN-YAS), Indian National Science Academy (INSA), held at the Halkarni, Tal. Gadhinglaj during 18th December 2021, D. Y. Patil Knowledge Campus Salokhenagar, during 16th & 17th December, 2022, and CIR, D. Y. Patil Education Society, (Deemed to be University), Kolhapur during 4th & 5th October 2024.
- 7) Participated in National Seminar on “Emerging Nano Materials for Renewable Energy” held on Monday, 26th December, 2022 and organized by Sanjay Ghodawat University, Kolhapur
- 8) Participated in Two Days International Conference on “Innovations in Smart & Technology materials” 16th & 17th January, 2023, S. G. M. College, Karad.
- 9) Participated in International Conference on “Recent Trends in Pure and Applied Sciences (ICRTPAS-2023) held on 24th & 25th March, 2023, Smt. K. R. P. College, Islampur.
- 10) Participated in International Conference on Nanotechnology Addressing the Convergence of Materials Science, Biotechnology and Medical Science (IC-NACMBM-2024) held at the CIR, D. Y. Patil Education Society, (Deemed to be University), Kolhapur, during 12th to 14th February 2024.

CONTENTS

Candidate's Declaration.....	ii
Certificate of Guide.....	iii
Acknowledgement.....	iv
List of Patents, Articles in International Journals and National/International Conferences Attended.....	vi
Contents.....	xi
List of Figures.....	xii
List of Tables and Charts.....	xix
List of Abbreviations.....	xx
Chapter 1: General Introduction and Literature Survey.....	1-33
Chapter 2: Theoretical Background of CBD, SILAR Methods and Thin Film Characterization Techniques.....	34-73
Chapter 3: Dy₂S₃ and rGO/Dy₂S₃ Thin Films by CBD Method: Characterization and Electrochemical Performance.....	74-106
Chapter 4: Dy₂Se₃ and rGO/Dy₂Se₃ Thin Films by SILAR Method: Characterization and Electrochemical performance.....	107-124
Chapter 5: Dy₂S₃ and rGO/Dy₂S₃ thin films by CBD method: Characterization and Gas Sensor Performance	125-139
Chapter 6: Fabrication and Performance Evaluation of FSSASCs Devices Based on rGO/Dy₂S₃ and rGO/Dy₂Se₃ Thin Films.....	140-155
Chapter 7: Summary and Conclusions.....	156-162
Chapter 8: 80-Recommendations.....	163-164

List of Figures

Chapter 1: General Introduction and Literature Survey

Figure No	Figure Caption	Page No
1.1	Ragone plot of power versus energy performance of several energy-storage systems available so far.....	02
1.2	Mechanism of charge storage in electrochemical capacitors (ECs)..	03
1.3	Schematic of charge storage mechanisms for i) EDLC and ii) pseudocapacitor.....	05

Chapter 2: Theoretical Background of CBD, SILAR Methods and Thin Film

Characterization Techniques

Figure No	Figure Caption	Page No
2.1	Schematic of chemical bath deposition (CBD) method.....	36
2.2	Schematic of four beakers SILAR method.....	43
2.3	Photograph of Rigaku MiniFlex600 diffractometer.....	47
2.4	Basic schematic of FT-IR with Michelson interferometer.....	49
2.5	a) Photograph of ALPHA II compact FT-IR spectrometer, and b) the basic ray diagram of FT- IR system.....	49
2.6	The basic block diagram of Raman spectrometer.....	51
2.7	a) Schematic of FE-SEM, and b) photograph of FE-SEM instrument.....	53
2.8	Schematic diagram of an XPS instrument.....	54
2.9	a) Photograph of Rame-Hart NRL contact angle meter, and b) contact angle of a liquid in contact with solid sample.....	55
2.10	Schematically depicts the dynamic flow method apparatus used for the volumetric method.....	57
2.11	Schematic of charge-storage mechanisms for a) an EDLC and (b–d) different types of pseudocapacitive electrodes: b) surface redox pseudocapacitor, c) intercalation pseudocapacitor, and d) battery-type Faradaic reaction.....	59
2.12	The typical cyclic voltammogram for a reversible single electron transfer reaction.....	60

2.13	Charge discharge curves of a SC.....	61
2.14	Representative shapes of GCD curves: a) EDLC, b) surface redox capacitance, c) intercalation capacitance, and d) Faradic battery-type.....	62
2.15	Nyquist plot with electrical equivalent circuit consisting charge R_{ct} in parallel with C	63
2.16	Nyquist plots with corresponding electrical equivalent circuit a) consisting R_s , R_{ct} , and, C , and b) consisting of R_s , R_{ct} , C , and W	64
2.17	a) Schematic of the gas sensor measurement assembly and b) Actual photograph of the gas sensor measurement assembly.....	66
2.18	The illustration of the band bending due to the adsorption of oxygen species for an n-type semiconductor such as a SnO_2 layer. The schematic of chemisorption a) water molecules and b) NO_2 at the surface of an n-type SnO_2	68

Chapter 3: Dy_2S_3 and $\text{rGO}/\text{Dy}_2\text{S}_3$ thin films by CBD method: Characterization and Electrochemical Performance

Figure No	Figure Caption	Page No
3.1	Schematic flow chart of rGO synthesis.....	76
3.2	The schematic of CBD method employed for Dy_2S_3 thin film electrode preparation.....	77
3.3	Schematic representation of $\text{rGO}/\text{Dy}_2\text{S}_3$ thin film preparation by CBD method.....	78
3.4	a) The electrochemical work station, b) experimental setup, and c) schematic representation of three electrode system.....	80
3.5	a) The XRD patterns, b) FT-IR spectra and c) Raman spectra of Dy_2S_3 thin films deposited at different deposition time.....	81
3.6	FE-SEM images of a) DS3, b) DS6, and c) DS9 at the magnification of 5,000x, and d) DS3, e) DS6, and f) DS9 at the magnification of 20,000x.....	83
3.7	The EDAX spectra of a) DS3, b) DS6, and c) DS9 thin films (insets show atomic percentages of constituting elements of Dy_2S_3 thin film).....	83

3.8	a) Photograph of water contact angle, b) N ₂ sorption isotherms (inset shows the BJH pore size distribution curve) of Dy ₂ S ₃ (DS6) thin film.....	85
3.9	The XRD patterns of i) rGO, ii) Dy ₂ S ₃ and iii) rGO/Dy ₂ S ₃ thin films.....	85
3.10	The FT-IR spectra of i) Dy ₂ S ₃ and ii) rGO/Dy ₂ S ₃ thin films.....	86
3.11	FE-SEM images of a) Dy ₂ S ₃ , and c) rGO/Dy ₂ S ₃ at the magnification of 5,000x, and b) Dy ₂ S ₃ , and d) rGO/Dy ₂ S ₃ at the magnification of 20,000x.....	87
3.12	The EDAX spectra of a) Dy ₂ S ₃ , and b) rGO/Dy ₂ S ₃ thin films (insets show atomic percentages of constituting elements).....	88
3.13	The XPS spectra of a) rGO/Dy ₂ S ₃ film wide survey scan, b) Dy 3d, c) Dy 4d, d) S2p, e) C1s, and f) O1s.....	89
3.14	The Raman spectra of i) rGO, ii) Dy ₂ S ₃ , and iii) rGO/Dy ₂ S ₃ thin films.....	90
3.15	a) Photograph of water contact angle, b) N ₂ sorption isotherms (inset shows the BJH pore size distribution curve) of rGO/Dy ₂ S ₃ thin film.....	91
3.16	a) Comparative CV curves of Dy ₂ S ₃ thin films at a scan rate of 100 mV s ⁻¹ , b) variation of C _s with the scan rates, and the CV curves at various scan rates from 5-100 mV s ⁻¹ of c) DS3, d) DS6, and e) DS9 thin film electrodes.....	92
3.17	a) Comparative GCD curves of Dy ₂ S ₃ thin film electrodes at a current density of 3.5 A g ⁻¹ , b) variation of C _s with the current densities, and the GCD curves at various current densities from 3.5 - 5.5 A g ⁻¹ of c) DS3, d) DS6, and e) DS9 thin film electrodes.....	94
3.18	a) Nyquist plots, (inset shows the fitted equivalent circuit for the EIS data), and b) the stability curves for Dy ₂ S ₃ thin film electrodes	95
3.19	a) The CV curves at various scan rates from 5-100 mV s ⁻¹ , b) the GCD curves at various current densities of 3.0 to 8.0 A g ⁻¹ , c) Nyquist plot of rGO electrode and simulated equivalent electrical	

	circuit is displayed as an inset image.....	96
3.20	The CV curves at various scan rates from 5-100 mV s ⁻¹ of a) Dy ₂ S ₃ , b) rGO/Dy ₂ S ₃ , thin film electrodes and c) variation of C _s with the scan rate.....	97
3.21	a) Plots of log <i>I</i> verses log <i>v</i> , of Dy ₂ S ₃ and rGO/Dy ₂ S ₃ thin film electrodes, and calculated charge storage by capacitive and diffusion processes for b) Dy ₂ S ₃ , and c) rGO/Dy ₂ S ₃ thin film electrodes.....	99
3.22	The GCD curves at various current densities from 3.5-5.5 A g ⁻¹ of a) Dy ₂ S ₃ , and b) rGO/Dy ₂ S ₃ thin film electrodes, and c) variation of C _s with the current densities.....	100
3.23	a) Nyquist plots of Dy ₂ S ₃ and rGO/Dy ₂ S ₃ thin films, (inset the fitted equivalent circuit for the EIS data) and b) the stability curves for Dy ₂ S ₃ and rGO/Dy ₂ S ₃ thin film electrodes.....	101

Chapter 4: Dy₂Se₃ and rGO/Dy₂Se₃ thin films by SILAR method: Characterization and Electrochemical Performance

Figure No	Figure Caption	Page No
4.1	a) Schematic of SILAR method for deposition of rGO/Dy ₂ Se ₃ thin film and b) the schematic illustration of the formation of rGO/Dy ₂ Se ₃ composite.....	109
4.2	a) The XRD patterns of i) rGO, ii) Dy ₂ Se ₃ , and iii) rGO/Dy ₂ Se ₃ thin films.....	111
4.3	The FT-IR spectra of i) Dy ₂ Se ₃ and ii) rGO/Dy ₂ Se ₃ composites.....	112
4.4	The FE-SEM images of a-b) Dy ₂ Se ₃ , c-d) rGO-Dy ₂ Se ₃ at magnifications of 10,000X, and 50,000X, and e-f) rGO thin films at magnifications of 10,000X, and 20,000X.....	113
4.5	The Raman spectra of i) Dy ₂ Se ₃ and ii) rGO/Dy ₂ Se ₃ composites.....	114
4.6	The EDAX spectra of a) Dy ₂ Se ₃ , and b) rGO/Dy ₂ Se ₃	115
4.7	The N ₂ adsorption–desorption isotherms of a) Dy ₂ Se ₃ , and b)	

	rGO/Dy ₂ Se ₃ , and c) pore size distributions of Dy ₂ Se ₃ , and rGO/Dy ₂ Se ₃	116
4.8	Water contact angle photographs of a) Dy ₂ Se ₃ and b) rGO/Dy ₂ Se ₃ thin films.....	117
4.9	The CV curves of a) Dy ₂ Se ₃ , b) rGO/Dy ₂ Se ₃ at various scan rates from 5-100 mV s ⁻¹ , and c) variation of C _s with the scan rate for Dy ₂ Se ₃ and rGO/Dy ₂ Se ₃ thin film electrodes.....	117
4.10	a) Plot of log <i>I</i> vs log <i>v</i> , and contribution of capacitive and diffusion-controlled currents with scan rates of b) Dy ₂ Se ₃ and c) rGO-Dy ₂ Se ₃ composite electrode.....	119
4.11	The GCD curves of a) Dy ₂ Se ₃ , and b) rGO/Dy ₂ Se ₃ at different current densities from 4-8 A g ⁻¹ and c) variation of C _s with charge-discharge current density.....	120
4.12	Nyquist plots of a) Dy ₂ Se ₃ and rGO/Dy ₂ Se ₃ electrodes, b) magnified Nyquist plot and c) the fitted equivalent circuit from the EIS data.....	121
4.13	Stability curves of a) Dy ₂ Se ₃ and b) rGO/Dy ₂ Se ₃ thin film electrodes.....	122

Chapter 5: Dy₂S₃ and rGO/Dy₂S₃ thin films by CBD method: Characterization and Gas Sensor Performance

Figure No	Figure Caption	Page No
5.1	The XRD patterns of i) Dy ₂ S ₃ and ii) rGO/Dy ₂ S ₃	126
5.2	FE-SEM images of a) Dy ₂ S ₃ and c) rGO/Dy ₂ S ₃ at the magnification of 10,000x and b) Dy ₂ S ₃ and d) rGO/Dy ₂ S ₃ at the magnification of 20,000x.....	127
5.3	Initial resistance stabilization curve of a) Dy ₂ S ₃ and b) rGO/Dy ₂ S ₃ composite.....	130
5.4	The bar chart shows the variation of response of Dy ₂ S ₃ at 423 K, and rGO/Dy ₂ S ₃ composite sensor at RT for 100 ppm of six different target gases.....	131
5.5	Response and resistance vs time transients of a) Dy ₂ S ₃ , and b) rGO/Dy ₂ S ₃ composite for 100 ppm NO ₂	132

5.6	The dynamic response curves of a) Dy ₂ S ₃ , and b) rGO/Dy ₂ S ₃ composite sensor exposed to various NO ₂ concentrations (1.0, 10, 50, and 100 ppm).....	134
5.7	Long-term stability of rGO/Dy ₂ S ₃ composite sensor exposed to 100 ppm NO ₂ for 40 days (every 10 days).....	135
5.8	Schematic of NO ₂ gas sensing mechanism of rGO/Dy ₂ S ₃ composite sensors.....	137

Chapter 6: Fabrication and Performance Evaluation of FSSASCs Devices Based on rGO/Dy₂S₃ and rGO/Dy₂Se₃ Thin Films

Figure No	Figure Caption	Page No
6.1	a) The schematic of flexible solid state Dy ₂ S ₃ //MnO ₂ FSSASCs device formation, b) the thickness of the FSSASCs device measured by the digital micrometer, c and d) flexibility (physical bending and twisting) of FSSASCs device.....	142
6.2	a) The XRD pattern, and SEM images at b) 50000x, and c) 100000x magnifications of MnO ₂ thin film.....	143
6.3	a) The CV curves at various scan rates from 5-100 mV s ⁻¹ , b) plot of specific capacitance at various scan rates, c) the GCD curves at various current densities from 3.20-6.40 A g ⁻¹ , d) plot of specific capacitance at various current densities, and e) Nyquist plot of MnO ₂ electrode in 1 M LiClO ₄ electrolyte.....	144
6.4	a) The CV curves at different potential windows, b) the CV curves at different scan rates, c) the GCD plots at different potential windows and d) the GCD plots at different current densities.....	145
6.5	a) The specific capacitance retention and Coulombic efficiency of MnO ₂ //rGO/Dy ₂ S ₃ FSSASCs device, b) the Nyquist plot; before and after stability, (inset image shows the fitted equivalent electrical circuit), c) capacitance retention of the device at different bending angles (inset displays CV curves at varying bending angles), d) Ragone plot of MnO ₂ //rGO/Dy ₂ S ₃ FSSASCs device, and e) The practical application of two series connected	

	MnO ₂ //rGO/Dy ₂ S ₃ FSSASCs devices to illuminate 211 red LEDs..	147
6.6	The procedure for fabrication of a) rGO/Dy ₂ Se ₃ //MnO ₂ FSSASCs device, b) the thickness of the FSSASCs device measured by the digital micrometer, c and d) flexibility (physical bending and twisting) of FSSASCs device.....	148
6.7	Electrochemical characterization of rGO/Dy ₂ Se ₃ //MnO ₂ FSSASCs device; a) the CV curves at different potentials, b) the CV curves at different scan rates, c) the GCD plots at different potentials, and d) the GCD curves at different current densities.....	149
6.8	The variation of C _s of FSSASCs device a) with different scan rates, b) with different current densities.....	150
6.9	a) The specific capacitance retention and Coulombic efficiency of FSSASCs device, b) the Nyquist plot; before and after stability, (inset image shows the fitted equivalent electrical circuit), c) capacitance retention of the device at various bending angles (inset shows CV curves at different bending angles), d) Ragone plot of FSSASCs device, and e) The practical application of two series connected rGO/Dy ₂ Se ₃ //MnO ₂ FSSASCs devices to illuminate table lamp of 11 white LEDs.....	151
6.10	The photographs of various bending positions of FSSASCs device a) 20°, b) 40°, c) 60°, d) 80°, e) 100°, f) 120°, g) 140°, and h) 160°.....	152

Chapter 7: Summary and Conclusions

Chapter 8: 80-Recommendations

List of Tables and Charts

Chart 1.1:	Classification of supercapacitor.....	4
Chart 1.2:	Classification of sensors.....	10
Table 1.1	Supercapacitor performances of rare earth metal chalcogenide and theirs composite thin films.....	18
Table 1.2	Gas sensing performance of various metal sulfide and its composite thin films.....	24
Chart 2.1	General classification of thin film deposition methods.....	35
Table 3.1	Electrochemical impedance spectroscopic fitted circuit parameters for Nyquist plots of Dy_2S_3 thin film electrodes.....	95
Table 3.2	Electrochemical impedance spectroscopic fitted circuit parameters for Nyquist plots of Dy_2S_3 and $\text{rGO/Dy}_2\text{S}_3$ thin film electrodes.....	101
Table 4.1	Electrochemical impedance spectroscopic data of Dy_2Se_3 and $\text{rGO/Dy}_2\text{Se}_3$ composite thin films.....	121
Table 7.1	The electrochemical parameters of Dy_2S_3 , $\text{rGO/Dy}_2\text{S}_3$, Dy_2Se_3 , and $\text{rGO/Dy}_2\text{Se}_3$ thin film electrodes deposited using CBD and SILAR methods in three electrode system.....	161
Table 7.2	The electrochemical parameters of FSSASCs devices evaluated using two electrode system.....	161
Table 7.3	Comparative gas sensor performance of Dy_2S_3 and $\text{rGO/Dy}_2\text{S}_3$ composite sensor.....	162

LIST OF ABBREVIATIONS

AC	Activated carbon	LED	Light emitting diodes
AR	Analytical grade	ME	Micromechanical exfoliation
ASC	Asymmetric supercapacitors	LiClO₄	Lithium perchlorate
BET	Brunauer-Emmett-Teller	MSs	Metal sulfides
BJH	Barrett-Joyner-Halenda	MOCVD	Metal organo-chemical vapor deposition
CBD	Chemical bath deposition	NF	Nickel foam
CNFs	Carbon nanofibers	PVA	Poly (vinyl alcohol)
CNTs	Carbon nanotubes	ppm	Part per million
CPE	Constant phase element	REMC	Rare earth metal chalcogenide
C_s	Specific capacitance	RT	Room temperature
CV	Cyclic voltammetry	R_{ct}	Charge transfer resistance
CVD	Chemical vapor deposition	rGO	Reduced graphene oxide
DDW	Double distilled water	SCE	Saturated calomel electrode
EC	Electrochemical capacitor	R_s	Solution resistance
ED	Energy density	S_E	Specific energy
EDAX	Energy dispersive X-ray spectroscopy	SS	Stainless steel
EDL	Electric double layer	S_P	Specific power
EDLC	Electric double-layer capacitor	S_B	Specific surface area
EES	Electrochemical energy storage	SILAR	Successive ionic layer adsorption and reaction
EGSs	Electrochemical gas sensors	SCs	Supercapacitors
EIS	Electrochemical impedance spectroscopy	SSC	Symmetric supercapacitor
ESR	Equivalent series resistance	S_T	Total surface area
FE-SEM	Field emission scanning electron microscopy	W	Warburg impedance
FSSASCs	Flexible solid-state asymmetric supercapacitors	XPS	X-ray photoelectron spectroscopy
FT-IR	Fourier transform infrared spectroscopy	XRD	X-ray diffraction
GCD	Galvanostatic charge-discharge		
GO	Graphene oxide		
LEL	Lower explosive limit		

CHAPTER-1

General Introduction and Literature Survey

CHAPTER-1

General Introduction and Literature Survey

Sr. No.	Title		Page No.
1.1	General Introduction of Supercapacitor		1
	<i>1.1.1</i>	<i>The Need for Supercapacitors</i>	1
	<i>1.1.2</i>	<i>Basics Working Principle of Supercapacitor</i>	3
	<i>1.1.3</i>	<i>Types of Supercapacitors</i>	4
	<i>1.1.3.1</i>	<i>Symmetric Supercapacitor (SSC)</i>	4
		<i>i) Electric Double Layer Capacitor (EDLCs)</i>	5
		<i>ii) Pseudocapacitor</i>	6
	<i>1.1.3.2</i>	<i>Asymmetric Supercapacitors (ASCs)</i>	7
	<i>1.1.3.3</i>	<i>Hybrid Supercapacitor (HSCs)</i>	7
		<i>i) Hybrid Electrolytic Supercapacitor</i>	8
		<i>ii) Composite Supercapacitor</i>	8
		<i>iii) Battery-type Supercapacitor</i>	8
1.2	General Introduction of Sensors		9
	<i>1.2.1</i>	<i>Sensors</i>	9
	<i>1.2.2</i>	<i>Classification of Sensors</i>	10
	<i>1.2.3</i>	<i>Gas Sensor</i>	12
	<i>1.2.4</i>	<i>Types of Gas Sensor</i>	13
1.3	Literature Survey of Supercapacitor and Gas Sensor		13
	<i>1.3.1</i>	<i>Literature Survey on Rare Earth Metal Chalcogenide and its Composite Thin Films for Supercapacitor Performance</i>	15
	<i>1.3.2</i>	<i>Literature Survey on Metal Sulphide and its Composite Thin Films for Gas Sensing Performance</i>	22
1.4	Orientation and Purpose of the Thesis		26
1.5	References		28

1.1 General Introduction of Supercapacitor:

1.1.1 The Need for Supercapacitors:

The world currently faces serious global challenges, such as energy shortages, environmental pollution, rapid population growth, declining natural resources, and the depletion of fossil fuels [1]. Global technological development is driven by the increasing demand due to the lifestyle of the people being changed, and they are moving towards highly developed technology-based products utilized in their daily lives. According to these the development of sustainable energy sources are instantly needed. There are mainly two types of energy sources: Renewable and non-renewable energy sources. Renewable energy sources are in high demand due to their ability to generate and store energy, as well as their cost effectiveness compared to non-renewable energy sources, which are in limited supply. Although, renewable energy sources such as the sun, wind, etc. are the continuous creation of energy but it's not stable, efficient storage is not possible and these intermittent energies face challenges such as being influenced by weather and uneven distribution [2, 3]. But this problem is overcome by the use of various electrochemical energy storage (EES) technologies such as batteries, fuel cells, capacitors, and supercapacitors (SCs) [4]. Among these, the charge accumulation mechanism is dissimilar for each of them. The Ragone plot presented in **Figure 1.1** demonstrates the status of power versus energy performance of several energy-storage systems available so far. Nowadays, rechargeable and non-rechargeable type of batteries is being widely used. They lie in the high-energy and low-power region, defining a time constant (operation time) ranging from one to tens of hours. In batteries, the chemical energy converted to get electrical energy due to redox reactions occurring at a cathode and an anode. But in the rechargeable type of batteries the process of redox reactions is reversed for limited times [5].

The dominant position of Li-ion batteries in the market can be attributed to their high energy density, reaching up to approximately 300 Wh kg^{-1} , and this technology is expected to maintain its superiority for a significant period of time. However, the cycle life of these batteries is limited to a few thousand cycles due to volume changes in the materials during cycling. Additionally, Li-ion batteries face challenges with slower recharge rates compared to discharge rates, primarily due to Li-metal plating at the negative electrode. Although ongoing efforts aim to increase battery lifespan and reduce charging time, there are inherent limitations associated with solid-state

diffusion rate, phase transformations, and volume changes during charge/discharge. Furthermore, the energy density decreases rapidly with size, which poses limitations on the use of micro-batteries for powering microscale and wearable devices. Currently, batteries have high energy density but cannot provide complete solution for electricity storage due to possess limitations like low power density and lifetime are caused by the charge-storage mechanism, which involves transformation of chemical bonds via electrochemical redox reactions in the bulk of active materials, cycle life limited to a few thousand cycles, due to volume changes in the materials upon cycling, high cost of manufacturing, heat generation, and several hours of charging time [6, 7].

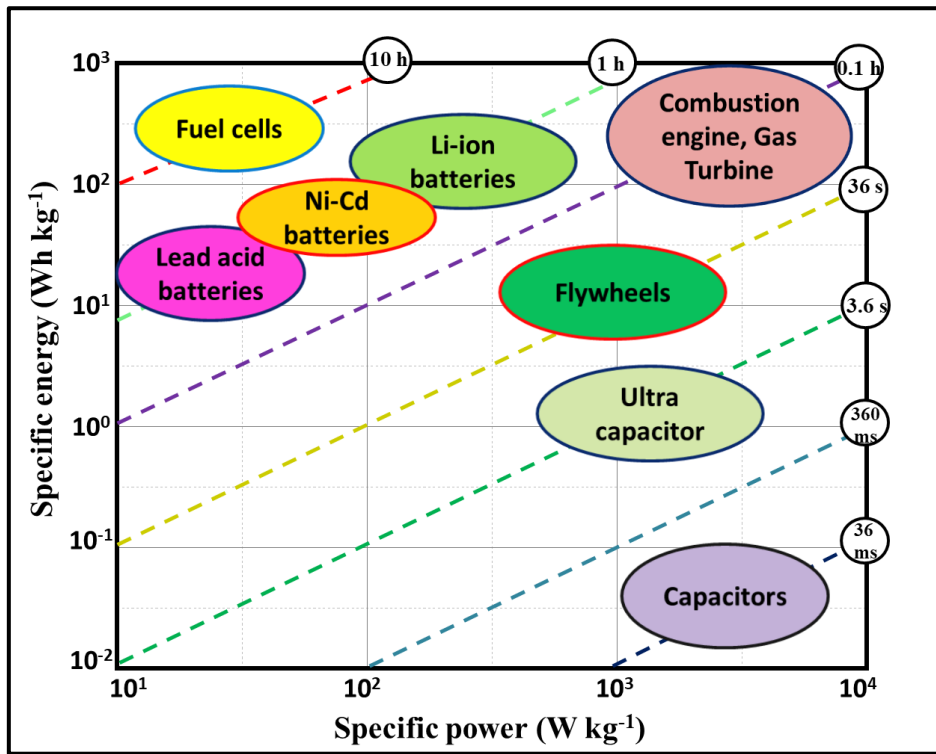


Figure 1.1: Ragone plot of power versus energy performance of several energy-storage systems available so far [8].

Therefore, there is a demand for long-lasting and safe electricity storage device with high power and energy density. This can be achieved using a SC also known as an electrochemical capacitor (EC), which has bridged the gap between battery and conventional capacitor, that has greater specific capacity and specific energy related to conventional capacitors and higher power than batteries, resulting in an operation time of tens of seconds to minutes. They reduce those limitations due to their ability to deliver energy at a high rate, shorter charging time, more efficient charging and

discharging than batteries, efficient fabrication process, and long cycle life and they cause no pollution in the environment and hence gained significant attention in recent time [9-11].

1.1.2 Basic Working Principle of Supercapacitor:

In the EC and conventional capacitors, the charge storage mechanisms are similar but the separating medium between the electrodes is different, i.e., the electrolyte utilized in the EC and the dielectric in traditional capacitors. In a conventional capacitor, the charges are accumulated electrostatically between two conducting electrodes that are separated by an insulating dielectric material. In the case of an Electric Double Layer Capacitor (EDLC), electric charge is stored at the surface of the metal/electrolyte interface. At the interface of the electrode, opposite ions form an Electric Double Layer (EDL). The created EDL is separated by a distance of a few Angstroms, by the specific electrolyte being used. **Figure 1.2** shows the schematic diagram of charge storage mechanism in EC. As compared to conventional capacitors and batteries the EC deliver high specific energy (S_E) and longer lifespan respectively. According to the following (**Equation 1.1**), EC achieves excellent performance when the electrode has a higher surface area and a smaller thickness of double layer.

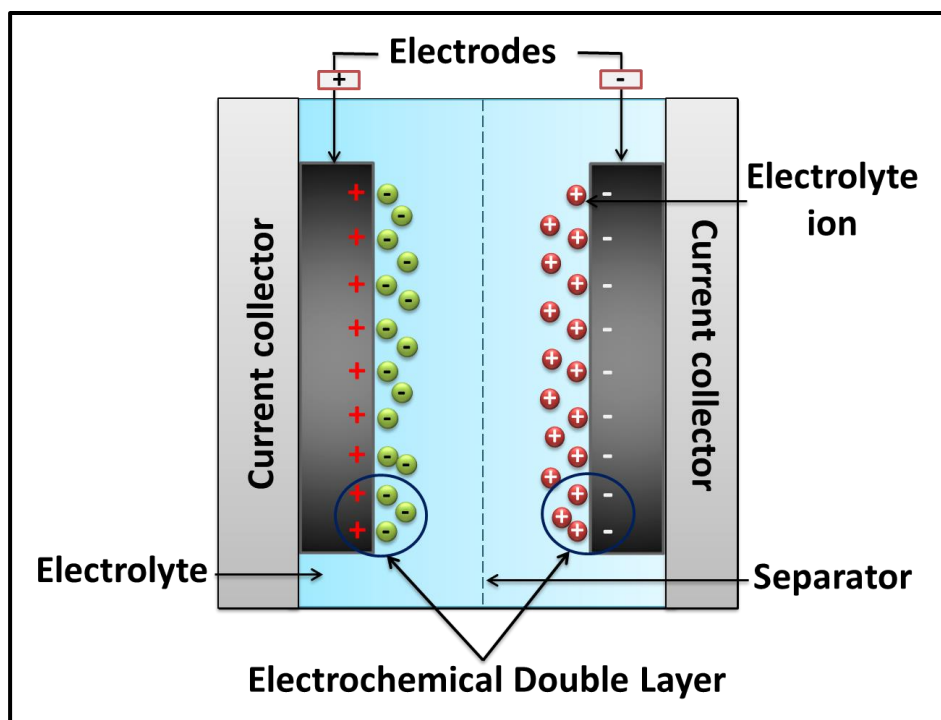


Figure 1.2: Mechanism of charge storage in electrochemical capacitors (ECs).

The capacitance C of an EC given by the equation:

$$C = \epsilon_r \frac{A}{d} \quad (1.1)$$

Where ϵ_r denotes the relative permittivity, A is the surface area of active material, and d represents the thickness of the double layer. The energy density (E) of an EC is determined using the following formula,

$$E = \frac{CV^2}{2} \quad (1.2)$$

where C denotes the capacitance and V represents the voltage range of the EC.

1.1.3 Types of Supercapacitors:

The types of ECs materials mainly depend on the charge storage mechanism. They are broadly listed into three categories, i.e. EDLC, pseudocapacitors and battery-type ECs. Charge accumulation in EDLCs is due to electrostatic mechanism across the electrode and electrolyte interface. The carbon derivatives and MXenes are of EDLCs type materials. In pseudocapacitors, redox reactions occurring on the surface and interior of the electrodes are responsible for charge accumulation. Metal oxides, chalcogenides as well as conducting polymers are pseudocapacitive electrode materials. The battery-type ECs obey the faradic mechanism of charge storage [12, 13]. Mostly nickel and iron oxides and phosphates are used as battery-type materials.

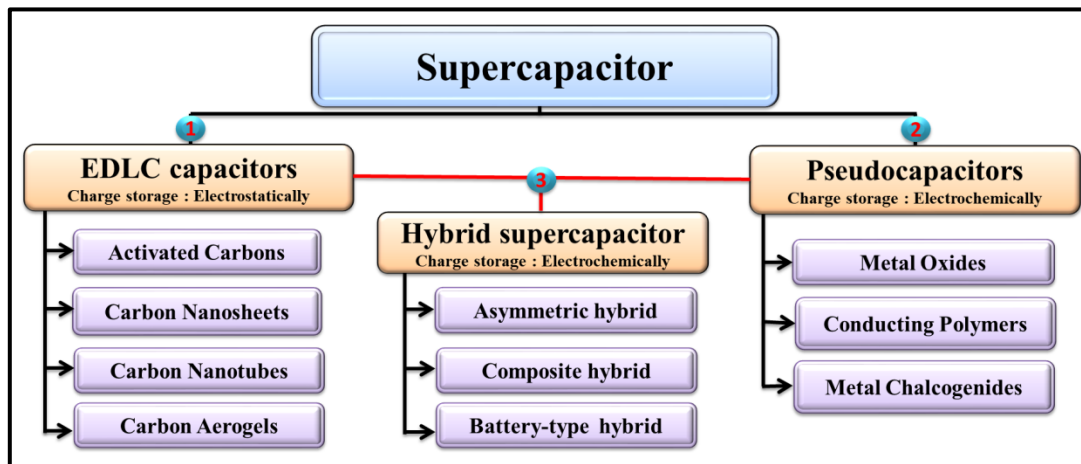


Chart 1.1: Classification of supercapacitor

1.1.3.1 Symmetric Supercapacitor (SSC):

The term "symmetric" is used to describe a type of SC where both electrodes are made of the same material and have identical designs. In practical terms, a similar

mass is deposited on both electrodes [14]. These electrodes exhibit equal and efficient charge storage principles, which can be either physical or chemical in nature, or a combination of both. **Chart 1.1** shows the classification of supercapacitor. Symmetric supercapacitors fall into two classes: **i)** EDLCs and **ii)** Pseudocapacitors.

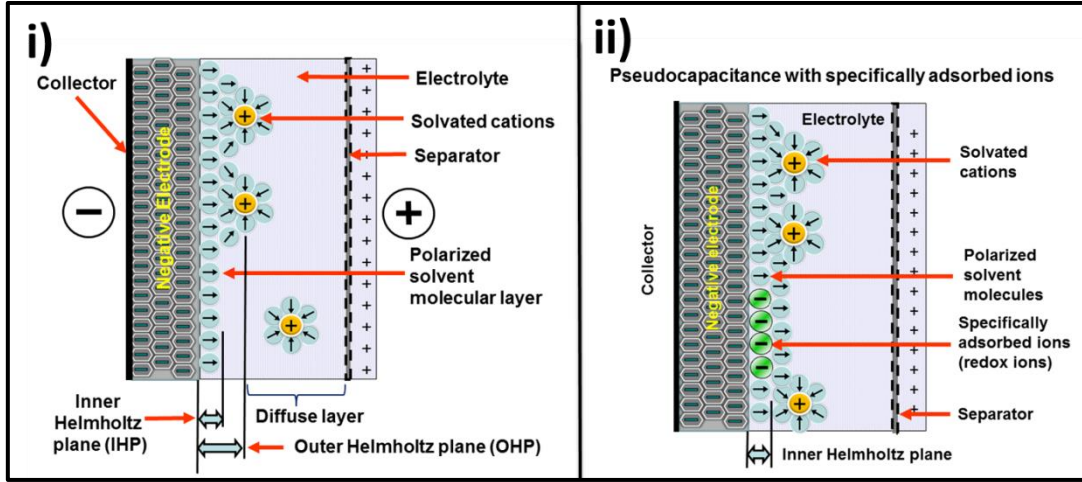


Figure 1.3: Schematic of charge storage mechanisms for **i)** EDLC and **ii)** pseudocapacitor [15].

i) Electric Double Layer Capacitor (EDLCs):

EDLCs, which are a common type of SCs. In EDLCs, the capacitance arises from the adsorption of both anions and cations at the interface between the electrode and electrolyte [16]. During the charging process, electrons flow from the negative electrode to the positive electrode through the external loop, while anions migrate towards the positive electrode and cations move towards the negative electrode. The direction of electron and ion movement is reversed during the discharging process [17, 18]. **Figure 1.3 (i)** shows the schematic representation of energy storage mechanism in EDLCs. A highly reversible EDLCs capacitor delivers high cycling stability and higher surface area of electrodes they achieve higher capacitance. Moreover, due to faster discharge rate and absence of charge transfer chemical reactions the EDLCs provide higher specific power density and superior cycle life respectively [19]. The Helmholtz model is a simplified description of the process of double-layer capacitance using the equation for a parallel plate capacitor,

$$C = \frac{\epsilon A}{d} \quad (1.3)$$

where C is the double-layer capacitance, ε is the permittivity of the dielectric separating the charges, A is the surface area of the electrode, and d is the distance between the electrode and electrolyte ions. The specific energy (S_E) and specific power (S_P) of electrochemical capacitor can be determined with these equations,

$$S_E = \frac{0.5 \times C_s \times (V_1^2 - V_0^2)}{3.6} \quad (1.4) \quad \text{and} \quad S_P = \frac{3600 \times S_E}{dt} \quad (1.5)$$

where C_s represents the specific capacitance, ΔV denotes the potential window of the supercapacitor, and Δt is the time duration. Typically, the carbon derivatives such as activated carbon (AC), [20] aerogels, [21] carbon nanotubes (CNTs), [22] carbon nanofibers (CNFs), [23] graphene, [24] and carbide-derived carbons [25] are generally shows EDLC type behavior and utilized as EDLC materials.

One of the limitations of carbon-based SCs is their relatively lower energy density, particularly in terms of volumetric energy density, which hinders their practical implementation. To address this limitation, research efforts are focused on optimizing synthesis conditions to enhance various performance-enhancing factors. Factors such as specific surface area, surface energy, electrical conductivity, and pore size distribution play crucial roles in improving the performance of carbon-based SCs. Increasing the specific surface area allows for more electrolyte ions to be adsorbed, resulting in higher capacitance. Controlling surface energy helps in achieving better ion adsorption and desorption kinetics. Enhancing electrical conductivity ensures efficient electron transport within the electrode material, enabling faster charge/discharge rates. Optimizing pore size distribution facilitates easy access for electrolyte ions, improving the overall performance of the EDLCs [26]. Therefore, future research in the field of EDLC-based materials should focus on fine-tuning synthesis conditions to maximize these performance-enhancing factors, ultimately leading to improved S_E and better practical viability of carbon-based SCs.

ii) Pseudocapacitor:

The charge storage mechanism in Pseudocapacitor is distinct from that of EDLCs, as it relies on reversible surface redox reactions between the electrode and the electrolyte to transfer charges. **Figure 1.3 (ii)** illustrates the schematic representation of the charge storage mechanism in a pseudocapacitor. Pseudocapacitors exhibit higher capacitance and energy densities compared to EDLCs due to the faradaic process involved. The performance of pseudocapacitors is affected

by several factors, such as the conductivity of the materials, the surface area of the active electrode, and the porosity of the materials. Their charge storage mechanism involves redox reactions, insertion and extraction processes, and electrosorption. Extensive research has been carried out on various transition metal compounds, including chalcogenides, silicates, carbides, nitrides, and polymers like polyaniline (PANI), polypyrrole (PPy), and polythiophene (PTh), metal-doped carbon, and phosphates among others [27-32]. These materials are gaining increasing interest due to their higher C_s and S_E [33, 34].

Among these materials, Transition Metal Chalcogenides (TMCs) have attracted considerable interest because of their superior electrical conductivity and thermal stability relative to other transition metal compounds and polymers. These properties make TMCs highly suitable for achieving high capacitance and S_E in portable energy storage devices [35, 36]. Based on the energy storage mechanism, pseudocapacitors can be classified into three categories: intrinsic (charge transfers (or redox reactions) occurring at the surface of the electrode), intercalation (faradaic charge transfer due to the intercalation of electrolyte ions into the tunnels or layers with no crystallographic phase change.), and extrinsic (materials show batterylike features (strong redox peaks and plateau in GCD) in the bulk phase, however, in the form of nanostructures, pseudocapacitive behavior emerges).

1.1.3.2 Asymmetric Supercapacitors (ASCs):

Asymmetric supercapacitors (ASCs) are distinguished by the dissimilar processes that occur within them based on their nature [37]. One electrode undergoes redox reactions, while the other electrode involves charge-discharge of electrostatic charge storage in the electric double-layer. This type of SCs is often referred to as "hybrid" in modern terminology. It encompasses improved versions of symmetric SCs where changes are made to the electrolyte compositions, mass loading, and electrode geometry, while keeping the active materials and operating processes unchanged.

1.1.3.3 Hybrid Supercapacitor (HSCs):

Hybrid supercapacitors (HSCs) represent a highly innovative approach that combines the superior performance aspects of different types of SCs. The primary objective of HSCs is to enhance technical characteristics and potentially reduce costs compared to conventional supercapacitors by utilizing different materials for each

electrode. Through ongoing research and development efforts, combinations of positive and negative electrodes from diverse technologies have been achieved. The key technological challenge in this field is to bridge the gap between SCs and electrochemical batteries, thereby achieving a balance that offers the best of both worlds.

The fundamental design of a HSCs involves using two electrodes made of dissimilar materials that employ different working processes, including faradic and non-faradic mechanisms. The objective of exploring these electrode combinations is to achieve an extended cycle life similar to EDLCs and the high power capacity of conventional capacitors. Additionally, the aim is to overcome the cost limitations of pseudocapacitors and enhance the energy density to approach that of batteries. This category of HSCs can be further classified into three main types: (i) hybrid electrolytic, (ii) composite, and (iii) battery-like SCs.

i) Hybrid Electrolytic Supercapacitor:

The pseudo-capacitive electrode, based on metal oxides, can be integrated with the electrode of a conventional electrolytic capacitor. This combination allows for the retention of the high power characteristics of electrolytic capacitors, while the addition of pseudo-capacitance on one electrode significantly increases the device's C_s .

ii) Composite Supercapacitor:

The second type of HSCs is the composite SCs, which involves combining the electrode of an EDLC with a composite electrode. This composite electrode incorporates carbon-based materials like carbon nanotubes, along with conducting polymers or metal oxides [38, 39]. These devices are also referred to as asymmetric HSCs.

iii) Battery-type Supercapacitor:

HSCs of this category consist of two distinct electrodes that belong to different energy storage mechanisms. One electrode is derived from SCs, while the other electrode is derived from batteries such as lead-acid (lead oxides), alkaline (nickel oxides) or lithium. Recent research has focused on exploring various combinations of SCs electrodes with battery-derived electrodes [37, 40]. These devices are of

particular interest not only because they offer potential solutions to overcome limitations associated with batteries but also due to their practical utility.

1.2 General Introduction of Sensors:

Industrial development on a massive scale has given rise to numerous environmental pollution issues worldwide. Pollution refers to the introduction of harmful contaminants into the environment, leading to undesirable alterations. The consequences of environmental pollution encompass global warming and various adverse effects on the delicate ecosystem. Regrettably, humans have not adequately addressed the severity of environmental pollution [41]. Consequently, the repercussions of environmental pollution have manifested in numerous natural and man-made disasters. The various types of pollution, air pollution has become a particularly severe threat to both the environment and living organisms.

Industrial processes release a plethora of toxic and hazardous gaseous pollutants into the atmosphere, making industries a major contributor to air pollution. Furthermore, air pollution also arises from domestic sources such as automobiles, home furnaces, stoves, open burning of refuse, and leaves. Factors like modern life styles, increasing urbanization, and the use of farming chemicals also play a significant role in worsening air quality. However, the primary culprit behind harmful gas emissions that cause air pollution remains the burning or combustion of fossil fuels [42]. Numerous harmful gases, including carbon dioxide (CO_2), carbon monoxide (CO), sulfur oxides (SO_x), nitrogen oxides (NO_x), chlorine (Cl_2), ethanol ($\text{C}_2\text{H}_5\text{OH}$), ammonia (NH_3), volatile organic compounds (VOC_s), and more, are released through industrial and human activities. These activities involve the combustion of fossil fuels in diverse sectors such as industries, vehicles, chemical plants, agriculture, and thermal power plants. Unfortunately, these harmful gases can have severe repercussions on human health, leading to respiratory infections, lung cancer, heart diseases, and other health issues. As a result, the real-time and effective detection of such harmful gases in the environment becomes a matter of utmost importance [43].

1.2.1 Sensors:

A sensor is an electronic devices or instruments that designed to receive physical, chemical, or biological signals and convert them into compatible electric

signals for electronic circuits and used for various purposes. The term ‘sensor’ is derived from the concept of mimicking or replicating human senses. Another term often used interchangeably with ‘sensor’ is ‘transducer’. Therefore, a sensor or transducer can detect an input signal and convert it into a suitable output signal. Sensors play a vital role in monitoring and controlling different systems, processes, and environments across various industries and applications. Sensors have diverse applications in numerous fields, including automobiles, airplanes, cellular telephones, radios, chemical plants, industrial facilities, and machinery integrity assessment. They are also utilized for monitoring the environment, detecting hazardous chemicals, toxic substances, explosive gases, and finding countless other applications [44].

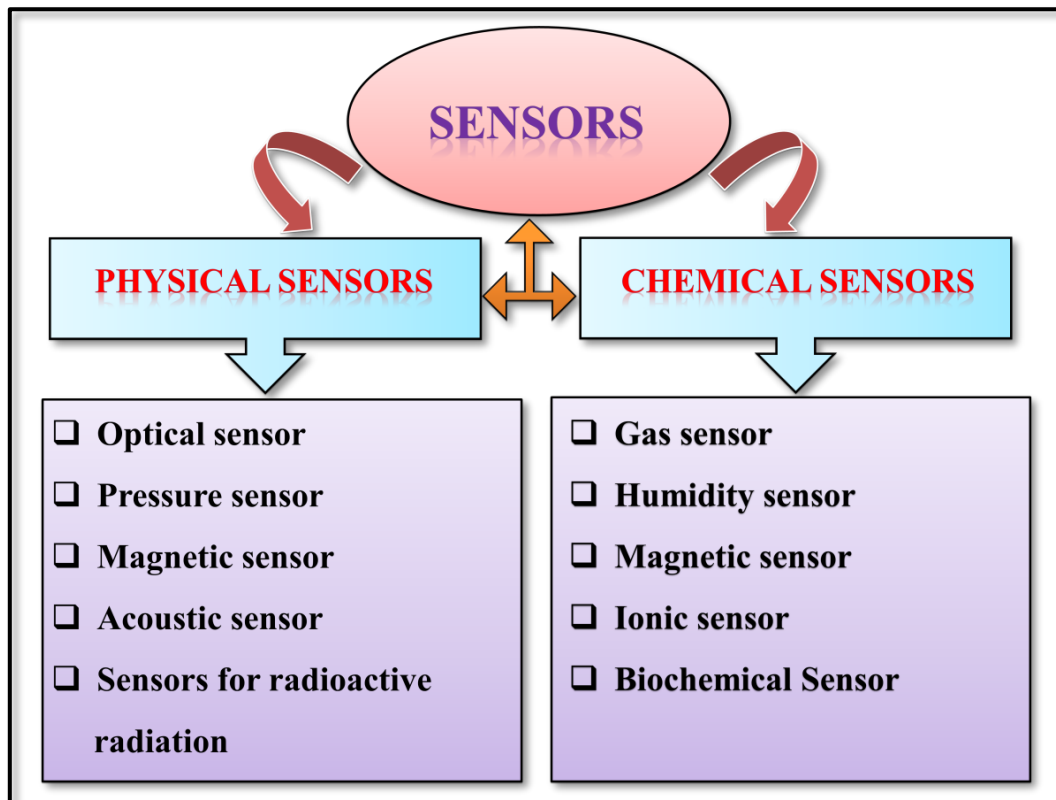


Chart 1.2: Classification of sensors

1.2.2 Classification of Sensors:

There are numerous types of sensors, each can be designed and categorized based on their purpose, conversion principle, fabrication technology, modes of applications, output signal, etc. The main classification of sensors is according to their principle of operation, which divides them into two categories: physical sensors and

chemical sensors. Physical sensors detect physical effects, while chemical sensors operate based on chemical effects, as depicted in **Chart 1.2**.

a) Physical Sensors: Physical sensors are devices used to collect data on the physical properties of a system. They operate based on different physical principles, such as photoelectric, piezoelectric, magnetostriction, ionization, thermoelectric, and magnetoelectric effects to carry out their operations. These sensors play a crucial role in detecting and measuring a wide range of physical parameters in different applications and industries.

b) Chemical Sensors: Chemical sensors are devices designed to convert chemical information into a useful analytical signal, which can vary from determining the concentration of a specific component in a sample to conducting a total composition analysis. These sensors operate based on chemical reactions occurring between the analyte (the chemical being detected) and the surface of the sensor. Various types of chemical sensors exist, including gas sensors, humidity sensors, magnetic sensors, ionic sensors, and biochemical sensors. They play a crucial role in detecting and monitoring different chemicals, enabling applications in environmental monitoring, healthcare, industrial processes, and other fields.

The progress in sensor technology has facilitated the creation of intelligent and interconnected systems commonly known as the Internet of Things (IoT). Through this network, data gathered from diverse sensors can be collected, analyzed, and utilized to make well-informed decisions, enhance efficiency, and deepen our comprehension of the environment and various processes. In recent years, there has been a growing global emphasis on addressing atmospheric pollution to safeguard the environment and mitigate health-related issues.

The detection of toxic and flammable gases has become a significant concern in both domestic and industrial sectors. As a result, the development of efficient gas sensors has garnered considerable attention in light of these concerns. Researchers worldwide are actively working towards advancing gas sensor technologies to enable accurate and reliable detection of hazardous gases, thereby addressing environmental and safety challenges.

1.2.3 Gas Sensor:

In the past few decades, the living standards of humans have experienced a remarkable uplift, due to industrial and technological revolutions. However, these advancements have also resulted in increased air pollution, posing significant environmental and human health challenges. As a consequence, the detection of toxic, hazardous, and flammable gases has become vital in safeguarding the environment and the well-being of living organisms [45]. Addressing these issues is crucial to ensure sustainable development and a healthier future for humanity.

As a result, the monitoring of air quality has become a crucial focus in current research activities. In parallel with industrialization, the development of technology for monitoring toxic and explosive gases has become necessary. While, the human olfactory system is effective in detecting and identifying many odors, it often falls short when it comes to hazardous gases or vapors. These substances may either be detectable only at extremely high concentrations or completely undetectable by our senses. This highlights the need for advanced technological solutions to accurately detect and monitor such hazardous gases in order to ensure environmental safety and human well-being.

The increasing need for gas sensors in environmental monitoring has spurred the creation of sensors employing a variety of materials, technologies, and principles. Significant advancements have been made in sensor technology, with future innovations expected. Gas detection devices are becoming crucial for applications including industrial safety, environmental monitoring, and process control.

As a result, significant research is ongoing in the field of gas sensors, with a focus on enhancing the performance of traditional devices through nano-engineering approaches. These efforts in gas sensor research aim to improve accuracy, reliability, and efficiency, ensuring their effectiveness in various monitoring applications. Depending on the required sensitivity and specific purposes, three comprehensive categories of gas monitoring are essential [46, 47].

The initial category is related to atmospheric oxygen monitoring. To maintain breathable atmospheres, it is crucial to monitor oxygen concentration at approximately 20%. For controlling combustion processes in devices like boilers and

internal combustion engines, a narrower range of 0-5% oxygen concentration monitoring is necessary.

The second category pertains to toxic gases present in the atmosphere, such as carbon monoxide (CO), hydrogen sulfide (H₂S), chlorine (Cl₂), nitrogen dioxide (NO₂), and others. To address this concern, the sensor must possess the ability to detect and measure concentrations of these toxic gases accurately, even at concentrations below hazardous levels, typically ranging from 1 part per million (ppm) to several hundred ppm.

The third category of gas monitoring focuses on explosive or flammable gases, such as acetylene (C₂H₂), ethylene (C₂H₄), propylene (C₃H₆), propane (C₃H₈), liquefied petroleum gas (LPG), and others. The primary objective here is to safeguard against potential fire or explosion incidents. To achieve this, the sensor must be capable of detecting and monitoring concentrations of explosive gases below their respective Lower Explosive Limit (LEL). For most gases, this LEL threshold lies within a range of up to a few percent concentrations in the air.

In summary, for toxic gas applications, the sensor should be proficient in measuring gases at low concentrations, typically in ppm. On the other hand, for combustible gas monitoring, the sensors capability lies in measuring high gas concentrations, often reaching several percent levels [46].

1.2.4 Types of Gas Sensor:

Based on their operating principles, chemical gas sensors can be categorized into following types,

- I) Solid electrolyte sensor,
- II) Catalytic combustion sensor, and
- III) Semiconductor gas sensor.

1.3 Literature Survey of Supercapacitor and Gas sensor:

Nanostructured rare earth metal sulfides and selenides have garnered significant interest for their impressive physical and electrical properties, which make them suitable for various applications in magnetic, catalysts, electronic, optical, and optoelectronic devices [48, 49]. The distinctive characteristics of Rare Earth Metal Chalcogenides (REMCs) include 4f vacant orbital, high mechanical stability, rapid

charge transfer, and high ionic conductivity at the electrode-electrolyte interaction [50, 51]. In recent years, nano-and microstructured rare earth metal sulfides and selenides have been explored as a novel class of energy storage materials. These materials share several advantageous properties, including a wider potential window, multiple valence states, improved charge-discharge performance, and higher energy density. One notable feature shared by sulfides and selenides is the ability of their metal component to exist in multiple valence states [52]. **Table 1.1** demonstrates the literature survey of rare earth chalcogenide and its composite based electrode materials for energy storage.

i) Dysprosium Sulfide:

Rare earth metal chalcogenides thin films have garnered significant attention for their wide range of applications, including electrochemical supercapacitors, solar cells, gas sensing and electrophotocatalysis, due to their favorable structural, electrical, and mechanical properties. Although they have not been extensively studied for energy storage purposes, they possess promising potential as quite competitive materials for supercapacitor applications. Dysprosium sulfide is an affordable and eco-friendly material that demonstrates good electrochemical performance. However, there are no available reports on the use of dysprosium sulfide in gas sensors, and only a few studies have investigated its application in SCs (**Table 1.1**). Dysprosium sulfide (Dy_2S_3) and dysprosium sulfide/reduced graphene oxide ($\text{Dy}_2\text{S}_3/\text{rGO}$) composite thin films were synthesized by Bagawde et al. [53, 54] via successive ionic layer adsorption and reaction (SILAR) method with C_s of 280 and 517 F g^{-1} at a scan rate 5 mV s^{-1} .

ii) Dysprosium Selenide:

Dysprosium selenide is another potential dysprosium chalcogenide that could be utilized as an electrode material for supercapacitors, especially when combined with reduced graphene oxide. Effective supercapacitor electrode design requires properties such as a wide potential window, high specific capacitance, high S_p , and rapid charge-discharge rates. Integrating metal chalcogenides with rGO can significantly enhance the electrochemical performance of the composite. However, no reports have been published on dysprosium selenide-based supercapacitors to date.

Consequently, this study focuses on exploring dysprosium selenide for supercapacitor applications.

1.3.1 Literature Survey on Rare Earth Metal Chalcogenide and its Composite Thin Films for Supercapacitor Performance:

Recently, Yadav et al. [55] prepared a honeycomb-like La_2O_3 using the spray pyrolysis method, achieving a C_s of 166 F g^{-1} at scan rate of 5 mV s^{-1} in 1 M LiClO_4 electrolyte, with 85 % cyclic retention after 3,000 cycles. In another study, Yadav et al. [56] fabricated a 3D irregular grain La_2O_3 thin film using the chemical bath deposition (CBD) method, obtaining a C_s of 147 F g^{-1} at scan rate of 5 mV s^{-1} in 1 M KOH electrolyte, with 96 % cyclic retention after 2,000 cycles. Yadav et al. [57] deposited microrod-like La_2O_3 electrode by hydrothermal method and reported C_s of 250 F g^{-1} with 81 % good cyclic stability after 1000 cycles. Zhang et al. [58] reported reduced graphene oxide/lanthanum oxide ($\text{RGO/La}_2\text{O}_3$) composites by simple reflux process and obtained high C_s of 156 F g^{-1} with 78% excellent cycle stability after 500 cycles. Miah et al. [59] synthesized La_2O_3 nanosheet decorated reduce graphene oxide ($\text{RGO/La}_2\text{O}_3$) by co-precipitation method and obtained C_s of 751 F g^{-1} with 67 % good cyclic stability. Naderi et al. [60] synthesis of Eu_2O_3 nanoparticles anchoring them onto the surface of reduced graphene oxide (rGO) ($\text{Eu}_2\text{O}_3\text{-rGO}$) by facile sonochemical procedure and reported C_s of 313 F g^{-1} at a scan rate of 2 mV s^{-1} in a $0.5 \text{ M Na}_2\text{SO}_4$ electrolyte. Aryanrad et al. [61] EuO_2 nanorods (EuNR)-RGO) were synthesized as electrode materials using the hydrothermal method, achieving a C_s of 403 F g^{-1} at scan rate of 2 mV s^{-1} in 3 M KCl electrolyte. Dhanalakshmi et al. [62] prepared gadolinia/nickel sulfide ($\text{Gd}_2\text{O}_3/\text{NiS}_2$) nanocomposite via simple two step hydrothermal method and found C_s of 354 F g^{-1} in 2 M KOH electrolyte. Kubra et al. [63] synthesised of praseodymium oxide/ hausmannite manganese oxide ($\text{Pr}_6\text{O}_{11}/\text{Mn}_3\text{O}_4$) nanocomposites by employing the hydrothermal route and obtained C_s of 795 F g^{-1} in 3 M KOH electrolyte. Ubale et al. [64] synthesised groundnuts-like samarium oxide (Sm_2O_3) thin film by hydrothermal method and exhibits maximum C_s of 155 F g^{-1} at 5 mVs^{-1} scan rate in 1 M KOH electrolyte.

Dezfuli et al. [65] prepared $\text{Sm}_2\text{O}_3/\text{RGO}$ nanocomposite by utilizing a facile sonochemical procedure and found C_s of 321 F g^{-1} in a $0.5 \text{ M Na}_2\text{SO}_4$ electrolyte. Prasanna et al. [66] prepared cerium oxide (CeO_2) by combustion approach with obtained C_s of 135 F g^{-1} in 1 M KOH electrolyte. Zahid et al. [67] prepared cerium

sulfide and graphene oxide ($\text{Ce}_2\text{S}_3/\text{GO}$) nanocomposite by hydrothermal method and obtained C_s of 53 F g^{-1} in 2 M KOH electrolyte. Pandit et al. [68] synthesized nanopebble like cerium selenide (CeSe_2) by SILAR method and obtained C_s of 285 F g^{-1} in $1 \text{ M Na}_2\text{SO}_3$ electrolyte. Patil et al. [69] reported C_s of 358 F g^{-1} at a scan rate of 5 mV s^{-1} in $1 \text{ M Na}_2\text{SO}_4$ electrolyte for SILAR deposited wave-like La_2S_3 thin films. Ghogare et al. [70] deposited nano petals-like lanthanum sulfide ($\beta\text{-La}_2\text{S}$) electrode by hydrothermal method and obtained C_s of 121 F g^{-1} at a scan rate of 5 mV s^{-1} in $1 \text{ M Na}_2\text{SO}_4$ electrolyte. Patil et al. [71] reported C_s of 256 F g^{-1} for porous $\alpha\text{-La}_2\text{S}_3$ thin films prepared by SILAR method.

Patil and Lokhande [72] achieved a specific capacitance of 294 F g^{-1} at a scan rate of 5 mV s^{-1} in 1 M LiClO_4 electrolyte using La_2S_3 thin films synthesized via CBD method. Ghogare et al. [73] prepared grass-like lanthanum sulfide/graphene oxide ($\text{La}_2\text{S}_3\text{-GO}$) composite thin films via SILAR method and reported C_s of 312 F g^{-1} at a scan rate of 5 mV s^{-1} in $1 \text{ M Na}_2\text{SO}_4$ electrolyte. Patil et al. [74] nanoflakes -like La_2Se_3 thin films synthesized and attained specific capacitance of 331 F g^{-1} at 5 mV s^{-1} scan rate in 2 M KOH electrolyte. Patil et al. [75] showed maximum C_s of 363 F g^{-1} for SILAR synthesized nanocubes La_2Se_3 thin films. Patil et al. [76] obtained C_s of 469 F g^{-1} at a scan rate of 2 mV s^{-1} in 1 M KOH electrolyte for CBD deposited cinnamon-like lanthanum telluride (La_2Te_3) thin films. Kumbhar et al. [77] prepared honeycomb-like samarium sulfide ($\alpha\text{-Sm}_2\text{S}_3$) thin films by SILAR and showed 294 F g^{-1} C_s at scan rate 5 mV s^{-1} in 1 M PC-LiClO_4 electrolyte. Kumbhar et al. [78] prepared Sm_2S_3 thin film material by CBD method for electrochemical behavior and reported C_s of 248 F g^{-1} with 94 % electrochemical stability in 1.5 M PC-LiClO_4 electrolyte. Kumbhar et al. [79] reported C_s of 294 F g^{-1} at a constant scan rate of 5 mV s^{-1} for SILAR synthesized $\alpha\text{-Sm}_2\text{S}_3$ thin films. Kumbhar et al. [80] deposited nanoflakes Sm_2S_3 thin films by CBD method and reported 213 F g^{-1} in 1 M PC-LiClO_4 electrolyte. Ghogare et al. [81] obtained the C_s of 360 F g^{-1} in $1 \text{ M Na}_2\text{SO}_4$ solution for SILAR synthesized nano-strips like graphene oxide /samarium sulfide ($\text{GO}/\text{Sm}_2\text{S}_3$) composite thin films.

Kumbhar et al. [82] prepared cross-linked nanorods of samarium selenide (Sm_2Se_3) thin film material by CBD method and reported C_s of 316 F g^{-1} with 87 % electrochemical stability in 1 M PC-LiClO_4 electrolyte. Kumbhar et al. [83] reported C_s of 207 F g^{-1} for barley-like Sm_2Te_3 films prepared via simple CBD method.

Kumbhar et al. [84] obtained cloud-like Sm_2Te_3 thin films which showed C_s of 144 F g^{-1} at a scan rate of 5 mV s^{-1} . Pujari et al. [85] showed C_s of 270 F g^{-1} for hydrothermally prepared monoclinic or nanoparticles and distributed nanorods-like ytterbium sulfide (Yb_2S_3) thin films. Ubale et al. [86] deposited nano grained Yb_2S_3 thin films through a CBD method and delivered C_s of 185 F g^{-1} in 1 M KOH electrolyte at a 5 mV s^{-1} scan rate. Ubale et al. [87] deposited Yb_2S_3 electrode by SILAR method and showed C_s of 181 F g^{-1} with 83% capacity retention up to 3000 CV cycles. Ubale et al. [88] reported graphene oxide/ytterbium sulfide ($\text{GO/Yb}_2\text{S}_3$) composite thin films exhibited the maximum C_s of 376 F g^{-1} in $1 \text{ M Na}_2\text{SO}_4$ electrolyte at scan rate of 5 mV s^{-1} . Bagawde et al. [53] reported SILAR synthesized dysprosium sulfide (Dy_2S_3) thin films showed a maximum C_s of 273 F g^{-1} in $1 \text{ M Na}_2\text{SO}_4$ electrolyte at scan rate of 5 mV s^{-1} . Bagawde et al. [54] reported $\text{Dy}_2\text{S}_3/\text{rGO}$ thin films synthesized by using SILAR method exhibited C_s of 517 F g^{-1} in an in $1 \text{ M Na}_2\text{SO}_4$ electrolyte at scan rate of 5 mV s^{-1} .

According to a review of the literature survey, few reports are available on Dy_2S_3 and $\text{rGO/Dy}_2\text{S}_3$ and no report available on Dy_2Se_3 and $\text{rGO/Dy}_2\text{Se}_3$ preparation by chemical methods. So, our aim is to prepare Dy_2S_3 , $\text{rGO/Dy}_2\text{S}_3$, Dy_2Se_3 and $\text{rGO/Dy}_2\text{Se}_3$ using simple chemical methods, such as CBD and SILAR. These are promising methods for the preparation of metal chalcogenide thin films over stainless steel (SS) substrate. Those methods are probably easiest, low cost, and suitable to prepare large-area, binder-free thin film electrodes for SC applications.

Table 1.1: Supercapacitor performances of rare earth metal chalcogenide and theirs composite thin films

Sr. No.	Deposited Materials	Method of Preparation	Substrate	Structure	Electrolyte	Potential Window (V)	Specific Capacitance (F g^{-1})	Electrochemical Stability (%) (Cycles)	Ref. No.
1	La_2O_3	Spray pyrolysis	Glass & FTO	Honey-comb like	1 M LiClO_4	0.0 to -0.6	166	85 (3000)	[55]
2	La_2O_3	CBD	Stainless steel (SS)	3D irregular grains	1 M KOH	-0.1 to -0.8	147	96 (2000)	[56]
3	La_2O_3	Hydrothermal	SS	Microrod like	1 M KOH	0.0 to -0.7	250	81 (1000)	[57]
4	RGO/ La_2O_3	Reflux	Nickel foam (NF)	Rod-like nanoparticles	3 M KOH	-1.0 to 0.0	156	78 (500)	[58]
5	RGO/ La_2O_3	Co-precipitation	Copper foil	Nano sheets	1 M H_2SO_4	0.0 to 0.9	751	67 (2000)	[59]
6	Eu_2O_3 -rGO	Facile sonochemical	SS	Layered and wrinkled	0.5 M Na_2SO_4	0.1 to -0.9	313	97.6 (5000)	[60]
7	Eu_2O_3 -rGO	Hydrothermal	Steel grid	Nanorods	3 M KCl	0.1 to -0.9	403	96.8 (5000)	[61]
8	$\text{Gd}_2\text{O}_3/\text{NiS}_2$	Hydrothermal	NF	Mesospheres-microspheres	2 M KOH	0.5 to -0.5	354	98 (5000)	[62]
9	Praseodymium oxide($\text{Pr}_6\text{O}_{11}/\text{Mn}_3\text{O}$)	Hydrothermal	NF	Regular network	3 M KOH	0 to 0.5	795	80 (800)	[63]
10	Sm_2O_3	Hydrothermal	SS	Porous groundnuts-like	1 M KOH	-1.2 to -0.5	155	Not reported	[64]

Sr. No.	Deposited Materials	Method of Preparation	Substrate	Structure	Electrolyte	Potential Window (V)	Specific Capacitance (F g ⁻¹)	Electrochemical Stability (%) (Cycles)	Ref. No.
11	Sm ₂ O ₃ -rGO	Sonochemical	SS	Layered and wrinkled	0.5 M Na ₂ SO ₄	-0.8 to 0.2	321	99 (4000)	[65]
12	CeO ₂	Combustion	NF	Soapsuds-like	1 M KOH	-0.3 to 0.45	135	92.5 (1000)	[66]
13	Cerium sesquisulfide/Graphene oxide (Ce ₂ S ₃ /GO)	Hydrothermal	NF	Grass like	2 M KOH	0 to 0.4	53	Not reported	[67]
14	Cerium selenide (CeSe ₂)	SILAR	SS	Nano-pebble like	1 M Na ₂ SO ₃	0 to -0.9	285	85.5 (4000)	[68]
15	Lanthanum sulfide (La ₂ S ₃)	SILAR	SS	Porous ridges	1 M Na ₂ SO ₄	-0.3 to -1.1	358	78 (1000)	[69]
16	Lanthanum sulfide (β-LaS ₂)	Hydrothermal	SS	Petals	1 M Na ₂ SO ₄	0 to -1.15	121	Not reported	[70]
17	Lanthanum sulfide (α-La ₂ S ₃)	SILAR	SS	Porous	1 M LiClO ₄	0 to -1.2	256	85 (1000)	[71]
18	Lanthanum sulfide (La ₂ S ₃)	CBD	SS	Compact and small grains	1 M LiClO ₄	0 to -1.2	294	89 (1000)	[72]
19	Lanthanum sulfide/graphene	SILAR	SS	Grass-like	1 M Na ₂ SO ₄	0 to -1.0	312	94 (1000)	[73]

Sr. No.	Deposited Materials	Method of Preparation	Substrate	Structure	Electrolyte	Potential Window (V)	Specific Capacitance (F g ⁻¹)	Electrochemical Stability (%) (Cycles)	Ref. No.
	oxide (La ₂ S ₃ -GO)								
20	Lanthanum selenide (La ₂ Se ₃)	CBD	SS	Nanoflakes	2 M KOH	-0.2 to -1.1	331	84 (1000)	[74]
21	Lanthanum selenide (La ₂ Se ₃)	SILAR	SS	Nanocubes	0.8 M PC-LiClO ₄	0 to -1.3	363	83 (1000)	[75]
22	Lanthanum telluride (La ₂ Te ₃)	CBD	SS	Cinnamon -like	1M KOH	-0.3 to -1.3	469	73 (1000)	[76]
23	Samarium sulfide (α-Sm ₂ S ₃)	SILAR	SS	Nanoporous honeycomb	1 M PC-LiClO ₄	0.0 to -1.2	294	89 (1000)	[77]
24	Samarium sulfide (Sm ₂ S ₃)	CBD	SS	Porous network	1.5 M PC-LiClO ₄	0.0 to -1.3	248	94 (1500)	[78]
25	Samarium sulfide (α-Sm ₂ S ₃)	SILAR	SS	Porous	1 M PC-LiClO ₄	0.0 to -1.2	294	Not reported	[79]
26	Samarium sulfide (Sm ₂ S ₃)	CBD	SS	Nanoflakes	1 M PC-LiClO ₄	0.0 to -1.3	213	81 (1000)	[80]
27	Graphene oxide /Samarium sulfide (GO/Sm ₂ S ₃)	SILAR	SS	Nano-strips like	1 M Na ₂ SO ₄	0.0 to -1.0	360	88 (2000)	[81]
28	Samarium selenide	CBD	SS	Nanorods	1 M PC-	0.0 to -1.3	316	87 (1000)	[82]

Sr. No.	Deposited Materials	Method of Preparation	Substrate	Structure	Electrolyte	Potential Window (V)	Specific Capacitance (F g ⁻¹)	Electrochemical Stability (%) (Cycles)	Ref. No.
	(Sm ₂ Se ₃)				LiClO ₄				
29	Samarium telluride (Sm ₂ Te ₃)	CBD	SS	Barley-like	1 M PC-LiClO ₄	0.0 to -1.3	207	78 (1000)	[83]
30	Samarium telluride (Sm ₂ Te ₃)	SILAR	SS	Cloud like	1 M PC-LiClO ₄	0.0 to -1.3	144	69.3 (1000)	[84]
31	Ytterbium sulfide (Yb ₂ S ₃)	Hydrothermal	SS	Nanorod like	1 M Na ₂ SO ₄	0.0 to -1.0	270	79.5 (1000)	[85]
32	Ytterbium sulfide (Yb ₂ S ₃)	CBD	SS	Nano grained	1 M KOH	-0.2 to -1.2	185	81 (2000)	[86]
33	Ytterbium sulfide (Yb ₂ S ₃)	SILAR	SS	Porous	1 M Na ₂ SO ₄	0.0 to -1.0	181	83 (3000)	[87]
34	Graphene oxide/ Ytterbium sulfide (GO/Yb ₂ S ₃)	SILAR	SS	Porous	1 M Na ₂ SO ₄	0.0 to -1.0	376	94 (3000)	[88]
35	Dysprosium sulfide (Dy ₂ S ₃)	SILAR	SS	Dense surface	1 M Na ₂ SO ₄	0.0 to -1.0	273	Not reported	[53]
36	Dysprosium sulfide/reduced graphene oxide (Dy ₂ S ₃ /rGO)	SILAR	SS	Compact nanosheets	1 M Na ₂ SO ₄	0.1 to -0.9	517	88 (5000)	[54]

1.3.2 Literature Survey on Metal Sulfide and its Composite Thin Films for Gas Sensing Performance:

Transition metal sulfide has received a lot of attention in various fields, including supercapacitors, solar cells, catalysis, and gas sensors. Due to its distinct morphology and superior mechanical, electrical, and electrochemical properties. The operation of metal sulfides (MSs) in gas sensors relies on changes in conductivity triggered by interactions with gas molecules, with performance primarily influenced by the operating temperature. An inorganic sulfur anion is known as sulfide, and one or more S^{2-} ions are known as sulfur dioxide, with the chemical formula S_2 . MS is a combination of sulfur anions and metal/semi-metal cations. In the form of M_xS_y ($x:y = 1:1, 1:2, 2:1, 3:4$) [89, 90]. However, there are no reports on dysprosium sulfide for gas sensors. Therefore, various other transition MSs and their composites for gas sensor performance are described in **Table 1.2**.

Burungale et al. [91] proposed a NO_2 gas sensor using PbS nanoparticulate thin films, synthesized by the simple SILAR method, which showed a high sensitivity of 35% towards NO_2 at 50 ppm concentration at 423 K temperature with a rapid response time of 6 s. Vanalakar et al. [92] synthesized CdS nanowire mesh via a wet chemical route at relatively low temperatures. The proposed NO_2 gas sensor showed a high gas response of about 1850% of 100 ppm of NO_2 gas at 473 K. Navele et al. [93] prepared a thin film of CdS by the CBD method and showed a high sensitivity of 61% for 200 ppm NO_2 at room temperature. Wang et al. [94] A thermo-evaporation-grown single-crystalline ZnS NWs-based gas sensor with good sensing selectivity 21% of 100 ppm for acetone at 593 K. Souissi et al. [95] fabricated In_2S_3 thin film by spray pyrolysis and proposed it for the detection of ethanol. The sensor response toward 5000 ppm NO_2 was 6% at 623 K. Kim et al. [96] A 2D NbS_2 -based NO_2 sensor at room temperature that showed a response of 18% to 5 ppm NO_2 . Xu et al. [97] reported ultra-thin WS_2 NSs by using a hydrothermal and calcination procedure, and the sensor response of 9 % toward 0.1 ppm NO_2 gas at ambient temperature. Ou et al. [98] 2D SnS_2 -based gas sensors demonstrated high NO_2 sensing selectivity and reversibility with a response of 35% to 10 ppm NO_2 at 393 K.

Late et al. [99] synthesized MoS_2 by using the micromechanical exfoliation (ME) method and the sensor response of 1372% of 1000 ppm towards NO_2 at room temperature. Navale et al. [100] The PbS thin films were fabricated using the CBD

method. The developed sensor showed high selectivity for NO₂, with a sensitivity of 74 for 100 ppm NO₂ gas at room temperature. Wang et al. [101] reported SnS thin film for NO₂ gas sensor, which exhibit excellent selectivity and reversibility at room temperature in addition to a high response of 20% towards NO₂ at 0.1 ppm concentration. Wang et al. [102] fabricated a flower shaped CuS by facile hydrothermal method-based ethanol gas sensor, which showed a sensing selectivity of 5.22% of 100 ppm ethanol concentration at 443 K temperature.

Fu T-X et al. [103] chemically synthesized a Bi₂S₃ thin film based NH₃ sensor with a high sensitivity of 40% of 200 ppm NH₃ at room temperature. Li et al. [104] fabricated flexible devices for formaldehyde detection at room temperature using gas sensors based on rGO/MoS₂ hybrid films. They showed a high sensitivity of 2.8% of 10 ppm towards formaldehyde at room temperature. Roshan et al [105] Prepared PbS NCs/rGO hybrids via the hydrothermal method. The sensor has shown a good response of 45% of 10000 ppm towards methane at room temperature. Wu et al. [106] synthesized SnS₂/rGO composite based NO₂ sensor and showed a high sensitivity of 50% of 8 ppm towards NO₂ at room temperature. Shao et al. [107] synthesized rGO-MoS₂-CdS nanocomposite films through solvothermal processing and evaluated their sensing performance. The sensor response toward 0.2 ppm NO₂ was 27%.

In summary of the literature survey, there are various reports on metal sulfides and their composites for gas sensors. However, there are no reports available for dysprosium sulfide and its composites for gas sensors. Therefore, the aim is to synthesize Dy₂S₃ and rGO/Dy₂S₃ by using chemical processes like the chemical bath deposition (CBD) method.

Table 1.2: Gas sensing performance of various metal sulfide and its composite thin films

Sr. No.	Material	Method of Preparation	Working Temperature (K)	Gas	Gas Concentration (ppm)	Sensitivity (%)	Sensitivity Definition (%)	Ref.
1	PbS	SILAR	423	NO ₂	50	35	$(R_a - R_g)/R_a$	[91]
2	CdS	Wet chemical route	473	NO ₂	100	1850	$(R_g - R_a/R_a) \times 100$	[92]
3	CdS	CBD	RT	NO ₂	200	61	$(R_g - R_a/R_a) \times 100$	[93]
4	ZnS	Thermal evaporation	593	Acetone	100	21	$S = R_a/R_g$	[94]
5	β -In ₂ S ₃	Spray pyrolysis	623	Ethanol	5000	6	I_{EtOH}/I_{Dryair}	[95]
6	NbS ₂	CVD	RT	NO ₂	5	18	$(\Delta R/R_0)$	[96]
7	WS ₂	Hydrothermal	RT	NO ₂	0.1	9	---	[97]
8	SnS ₂	Solvothermal	393	NO ₂	10	35	R_g/R_a for $R_g > R_a$, or R_a/R_g for $R_g < R_a$	[98]
9	MoS ₂	ME	RT	NO ₂	1000	1372	$(R_g - R_{N_2}) / R_{N_2}$	[99]
10	PbS	CDB	RT	NO ₂	100	74	$(R_g - R_a/R_a) \times 100$	[100]
11	SnS	Solvothermal	RT	NO ₂	0.1	20	$(R_a - R_g)/R_a$	[101]
12	CuS	Hydrothermal	443	Ethanol	100	5.22	R_g/R_a	[102]
13	Bi ₂ S ₃	Chemical synthesis	RT	NH ₃	200	40	(R_a/R_g)	[103]
14	rGO/MoS ₂	Layer-by-Layer (LBL) self-assembled	RT	Formaldehyde	10	2.8	$(\Delta R/R) \times 100$	[104]

Sr. No.	Material	Method of Preparation	Working Temperature (K)	Gas	Gas Concentration (ppm)	Sensitivity (%)	Sensitivity Definition (%)	Ref.
15	PbS NCs/rGO	Hydrothermal	RT	Methane (CH ₄)	10000	45	$(R_g - R_a)/R_a \times 100$	[105]
16	SnS ₂ /rGO	Hydrothermal	RT	NO ₂	8	50	--	[106]
17	rGO-MoS ₂ -CdS	Solvothermal	373	NO ₂	0.2	27	$(R_g - R_a)/R_a \times 100$	[107]

1.4 Orientation and Purpose of the Thesis:

Recently, researchers have concentrated on improving SCs in four key areas: S_E , S_P , cycle life, and cost-effective electrodes. The performance of SCs largely depends on having a high surface area and rapid reversible redox reactions. To boost SC performance, it is essential to explore new electrode materials that exhibit greater conductivity, higher redox potential of cations, and a large surface area with a porous electrode structure.

In the present times, the environment is contaminated with a variety of toxic gases, including CO, H₂S, CO₂, NH₃, NO₂, CH₄, and H₂. These gases play a significant role in global warming, and climate change and have adverse effects on human health. Therefore, there is a pressing need for devices that can detect flammable, explosive, and toxic gases early. Gas sensors have been developed to effectively monitor the concentration of these harmful gases. Semiconductor-based resistive gas sensors are particularly popular for their straightforward construction and simple design. These sensors offer a practical and efficient solution for identifying hazardous gases, enabling timely responses, and safeguarding the environment and human well-being.

The literature study reveals a diverse range of materials, including REMC, carbon materials, and their composites, which have been extensively studied as electrode materials for SC fabrication. Recent research trends have shifted towards depositing mixed metal chalcogenide or carbon-based composites to achieve enhanced SC performance in terms of S_E and S_P . Notably, the use of REMC electrodes has shown promising results, with an expanded operating potential window contributing to overall improved SC performance.

Among the various materials, rGO composite with REMC holds significant potential for SC applications, yet it remains relatively unexplored in current research. To advance the development of high-performance and efficient SC, there is a critical need to create advanced electrode materials that can deliver high C_s while simultaneously enhancing S_E without compromising S_P . To produce this type of electrode material, using a simple, cost-effective chemical method is crucial to keep SC costs low. CBD and SILAR offer several benefits and are commonly used for large-area deposition, which is advantageous for device fabrication. For the

preparation of such electrode materials, it is crucial to cost-effective and convenient chemical route to ensure the overall affordability of the SC cell.

The objective of this study to investigation the electrochemical properties of Dy_2S_3 , $\text{rGO/Dy}_2\text{S}_3$, Dy_2Se_3 and $\text{rGO/Dy}_2\text{Se}_3$ electrodes are employed in techniques like cyclic voltammetry (CV), galvanostatic charge-discharge (GCD), and electrochemical impedance spectroscopy (EIS). For these measurements, Dy_2S_3 , $\text{rGO/Dy}_2\text{S}_3$, Dy_2Se_3 and $\text{rGO/Dy}_2\text{Se}_3$ working electrode will be used, with a Saturated Calomel Electrode (SCE) as the reference electrode and a platinum sheet as the counter electrode. The performance of Dy_2S_3 , $\text{rGO/Dy}_2\text{S}_3$, Dy_2Se_3 and $\text{rGO/Dy}_2\text{Se}_3$ thin films will be thoroughly assessed based on various parameters, including C_s , electrochemical stability, and equivalent series resistance (R_s). Subsequently, Flexible Solid-State Asymmetric Supercapacitors (FSSASCs) devices will be fabricated, and their electrochemical performance will be evaluated. The evaluation will involve assessing C_s , S_E , S_P , electrochemical stability, and R_s . Furthermore, the impact of device bending on the electrochemical performance of the solid-state devices will be studied to assess their applicability in diverse portable electronic devices. This study aims to provide valuable insights into the potential practical applications of these materials in flexible and portable electronic devices.

Another sensor application of thin films of Dy_2S_3 and $\text{rGO/Dy}_2\text{S}_3$ will be studied on the exposure of analyte gas at optimized operating temperature. These films will be evaluated for their potential applications in gas sensors. The gas sensing properties of Dy_2S_3 and $\text{rGO/Dy}_2\text{S}_3$ films will be investigated using a custom-built computer-based gas sensor assembly. Further, the sensitivity, response, and recovery time of the sensors will be studied at an optimized operating temperature and a fixed concentration of gas. Finally, the selectivity of these films will be determined in the presence of other gases to assess their ability to discriminate against different gases. By conducting these analyses and evaluations, this study aims to provide valuable insights into the gas sensing potential of $\text{rGO/Dy}_2\text{S}_3$ thin films, which could lead to their application in various sensors.

1.5 References:

- [1] P. Simon, and Y. Gogotsi, *Nat. Mater.*, 7, (2008), 845-854.
- [2] G. Zhou, L. Xu, G. Hu, L. Mai, Yi Cui, *Chem. Rev.*, 119, (2019), 11042-11109.
- [3] G. Eranna, B. Joshi, D. Runthal, R. Gupta, *Crit. Rev. Solid State Mater. Sci.*, 29, (2004), 111-188.
- [4] X. Wei, E. Li, Y. Guan, Y. Chong, *J. Electromag. Wave*, 23, (2009), 925-934.
- [5] W. Martin and J. Brodd, *Chem. Rev.*, 104, (2004), 4245-4270.
- [6] H. Omanda, T. Brousse, C. Marhi, D. Schleich, *J. Electrochem. Soc.*, 151, (2004), 922-929.
- [7] J. Tarascon and M. Armand, *Nature*, 414, (2001), 171-179.
- [8] S. Moura, J. Siegel, D. Siegel, H. Fathy, A. Stefanopoulou, 2010 IEEE Veh. Power Propuls. Conf. VPPC, (2010), 1-6.
- [9] L. Zhang, and X. Zhao, *Chem. Soc. Rev.*, 38, (2009), 2520-2531.
- [10] D. Dubal, J. Kim, Y. Kim, R. Holze, C. Lokhande, W. Kim, *Energy Technol.* 2, (2014), 325–341.
- [11] P. Nikam, P. Baviskar, J. Sali, K. Gurav, J. Kim, B. Sankapal, *Ceram. Int.* 41, (2015), 10394–10399.
- [12] C. Lokhande, D. Dubal, O. Joo, *Curr. Appl. Phys.* 11, (2011), 255–270.
- [13] V. Lokhande, A. Lokhande, C. Lokhande, J. Kim, T. Ji, *J. Alloy. Compd.* 682, (2016), 381–403.
- [14] G. Gund, D. Dubal, S. Shinde, C. Lokhande, *ACS Appl. Mater. Interfaces*, 6, (2014), 3176-3188.
- [15] <https://en.wikipedia.org/wiki/Supercapacitor>.
- [16] J. Long, D. Bélanger, T. Brousse, W. Sugimoto, M. Sassin, O. Crosnier, *MRS Bull.* 36, (2011), 513-522.
- [17] G. Wang, L. Zhang, J. Zhang, *Chem. Soc. Rev.* 41, (2012), 797-828.
- [18] F. Shi, L. Li, X. Wang, C. Gu, J. Tu, *RSC Adv.* 4, (2014), 41910-41921.
- [19] M. Jayalakshmi and K. Balasubramanian, *Int. J. Electrochem. Sci.*, 3, (2008), 1196-1217.
- [20] F. Ma, S. Ding, H. Ren, Y. Liu, *RSC Adv.* 9, (2019), 2474-2483.

-
- [21] J. Guo, Q. Zhang, Q. Li, J. Sun, C. Li, B. He, Z. Zhou, L. Xie, M. Li, Y. Yao, *ACS Appl. Mater. Interfaces*, 10, (2018), 29705-29711.
- [22] D. Dubal, N. Chodankar, Z. Caban-Huertas, F. Wolfart, M. Vidotti, R. Holze, C. Lokhande, P. Gomez-Romero, *J. Power Sources*, 308, (2016), 158-165.
- [23] J. Ren, W. Bai, G. Guan, Y. Zhang, H. Peng, *Adv. Mater.*, 25, (2013), 5965-5970.
- [24] B. Nagar, D. Dubal, L. Pires, A. Merkoci, P. Gomez-Romero, *ChemSusChem.*, 11, (2018), 1849-1858.
- [25] K. Pinkert, M. Oschatz, L. Borchardt, M. Klose, M. Zier, W. Nickel, L. Giebeler, S. Oswald, S. Kaskel, J. Eckert, *ACS Appl. Mater. Interfaces*, 6, (2014), 2922-2928.
- [26] N. Chodankar, H. Pham, A. Nanjundan, J. Fernando, K. Jayaramulu, D. Golberg, Y. Han, D. Dubal, *Small*, 16, (2020), 2002806-2002841.
- [27] Z. Wen, W. She, Y. Li, R. Che, *J. Mater. Chem. A*, 2, (2014), 20729-20738.
- [28] W. Chen, R. Rakhi, H. Alshareef, *Nanoscale*, 5, (2013), 4134-4138.
- [29] J. Xu, T. Xiao, X. Tan, P. Xiang, L. Jiang, D. Wu, J. Li, S. Wang, *J. Alloys Compd.*, 706, (2017), 351-357.
- [30] K. Xing, L. Huang, L. Fang, *Dalton Trans.*, 45, (2016), 17439-17446.
- [31] S. Lyu, H. Chang, F. Fu, L. Hu, J. Huang, S. Wang, *J. Power Sources*, 327, (2016), 438-446.
- [32] K. Naoi and P. Simon, *Electrochem. Soc. Interface*, 17, (2008), 7-34.
- [33] J. Shayeh, M. Sadeghinia, S. Siadat, A. Ehsani, M. Rezaeid, M. Omid, *J. Colloid Interface Sci.*, 496, (2017), 401-406.
- [34] A. Muzaffar, M. Ahamed, K. Deshmukh, J. Thirumalai, *Renew. Sustain. Energy Rev.*, 101, (2019), 123-145.
- [35] K. Kumar, N. Choudhary, Y. Jung, J. Thomas, *ACS Energy Lett.*, 3, (2018), 482-495.
- [36] A. Bryan, L. Santino, Y. Lu, S. Acharya, J. D'Arcy, *Chem. Mater.*, 28, (2016), 5989-5998.
- [37] D. Dubal, G. Gund, C. Lokhande, R. Holze, *ACS Appl. Mater. Interfaces*, 5, (2013), 2446-2454.
- [38] H. Wang and L. Pilon, *J. Phys. Chem. C*, 115, (2011), 16711-16719.
- [39] Y. Wang and Y. Xia, *Electrochim. Acta*, 51, (2006), 3193-3384.
-

- [40] S. Kulkarni, A. Jagadale, V. Kumbhar, R. Bulakhe, S. Joshi, C. Lokhande, *Int. J. Hydrogen Energy*, 38, (2010), 4046-4053.
- [41] G. Gund, D. Dubal, B. Patil, S. Shinde, C. Lokhande, *Electrochim. Acta*, 92, (2013), 205-215.
- [42] P. Moore, *Nature*, 374, (1995), 117-118.
- [43] S. Patil, V. Patil, S. Shendage, N. Harale, S. Vanalakar, J. Kim, *Ceram. Int.*, 42, (2016), 16160-16168.
- [44] J. Fraden, *Handbook of modern sensors: physics, designs, and applications* 5th edition springer, 1994.
- [45] R. Ionescu, A. Hoel, C. G. Granqvist, E. Llobet, P. Heszler, *Sens. Actuators B chem.*, 104, (2005), 124-131.
- [46] Ph. D. thesis, V. R. Shinde, Chemical preparation of zinc oxide thin films and their applications in gas sensors, (2005), Shivaji University, Kolhapur.
- [47] P. Moseley, *Meas. Sci. Technol.*, 8, (1997), 223-237.
- [48] S. Shen and Q. Wang, *Chem. Mater.*, 25, (2013), 1166-1178.
- [49] S. Yang, H. Yao, M. Gao, S. Yu, *Cryst. Eng. Comm.*, 11, (2009), 1383-1390
- [50] S. Liang, H. Wang, Y. Li, H. Qin, Z. Luo, B. Huang, X. Zhao, C. Zhao, L. Chen, *Sustain. Energy Fuels*, 4, (2020), 3825-3847.
- [51] S. Arunachalam, B. Kirubasankar, D. Pan, H. Liu, C. Yan, Z. Guo, S. Angaiah, *Green Energy Environ.*, 5, (2020), 259-273.
- [52] R. Barik and P. Ingole, *Curr. Opin. Electrochem.*, 21, (2020), 327-334.
- [53] P. Bagwade, D. Malavekar, S. Ubale, T. Ghogare, R. Bulakhe, I. In, U. Patil, C. Lokhande, *Solid State Sci.*, 119, (2021), 106693-106699.
- [54] P. Bagwade, D. Malavekar, T. Ghogare, S. Ubale, V. Mane, R. Bulakhe, I. In, C. Lokhande, *J. Alloys Compd.*, 859, (2021), 157829-157838.
- [55] A. Yadav, A. Lokhande, R. Pujari, J. Kim, C. Lokhande, *J. Colloid Interface Sci.* 484, (2016), 51–59.
- [56] A. Yadav, V. Kumbhar, S. Patil, N. Chodankar, C. Lokhande, *Ceram. Int.*, 42, (2016), 2079-2084.
- [57] A. Yadav, A. Lokhande, J. Kim, C. Lokhande, *Int. J. Hydrog. Energy*, 41, (2016), 18311-18319.

- [58] J. Zhang, Z. Zhang, Y. Jiao, H. Yang, Y. Li, J. Zhang, P. Gao, J. Power Sources, 419, (2019), 99-105.
- [59] M. Miah, S. Bhattacharya, D. Dinda, S. Saha, Electrochim. Acta, 260, (2018), 449-458.
- [60] H. Naderi, M. Ganjali, A. Dezfuli, J. Mater. Sci. Mater. Electron., 29, (2018), 3035–3044.
- [61] P. Aryanrad, H. Naderi, E. Kohan, M. Ganjali, M. Baghernejade, A. Dezfuli, RSC Adv., 10, (2020), 17543-1752.
- [62] S. Dhanalakshmi, A. Vathani, V. Muthuraj, N. Prithivikumaran, S. Karuthapandian, J. Mater. Sci. Mater. Electron., 31, (2020), 3119–3129.
- [63] K. Kubra, A. Javaid, B. Patil, R. Sharif, A. Salman, S. Shahzadi, S. Siddique, S. Ghani, Ceram. Int., 45, (2019), 6819-6827.
- [64] S. Ubale, T. Ghogare, V. Lokhande, T. Ji, C. Lokhande, SN Appl. Sci., 2, (2020), 756-761.
- [65] A. Dezfuli, M. Ganjali, H. Naderi, Appl. Surf. Sci., 402, (2017), 245-253.
- [66] K. Prasannaa, P. Santhoshkumar, Y. Joa, I. Sivagami, S. Kanga, Y. Joea, C. Lee, Appl. Surf. Sci., 449, (2018), 454-460.
- [67] M. Zahid, N. Yasmin, M. Ashiq, M. Safdar, M. Mirza, Phys. B: Condens. Matter, 624, (2022), 413359-413376.
- [68] B. Pandit, A. Agarwal, P. Patel, B. Sankapal, Nanoscale Adv., 3, (2021), 1057-1066
- [69] S. Patil, A. Lokhande, C. Lokhande, Mater. Sci. Semicond. Process, 41, (2016), 132-136.
- [70] T. Ghogare, R. Pujari, A. Lokhande, C. Lokhande, Applied Physics A, 124, (2018), 248-253.
- [71] S. Patil, V. Kumbhar, B. Patil, R. Bulakhe, C. Lokhande, J. Alloys Compd., 611, (2014), 191-196.
- [72] S. Patil, and C. Lokhande, Mater. Des., 87, (2015), 939-948.
- [73] T. Ghogare, A. Lokhande, R. Pujari, C. Lokhande, SN Appl. Sci., 110, (2019), 1-7
- [74] S. Patil, R. Bulakhe, C. Lokhande, ChemPlusChem., 80, (2015), 1478-1487.
- [75] S. Patil, V. Lokhande, N. Chodankar, C. Lokhande, J. Colloid Interface Sci., 469, (2016), 318-324.
- [76] S. Patil, B. Patil, R. Bulakhe, C. Lokhande, RSC Adv., 4, (2014), 56332-56341.

- [77] V. Kumbhar, A. Jagadale, C. Lokhande, J. Power Sources, 234, (2013), 107-110.
- [78] V. Kumbhar, A. Lokhande, N. Gaikwad, C. Lokhande, Phys. B: Condens. Matter, 33, (2015), 136–139.
- [79] V. Kumbhar, A. Jagadale, N. Gaikwad, C. Lokhande, Mater. Res. Bull, 56, (2014), 39-44.
- [80] V. Kumbhar, A. Lokhande, N. Gaikwad, C. Lokhande, Ceram. Int., 41, (2015), 5758-5764.
- [81] T. Ghogare, V. Lokhande, T. Ji, U. Patil, C. Lokhande, Surf. Interfaces, 19, (2020), 100507-100514.
- [82] V. Kumbhar, A. Lokhande, N. Chodankar, N. Gaikwad, C. Lokhande, Mater. Lett., 223, (2018), 45-48.
- [83] V. Kumbhar, A. Lokhande, N. Gaikwad, C. Lokhande, J. Phys. Chem. Lett., 645, (2016), 112-117.
- [84] V. Kumbhar, A. Lokhande, N. Gaikwad, C. Lokhande, Mat. Sci. Semicon. Proc., 46, (2016), 29-34.
- [85] R. Pujari, A. Lokhande, T. Ghogare, S. Kale, C. Lokhande, J. Mater. Sci.: Mater. Electron, 29, (2018), 14116-14121.
- [86] S. Ubale, R. Bulakhe, V. Mane, D. Malavekar, I. In. C. Lokhande, Appl Nanosci, 10, (2020), 5085–5097.
- [87] S. Ubale, S. Kale, V. Mane, P. Bagwade, C. Lokhande, J Solid State Electrochem, 25, (2021), 1753–1764.
- [88] S. Ubale, S. Kale, V. Mane, U. Patil, C. Lokhande, J. Electroanal. Chem., 897, (2021), 115589-115607.
- [89] S. Chandrasekaran, L. Yao, L. Deng, C. Bowen, Y. Zhang, S. Chen, Z. Lin, F. Peng and P. Zhang, Chem. Soc. Rev., 48, (2019), 4178-4280.
- [90] Y. Cui, Z. Zhou, T. Li, K. Wang, J. Li and Z. Wei, Adv. Funct. Mater, 29, (2019), 1900040-1900073.
- [91] V. Burungale, R. Devan, S. Pawar, N. Harale, V. Patil, V. Rao, Y. Ma, J. Ae, J. Kim, P. Patil, Mater. Sci.-Pol., 34, (2016), 204-211.
- [92] S. Vanalakar, V. Patil, P. Patil, J. Kim, New J. Chem., 42, (2018), 4232-4239.
- [93] S. Navale, A. Mane, M. Chougule, N. Shinde, J. Kim, V. Patil, RSC Adv., 4, (2014), 44547-44555.

- [94] X. Wang, Z. Xie, H. Huang, Z. Liu, D. Chen and G. Shen, *J. Mater. Chem.*, 22, (2012), 6845-6850.
- [95] R. Souissi, N. Bouguila and A. Labidi, *Sens. Actuators B Chem.*, 261, (2018), 522-530.
- [96] Y. Kim, K. Kwon, S. Kang, C. Kim, T. Kim, S. Hong, S. Park, J. Suh, M. Choi, S. Han, H. Jang, *ACS Sensors*, 4, (2019), 2395-2402.
- [97] T. Xu, Y. Liu, Y. Pei, Y. Chen, Z. Jiang, Z. Shi, J. Xu, D. Wu, Y. Tian, X. Li, *Sens. Actuators B Chem.*, 569, (2018), 789-796.
- [98] J. Ou, W. Ge, B. Carey, T. Daeneke, A. Rotbart, W. Shan, Y. Wang, Z. Fu, A. Chrimes, W. Wlodarski, S. Russo, Y. Li, K. Kalantar-zadeh, *ACS Nano*, 9, (2015), 10313-10323.
- [99] D. Late, Y. Huang, B. Liu, J. Acharya, S. Shirodkar, J. Luo, A. Yan, D. Charles, U. Waghmare, V. Dravid, C. Rao, *ACS Nano*, 7, (2013), 4879-4891.
- [100] S. Navale, D. Bandgar, M. Chougule, V. Patil, *RSC Advances*, 5 (2015), 6518-6527.
- [101] J. Wang, G. Lian, Z. Xu, C. Fu, Z. Lin, L. Li, Q. Wang, D. Cui, C. Wong, *ACS Appl. Mater. Interfaces*, 8, (2016), 9545-9551.
- [102] D. Wang, M. Sun, G. Feng, C. Song, *J. of Materi. Eng. and Perform.*, 28, (2019), 6649-6655.
- [103] Fu T-X, *Mater. Res. Bull.*, 99, (2018) 460-465.
- [104] X. Li, J. Wang, D. Xie, J. Xu, Y. Xia, W. Li, L. Xiang, Z. Li, S. Xu and S. Komarneni, *Nanotechnology*, 28, (2017), 325501-325526.
- [105] H. Roshan, M. Sheikhi, M. Haghighi, P. Padidar, *IEEE Sensors Journal*, 20, (2020), 2526-2532.
- [106] J. Wu, Z. Wu, H. Ding, Y. Wei, W. Huang, X. Yang, Z. Li, L. Qiu, X. Wang, *Sens. Actuators B Chem.*, 305, (2020), 127445-127485.
- [107] S. Shao, L. Che, Y. Chen, M. Lai, S. Huang, R. Koehn, *J. Alloys Compd.*, 774, (2019), 1-10.

CHAPTER-2

**Theoretical Background of CBD, SILAR
Methods, and Thin Film Characterization
Techniques**

CHAPTER-2

Theoretical Background of CBD, SILAR Methods, and Thin Film Characterization Techniques

Sr. No.	Title	Page No.
2.1	General Introduction of Chemical Methods	34
2.2	Theoretical Background of Chemical Bath Deposition (CBD) Method	36
	2.2.1 Basics and Film Growth in CBD	37
	2.2.2 Impact of Preparative Parameters	38
	2.2.3 Advantages of CBD Method	40
2.3	Theoretical Background of Successive Ionic Layer Adsorption and Reaction (SILAR) Method	40
	2.3.1 Processes Involved in SILAR Method	41
	2.3.2 Impact of Preparative Parameters	42
	2.3.3 Advantages of SILAR Method	45
2.4	Thin Film Characterization Techniques	46
	2.4.1 Physico-Chemical Characterization Techniques	46
	2.4.2 X-ray Diffraction (XRD)	46
	2.4.3 Fourier Transform Infrared Spectroscopy (FT-IR)	48
	2.4.4 Raman Spectroscopy	50
	2.4.5 Field Emission Scanning Electron Microscopy (FE-SEM)	51
	2.4.6 X-ray Photoelectron Spectroscopy (XPS)	53
	2.4.7 Contact Angle Measurement	55
	2.4.8 Brunauer-Emmett-Teller (BET) Analysis	56
2.5	Electrochemical Characterization Techniques	57
	2.5.1 Cyclic Voltammetry (CV)	60
	2.5.2 Galvanostatic Charge-Discharge (GCD)	61
	2.5.3 Electrochemical Impedance Spectroscopy (EIS)	62
2.6	Gas Sensor Measurements	64
2.7	Gas Sensor Techniques	66

	2.7.1	<i>Resistance stabilization</i>	66
	2.7.2	<i>Sensitivity</i>	66
	2.7.3	<i>Response and Recovery Time</i>	66
	2.7.4	<i>Selectivity</i>	67
	2.7.5	<i>Reproducibility</i>	67
	2.7.6	<i>Long-term Stability</i>	67
2.8	Theoretical Background of Gas Sensor Mechanism		67
2.9	References		70

2.1 General Introduction of Chemical Methods:

The synthesis of materials is a fundamental aspect of materials science and engineering, and it involves combining atoms and molecules to form new materials with specific properties. Advances in synthesis techniques have led to the development of new materials with unique properties, and the ability to control the structure and composition of materials has become increasingly important. Sophisticated instruments are used to monitor synthesis reactions and gain information on the composition, crystallinity, and contents of hybrid materials. Understanding the physical phenomena that underpin materials synthesis, such as diffusion, nucleation, and phase transitions, is crucial for developing new methods to synthesize materials with desired structure, properties, or behavior, which has attracted the attention of academics and scientists around the world [1]. Over the past decade, the integration of computer-based simulations using various computational methods has complemented traditional preparation techniques in the study of materials and material systems across different dimensions.

There are many application areas of computer simulation in materials science including the heat treatment, material microstructure, corrosion and protection, casting, and material design areas [2]. During the past decade, computer simulations based on a quantum-mechanical description of the interactions between electrons and atomic nuclei have strongly influenced the development of materials science. The field of computer simulations of materials has grown dramatically in the past few decades with new ingenious methods and applications [3]. Thin films have emerged as the predominant approach in numerous fields for enhancing the physical and chemical characteristics of materials. These solid thin films have found extensive application in diverse engineering systems, including photovoltaics, sensors, transducers, energy storage, electronics, catalysis, and biological applications [4].

The reliability and performance of these devices are directly influenced by the properties of the materials used in their fabrication. Careful control of preparation and treatment processes allows for precise modification of thin film properties. A key advantage is the ability to manipulate the film thickness, which can range from a few nanometers to several micrometers. It is important to note that defining a specific threshold below which a film is considered ‘thin’ is challenging, properties of thin films can vary significantly from their bulk materials and change with thickness,

differing from one material to another, predominantly due to the nanocrystalline nature of thin films. This nano crystallinity leads to changes such as reduced density and thermal conductivity, increased volume-to-mass ratio, and modified electrical conductivity, which are major contributing factors to the unique characteristics of thin films. Additionally, the method used for film preparation profoundly influences properties such as crystal structure, crystallinity, roughness, morphology, and reactivity [5, 6].

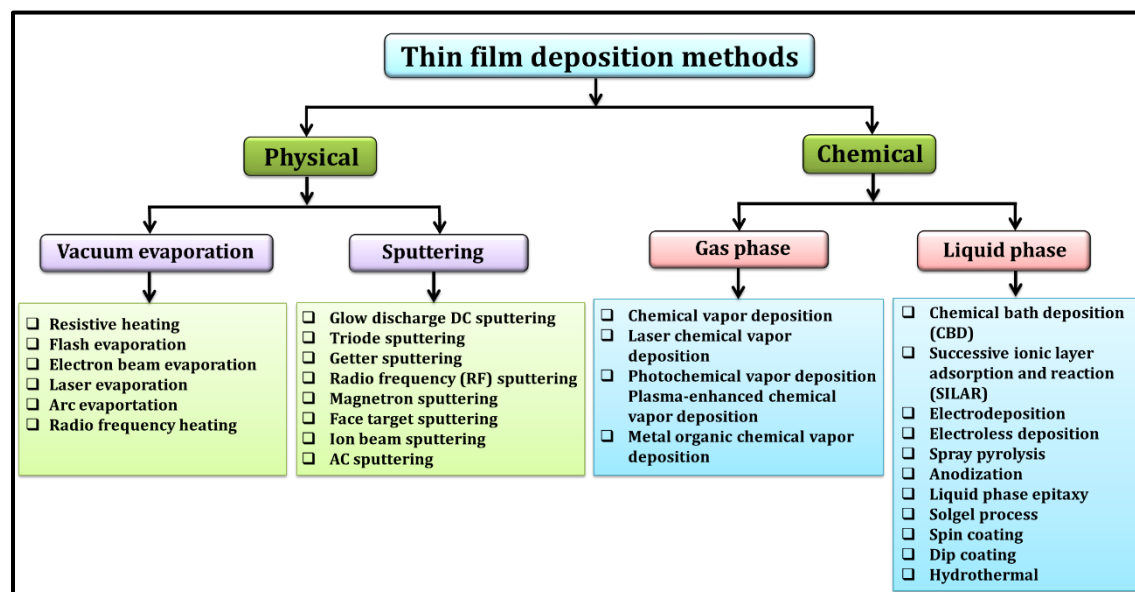


Chart 2.1: General classification of thin film deposition methods.

Thin film deposition methods fall into two main categories: physical methods, such as vacuum evaporation and sputtering, and chemical methods, which include chemical vapor deposition (CVD), photo CVD, laser CVD, metal-organic chemical vapor deposition (MOCVD), plasma-enhanced CVD, chemical bath deposition (CBD), and electrodeposition, successive ionic layer adsorption and reaction (SILAR), hydrothermal synthesis, anodization, spin coating, spray pyrolysis, liquid phase epitaxy, and sol-gel methods, among others. A general classification of thin film deposition methods is presented in **Chart 2.1**. Physical methods tend to incur higher costs due to the requirement for sophisticated instruments capable of creating high vacuum and controlled temperature conditions. In contrast, chemical deposition methods offer advantages such as simpler instrumentation, cost-effectiveness, scalability, lower effective temperatures, the capability to deposit materials on large substrates and a broader selection of substrate options [6-8]. The lower working

temperatures associated with chemical deposition methods also prevents the oxidation of metallic substrates [9].

The utilization of thin films to enhance material properties has gained traction in various disciplines. Lower working temperatures in thin film deposition provide advantages such as the prohibition of oxidation and the exploration of low-dimensional materials. These films exhibit enhanced physical and chemical properties influenced by dimensions, nanocrystalline structure, and deposition methodologies. Advanced instrumentation and computational simulations expedite progress, enabling comprehensive understanding and material design for diverse applications. Continued research in thin films holds promise for further innovations in materials science and engineering.

2.2 Theoretical Background of Chemical Bath Deposition (CBD) Method:

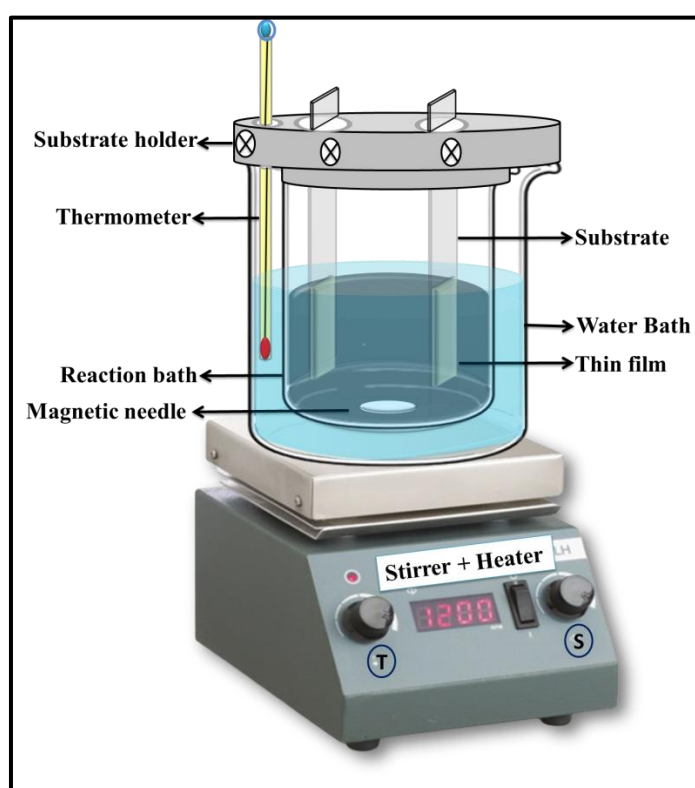


Figure 2.1: Schematic of chemical bath deposition (CBD) method.

The chemical bath deposition (CBD) method is binder-free, simple, and cost-effective which offers a cost-effective and straightforward approach to preparation of thin films without the need for expensive vacuum systems or specialized equipment. In CBD method, there are mainly two reaction mechanisms; one is homogeneous and the other is heterogeneous. This method provides a convenient way to adjust

preparative parameters to achieve the desired thin film thickness. The reaction mechanisms involved in the CBD method for thin film formation with the effect of preparative parameters have provided a detailed explanation in previous research articles Mane and Lokhande [10]. Furthermore, a various review articles have extensively covered chemical approaches to depositing thin films, offering valuable insights into the field [10-14].

2.2.1 Basics and Film Growth in CBD:

2.2.1. (a) Basics of Nucleation and Growth:

The CBD is a process for preparing a solid film on a substrate on a single immersion through controlling the kinetics of solid formation. This method encompasses various stages, including the mass transport of reactants, adsorption onto the substrate, surface diffusion, chemical reactions, desorption, nucleation, and subsequent growth of the film. Film formation can occur through two distinct mechanisms, i.e. ion-by-ion and hydroxide cluster mechanisms independently. In practical situations both processes may interact, leading to the formation of nuclei can occur by heterogeneous nucleation on the substrate or by homogeneous nucleation in the bulk solution respectively.

I) Ion-by-Ion Growth Mechanism:

The ion-by-ion mechanism is one of the simplest mechanisms, which involves the growth of the film through the reaction of individual atomic species at the substrate surface. This process precedes atom by atom or ion by ion, leading to the gradual formation of the solid film. For homogenous nucleation requires a high degree of saturation. The existence of free particles, along with the presence of a surface introduces a degree of heterogeneity that facilitates the nucleation. As a result, deposition via the ion-by-ion process predominantly occurs on the substrate or other surfaces, rather than yielding as large amount of precipitate, (which is more characteristic of the cluster mechanism). Here, the surface acts as a catalyst for nucleation.

II) Hydroxide Cluster Mechanism:

In cluster mechanism, the aggregation of colloidal particles formed in the solution. In this case, the film growth can be done by the clustering of these colloids, resulting in a cluster-by-cluster growth pattern. In cluster mechanisms, (also referred

as a hydroxide mechanisms), nucleation of the chalcogenide is simplified because there is already a solid phase present. The process takes place through a substitution reaction on this existing solid phase. In this instance, the initial stage involves depositing and adhering the hydroxide onto the substrate. Subsequently, this hydroxide undergoes a conversion into the chalcogenide.

2.2.1 (b) Concept of Ionic and Solubility Product:

When, sparingly soluble salt XY, placed in water, a saturated solution containing X^+ and Y^- ions in contact with undissolved solid XY are obtained and equilibrium is established between the solid phase and ions in the solution as,



By the law of mass action to equilibrium condition,

$$M = C_x^+ \cdot C_y^- / C_{xy}(S) \quad (2.2)$$

Where, C_x^+ : concentrations of X^+ , C_y^- : concentrations of Y^- and C_{xy} : concentrations of XY ions in the solution. The concentration of a pure solid phase is a constant number,

$$\text{i. e. } C_{xy}(S) = \text{constant} = M'$$

$$M = C_x^+ \cdot C_y^- / M' \quad (2.3)$$

$$M M' = C_x^+ \cdot C_y^- \quad (2.4)$$

Since M and M' are constant, the product MM' is also constant, say Ms, therefore above equation becomes,

$$Ms = C_x^+ \cdot C_y^- \quad (2.5)$$

Ms is known as the solubility product (SP) and $(C_x^+ \cdot C_y^-)$ is known as the ionic product (IP). In case of a saturated solution, the IP of ions is equal to the SP. But when IP exceeds the SP i.e. $IP/SP = S > 1$, the solution is supersaturated, precipitation occurs and ions combine on the substrate and in the solution to form nuclei [10, 15].

2.2.2 Impact of Preparative Parameters:

Figure 2.1 shows the experimental setup for synthesizing metal chalcogenide thin films. The deposition rate and film thickness are influenced by factors such as solution supersaturation, stirring rate, and nucleation site density. Growth kinetics are

governed by solute concentration and the velocities of the ions in the solution. Here the explanations for the synthesis parameters:

A) pH of the Bath:

The pH measures the negative logarithm of H^+ ion concentration and is controlled by a complexing agent. The reaction speed and thin film deposition rate depend on supersaturation levels; lower supersaturation slows the formation of MX (metal and chalcogenide ions). The generation of numerous X ions from a specific anionic source is primarily influenced by the pH of the solution. An increase in bath pH results in a reduced rate of X ion formation, consequently slowing down the overall formation rate. Conversely, decreasing the pH leads to an elevated concentration of X ions, facilitating the formation of a feasible thin film.

B) Complexing Agent:

The primary role of a complexing agent is to sequester metal cations and avoid the precipitation of the desired material. In the process of forming the thin film, the complexing agent gradually releases these cations to interact with the anions present in the solution. Nevertheless, if the concentration of the complexing agent is elevated, it results in a decrease in the concentration of metal ions. Consequently, this reduction in metal ion concentration leads to a decrease in the reaction rate and a decrease in precipitation, ultimately resulting in a slower rate of thin film deposition.

C) Temperature:

The rate at which the thin film forms is influenced by temperature. As the temperature rises, the dissociation rate of complexed anions and cations increases, leading to higher concentrations of M^+ and X^- ions, leading to an accelerated deposition rate. However, in certain cases, increasing the temperature can lead to a reduction in the thickness of the thin film. For instance, when the solution is supersaturated at a lower pH and the temperature is raised, this can cause the formation of precipitates, resulting in a thinner film. Conversely, at higher pH values, precipitation is significantly reduced due to lower supersaturation levels, and the material is more likely to form on the surface of the substrate. Furthermore, maintaining a higher pH while raising the temperature provides more M^+ and X^- ions for the formation of MX, leading to the production of thicker films.

D) Concentration:

In this scenario, increasing the X^- ion concentration can indeed lead to the formation of MX with a greater film thickness. However, it's important to note that if the X^- ion concentration is raised beyond a certain threshold, it can result in an elevated rate of precipitation. This, in turn, leads to a lower quantity of MX forming on the surface of the substrate, ultimately resulting in a thinner film.

E) Substrate:

The choice of substrate for thin film formation is a crucial factor that influences both the thickness of the film and the deposition rate. When the lattice of the deposited material matches that of the substrate, there is minimal change in free energy. This favorable condition promotes nucleation and facilitates the subsequent growth of the film.

2.2.3 Advantages of CBD Method:

- i) The method is straightforward, cost-effective, and does not require binders, making it suitable for large-area film deposition.
- ii) It operates at low or room temperature.
- iii) It is compatible with a variety of substrates.
- iv) The method does not require vacuum conditions or expensive equipment.
- v) Stoichiometric synthesis is ensured as the process relies on ionic rather than atomic building blocks.
- vi) It produces uniform, pinhole-free films due to continuous contact between the solution and substrates.
- vii) Preparative parameters such as concentration and deposition time can be easily controlled to affect film thickness.
- viii) The toxic gases have not evolved.

2.3 Theoretical Background of Successive Ionic Layer Adsorption and Reaction (SILAR) Method:

It provides theoretical background of the SILAR method. The SILAR method is widely used for depositing thin films with precise control over their thickness and composition. Understanding the theoretical principles underlying SILAR is essential for optimizing the deposition process and achieving desired film properties.

2.3.1 Processes Involved in SILAR Method:

The SILAR method consists of several distinct processes that occur during the deposition of thin films. **Figure 2.2** shows the schematic of four beaker SILAR method. These processes are elaborated as follows:

2.3.1. (a) Adsorption:

The initial stage of the SILAR method involves the adsorption of precursor ions onto the substrate surface. This process entails submerging the substrate in a solution containing the desired metal ions. The precursor ions attach themselves to the substrate surface, creating a monolayer of adsorbed species. The adsorption process is influenced by various factors, such as solution concentration, temperature, pH, and the properties of the substrate itself. During adsorption, the precursor ions interact through different mechanisms, including electrostatic interactions, coordination bonding, or chemical reactions. The adsorption step in SILAR is of utmost importance as it provides the foundation for subsequent reactions. It plays a vital role in creating the Helmholtz electric double layer on the substrate surface, wherein positively charged ions (cations) form the inner layer and counter ions (typically anions) form the outer layer. This double layer is crucial for enabling the subsequent chemical reactions to occur, ultimately facilitating the growth of the thin film [16].

2.3.1. (b) Reaction:

In the reaction step of SILAR, chemical interactions occur between the adsorbed precursor ions and the substrate. The nature of these reactions is determined by the specific precursor ions and the substrate material involved. Various processes, such as ion-exchange, complexation, redox reactions, or ligand substitution, may take place during this stage. The reaction kinetics are influenced by factors like temperature, immersion time, and the presence of catalysts or additives. As a result of these chemical reactions, the adsorbed species undergo transformation, leading to the formation of a solid thin film layer on the substrate surface. This reaction step serves as the core of the SILAR method, where the interactions between the adsorbed cations and anions occur. The product of these reactions is a solid compound with the specific chemical composition, represented by the notation K_pA_a , where ' K ' represents the cationic species, ' A ' is the anionic species, and ' p ' and ' a ' are the corresponding stoichiometric coefficients of each species.

The chemical reactions that occur at the interface between the cations and anions are typically irreversible, ensuring the growth of the desired thin film with the intended composition and properties. This pivotal reaction step is responsible for the successful deposition of thin films using the SILAR method.

(i) First Rinsing:

During the first rinsing step, it is essential to remove any loosely adsorbed cations from the substrate surface. The rinsing process is critical as it helps in achieving a clean and well-prepared substrate, which directly impacts the quality of the thin film. Rinsing with double distilled water (DDW) is chosen because of its high purity and low chemical reactivity, ensuring minimal interference with the deposition process.

(ii) Second Rinsing:

After the reaction step, the substrate may still contain unreacted, excess species, and secondary products of the reaction. These need to be removed to ensure a pure and uniform thin film. The second rinsing step, similar to the first rinsing, involves using DDW to wash away any residual species and by-products, which could otherwise interfere with the thin film's properties.

2.3.1. (c) Layer-by-Layer Growth:

The layer-by-layer growth mechanism is a fundamental characteristic of SILAR, enabling precise control over the film thickness and composition. The repeated cycles of immersion and reaction lead to the sequential deposition of additional layers onto the growing film. This growth mechanism allows for the precise control of film properties by adjusting the number of cycles and the duration of each step. The layer-by-layer growth can be achieved by carefully controlling the precursor solution concentration, immersion time, reaction conditions, and the diffusion of precursor species.

2.3.2 Impact of Preparative Parameters:

Various preparative parameters significantly influence the SILAR deposition process and the properties of the resulting thin films. The effect of these parameters is discussed as follows:

2.3.2. (a) Precursor Solution:

The choice of precursor solution in SILAR significantly influences the film composition and properties. The precursor solution provides the source of the desired metal ions or molecular species for the deposition process. Factors such as precursor concentration, pH, and the presence of complexing agents can affect the adsorption and reaction behavior. Optimal precursor solution design is essential to control film composition, stoichiometry, and functionality. By carefully selecting and optimizing the precursor solution, researchers can achieve tailored film properties, such as specific elemental ratios, desired chemical functionalities, or specific dopants.

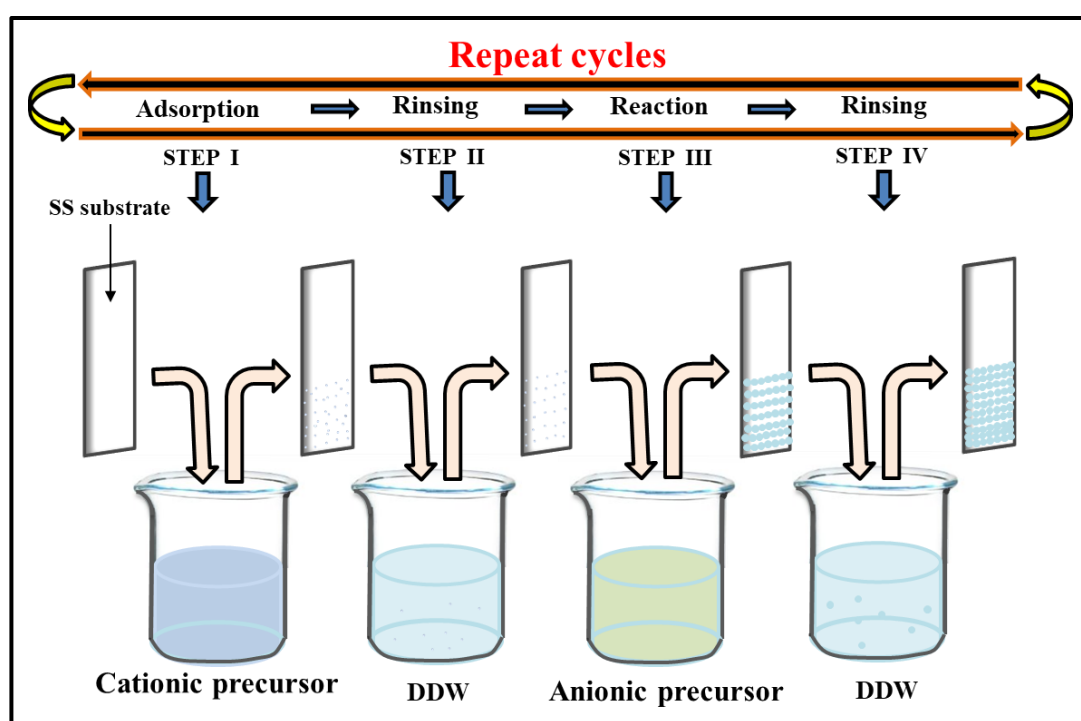


Figure 2.2: Schematic of four beakers SILAR method.

(i) Concentration of Precursors:

The concentration of the precursor solutions is a critical parameter affecting the growth rate and film characteristics. Higher concentrations of cationic precursors can lead to thicker films, while higher concentrations of anionic precursors may promote faster reaction rates but could also result in larger particle sizes. Therefore, finding the optimal concentration for both cations and anions is crucial for obtaining the desired film properties.

(ii) pH:

The pH of the precursor solutions plays a significant role in controlling the deposition process. It can influence the surface charge of the substrate and the reactivity of the ions. Maintaining the appropriate pH is vital for ensuring proper adsorption and reaction rates, and it is often adjusted using a suitable complexing agent.

(iii) Complexing Agent:

Complexing agents are essential additives used to control the concentration of metal ions in the precursor solution. They form coordination complexes with metal ions, stabilizing them and preventing premature precipitation. The choice of complexing agent and its concentration can influence the reaction rate, deposition efficiency, and film characteristics.

2.3.2. (b) Immersion Time:

The immersion time, representing the duration of immersion in each precursor solution, plays a crucial role in SILAR film growth. Longer immersion times generally lead to thicker films, as more precursor species are adsorbed and reacted. However, there is an optimum immersion time for achieving the desired film properties. Prolonged immersion times may lead to undesired effects, such as increased roughness or poor film quality. Optimizing the immersion time is crucial to control film thickness, ensure good film morphology, and achieve the desired film characteristics.

2.3.2. (c) Temperature:

The deposition temperature is a critical parameter in SILAR, affecting the reaction kinetics and film properties. Higher temperatures generally accelerate the reaction rate, facilitating faster film growth. However, elevated temperatures may also introduce other effects, such as enhanced diffusion, increased surface mobility, phase transformations, which can impact on film structure and properties. The choice of deposition temperature depends on the specific precursor system, substrate material, and desired film properties. Optimizing the deposition temperature allows researchers to balance the desired reaction kinetics with the prevention of undesired thermal effects, leading to films with desired properties.

2.3.2. (d) Additives and Surface Modification:

Additives and surface modifications can significantly influence the SILAR deposition process and resulting film properties. The addition of specific additives, such as surfactants or complexing agents, can help control the nucleation and growth of individual layers. These additives can improve the film uniformity, enhance adhesion to the substrate, or modify the crystalline structure. Surface modifications, such as functionalization or pre-treatments, can alter the surface energy, chemical reactivity, or binding sites, affecting the adsorption and reaction behavior during SILAR. By carefully selecting and utilizing additives and surface modifications, researchers can enhance the SILAR process and tailor the film properties to meet specific application requirements [17].

2.3.3 Advantages of SILAR Method:

The SILAR method offers several advantages for thin film deposition. These advantages are discussed as follows:

2.3.3. (a) Controlled Film Growth:

One of the significant advantages of the SILAR method is the ability to achieve precise control over film growth. The layer-by-layer deposition mechanism allows for the control of film thickness at the atomic or molecular level. This control is crucial for various applications where specific film characteristics, such as thickness uniformity, crystallinity, or elemental composition, are desired. By precisely tuning the deposition parameters and the number of SILAR cycles, researchers can tailor the film properties to meet specific application requirements.

2.3.3. (b) Compatibility with Various Substrates:

The SILAR method exhibits compatibility with a wide range of substrates, making it versatile for different applications. It can be used with diverse substrate materials, including metals, metal oxides, semiconductors, polymers, and even flexible or temperature-sensitive substrates. The ability to operate at relatively low temperatures allows for the deposition on substrates that cannot withstand high-temperature processes. This compatibility with various substrates expands the potential applications of SILAR in fields such as electronics, optoelectronics, energy storage, and catalysis.

2.3.3. (c) Scalability and Cost-Effectiveness:

SILAR is considered a relatively simple and cost-effective deposition method. The sequential nature of the process, involving alternating immersion and reaction steps, allows for straightforward implementation on both laboratory and industrial scales. The method does not require complex equipment or specialized infrastructure, contributing to its cost-effectiveness. The scalability of SILAR makes it attractive for large-scale production, where cost and efficiency are critical considerations. The ability to produce high-quality thin films at a reasonable cost makes SILAR a promising deposition method for industrial applications.

This chapter provided a comprehensive theoretical background of the SILAR method, including the processes involved, advantages offered, and the influence of preparative parameters. Understanding these theoretical aspects are essential for optimizing SILAR and tailoring thin film properties for specific applications. By carefully adjusting these preparative parameters, researchers can tailor the SILAR method to deposit thin films with precise characteristics, making it a versatile and valuable technique for various applications in material science and engineering.

2.4 Thin Film Characterization Techniques:

2.4.1 Physico-Chemical Characterization Techniques:

The electrochemical properties of thin films are strongly linked to their physicochemical properties, including crystal structure, specific surface area, surface texture, conductivity, and elemental composition. As a result, thorough characterization of these materials using various procedures and specified analysis of the results to understanding the relationships between various properties is essential for research. This analysis aids in the selection of appropriate materials for specific applications and facilitates the examination of material modifications. In the present study, the thin film electrodes were subjected to different material characterization techniques to gain comprehensive insights into their properties.

2.4.2 X-ray Diffraction (XRD):

X-ray diffraction (XRD) is a fundamental, well-established, and widely used nondestructive characterization technique in materials science. It provides valuable information about the atomic-scale structure of various substances in different states [18]. The technique provides perceptions into atomic-scale structures, unit cell

dimensions, crystallite size, lattice strain, chemical composition, ordering, and phase diagrams.

Working of the Instrument:

The X-ray diffractometer consists of a monochromatic X-ray source, a specimen holder, and an X-ray detector. The X-ray generator, or cathode ray tube, includes a cathode, monochromator, and target material in a vacuum. Electrons from the heated cathode are accelerated toward the target material (e.g., Cu, Fe, Mo, or Cr), causing emission of characteristic radiation when inner shell electrons are ejected. This radiation is filtered to produce monochromatic X-rays, such as $\text{CuK}\alpha = 1.5418 \text{ \AA}$ for copper. These X-rays are directed at the specimen, and diffraction peaks are recorded as the specimen and detector rotate.



Figure 2.3: Photograph of Rigaku MiniFlex600 diffractometer.

The crystal structure of a sample can be determined using the Laue, rotating crystal, or powder methods. For the simple analysis of samples crystal structure, the powder method is commonly used. The Laue method, on the other hand, is the oldest used to determine crystal structures, employing a continuous spectrum of X-rays with a fixed angle of incidence. This method provides faster diffraction results and is useful for observing dynamic processes in crystal structures. The rotating crystal method uses a monochromatic X-ray beam and rotates the sample at a constant speed, while the powder method keeps the wavelength fixed and varies the angle of incidence.

One important application of XRD, especially with nanocrystals, is the estimation of crystal dimensions using the Scherrer relationship [19]:

$$D = k\lambda/\beta\cos\theta \quad (2.6)$$

Here, β represents the full width at half maximum (FWHM) of the diffraction peak, and θ is the peak position in radians. In this study, XRD patterns of the thin film electrodes were obtained using a RIGAKU MiniFlex600 diffractometer with Cu K α radiation ($\lambda = 1.5406 \text{ \AA}$) at 30 kV in $\theta/2\theta$ mode. The photograph of the Rigaku MiniFlex600 diffractometer is shown in **Figure 2.3**.

2.4.3 Fourier Transform Infrared Spectroscopy (FT-IR):

Fourier Transform Infrared Spectroscopy (FT-IR) is a powerful technique used to obtain qualitative information about the chemical bonding in materials. This nondestructive analysis method can be applied to study solids, liquids, and gases. The name "Fourier Transform Infra-red" reflects how data is collected and converted from an interference pattern to a spectrum.

Working Principle:

Molecular bonds in materials vibrate at specific frequencies depending on the type of bond and the elements involved in the bonding. According to quantum mechanics, these frequencies correspond to the ground state and various excited states of the molecules. When these bonds absorb light energy at specific frequencies, they become excited to higher energy states. The absorbed wavelength corresponds to the characteristics of the chemical bond and can be observed in the spectrum. The mid-infrared region, which FT-IR analyzes, typically ranges from 4000 to 200 cm^{-1} .

The FT-IR instrument incorporates a Michelson interferometer, as shown in **Figure 2.4 [20]**. The interferometer splits the incoming infrared light into two beams, one of which is directed towards a stationary mirror and the other towards a moving mirror. The beams are then reflected and recombined, resulting in an interference pattern.

Working of the Instrument:

A standard FT-IR spectrometer comprises a source, interferometer, sample compartment, detector, amplifier, A/D converter, and a computer. **Figure 2.5 (a)** shows a photograph of the ALPHA II compact FT-IR spectrometer, and **Figure 2.5 (b)** illustrates the basic ray diagram of the FT-IR system. The IR spectrum is a graph

of the substance's infrared light absorbance on the vertical axis and the frequency (wavenumber) on the horizontal axis.

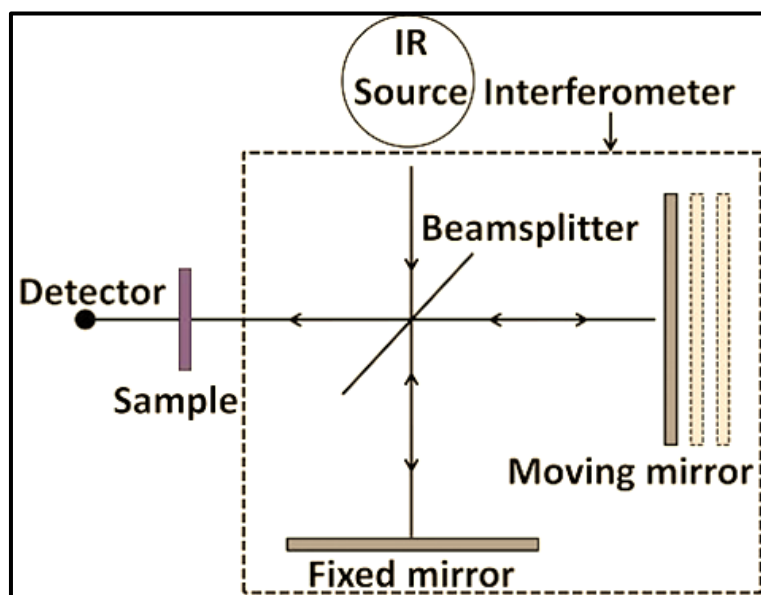


Figure 2.4: Basic schematic of FT-IR with Michelson interferometer.

Various materials, such as silicon carbide rod, nichrome and kanthal wire coils, Nernst glowers, and carbon arcs, can serve as sources of IR radiation.

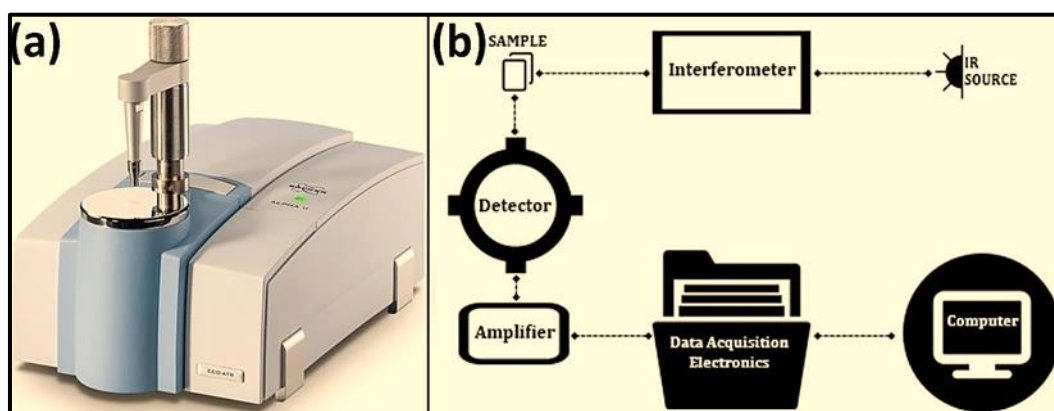


Figure 2.5: a) Photograph of ALPHA II compact FT-IR spectrometer [21], and b) the basic ray diagram of FT-IR system [22].

The FT-IR instruments sample compartment requires the sample to be thin enough for the IR radiations to pass through it. This advantage of FT-IR analysis allows for the use of very small sample quantities. When the IR radiation passes through the sample, some of it is absorbed by the sample, while the rest is transmitted. The detectors used in FT-IR instruments can be thermal or quantum detectors. Thermal detectors measure received light as heat, while quantum detectors measure it

as light, making them highly sensitive. The acquired data, represented in terms of intensities, are then processed through Fourier transform and plotted against wavenumber. For analysis purposes, the observed data is compared with available reference patterns. Each molecular structure yields a unique infrared spectrum, making infrared spectroscopy useful for a variety of analyses.

Using FT-IR spectroscopy, the following information can be obtained [23]:

- Identification of unknown materials.
- Determination of the quality or consistency of a thin film sample.
- Quantification of the amount of components in a mixture.

In the present study, the FT-IR spectra of the synthesized materials were recorded using the ALPHA II interferometer with a diode laser as an IR source. This technique allows for a detailed examination of the chemical bonding in the thin film materials under investigation.

2.4.4 Raman Spectroscopy:

Raman spectroscopy is a versatile and non-destructive technique used for rapid analysis of both organic and inorganic materials [24]. It relies on the interaction of light with the material to reveal information about its molecular characteristics, including rotational, vibrational, and low-frequency modes [25].

Working Principle:

Raman scattering involves a two-photon process where monochromatic light interacts with electrons in the sample. Electrons, with distinct vibrational levels and energy differences absorb energy from the incident photon and transition to a higher energy state. As the electron returns to its initial state, it loses energy and emits a secondary photon. In some cases, the electron can fall back to a different vibrational level, resulting in the emitted photon having a different energy than the incident photon. This phenomenon is known as Raman scattering.

A standard Raman spectrometer consists of three primary components: an excitation source, a sampling apparatus, and a detector. **Figure 2.6** shows the basic block diagram of a Raman spectrometer. The excitation source used in Raman spectroscopy is typically a monochromatic laser with stable and narrow bandwidth characteristics. To minimize fluorescence in organic molecules, it is essential to shift

the laser wavelength into the near-infrared region without exceeding charge coupled devices (CCD) spectral detection limits. For this purpose, 785 nm diode lasers are commonly preferred. For samples with strong fluorescence or high color intensity, a 1064 nm laser is a better choice. On the other hand, for inorganic molecules, a 532 nm laser offers increased sensitivity [26].

The sample interface of the spectrometer often uses a fiber optic probe, offering flexibility for measuring solid samples and immersing in liquids or slurries. This probe can also be connected to microscopes and cuvette holders. The spectrometer should be compact, high-resolution, energy-efficient, and low-noise to detect weak Raman scattering [27]. CCDs are commonly used as detectors, with back-thinned CCDs enhancing sensitivity for low concentrations or weak scattering [28, 29].

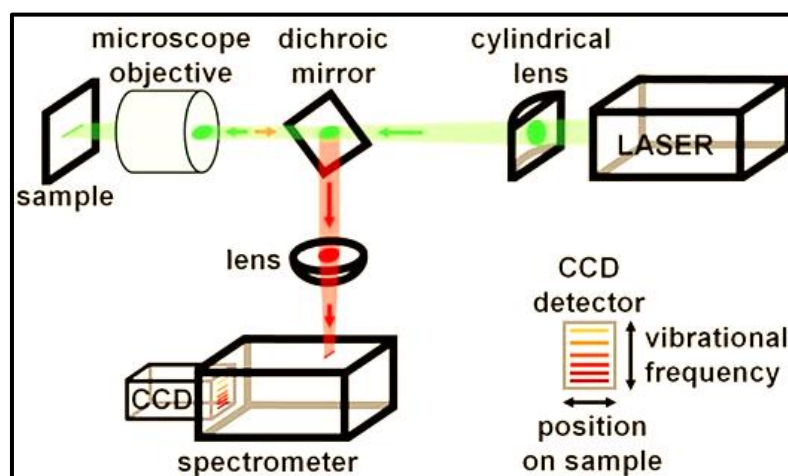


Figure 2.6: The basic block diagram of Raman spectrometer [30].

Raman spectroscopy serves as an invaluable tool for studying the vibrational properties and molecular structure of materials, aiding in diverse fields such as materials science, chemistry, pharmaceuticals, and biomedical research. Its nondestructive nature and ability to provide detailed molecular information make it a preferred technique for various analytical applications.

2.4.5 Field Emission Scanning Electron Microscopy (FE-SEM):

Field emission scanning electron microscopy (FE-SEM) is a prominent instrument used for high-resolution analysis of surface microstructures. Unlike traditional optical microscopes that use photons, FE-SEM employs electrons for imaging. These electrons are emitted by a field emission source. FE-SEM enables the

visualization of topographical and elemental information at magnifications ranging from 10X to 300,000X, with unlimited depth of field.

Working Principle:

FE-SEM images a sample surface by scanning it with a high-energy electron beam. The primary electrons, generated by a field emission source, are accelerated in an electric field and then focused into a narrow beam using electromagnetic lenses. This focused beam strikes the sample, resulting in various interactions with the atoms within the sample. One such interaction is the emission of secondary electrons from the sample surface. These secondary electrons carry valuable information about the sample's surface topography and composition. The detector converts these electrons into an electric signal, which is then amplified and turned into an image.

Working of the Instrument:

The FE-SEM instrument consists of an electron gun, an anode, magnetic lenses, a sample holder, and a detector, as shown in **Figure 2.7 (a)**. It is set up on a desk and requires vacuum conditions to operate. The column chamber valve remains closed until the desired pressure is reached, after which nitrogen gas is introduced. For effective FE-SEM analysis, samples must be conductive. Thus, they are coated with a thin layer of conductive metal such as gold or platinum to prevent charging, reduce thermal damage, and enhance the signal-to-noise ratio [31].

In FE-SEM, high-energy electrons are produced by a tungsten filament placed at a sharp point within a strong electrical potential gradient (cathode). The voltage difference between the anode and cathode accelerates these electrons towards the sample, with voltages typically ranging from 0.5 to 30 kV, and a high vacuum ($\sim 10^{-6}$ Pa) is maintained in the microscope column. Electromagnetic lenses focus the electron beam into a sharp spot, with the condenser lens controlling magnification and the objective lens focusing the beam on the specimen. The objective lens includes both electromagnetic and electrostatic components. A deflection system with scan coils moves the beam in a point-to-point scan. When the beam hits the sample, it interacts with sample atoms, scattering electrons and interacting at various depths [32].

The extent of scattering and interaction volume depends on factors such as the atomic number, concentration of sample atoms, and the energy of primary electrons.

The detector collects and separates signals by energy, using backscattered and secondary electrons to form and amplify the sample image. When primary electrons strike inner shell electrons, they eject them and cause electrons from higher energy levels to fall to lower ones, emitting characteristic X-rays. Energy-dispersive X-ray spectroscopy (EDAX), integrated with FE-SEM, uses these X-rays to analyze the sample's elemental composition. A photo of the FE-SEM instrument is shown in **Figure 2.7 (b)** [33].

This study used the Philips SEMXL30S with EDAX for analysis. This advanced analytical technique allows for high-resolution imaging and precise elemental identification, providing valuable insights into the microstructure and composition of the materials under investigation.

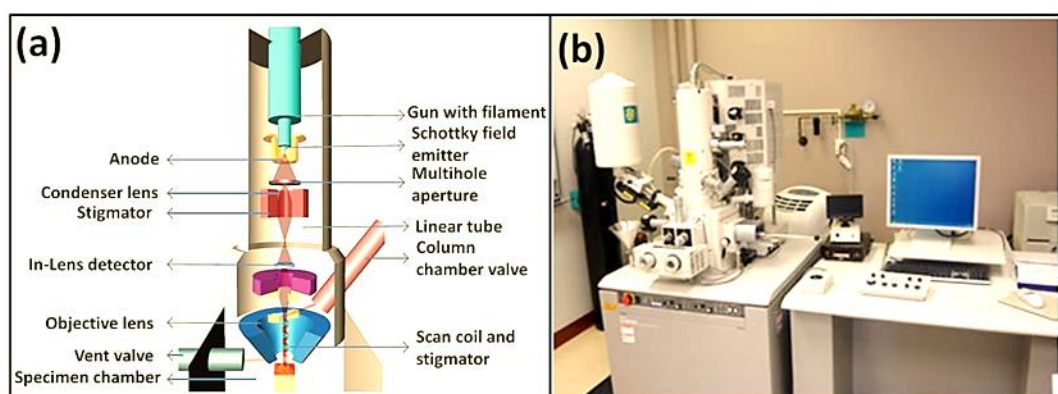


Figure 2.7: a) Schematic of FE-SEM, and b) photograph of FE-SEM instrument.

2.4.6 X-ray Photoelectron Spectroscopy (XPS):

X-ray photoelectron spectroscopy (XPS) is a key analytical method used to examine the surface composition and oxidation states of elements in materials. XPS provides valuable insights into the top 1-10 nm depth of the sample being analyzed. The basis of XPS lies in the photoelectric effect, as described by Einstein, where electromagnetic radiation, in this case X-rays, interacts with a material, causing the emission of electrons known as photoelectrons. **Figure 2.8** shows the schematic diagram of an XPS instrument.

Working Principle:

When an incident X-rays possess sufficient energy, they are absorbed by atoms in the material, leading to the ejection of an inner shell electron. The kinetic

energy of the emitted photoelectrons is measured, and the binding energy can be determined using the known energy of the incident X-rays and the formula:

$$E_{\text{binding}} = E_{\text{photon}} - (E_{\text{kinetic}} + \varphi) \quad (2.7)$$

where φ represents the work function of the element. By examining the photoelectron counts versus binding energy, one can identify the sample's composition and the oxidation states of its elements.

Working of the Instrument:

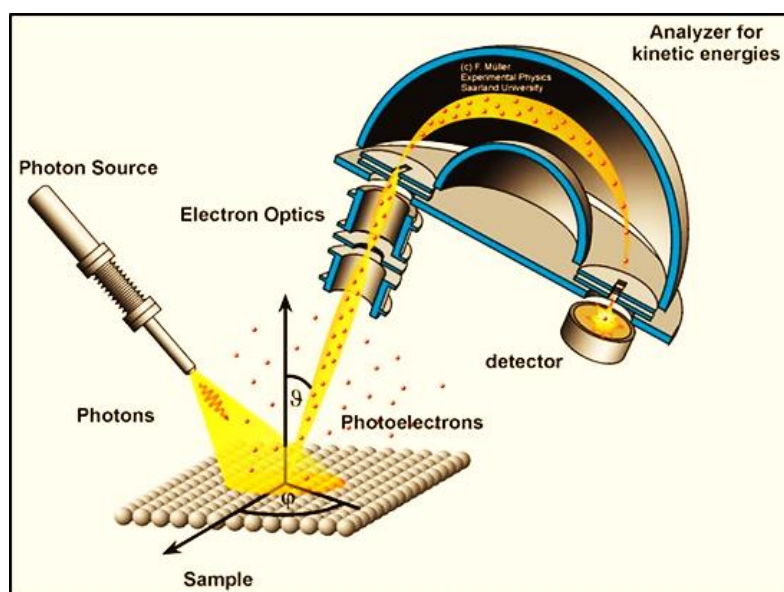


Figure 2.8: Schematic diagram of an XPS instrument [34].

In XPS, X-rays, often $\text{MgK}\alpha$ or $\text{AlK}\alpha$, are generated and monochromatized using a monochromator in a high vacuum environment. These monochromatic X-rays are directed onto the sample's surface, exciting the electrons within the atoms. The resulting photoelectrons are then detected by an electron detector, which measures both their incoming count and kinetic energy. The kinetic energy data is presented as a spectrum, where specific energy peaks correspond to the elements present in the sample. The Thermo Fisher Scientific K-alpha XPS system from the UK is used in the present study.

The XPS is a valuable tool for characterizing surface chemistry and elemental states in various materials. Its high sensitivity and ability to probe the top atomic layers make it particularly useful in understanding surface phenomena, material modifications, and interfacial properties.

2.4.7 Contact Angle Measurement:

Contact angle measurement is a crucial technique employed to assess the contact angle and surface wettability of thin film surfaces. It provides valuable information about the ability of a material to interact with liquids and can even be used to calculate surface free energy. Wettability refers to how well a liquid spreads on the surface of a material. **Figure 2.9 (a)** displays a photograph of the Rame-Hart NRL contact angle meter and **Figure 2.9 (b)** shows contact angle image of a liquid sample on a solid thin film surface.

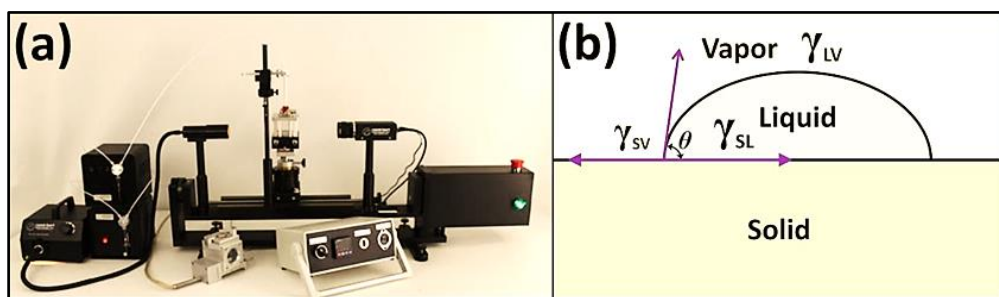


Figure 2.9: a) Photograph of Rame-Hart NRL contact angle meter [35], and b) contact angle of a liquid in contact with solid sample.

The contact angle measures the angle between the solid surface and the tangent to the liquid surface. Angles greater than 90° indicate a hydrophobic, less wettable surface, with superhydrophobic surfaces exhibiting angles above 170° [36]. Conversely, angles less than 90° denote a hydrophilic, more wettable surface, with superhydrophilic surfaces showing angles below 5° . Various methods are employed to measure the contact angle. When the solid, liquid, and vapor phases reach equilibrium, the net force becomes zero. The contact angle (θ) can be determined using Young's relation [37]:

$$\gamma_{s,v} = \gamma_{s,l} + \gamma_{l,v} \cos\theta \quad (2.8)$$

where γ_{sv} is the solid-vapor interfacial energy, γ_{sl} is the solid-liquid interfacial energy, and γ_{lv} is the liquid-vapor interfacial energy.

In the present study, contact angle images of the deposited thin film electrodes are recorded using the Rame-Hart goniometer (model 260). This contact angle measurement helps to understanding the wetting behavior and surface properties of the thin film samples, providing essential insights for material characterization and applications.

2.4.8 Brunauer-Emmett-Teller (BET) Analysis:

The Brunauer-Emmett-Teller (BET) analysis is a valuable technique used to determine the specific surface area of thin film materials based on the physical adsorption of a gas onto their surfaces. By measuring the amount of adsorbate gas, one can obtain information about the surface porosity and particle size. Typically, nitrogen gas is employed for BET measurements [38].

Working Principle:

The BET analysis involves the adsorption of gas on the specimen's surface as well as within its pores. The pore size structure of the sample is assessed by measuring the volume of gas adsorbed at various pressures. This is done using gravimetric or volumetric methods to obtain the adsorption isotherm. In these methods, the adsorbent is maintained at a constant temperature close to the adsorptive's boiling point. The pressure of the adsorptive is gradually increased and held steady for a set period to allow for adsorption and temperature equilibrium. The isotherm, which is a plot of the amount of gas adsorbed versus the adsorptive pressure, provides valuable insights into the adsorption behavior. **Figure 2.10** shows the schematically depicts the dynamic flow method apparatus used for the volumetric method.

The BET analysis is classified into six types of isotherms, each corresponding to specific material and adsorbate interactions. Type I isotherms are observed in materials with very small pores, where either chemisorption or physisorption occurs. Type II isotherms indicate nonporous or macroporous materials with high adsorption energy, while Type III signifies low adsorption energy. Type IV isotherms are associated with mesoporous materials with high adsorption energy, and Type V reflects those with low energy. Type VI isotherms can result from various factors, including different pore sizes. The evaluation of specific surface area (A_s) is based on the cross-sectional area of the adsorbate molecule (a) and the number of moles of adsorbate in a monolayer (n_m), given by the formula:

$$A_s = n_m N_A a \quad (2.9)$$

where $a = (M/\rho)^{2/3} N_A^{1/3}$, M is the molar mass (g mol^{-1}), ρ is the liquid density (gm^{-3}), and N_A is Avogadro's number ($6.022 \times 10^{23} \text{ mol}^{-1}$).

Working of the Instrument:

The BET analysis can be performed using either the volumetric or gravimetric method. In both methods, adsorption is performed at temperatures and pressures slightly below the gas's boiling point. The amount of gas adsorbed at different pressures is measured, which helps determine surface area, adsorption strength, and porosity.

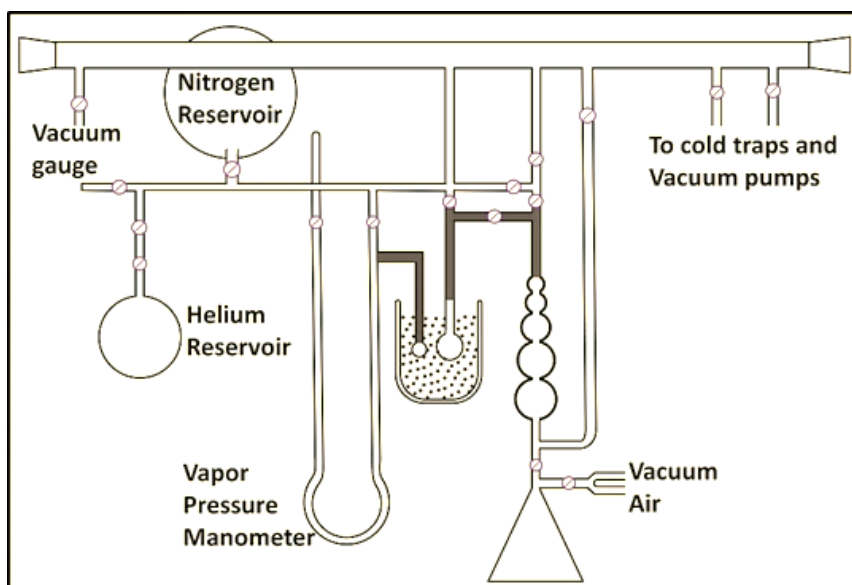


Figure 2.10 Schematically depicts the dynamic flow method apparatus used for the volumetric method [39].

To determine the total surface area (S_T) and specific surface area (S_B), the following equations are utilized:

$$S_T = \frac{v_m N s}{V} \quad (2.10), \quad \text{and} \quad S_B = \frac{S_T}{a} \quad (2.11)$$

where S is the adsorption cross-section of the adsorbing species, N is Avogadro's number, v_m is the molar volume of the adsorbate gas, and m is the mass of the adsorbent [40]. The BET analysis is a valuable tool for understanding the surface characteristics of thin film materials, and it aids in various applications in fields such as materials science, chemistry, and nanotechnology.

2.5 Electrochemical Characterization Techniques:

The need for diverse electrical energy storage devices, tailored for specific applications such as wearable electronics, portable devices, and healthcare systems, has sparked increased interest in electrochemical energy storage among the scientific

community. **Figure 1.1**, depicting the Ragone plot, illustrates the high specific energy (S_E) of fuel cells and the higher specific power (S_P) of capacitors compared to batteries and supercapacitors (SCs). SCs, also known as ultracapacitors, serve as a bridge between fuel cells and capacitors, attracting global research interest due to their versatility in electrode materials, electrolytes, and design possibilities for various fields such as aerospace, medical, military, and transportation [41].

The SCs are classified based on charge storage mechanism, configuration, and physical state of electrolyte. Electrode materials are categorized into EDLCs (non-Faradic mechanism), pseudocapacitors (Faradic mechanism), and battery-type SCs. Supercapacitors are further classified as symmetric or asymmetric by configuration, and as liquid-state or solid-state by electrolyte type [42]. A typical SCs setup includes two conductive electrodes separated by a porous membrane and immersed in an electrolyte. Key parameters for evaluating SCs specific capacitance (C_s), specific capacity (C), and areal capacitance (C_a) are measured using cyclic voltammetry (CV) and galvanostatic charge-discharge (GCD) techniques. Such devices are characterized by the following relationships:

$$\text{Specific capacitance } (C_s) = \frac{1}{m v \Delta V} \int_{V_1}^{V_2} I(V) dV \quad (\text{CV study}) \quad (2.12)$$

$$\text{Areal capacitance } (C_a) = \frac{1}{a v \Delta V} \int_{V_1}^{V_2} I(V) dV \quad (\text{CV study}) \quad (2.13)$$

$$C_s = \frac{I \times t}{m \times \Delta V} \quad (\text{GCD study}) \quad (2.14)$$

$$C_a = \frac{I \times t}{a \times \Delta V} \quad (\text{GCD study}) \quad (2.15)$$

$$\text{Specific capacity } (C) = \frac{C_s \times \Delta V}{3600} \quad (2.16)$$

where $\int_{V_1}^{V_2} I(V) dV$ represents the area enclosed in the cyclic voltammetry (CV) curve, m (g) is the mass of the material deposited on both electrodes, v (V s^{-1}) is the potential scan rate, ΔV (V) is the operational potential window, and I (A) is the current response, a (cm^2) is the area of the SC. Furthermore, the S_E and S_P of the SC are calculated using the **Equations (1.4)** and **(1.5)**, respectively. To achieve higher S_E and S_P values, the SC must operate at higher working voltages and possess a high specific capacitance (C_s) with lower interfacial resistance. However, C_s and working voltage are influenced by the combination of electrode materials and electrolytes used in SC fabrication [43].

Typically, EDLC-type materials can function up to 1 V with water-based electrolytes, but this potential window can be extended to 2.5 V or even 3.0 V with organic electrolytes. In EDLCs, the electric charge is stored in the electric double layer formed at the interface between the electrically conducting electrode and the ionically conducting electrolyte. The charge storage capacity in EDLC-type supercapacitors, as illustrated in **Figure 2.11 (a)**, can be expressed as:

$$E_{s1} + E_{s2} + K^+ + A^- \leftrightarrow E_{s1}^-//K^+ + E_{s2}^+/A^- \quad (2.17)$$

Where E_{s1} and E_{s2} represent the specific surface areas of the negative and positive electrodes, respectively. The ‘//’ notation signifies the electric double layer, where charges accumulate on each side, with K^+ and A^- representing the cations and anions in the electrolyte. The charging and discharging of EDLCs are due to adsorption and desorption processes, without any charge transfer occurring at the interface. Since the active electrodes remain chemically inert, this process is categorized as non-Faradaic. The electric charge storage in EDLCs involves the formation of an electric double layer at the interface between electrically conducting electrodes and ionically conducting electrolytes, as shown in **Figure 2.11 (a)**. This process is known as non-Faradaic, involves adsorption and desorption of charges, with no charge transfer occurring around the interface [44].

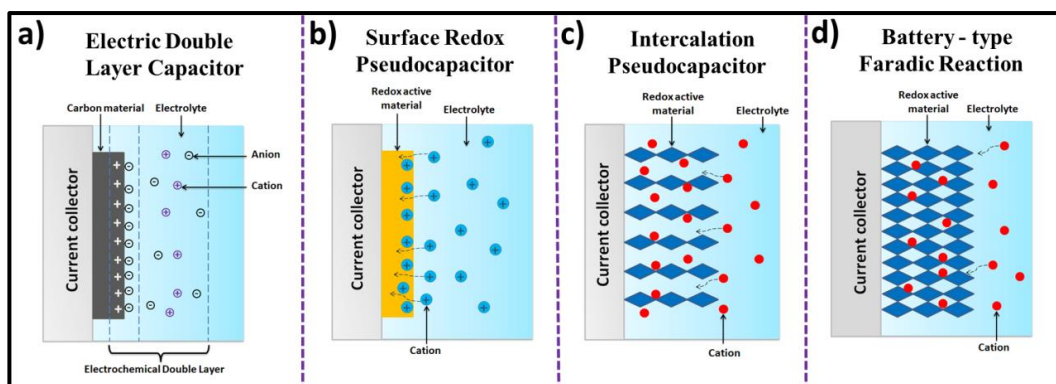


Figure 2.11: Schematic of charge-storage mechanisms for a) an EDLC [45] and (b–d) different types of pseudocapacitive electrodes: b) surface redox pseudocapacitor, c) intercalation pseudocapacitor, and d) battery-type Faradaic reaction [46].

In contrast, pseudocapacitors exhibit fast and reversible redox reactions, resulting in double-layer capacitance and pseudocapacitance. Charge storage in pseudocapacitors is due to Faradaic reactions at the electrode-electrolyte interface, as depicted in **Figure 2.11 (b-d)**. Pseudocapacitance is dependent on applied potential

and involves charge accumulation on the electrode surface and redox reactions within the bulk of the electrode material [47]. To fully assess the electrochemical properties of electrode materials, techniques such as CV, GCD, and EIS are essential. Comprehensive electrochemical characterization is critical for effectively utilizing thin films as active electrodes in SC devices.

2.5.1 Cyclic Voltammetry (CV):

Cyclic voltammetry (CV) is a highly informative and fundamental characterization technique that provides valuable insights into the thermodynamic and kinetic aspects of many chemical systems. It serves as a powerful tool to study the electroactivity of electrodes in various electrolytes. The process involves a linear scan of voltage, and the scan direction is reversed at specific potentials, giving rise to "reversal linear scan voltammetry," commonly known as CV. For conducting CV measurements, a stationary electrode with an area of 1 cm^2 is immersed in the electrolyte solution. Using a three-electrode system is beneficial because it reduces the ohmic resistance of the electrodes. In this setup, the potential is applied between the working and reference electrodes, while the current is measured between the working and counter electrodes.

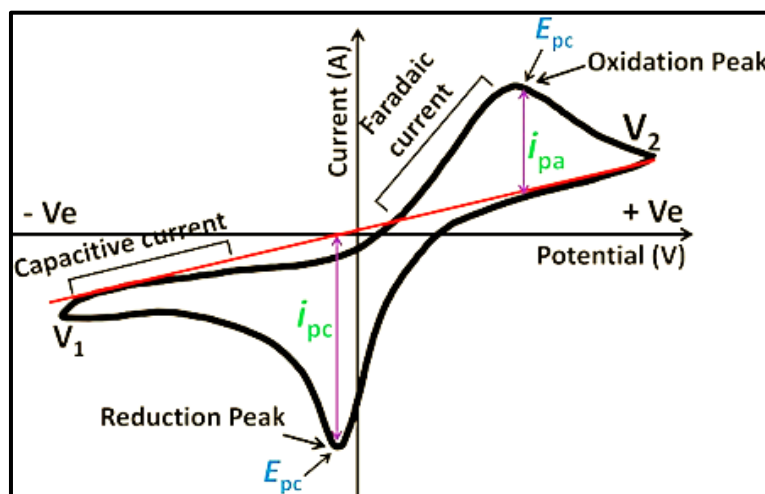


Figure 2.12: The typical cyclic voltammogram for a reversible single electron transfer reaction [48].

During a CV measurement, the potential is varied within a specified range. Once the maximum potential is reached, the scan direction reverses, returning to the minimum potential. **Figure 2.12** shows a typical CV curve for a reversible single-electron transfer reaction between the potential limits V_2 and V_1 .

The cathodic peak current (I_{pc}) and anodic peak current (I_{pa}) correspond to the cathodic and anodic peak voltages (E_{pc} and E_{pa}) of the electrode material. Selecting appropriate potential limits is essential for accurate characterization of oxidation and reduction processes. CV is extensively used in fields such as metal-ligand interactions, solid and solution analyses, polymer studies, and biological systems, including enzyme reactions [49-54].

2.5.2 Galvanostatic Charge-Discharge (GCD):

The galvanostatic charge-discharge (GCD) technique involves the application of a constant current to the working electrodes potential is monitored relative to the reference electrode over time. Initially, there is a sudden change in potential due to the potential drop, followed by a gradual change in potential. **Figure 2.13** shows the charge-discharge curve of a SC, which is influenced by the depletion of reactants at the electrode surface [55, 56].

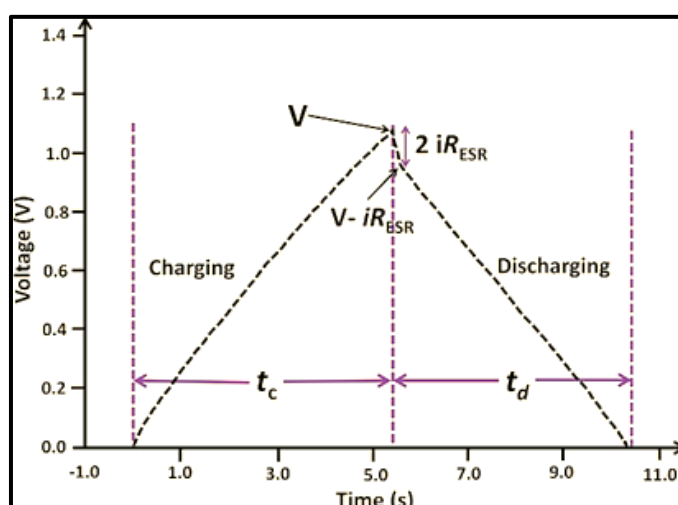


Figure 2.13: Charge discharge curves of a SC [57].

During discharge, potential drop from solution and interfacial resistance can be adjusted with a constant potential offset. Examining the charge-discharge curve reveals the charge storage mechanism. A symmetric curve typically indicates charge storage via the EDLC mechanism. **Figure 2.14** shows the representative shapes of GCD curves: a) EDLC, b) surface redox capacitance, c) intercalation capacitance, and d) Faradic battery-type. Conversely, deviations from symmetry suggest charge storage through the pseudocapacitive mechanism [58, 59]. Additionally, GCD analysis plays a crucial role in determining the Specific Energy (S_E) and Specific Power (S_P) of the SC.

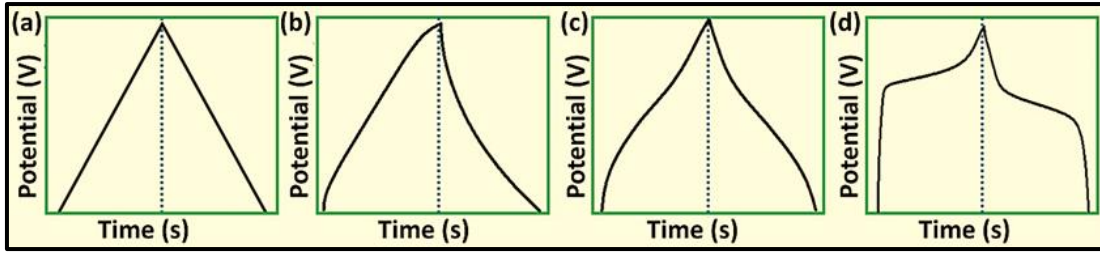


Figure 2.14: Representative shapes of GCD curves: a) EDLC, b) surface redox capacitance, c) intercalation capacitance, and d) Faradic battery-type [60].

2.5.3 Electrochemical Impedance Spectroscopy (EIS):

The EIS is a technique used to study the charge storage mechanism at an electrode-electrolyte interface and is also known as AC impedance spectroscopy. EIS is advantageous as it covers a wide range of frequencies, enabling accurate determination of resistances at the electrode-electrolyte interface. In this method, a small AC signal (5 to 10 mV) is applied across the SC cell over a frequency range from 1 mHz to 1 MHz. The current response is measured, and the Nyquist plot is generated by plotting imaginary impedance against real impedance [61, 62].

The EIS technique is useful in recording frequency-independent and dependent resistive parameters of the system. If is the input sinusoidal voltage and is its output response $V(\omega) = V_0 \sin \omega t$ and $I(\omega) = I_0 \sin(\omega t + \phi)$, then the impedance of the electrode material is given by:

$$Z(\omega) = \frac{V(\omega)}{I(\omega)} = \frac{V_0 \sin(\omega t)}{I_0 \sin(\omega t + \phi)} = Z_0 \frac{\sin(\omega t)}{\sin(\omega t + \phi)} \quad (2.18)$$

Impedance is characterized by its magnitude Z_0 and phase shift (ϕ). In the Nyquist plot, impedance is represented by its real and imaginary components, as illustrated in **Figure 2.15**. The inset shows a typical equivalent circuit (Randles cell) related to the Nyquist plot. In the Nyquist plot, R_{ct} represents the charge transfer resistance (**Figure 2.15**), and the transfer of charges is determined by actors such as kinetics, temperature, concentration, and potential of reaction products affect impedance measurements. In a Nyquist plot, the solution resistance (R_s) is generally small and the plot intercepts close to the origin of the Z_{re} -axis.

However, due to inherent internal resistance, the Nyquist plot's first intercept on the Z_{re} -axis is slightly positive, representing the equivalent R_s , which is in series with the charge transfer resistance (R_{ct}) (**Figure 2.16 (a)**). Additionally, in the lower

frequency region, indicated by the straight line in **Figure 2.16 (b)**, there is a resistance offered to the diffusion of electrolyte ions, known as Warburg impedance (W), which is added to the equivalent circuit in series with R_{ct} . The W is smaller at higher frequencies because the diffusing reactant does not need to travel a long distance [63].

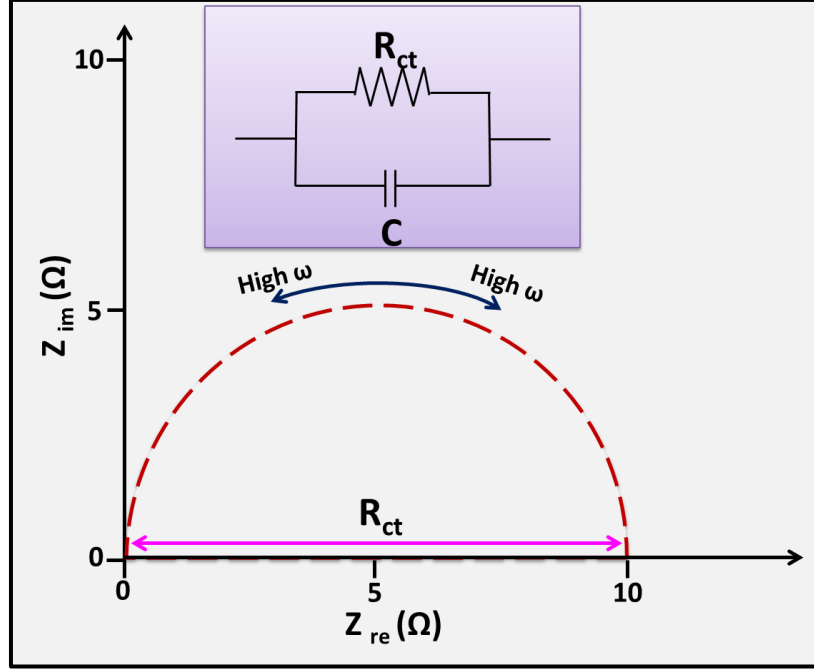


Figure 2.15: Nyquist plot with electrical equivalent circuit consisting charge R_{ct} in parallel with C [64].

Using EIS, the capacitance as a function of frequency can be evaluated. At low frequencies, a supercapacitor behaves like a pure resistor, while at high frequencies, it acts as a pure capacitor. In the intermediate frequency range, both the physical and morphological characteristics of the electroactive material affect the capacitance, resulting in a combination of resistive and capacitive behavior. The data are then analyzed and fitted using various interface parameters and algorithms.

$$V(\omega) = V_0 e^{i\omega t} \quad (2.19)$$

$$I(\omega) = I_0 e^{i\omega t - \phi} \quad (2.20)$$

The complex quantity is written as,

$$Z(\omega) = Z_0 e^{i\phi} = Z_0 e^{(\cos\phi + i \sin\phi)} \quad (2.21)$$

The expression for $Z(\omega)$ is represented by its real and imaginary components:

The ZIVE MP1 electrochemical workstation was used to conduct all the tests in [section 2.5](#). Data collected from these tests were analyzed to determine properties like C_s , S_E , S_P , R_s , and R_{ct} . EIS measurements were taken with a 10 mV potential amplitude and a frequency range of 0.1 MHz to 0.01 Hz [65]. While maintaining a bias potential equivalent to the open circuit potential. To analyze the EIS data and derive the equivalent circuit, the "ZSimpWin" editor was utilized, allowing for a comprehensive understanding of the charge storage mechanisms and electrical properties of the SC cell.

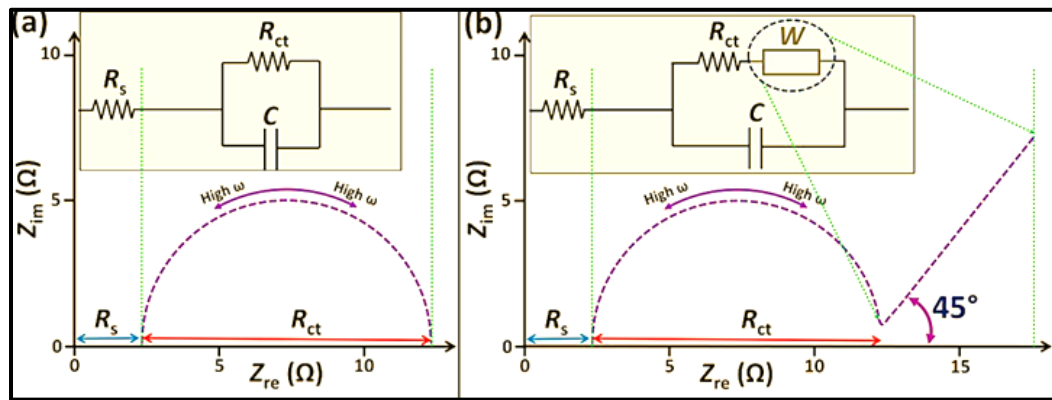


Figure 2.16: Nyquist plots with corresponding electrical equivalent circuit a) consisting of R_s , R_{ct} , and, C , and b) consisting of R_s , R_{ct} , C , and W .

2.6 Gas Sensor Measurements:

Evaluating sensors for real-time applications involves assessing their sensitivity by measuring resistance changes in response to known concentrations of analyte gas. Known gas concentrations can be obtained through methods such as permeation tubes, gas canisters, evaporation, diffusion, and gas flow meters. Two main methods are used to measure gas response:

i) Flow-Through Method:

In this method, gas flow meters are used to record the response curve while a controlled amount of analyte gas flows continuously. The concentration of the analyte gas is adjusted by mixing it with a carrier gas, usually nitrogen. This approach allows for repeated measurements, making it possible to monitor variations in gas concentration.

ii) Static Environment Method:

In the static environment method, a sensor is placed in a sealed chamber of known volume. A specific amount of gas at a defined concentration is injected into the chamber using a syringe. The sensor's resistance is monitored until it stabilizes. To assess recovery, the sensor is exposed to air after the gas is removed [66]. This study employs the static environment method for gas sensor measurements. The setup for these measurements includes the components illustrated in **Figure 2.17**.

The test chamber, made of stainless steel with a capacity of 315 cm³, is designed to resist corrosion from various gases.

iii) Temperature Controller:

Semiconductor sensors respond significantly at elevated temperatures. Therefore, a digital temperature controller (DTC) is employed to regulate the temperature at which the sensor's response to the analyte gas is measured.

iv) Septum for Gas Insertion:

To prevent gas leakage, introduce an analyte gas with a specified concentration through a small opening fitted with a rubber gasket.

v) Hot Plate:

A hot plate, heated to the temperature specified by the DTC, functions as the sensor stage. The sensor element, which measures 1 cm × 1 cm, is placed on this hot plate and preheated to the target temperature before measurements are taken. By employing these methods and equipment, we can accurately evaluate the gas sensors for their responsiveness to analyte gases.

vi) Electrical Contacts and Probes:

Silver paste is used to create electrical contacts on the sensor element, which is then linked to an electrometer using two probes.

vii) Probes to Electrometer:

The probes are connected to a Keithley 6514 electrometer to precisely measure resistance changes before and after introducing the analyte gas into the test chamber.

viii) Insulation:

The test chamber, made of stainless steel with a capacity of 315 cm³, is designed to resist corrosion from various gases.

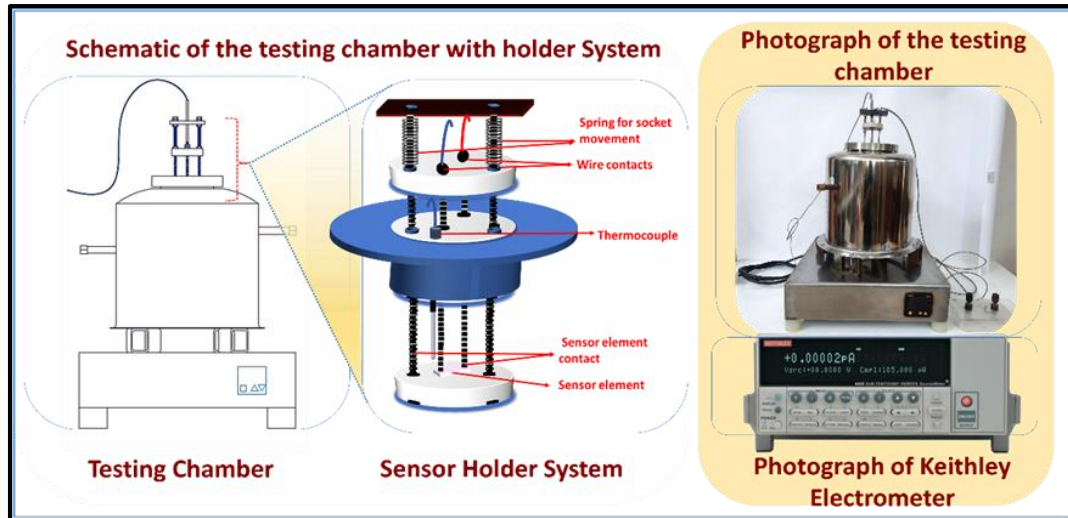


Figure 2.17: (a) Schematic of the gas sensor measurement assembly and (b) Actual photograph of the gas sensor measurement assembly.

2.7 Gas Sensor Techniques:

Gas sensor measurement techniques assess parameters including resistance stabilization, sensitivity, selectivity, response time, recovery time, repeatability, and long-term stability.

2.7.1 Resistance Stabilization:

For gas sensing applications, achieving a stable reference resistance level is vital before subjecting the sensor element to reducing or oxidizing gases. This stability is essential because changes in oxygen concentration due to adsorption lead to equilibrium in the chemisorption process [67].

2.7.2 Sensitivity:

Sensitivity is a key parameter that indicates how much a specific gas affects the sensor's resistance. It is defined by the equation,

$$S (\%) = (R_a - R_g / R_a) \times 100 \quad (2.22)$$

Where R_a is the sensor's resistance in air, and R_g is the resistance in the presence of the gas [59].

2.7.3 Response and Recovery Time:

Response time is the duration required for the sensor's signal to reach 90% of its maximum value from its initial value. For semiconductor sensors, it specifically refers to the time needed for the resistance to achieve 90% of its saturation value after

gas exposure. Recovery time is the period needed for the sensor's resistance to return to 90% of its original value after reaching its maximum or saturation level. This measurement begins once the gas is removed or turned off. For semiconductor sensors, it indicates how long it takes for the resistance to recover to 90% of its initial state.

2.7.4 Selectivity:

Selectivity refers to sensors ability to specifically respond to a particular gas, which is closely related to its operating temperature.

2.7.5 Reproducibility:

Reproducibility refers to a sensors capability to produce consistent measurements when placed in the same environment; the sensor should show nearly identical dynamic characteristics for each cycle of gas exposure and removal, ensuring consistent performance.

2.7.6 Long-Term Stability:

Long-term stability denotes the ability of the sensor to maintain its properties while, continuously operating in an antagonistic environment for an extended period. A reliable sensor is expected to perform consistently over several years.

2.8 Theoretical Background of Gas Sensor Mechanism:

The gas sensing mechanism involves the following processes:

- A) Electron Depletion
- B) Band Bending
- C) Resistance Change

The gas sensing mechanism relies on these fundamental processes to detect and measure the presence of gases effectively.

A) Electron Depletion:

Crystalline semiconductor gas sensors consist of interconnected grains forming aggregates connected by grain boundaries. When oxygen adsorbs on these surfaces, it captures electrons from the conduction band, creating a space-charge layer. Sensor sensitivity improves when the particle size of the sensing film is about or less than twice the space-charge layer thickness [68].

Adsorbed gases either donate or accept electrons, altering the sensor's conductivity. Donor gases increase conductivity, while acceptor gases decrease it. The gas sensing mechanism depends on the interaction between gases and the semiconductor surface, especially at the grain boundaries of polycrystalline materials like metal oxides [69, 70].

B) Band Bending:

When heated to high temperatures, a semiconductor gas sensor allows free electrons to flow through its grain boundaries. In an oxygen-rich environment, oxygen adsorbs onto the semiconductor's surface, forming a potential barrier at the grain boundaries. This adsorption creates a layer of charged oxygen species that traps electrons from the material's bulk, leading to an electron-depleted region and an elevated potential barrier. As a result, the flow of electrons decreases, increasing the sensor's resistance [71]. The temperatures below the 420 K, the oxygen is ionosorbed as O^{2-} , if the temperature is between 420 to 670 K, the oxygen mainly ionosorbed as O^- . This corresponds to the gas sensors operating temperature. Above the temperature of 670 K, the formation of O^{2-} occurs.

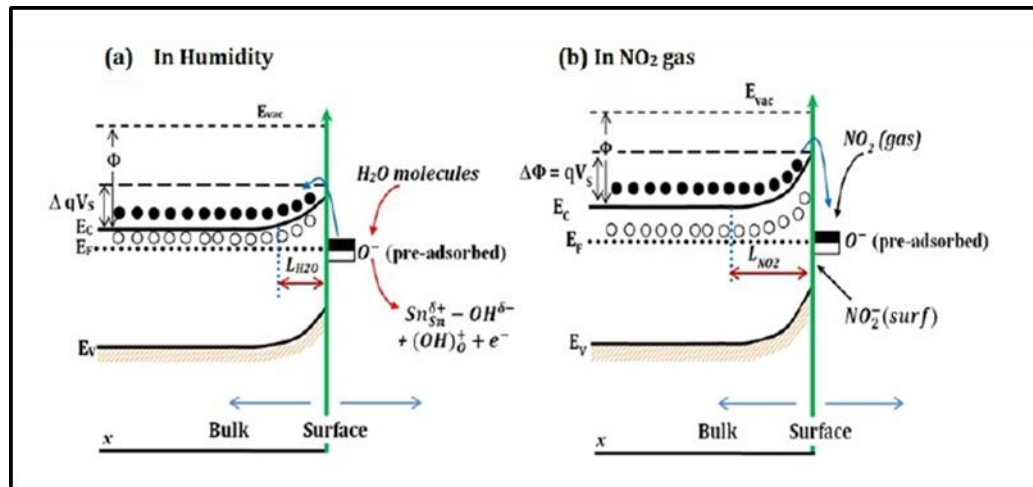


Figure 2.18: The illustration of the band bending due to the adsorption of oxygen species for an n-type semiconductor such as a SnO_2 layer. The schematic of chemisorption a) water molecules and b) NO_2 at the surface of an n-type SnO_2 [72].

The electrons required for this process originate from the donor site, which contains intrinsic oxygen vacancies. These electrons are extracted from the conduction band and trapped on the surface, creating an electron depletion layer known as the space charge layer [73]. The schematic representation of gas sensing

mechanism has been reported in Elsevier [72]. When oxygen in the air chemisorbs onto a materials surface, it interacts with excess electrons to form oxygen species. This process leads to the formation of a space charge layer at the surface, and reducing the carrier concentration. When the material is then exposed to NO₂ gas, the adsorbed oxygen species react with the NO₂, further reduces the electron concentration near the surface of the material. As a result, the material resistance increases [74]. **Figure 2.18 (a and b)** shows the illustration of the band bending due to the adsorption of oxygen species for an n-type semiconductor.

C) Resistance Change:

When a sensor is exposed to a reducing gas, gas molecules are adsorbed on the surface of the semiconductor sensor element. This adsorption process reduces the potential barrier by injecting electrons into the conduction band, which enhances electron flow and lowers electrical resistance. As a result, metal oxide semiconductor gas sensors act as variable resistors, with their resistance changing according to the gas concentration [75]. On the other hand, when exposed to oxidizing gases, the opposite effect occurs, and the resistance of n-type semiconductor gas sensors increases [76].

2.9 References:

- [1] N. Baig, I. Kammakakam, W. Falath, *Mater. Adv.*, 2, (2021), 1821-1871.
- [2] J. Hafner, *Computer physics communications*, 177, (2007), 6-13.
- [3] S. Louie, Y. Chan, F. da Jornada, Z. Li, D. Qiu, *Nat. Mater.*, 20, (2021), 728-735.
- [4] H. Frey, *Handbook of Thin-Film Technology*, Springer, Berlin, Heidelberg. (2015), 117-132.
- [5] K. Wasa, *Handbook of Sputter Deposition Technology: Fundamentals and Applications for Functional Thin Films, Nano-Materials and MEMS*, (2012), 1-660.
- [6] P. Innocenzi and L. Malfatti, *Chem Soc Rev.*, 42, (2013), 4198-4216.
- [7] O. Abegunde, E. Akinlabi, O. Oladijo, S. Akinlabi, A. Ude, *AIMS Mater. Sci.*, 6, (2019), 174-199.
- [8] R. Birney, *Coatings*, 10, (2020), 1228-1232.
- [9] T. Schneller, R. Waser, M. Kosec, D. Payne, Vienna: Springer Vienna; (2013), 1-796.
- [10] R. Mane and C. Lokhande, *Mater. Chem. Phys.*, 65, (2000), 1-31.
- [11] S. Pawar, B. Pawar, J. Kim, O. Joo, C. Lokhande, *Curr. Appl. Phys.*, 11, (2011), 117-161.
- [12] A. Lundin and G. Kitaev, *Inorg. Mater.*, 1, (1965), 2107-2111.
- [13] M. Ristov, G. Sinadinovski, I. Grozdanov, M. Mitreski, *Thin Solid Films*, 149, (1987), 65-71.
- [14] Y. Nicolau and J. Menard, *J. Cryst. Growth*, 92, (1988), 128-142.
- [15] G. Hodes, *Electrochemistry of Nanomaterials*, (2001), ISBN:9783527298365, 1-310.
- [16] H. Pathan, and C. Lokhande, *Bull. Mater. Sci.*, 27, (2004), 85-111.
- [17] Y. Nicolau, *Appl. Surf. Sci.*, 22, (1985), 1061-1074.
- [18] M. Birkholz, John Wiley & Sons; 12, (2006), 1-30.

- [19] D. Cullity, Second ed., Addison-Wesley, London (1978).
- [20] <https://www.findlight.net/blog/2019/03/27/ftir-principles-applications>
- [21] <https://www.sigmaaldrich.com/technical-documents/articles/biology/ir-spectrumtable.html#ir-table-by-compound>
- [22] <https://www.bruker.com/products/infrared-near-infrared-and-ramanspectroscopy/ft-ir-routine-spectrometers/compact-ftir-alpha-ii.html>
- [23] A. Munajad, C. Subroto, Suwarno, *Energies*, 11, (2018), 364-376.
- [24] https://en.wikipedia.org/wiki/Raman_spectroscopy
- [25] I. Ebenezar, S. Ramalingam, C. Raja, P. Prabakar, *J. Nano. Adv. Mat.*, 2, (2014), 11-25.
- [26] J. Breier, S. White, C. German, *Phil. Trans. R. Soc. A*, 368, (2010) 3067-3086.
- [27] A. Downes, A. Elfick, *Sens.*, 10, (2010), 1871-1889.
- [28] <https://bwtek.com/raman-components-of-a-raman-spectrometer>
- [29] https://www.mt.com/in/en/home/applications/L1_AutoChem_Applications/Raman-Spectroscopy.html
- [30] H. Vašková, *Math Models Methods Appl Sci.*, 5, (2011), 1205-1212.
- [31] <https://www.thermofisher.com/blog/microscopy/sputter-coating-for-sem-howthis-sample-preparation-technique-assists-your-imaging>
- [32] A. Mayeen, L. Shaji, A. Nair, N. Kalarikkal, *MNT*, (2018), 335-364.
- [33] <https://www.hitachihightech.com/global/science/products/microscopes/electronmicroscope/fe-sem>.
- [34] https://epm.univie.ac.at/fileadmin/user_upload/p_epm/xps-machine.png
- [35] <http://www.ramehart.com/790.htm>
- [36] M. Vadiyar, S. Bhise, S. Patil, S. Kolekar, A. Shelke, N. Deshpande, J. Chang, K. Ghule, A. Ghule, *Chem. Commun.*, 52, (2016), 2557-2560.
- [37] T. Chau, W. Bruckard, P. Koh, A. Nguyen, *Adv. Colloid Interface Sci.*, 150, (2009), 106-115.
- [38] P. Sinha, A. Datar, C. Jeong, X. Deng, Y. Chung, L. Lin, *J. Phys. Chem. C*, 123, (2019), 520209-520248.
- [39] http://www.pharmacopeia.cn/v29240/usp29nf24s0_c846.html

-
- [40] D. Lapham and J. Lapham, *Int J Pharm.*, 568, (2019), 118522-118566.
- [41] A. Forse, C. Merlet, J. Griffin, C. Grey, *J. Am. Chem. Soc.*, 138, (2016), 5731-5744.
- [42] A. Afif, S. Rahman, A. Azad, J. Zaini, M. Islan, A. Azad, *J. Energy Storage*, 25, (2019), 100852-100876.
- [43] Y. Wu and C. Cao, *Sci. China Mater.*, 61, (2018), 1517-1526.
- [44] J. Park, B. Kim, Y. Yoo, H. Chung, W. Kim, *ACS Appl. Mater. Interfaces*, 6, (2014), 19499-19503.
- [45] Y. Shao, M. El-Kady, J. Sun, Y. Li, Q. Zhang, M. Zhu, H. Wang, B. Dunn, R. B. Kaner, *Chem. Rev.*, 118, (2018), 9233-9280.
- [46] V. Augustyn, P. Simon, B. Dunn, *Energy Environ. Sci.*, 7, (2014), 1597-1614.
- [47] S. Perera, X. Ding, A. Bhargava, R. Hovden, A. Nelson, L. Kourkoutis, R. Robinson, *Chem. Mater.*, 27, (2015), 7861-7873.
- [48] V. Climent and J. Feliu, *Annu. Rev. Anal. Chem.*, 13, (2020), 201-222.
- [49] M. Portales, A. Fraga, A. García, O. García-Zaldívar, A. Barranco, M. Frutis, *J. Solid State Electrochem.*, 22, (2018), 471-478.
- [50] A. Wardak and H. Tien, *Bioelectrochem. Bioenerg.*, 24, (1990), 1-11.
- [51] H. Qu, M. Harada, T. Okada, *ChemElectroChem*, 4, (2017), 35-38,
- [52] C. Peng, G. Snook, D. Fray, M. Shaffer, G. Chen, *Chem. Commun.*, 44, (2006), 4629-4631.
- [53] R. Bushby, O. Lozman, L. Mason, N. Taylor, S. Kumar, *Mol. Cryst. Liq. Cryst.*, 410, (2004), 171-181.
- [54] D. Qazzazie, O. Yurchenko, S. Urban, J. Kieninger, G. Urban, *Nanoscale*, 9, (2017), 6436-6447.
- [55] R. Salunkhe, Y. Kaneti, Y. Yamauchi, *ACS Nano*, 11, (2017), 5293-5308.
- [56] P. Veerakumar, A. Sangili, S. Manavalan, P. Thanasekaran, K. Lin, *Ind. Eng. Chem. Res.*, 59, (2020), 6347-6374.
- [57] B. Kim, S. Sy, A. Yu, J. Zhang, *J. Electrochemical supercapacitors for energy storage and conversion, Handbook of clean energy systems*, (2015), 1-25.
- [58] K. Kumar, N. Choudhary, Y. Jung, J. Thomas, *ACS Energy Lett.*, 3, (2018), 482-495.
- [59] K. Breitsprecher, C. Holm, S. Kondrat, *ACS Nano*, 12, (2018), 9733-9741.
-

- [60] N. Chodankar, H. Pham, A. Nanjundan, J. Fernando, K. Jayaramulu, D. Golberg, Y. Han, D. Dubal, Small, 16, (2020), 2002806-2002841.
- [61] B. Mei, O. Munteshari, J. Lau, B. Dunn, L. Pilon, J. Phys. Chem. C, 122, (2018), 194-206.
- [62] D. Kampouris, X. Ji, E. Randviira, C. Banks, RSC Adv., 5, (2015), 12782-12791.
- [63] A. Bredar, A. Chown, A. Burton, B. Farnum, ACS Appl. Energy Mater., 3, (2020), 66-98.
- [64] B. Mei, J. Lau, T. Lin, S. H. Tolbert, B. S. Dunn, L. Pilon, J. Phys. Chem. C, 122, (2018), 24499-24511.
- [65] http://wonatech.com/public_html/index.php?module=Goods&action=SiteGoodseng&sMode=VIEW_FORM&CurrentPage=1&sCurrSortCd=003001002&iGoodsCd=500&iNo=1
- [66] D. Aswal, S. Gupta, Science and technology of chemiresistor gas sensors, Nova Science Publishers, New York, (2007), 1-381.
- [67] J. Gunjekar, A. More, C. Lokhande, Sens. Actuators B: Chem., 131, (2008), 356-361.
- [68] V. Patil, S. Vanalakar, P. Patil, J. Kim, Sens. Actuators B: Chem., 239, (2017), 1185-1193.
- [69] Y. Sun, S. Liu, F. Meng, J. Liu, Z. Jin, L. Kong, J. Liu, Sens., 12, (2012), 2610-2631.
- [70] M. Graf, A. Gurlo, N. Barsan, U. Weimar, A. Hierlemann, J. Nanopart. Res., 8, (2006), 823-839.
- [71] G. Korotcenkov, Mater. Sci. Eng. B, 139, (2007), 1-23.
- [72] A. Haidry, N. Kind, B. Saruhan, J. Sens. Sens. Syst., 4, (2015), 271-280.
- [73] S. Kanan, O. El-Kadri, I. Abu-Yousef, M. Kanan, Sens., 9, (2009), 8158-8196.
- [74] V. Patil, S. Kumbhar, S. Vanalkar, N. Tarwal, S. Mali, J. Kim, P. Patil, New J. Chem., 42, (2018), 13573-13580
- [75] S. Chang and J. Vac. Sci. Technol, 17, (1980), 366-369.
- [76] G. Eranna, B. Joshi, D. Runthala, R. Gupta, Crit. Rev. Solid State Mater. Sci., 29, (2004), 111-188.

CHAPTER-3

**Dy₂S₃ and rGO/Dy₂S₃ Thin Films by CBD
Method: Characterization and
Electrochemical Performance**

CHAPTER-3

Dy₂S₃ and rGO/Dy₂S₃ Thin Films by CBD Method: Characterization and Electrochemical Performance

Sr. No.	Title		Page No.
3.1	Introduction		74
3.2.	Synthesis of Dy ₂ S ₃ and rGO/Dy ₂ S ₃ Thin Films		75
	3.2.1	Introduction	75
	3.2.2	Experimental Details	75
		3.2.2.1 Cleaning Substrate	75
		3.2.2.2 Chemicals	76
		3.2.2.3 Synthesis of rGO	76
		3.2.2.4 Synthesis of Dy ₂ S ₃ Thin Films	77
		3.2.2.5 Synthesis of rGO/Dy ₂ S ₃ Thin Films	78
3.3	Material Characterizations		79
	3.3.1	Physico-Chemical Characterizations	79
	3.3.2	Electrochemical Characterizations	79
3.4	Results and Discussion		80
	3.4A	Physico-Chemical Characterizations	80
		3.4A.1 Physico-Chemical Characterizations of Dy ₂ S ₃ Thin Films	80
		3.4A.2 Physico-Chemical Characterizations of rGO/Dy ₂ S ₃ Thin Films	85
	3.4B	Electrochemical Characterizations	92
		3.4B.1 Electrochemical Characterizations of Dy ₂ S ₃ Thin Films	92
		3.4B.2 Electrochemical characterizations of rGO and rGO/Dy ₂ S ₃ Thin Films	96
3.5	Conclusions		102
3.6	References		103

3.1 Introduction:

Currently, worldwide technological development is drastically increasing due to the lifestyle of the people being changed, and they are moving towards highly developed technology-based products utilized in their daily lives, such as wearable electronics products, home appliances, auto industries, medical healthcare, intelligent devices, micro-robotics, smartphones, flexible touch screen display, electronic skin, implantable medical treatment, etc. Accordingly, energy storage systems are highly required to fulfill this consumer demand. Mainly the various kinds of energy storage systems, but among these, the supercapacitor is one of the emerging trends growing towards the development of technology due its various unique properties i.e. their energy densities are higher than capacitors and power densities than batteries, flexibility nature, and long cycle life etc. [1-4].

In the past few years, rGO has been composited with metal chalcogenides and extensively studied in supercapacitor applications [5, 6]. The carbon-containing materials like GO, rGO, CNT, and AC are usual materials with a range of various unique properties, including high specific surface area, pores of various sizes and shapes, and excellent electronic conductivity, which make them useful in energy storage [7-9]. For improved electron transfer, the synthesis methods optimization of the EDLC and pseudocapacitive materials, nanoparticle size, and surface microstructure is needed [10]. The composition with rGO modifies structural and morphological properties and provides a stable interactive surface and layered structural growth, which favors improvement in the desired electrochemical properties of the pristine electrodes [11, 12].

With ongoing research in this area, rare-earth-based compounds hold great potential for advancing the development of high-performance energy storage devices [13]. Kumbhar et al. [14] reported nanoflakes like nanostructured Sm_2S_3 film prepared by chemical method and exhibited maximum C_s of 213 F g^{-1} at 5 mVs^{-1} scan rate in LiClO_4 -propylene carbonate electrolyte. Patil et al. [15] reported La_2S_3 films by successive ionic layer adsorption and reaction (SILAR) method and achieved a C_s of 256 F g^{-1} . Ubale et al. [16] reported Yb_2S_3 thin film by CBD method and exhibited maximum C_s of 184.6 F g^{-1} in 1 M KOH electrolyte at a 5 mV s^{-1} scan rate. Bagwade et al. [17] reported Dy_2S_3 thin films deposited by SILAR method and obtained maximum C_s of 273 F g^{-1} at a scan rate of 5 mV s^{-1} . Ghogare et al. [18] reported β -

LaS₂ thin films by hydrothermal method and obtained C_s of 121.42 F g⁻¹ in 1 M Na₂SO₄ electrolyte at a 5 mV s⁻¹ scan rate. Ubale et al. [19] reported SILAR deposited Yb₂S₃ thin film and achieved a C_s of 181 F g⁻¹ at a 5 mV s⁻¹ scan rate. The present chapter deals with the synthesis of Dy₂S₃ and rGO/Dy₂S₃ thin films by CBD method and their characterization.

3.2 Synthesis of Dy₂S₃ and rGO/Dy₂S₃ Thin Films:

3.2.1 Introduction:

In a SC, the electrode material must have good electrical conductivity, appropriate pore size, high surface area, chemical stability, and thermal stability. The electrode material preparation process is inexpensive and scalable, allowing for the commercialization of SCs in large-scale applications.

From these perspectives, Dy₂S₃ and rGO/Dy₂S₃ films are fabricated on flexible SS substrate. By using CBD method, Dy₂S₃ nanoparticles are composited with rGO sheets to create the porous electrode structure. Subsequently, crystal structure, surface morphology, and wettability of Dy₂S₃ and rGO/Dy₂S₃ films film were studied using different physico-chemical techniques like XRD, FT-IR spectroscopy, FE-SEM, and XPS to determine chemical states, EDAX for elemental composition, and BET for determination of specific surface area of thin film material. Also, the wettability measurement was carried out to study the interaction between Dy₂S₃ and rGO/Dy₂S₃ thin film electrodes with DDW.

3.2.2 Experimental Details:

3.2.2.1 Cleaning of Substrate:

To prepare thin films of high quality using chemical methods, a very clean substrate surface is a necessary requirement. Furthermore, on the substrate surface, any materials impurity acts as a nucleation centre. The primary requirement for SCs is a conducting substrate. The SS substrate is suitable for SCs, because of its low cost and high electrical conductivity. Were the SS substrates were cleaned using acetone and DDW after polished with zero grade polish paper. Subsequently, the substrates were ultrasonically cleaned for 10 min. Finally, substrates were utilized for material deposition after air dried.

3.2.2.2 Chemicals:

All analytical grade (AR) chemicals dysprosium nitrate $\text{Dy}(\text{NO}_3)_3$, sodium thiosulfate ($\text{Na}_2\text{S}_2\text{O}_3$), citric acid ($\text{C}_6\text{H}_8\text{O}_7$), and sodium sulfate (Na_2SO_4) were used as received. A clean and polished SS sheet sized $5 \times 1 \text{ cm}^2$ (304 grade) was used as a substrate and DDW as a solvent.

3.2.2.3 Synthesis of rGO:

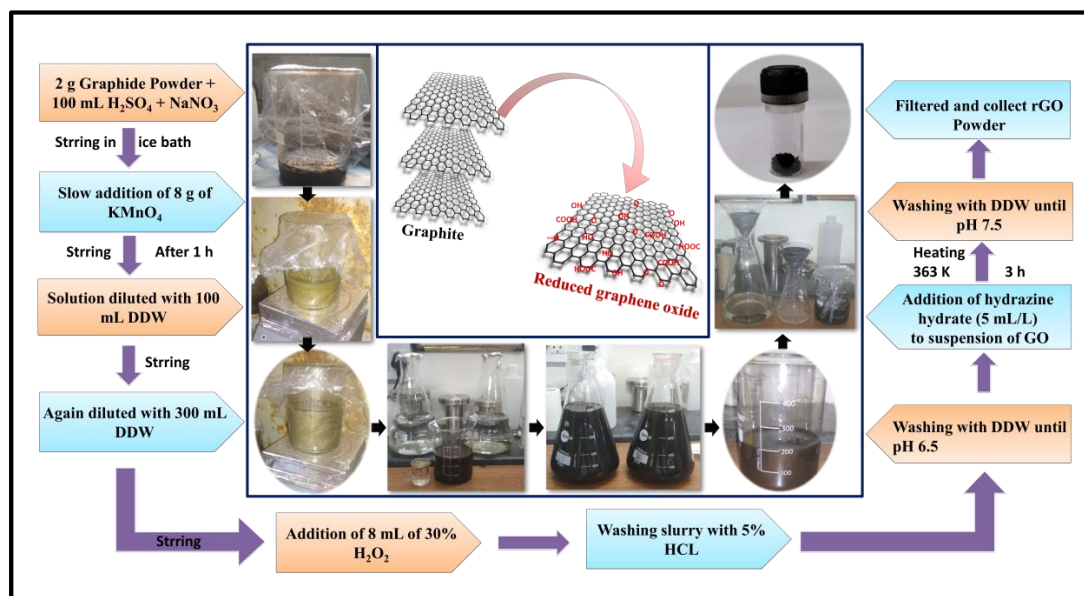


Figure 3.1: Schematic flow chart of rGO synthesis.

A Modified Hummer's method was used to synthesize GO [20]. Flakes of graphite were bought from Sigma-Aldrich and used to synthesize GO. The 2 grams of graphite flakes (with an average diameter of $100 \mu\text{m}$) and 100 mL of concentrated H_2SO_4 were mixed in a 500 mL conical flask, and the mixture was placed in an ice bath with continuous stirring. Then 1 g of NaNO_3 was added.

Slowly, 8 g of KMnO_4 was added into this mixture to maintain a reaction temperature below 293 K. After the addition, the reaction mixture was kept at room temperature with continuous stirring for 12 hours. Subsequently, 100 mL of DDW was added, followed by an additional 300 mL of DDW and 8 mL of H_2O_2 (30%) after 1.5 hours. This addition resulted in a yellowish solution. The mixture was then rinsed with 5% HCl multiple times, followed by rinsing with DDW several times until reaching a pH of 6.5. The previously reported procedures for the chemical reduction of GO were followed [21]. Hydrazine hydrate was used as a reducing agent for GO. 5 mL of hydrazine hydrate was added to 500 mL of GO suspension of density 1 mg

mL^{-1} , and heated for 3 h at 363 K. After completion of the reaction, the residue was washed using DDW several times to remove unwanted traces of hydrazine hydrate. The slurry of rGO was used to papered rGO films on the SS substrate by using the layer-by layer (LBL) method. To obtain a uniform suspension, 1 mg mL^{-1} rGO suspension was sonicated for 1 h. The cleaned SS substrate was immersed in rGO suspension for 20 s and dried for 40 s at room temperature, and such 200 cycles were repeated to achieve the optimum film thickness. The prepared rGO thin film was used for further characterizations. **Figure 3.1** provides a schematic representation of the entire rGO synthesis process.

3.2.2.4 Synthesis of Dy_2S_3 Thin Films:

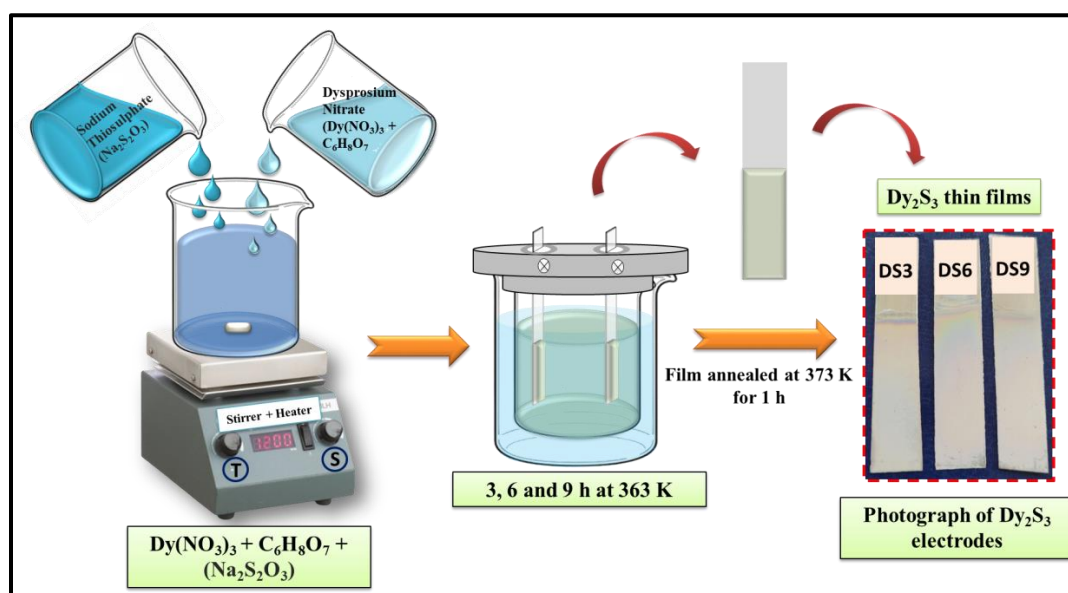


Figure 3.2: The schematic of CBD method employed for Dy_2S_3 thin film electrode preparation.

The deposition of Dy_2S_3 thin films was carried out using CBD method. In a typical synthesis, 0.05 M $\text{Dy}(\text{NO}_3)_3$, and 0.1 M ($\text{Na}_2\text{S}_2\text{O}_3$) used as a cationic and anionic precursors and citric acid was used as a complexing agent. The both cationic and anionic precursors were mixed together with 20 mL DDW and citric acid was added slowly to maintain pH ~ 10 of bath. The above solution was stirred well for 15 min. The cleaned SS substrates were immersed vertically in the above bath and the bath kept in water bath at a constant 363 K temperature maintained for different time periods (3, 6, and 9 h). The schematic for chemical deposition of Dy_2S_3 films by CBD method is shown in **Figure 3.2**.

When the ionic product of Dy^{3+} and S^{2-} exceeds the solubility product of Dy_2S_3 , the precipitate of Dy_2S_3 occurs. During the precipitation, colour of the solution changed from colourless to whitish, and heterogeneous reaction takes place. After deposition, 3, 6, and 9 h, the whitish colored Dy_2S_3 thin films on SS substrate were taken out from the bath, washed with DDW and dried at room temperature. These samples were denoted as DS3, DS6 and DS9, for 3, 6, and 9 h deposition period, respectively. These samples were used for further characterizations. To study the effect of deposition time, the other preparative parameters such as concentration of $\text{Dy}(\text{NO}_3)_3$, and $(\text{Na}_2\text{S}_2\text{O}_3)$ precursors, bath temperature and pH of the bath were kept constant and only depositing time period was varied from 3 to 9 h.

3.2.2.5 Synthesis of rGO/ Dy_2S_3 Thin Films:

To prepare rGO suspension, 1 mL of the rGO solution was dried at 373 K, and the concentration was determined by measuring it. From this concentration, rGO dispersion in DDW was prepared at concentration of 1.0 mg mL^{-1} , followed by a similar process to deposit Dy_2S_3 as described above. Briefly, 0.05 M $\text{Dy}(\text{NO}_3)_3$, cationic and 0.1 M $(\text{Na}_2\text{S}_2\text{O}_3)$ anionic precursors mixed together with 20 mL DDW.

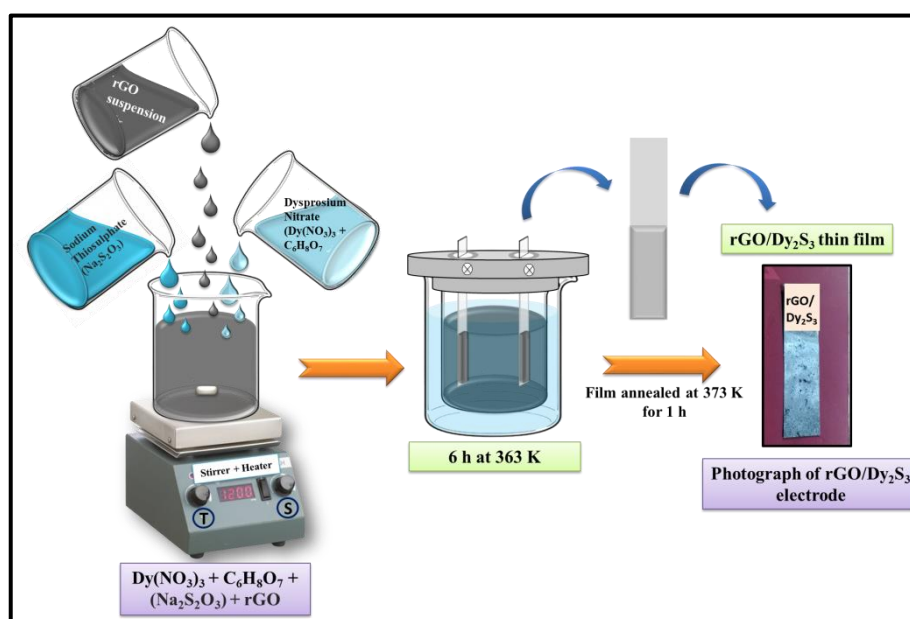


Figure 3.3: Schematic representation of rGO/ Dy_2S_3 thin film preparation by CBD method.

Further, the 10 mg of as-prepared rGO solution was dispersed in the mixed solution. After magnetic stirring for 15 min, citric acid solution was dropwise added in the mixture. Then, SS substrates were vertically immersed in above bath and

deposition was carried out for 6h at 363K. After deposition, the SS substrates were removed from the bath and cleaned with DDW water. Finally, the prepared rGO/Dy₂S₃ composite thin films on SS substrate were used for further characterizations. An illustrative representation of the formation of a layered structure of rGO/Dy₂S₃ composite is provided in **Figure 3.3**.

3.3 Material Characterizations:

3.3.1 Physico-Chemical Characterizations:

Rigaku miniflex-600 operating with Cu K α radiation (λ = 0.1540 nm) was used to acquire the XRD patterns of samples. FT-IR analysis recorded using Bruker Tensor 27 FT-IR instrument was used for the qualitative analysis of functional groups and bonding present in Dy₂S₃, and rGO/Dy₂S₃ materials. FE-SEM (JEOL JEM 2100) was utilized to study the surface morphology, while EDAX was employed to investigate the elemental composition of the substance. The XPS was used for the surface chemical composition of rGO/Dy₂S₃ film. The specific surface area and pore size distribution of Dy₂S₃ and rGO/Dy₂S₃ composites were measured by BET analysis using the quantachrome V11.02 instrument. The contact angle measurement was carried out using the Rame-Hart instrument. The Raman spectra of samples were measured using JASCO NRS-5100 equipment using a laser of λ = 532 nm.

3.3.2 Electrochemical Characterizations

The electrochemical workstation (ZIVE MP1) was utilized to analyze the electrochemical properties of thin film electrodes. The typical three-electrode system consists of thin films of Dy₂S₃, rGO/Dy₂S₃, and rGO as working electrodes, a saturated calomel electrode (SCE) as a reference, and a platinum sheet as a counter electrode. Electrochemical techniques like voltammetry and chronopotentiometry were performed in the potential window of -1.0 to 0 V/SCE to get CV and GCD curves.

Figure 3.4 shows the electrochemical work station, b) experimental setup, and c) schematic representation of three electrode system. All electrodes were tested in 1 M Na₂SO₄ electrolyte at room temperature. 1 cm² area of the working electrode was exposed to the electrolyte. The EIS measurements were performed with potential amplitude of 10 mV and a frequency range of 0.01 Hz to 0.1 MHz.

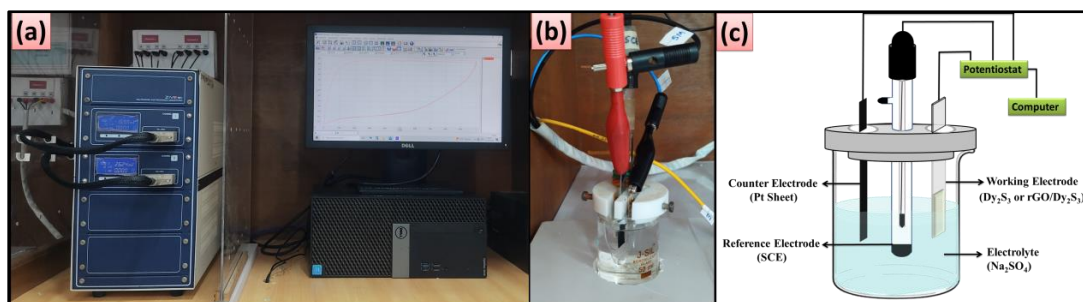


Figure 3.4: a) The electrochemical work station, b) experimental setup, and c) schematic representation of three electrode system.

3.3.2.1 Cyclic Voltammetry (CV) Study:

The CV is a crucial technique for determining electronic transfer redox reactions and redox potentials; it is used to calculate the C_s of electrode materials. The CV study of Dy₂S₃, and rGO/Dy₂S₃ thin film electrodes was carried out within the potential window of -1.0 V to 0 V/SCE in 1 M Na₂SO₄ electrolyte. The C_s of electrode material was estimated using **Equation 2.12** and charge storage mechanism was analyzed using power law.

3.3.2.2 Galvanostatic Charge Discharge (GCD) Study:

The GCD study of Dy₂S₃, and rGO/Dy₂S₃ thin film electrodes was carried out in the same potential window as that of CV. The shape of the GCD curves identifies the nature of charge storage mechanism. **Equation 2.14** is used to calculate the C_s values of thin film electrode using GCD curves.

3.3.2.3 Electrochemical Impedance Spectroscopy (EIS):

A resistive parameter analysis of the electrode-electrolyte interface was performed using the EIS. Using the electrochemical workstation (ZIVE MP1), the EIS measurement was used to describe the quality of the interface between the electrode and electrolyte. In the frequency range of 0.01 Hz to 0.1 MHz, the EIS study was conducted at an open circuit potential bias using 10 mV potential amplitude.

3.4 Results and Discussion:

3.4A Physico-Chemical Characterizations:

3.4A.1 Physico-Chemical Characterizations of Dy₂S₃ Thin Films:

3.4A.1.1 XRD Study:

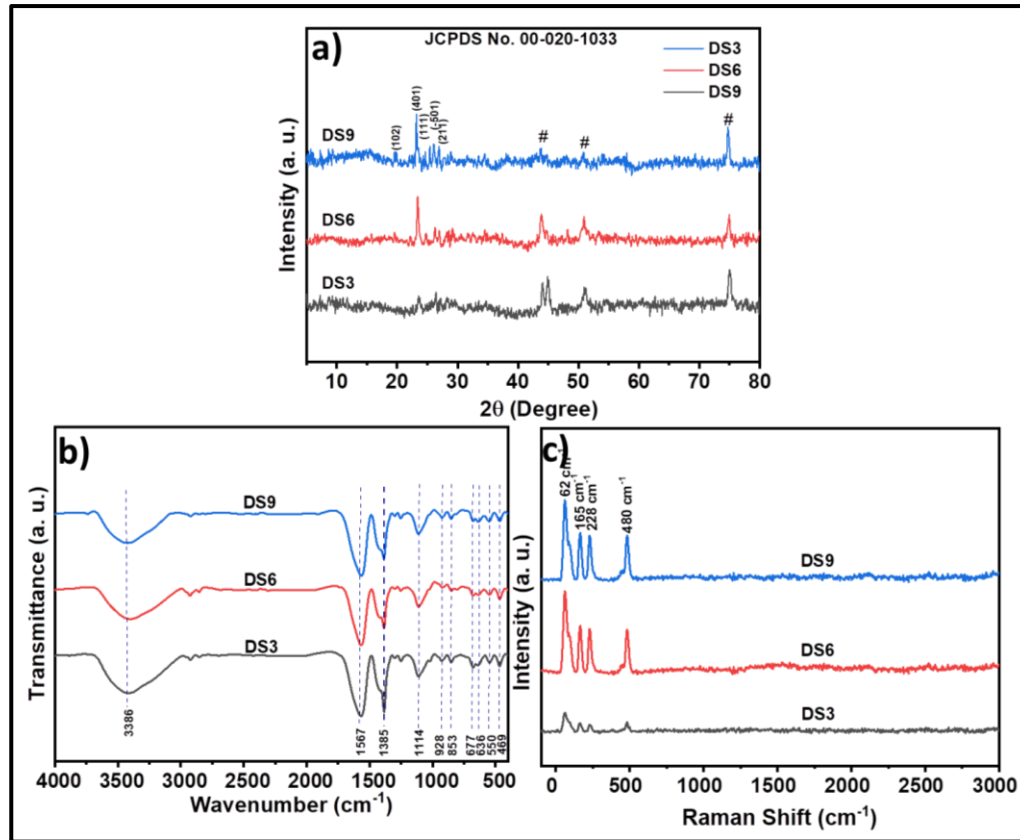


Figure 3.5: a) The XRD patterns, b) FT-IR spectra and c) Raman spectra of Dy₂S₃ thin films deposited at different deposition time.

The XRD technique has been used to study the crystal structure of Dy₂S₃ thin film. **Figure 3.5 (a)** shows the XRD patterns of Dy₂S₃ thin film at different deposition time over the range of 5° - 80°. The intense peaks for Dy₂S₃ appeared at 19.57°, 23.39°, 24.76°, 26.32°, and 26.99° with plane of (102), (401), (111), (-501), and (211), respectively. The (h k l) values match well with those given in the standard JCPDS card no 00-020-1033 suggesting monoclinic phase of the Dy₂S₃. The XRD data indicates the low intensity of Dy₂S₃ peaks for films at 3 h of deposition (**Figure 3.5 (a) DS3**). The intensity of the peaks was increased indicating good crystallinity as the deposition time was increased to 6 and 9 h (**Figure 3.5 (a) DS6, DS9**) [22, 23].

It shows that the structural properties of Dy₂S₃ films are influenced by the growth duration time. In **Figure 3.5 (a)** the sharp peaks examined at 43°, 51° and 74° correspond to stainless steel and which are indicated with #. The crystallite size "D" of Dy₂S₃ thin film was calculated using Scherer's formula (**Equation 2.6**). The crystallite size estimated along (401) plane was 26 nm. The XRD results confirm the formation of Dy₂S₃ thin films.

3.4A.1.2 FT-IR Study:

The functional groups in the materials are examined using FT-IR spectroscopy; the IR spectra of Dy₂S₃ (DS3, DS6 and DS9) thin films, were obtained over a range of 4000-400 cm⁻¹ and are presented in **Figure 3.5 (b)**. The strong absorption bands of S-S and Dy-S are observed at 1114, 928, 853, 677, 636, 550 and 469 cm⁻¹, respectively [24, 25]. According to the spectra, the large peak at wavenumber 3386 cm⁻¹ is due to the O-H bonds stretching vibrations, also the absorptions peak at 1567 and 1385 cm⁻¹ are ascribed to bending modes of -OH of adsorbed water molecules [26]. The FT-IR analysis revealed the presence of adsorbed water in Dy₂S₃ thin films. Additionally, the results confirmed Dy₂S₃ formation on the SS substrate.

3.4A.1.3 RAMAN Study:

The Raman spectra recorded over 110-400 cm⁻¹ of Dy₂S₃ thin film is presented in **Figure 3.5 (c)**. The figure shows four broad and distinct well-defined peaks at 62, 165, 228, 480 cm⁻¹ which are in good agreement with previous reported Raman spectrum of rare earth metal sulphides [27, 28]. The first three peaks at 62, 165, and 228 cm⁻¹ are correspond to the vibrations modes in the resonance spectrum of Dy₂S₃. The peak at ~480 cm⁻¹ is assigned to the S-S stretching of Dy₂S₃ thin film [29]. FT Raman analysis confirms the formation of Dy₂S₃.

3.4A.1.4 FE-SEM study

The morphology of the electrode material has a major impact on the performance of active materials. The FE-SEM micrographs of Dy₂S₃ thin film deposited at different deposition time on SS substrate taken at two different magnifications (5,000 and 20,000x) are shown in the **Figure 3.6**.

The observation illustrated in **Figure 3.6 (a and d)** shows the DS3 film exhibit non-uniformity, with smaller grains and a surface constituted with an arrangement of coarsened grains. The FE-SEM images (**Figure 3.6 (b and e)**), the DS6 film reveal the formation of spherical-shaped grains like porous hollow microsphere morphology and a smooth, uniform, and well-covered surface with small voids distributed over the substrate of the surface. The random distribution of porous hollow microsphere particles is due to the rapid reaction rate in the alkaline bath, where nucleation and grain growth occur simultaneously.

Similarly, DS9 thin film (**Figure 3.6 (c and f)**), the higher deposition time thin film shows the nucleation overgrowth on the film surface with hollow microspheres compact morphology. The materials exhibiting microstructured morphology tend to enhance specific surface area, which makes it easier for electrolytic ions to adsorb and desorb. Consequently, this improves the electrodes electrochemical performance.

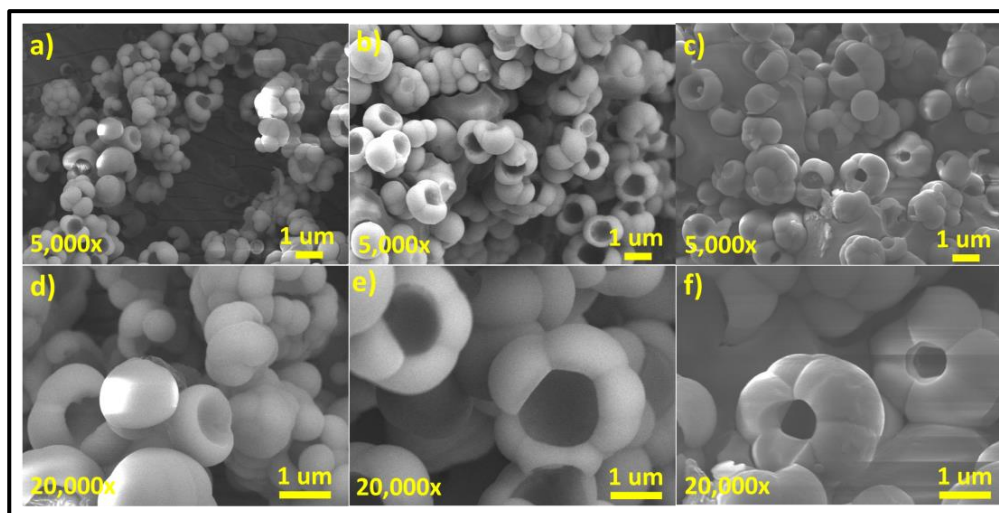


Figure 3.6: FE-SEM images of a) DS3, b) DS6, and c) DS9 at the magnification of 5,000x, and d) DS3, e) DS6, and f) DS9 at the magnification of 20,000x.

3.4A.1.5 EDAX Study:

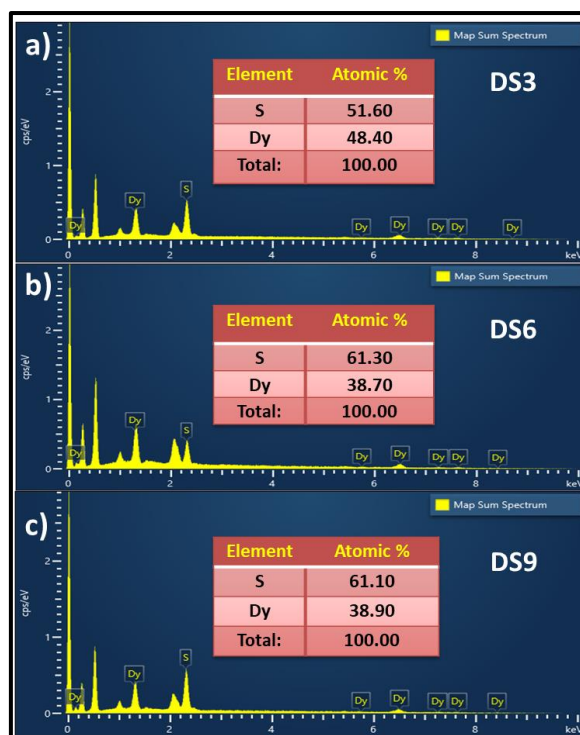


Figure 3.7: The EDAX spectra of a) DS3, b) DS6, and c) DS9 thin films (insets show atomic percentages of constituting elements of Dy_2S_3 thin film).

The EDAX is a technique used to analysis of elemental composition of Dy_2S_3 thin films. **Figure 3.7** presented the EDAX spectra of Dy_2S_3 thin films. The EDAX spectra signify the presence of Dy and S elements in Dy_2S_3 thin film without any other impurity. In DS6 thin film, the atomic percentage of Dy and S are 38.70 and 61.30%, respectively. The table of elemental composition of Dy_2S_3 thin films is shown in the inset of each image. The observed Dy:S atomic ratios for DS3, DS6, and DS9 thin film electrodes are 2:2.13, 2:3.17, and 2:3.14, respectively. The EDAX analyse confirmed the formation of Dy_2S_3 thin film.

3.4A.1.6 Contact Angle Measurement:

The wettability of water-based electrolytes on the surface of a solid film is mainly determined by its surface structure. The electrochemical performance can be significantly improved by achieving a smaller contact angle and higher surface energy. The shape, size, purity, surface roughness, cleanliness, and heterogeneity of the particles play crucial roles in determining contact angle values [30-32]. **Figure 3.8 (a)** illustrates the water contact angle image of DS6 film.

The DS6 thin film exhibits a contact angle of 60° , which indicates that it is hydrophilic nature. The porous structure of the DS6 film contributes to this lower water contact angle. The hydrophilic nature of thin film is beneficial for SC applications as it facilitates enhanced interaction between electrolyte ions and the active electrode surface. Also, its promotes intimate contact with the water-based electrolyte, potentially leading to decreased resistances [33, 34].

3.4A.1.7 BET Study:

BET and BJH technique is used to determine the specific surface area and average pore size distribution of DS6 thin film electrode by N_2 sorption isotherms. **Figure 3.8 (b)** shows the BET and BJH plot of Dy_2S_3 thin film. In **Figure 3.8 (b)**, the DS6 thin film demonstrates type IV isotherms, having a H3-type hysteresis curve within the relative pressure range of 0.40 to 1.0. This suggests the presence of both meso and micropores structure in DS6. The BJH technique was used to determine the average pore diameter of the electrodes, which is illustrated in **Figure 3.8 (b)**. The DS6 sample exhibits a BET specific surface area of $23 \text{ m}^2 \text{ g}^{-1}$, with an observed average pore diameter of 15 nm.

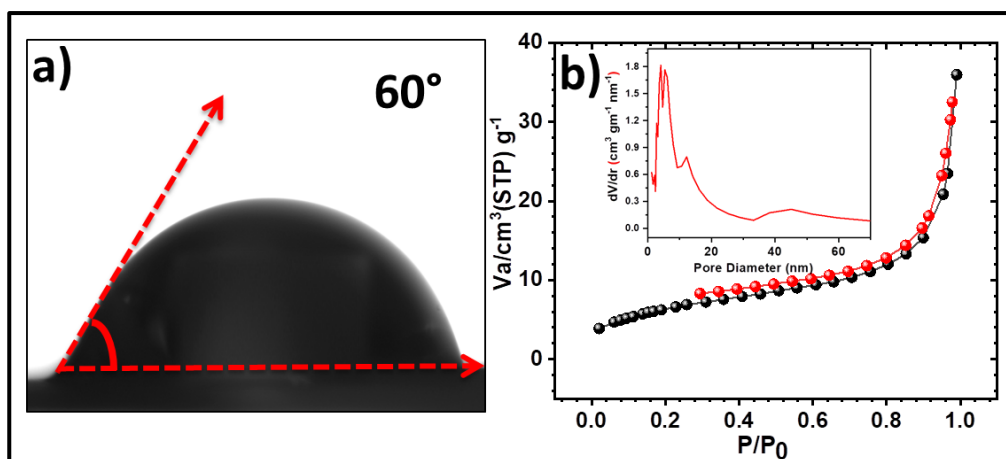


Figure 3.8: a) Photograph of water contact angle, b) N_2 sorption isotherms (inset shows the BJH pore size distribution curve) of Dy_2S_3 (DS6) thin film.

3.4A.2 Physico-Chemical Characterizations of rGO/ Dy_2S_3 Thin Films:

3.4A.2.1 XRD Study:

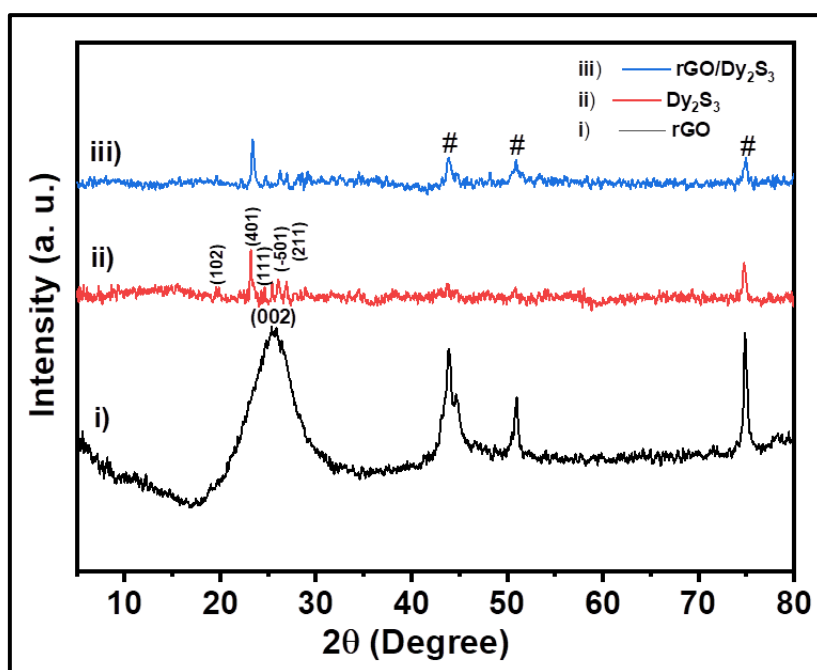


Figure 3.9: The XRD patterns of i) rGO, ii) Dy_2S_3 and iii) rGO/ Dy_2S_3 thin films.

The XRD patterns of rGO, Dy_2S_3 and rGO/ Dy_2S_3 thin films are shown in **Figure 3.9**. The broader peak for rGO at $2\theta = 24.10^\circ$ corresponds to (002) plane (**Figure 3.9 (i)**) [35]. This indicates oxygen-containing functional groups were eliminated significantly during the chemical reduction of GO. The intense peaks for Dy_2S_3 appeared at 19.57° , 23.39° , 24.76° , 26.32° , and 26.99° corresponds to (102), (401), (111), (-501) and (211) planes monoclinic crystal structure of the Dy_2S_3 . (JCPDS card no 00-020-1033).

The XRD patterns of Dy_2S_3 and $\text{rGO}/\text{Dy}_2\text{S}_3$ thin films are shown in **Figure 3.9 (ii and iii)**. The variation in the peak intensity indicates that the growth rate of Dy_2S_3 nanoparticles on rGO sheet is influenced by the composition with rGO. The monoclinic crystal structure of Dy_2S_3 in $\text{rGO}/\text{Dy}_2\text{S}_3$ thin films has been confirmed by the calculated d values (Bragg's Eq), which match well with standard d values. The small amount of rGO with less ordered stacking of rGO sheets is the reason for the absence of a diffraction peak for rGO in the composite thin film. Using Scherrer's formula (**Equation 2.6**) for (401) plane, the crystallite size was determined to be 31 nm. The $\text{rGO}/\text{Dy}_2\text{S}_3$ crystallite size is larger than the Dy_2S_3 crystallite size. The SS substrate can be identified by the peaks highlighted by the symbol #. The composition of rGO with Dy_2S_3 affects the growth of Dy_2S_3 particles, as confirmed by an XRD study.

3.4A.2.2 FT-IR Study:

The FTIR spectra of Dy_2S_3 and $\text{rGO}/\text{Dy}_2\text{S}_3$ are presented in **Figure 3.10**. The presence of the O-H bond (hydroxyl group) is confirmed by the intense and broad peak that appeared at a wavelength of 3386 cm^{-1} in the **Figure 3.10 (i)**. But in **Figure 3.10 (ii)** the peak at 3386 cm^{-1} became less broad as compared with Dy_2S_3 due to less presence of hydroxyl group in $\text{rGO}/\text{Dy}_2\text{S}_3$ and also significantly reduction of rGO.

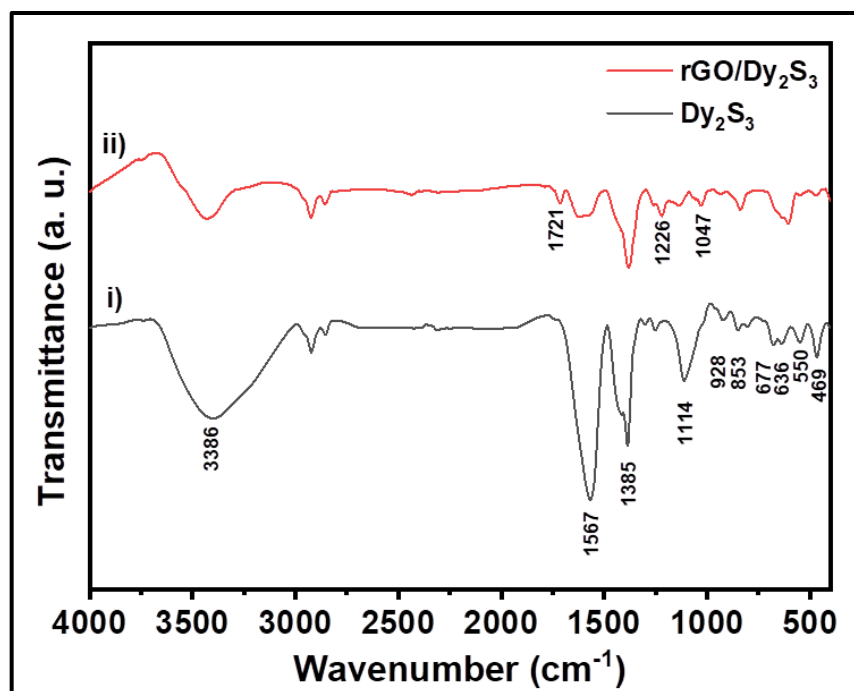


Figure 3.10: The FT-IR spectra of i) Dy_2S_3 and ii) $\text{rGO}/\text{Dy}_2\text{S}_3$ thin films.

The strong absorption band of S-S and Dy-S bond observed at 1114, 928, 853, 677, 636, 550, and 469 cm^{-1} , are assigned to the characteristic absorption of Dy_2S_3 . **Figure 3.10 (ii)** ($\text{rGO}/\text{Dy}_2\text{S}_3$ thin films) show additional rGO absorption bands at 1721 cm^{-1} for $\text{C}=\text{O}$ stretching ($-\text{COOH}$ group), 1226 and 1047 cm^{-1} for C-O-C stretching (epoxy group) in comparison to the FT-IR spectrum of Dy_2S_3 thin films [35]. From the results, it is confirmed by the formation of $\text{rGO}/\text{Dy}_2\text{S}_3$ thin film on SS substrate.

3.4A.2.3 FE-SEM Study:

The FE-SEM images of Dy_2S_3 and $\text{rGO}/\text{Dy}_2\text{S}_3$ thin films at two magnifications are shown in **Figure 3.11 (a-d)**. From the FE-SEM images, the microstructures of $\text{rGO}/\text{Dy}_2\text{S}_3$ observed. **Figure 3.11 (c and d)** presents the images of the $\text{rGO}/\text{Dy}_2\text{S}_3$ thin films at 5,000x and 20,000x magnifications; the images reveal a discontinuous and irregular arrangement of rGO sheets within the thin films. At higher magnification at 20,000x (**Figure 3.11 (d)**), the FE-SEM images illustrate that rGO network is interconnected by Dy_2S_3 nanoparticles, forming a sandwich-like structure between rGO sheets. The rGO sheets are uniformly coated with Dy_2S_3 nanoparticles. These nanoparticles prevent rGO sheets from being anchored and also offer easy access to electrolyte ions at the bulk of the electrode material by diffusion.

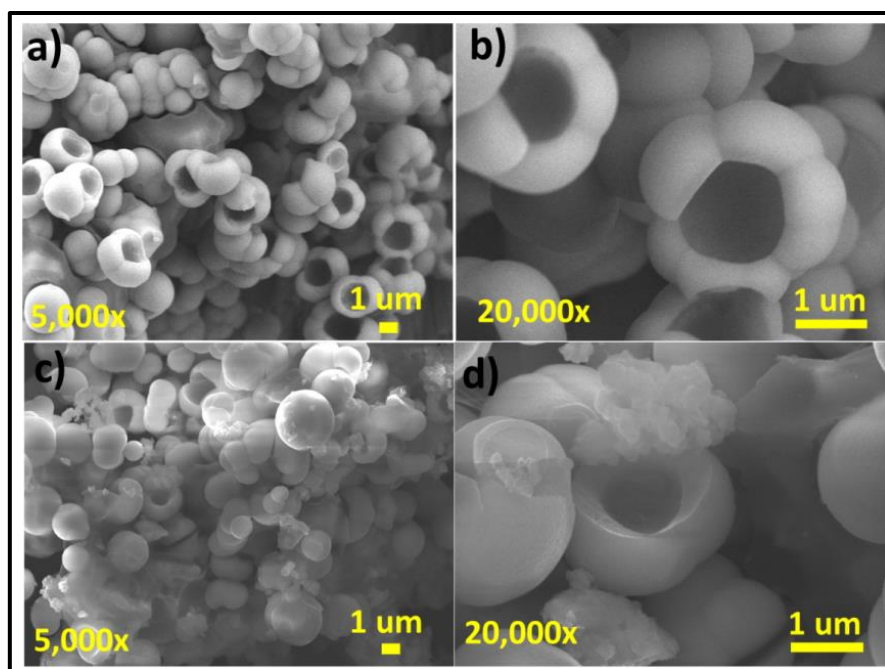


Figure 3.11: FE-SEM images of a) Dy_2S_3 , and c) $\text{rGO}/\text{Dy}_2\text{S}_3$ at the magnification of 5,000x, and b) Dy_2S_3 , and d) $\text{rGO}/\text{Dy}_2\text{S}_3$ at the magnification of 20,000x.

3.4A.2.4 EDAX Study:

The EDAX technique is used to examine the chemical composition of rGO/Dy₂S₃ thin films. **Figure 3.12 (a and b)** displays the Dy₂S₃ and rGO/Dy₂S₃ thin film EDAX spectra. The inset of **Figure 3.12 (a and b)** displays the atomic percentages of the elements Dy, S, C, and O, confirming the formation of rGO/Dy₂S₃ thin film. In the rGO/Dy₂S₃ composite thin film, the atomic ratio varies from the ideal value of 2:3.

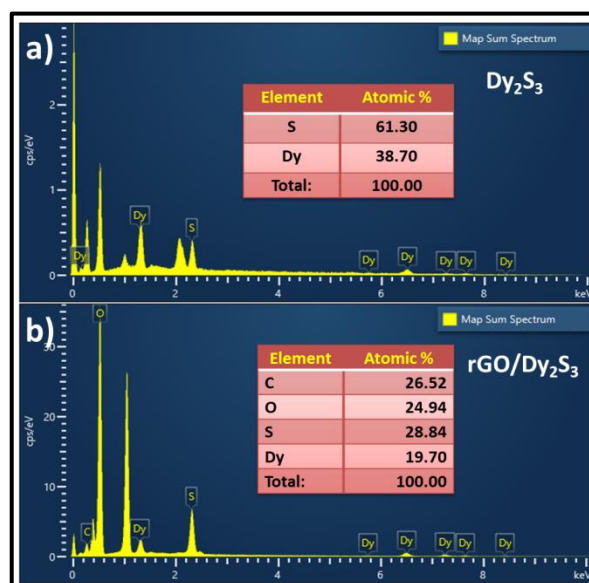


Figure 3.12: The EDAX spectra of a) Dy₂S₃, and b) rGO/Dy₂S₃ thin films (insets show atomic percentages of constituting elements).

The atomic percentages of Dy, S, C, and O are 19.70, 28.84, 24.94, and 26.52%, respectively. A slightly more oxygen indicates that the graphite flakes are effectively oxidized into rGO sheets. A composite thin films performance of energy storage may be enhanced by the nonplaner oxygen containing groups found in rGO sheets, which allow the growth of Dy₂S₃ nanoparticles and offer more active sites for interaction with ions from the electrolyte.

3.4A.2.5 XPS Study:

The XPS technique is fundamental type to providing the important information about the elemental presence, chemical environment, and oxidation state present at the surface of film. Therefore, the XPS technique is used to identify the elemental presence of Dy₂S₃ thin film. **Figure 3.13 (a)** shows a wide survey scan of the XPS spectrum taken in the 0–1350 eV range. The Dy, S, O, and C elements peaks

suggest the formation of rGO/Dy₂S₃ composite thin film on SS substrate. **Figure 3.13 (b and c)** shows the peaks at binding energies 1335 and 1297 eV correspond to Dy³⁺ 3d and 4d core-level splitting into 3d_{3/2} and 3d_{5/2} and peaks at binding energies 155.2 and 158.1 eV corresponds to 4d_{3/2} and 4d_{5/2}, respectively [36, 37]. Other rare-earth metals are also observed a doublet energy gap as a result of the spin–orbital interaction [38].

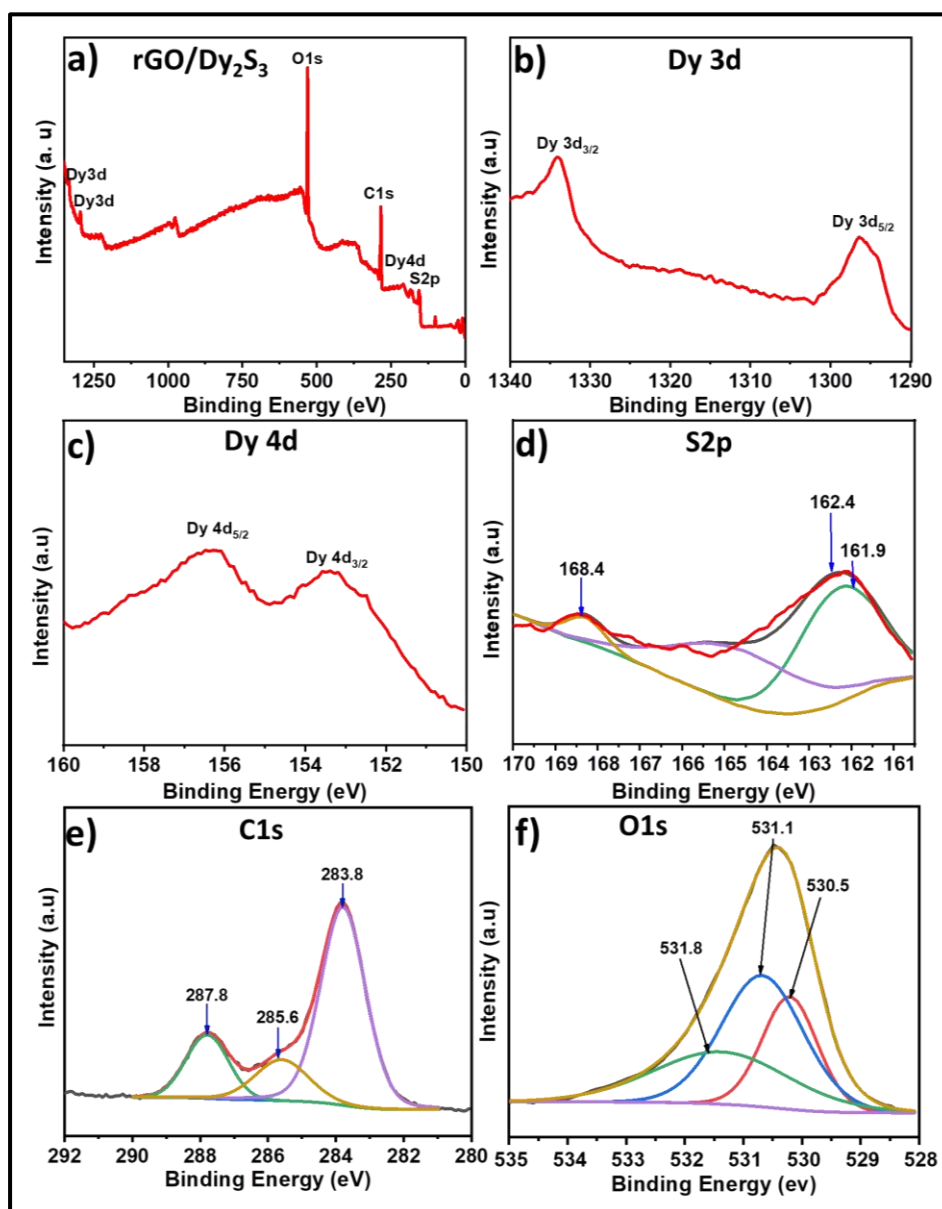


Figure 3.13: The XPS spectra of a) rGO/Dy₂S₃ film wide survey scan, b) Dy 3d, c) Dy 4d, d) S2p, e) C1s, and f) O1s.

The XPS spectrum of S2p (**Figure 3.13 (d)**) show that sulfur is present in a rGO/Dy₂S₃. The sulfide (S²⁻) species are represented by the peaks located at binding energies of 161.9, 162.4, and 168.4 eV [39]. Three components related to C atoms in

different functional groups are shown in the XPS spectrum of C1s from rGO (**Figure 3.13 (e)**); the peak at 283.8 eV indicates the (C=C) ring of rGO, the peak at 285.6 eV indicates the C-O bond confirming the hydroxyl group attached to the rGO sheet, and the peak of C (C=O) at 287.8 eV also confirms the carboxylic group [40].

The sample surface exhibits a very high atomic percentage of O, as shown in **Figure 3.13 (f)**. This high percentage is attributed to different oxidation states, as indicated by the variations in the position and shape of O1s peak. Further the O1s is deconvoluted into three peaks, the signals at 530.5, 531.1 and 531.8, eV, which are attributed to lattice oxygen confirms formation of O-C bond, nonlattice oxygen from the carboxyl, sulfonyl, and hydroxyl groups, respectively [41-43]. Overall, the XPS result confirms the formation of rGO/Dy₂S₃ composite thin film.

3.4A.2.6 Raman Study:

The Raman spectra of rGO, Dy₂S₃ and rGO/Dy₂S₃ thin films are shown in **Figure 3.14**. **Figure 3.14 (i)** shows the peaks present at 1350, 1599 cm⁻¹, and broad peaks at 2691 and 2944 cm⁻¹ related to the D, G, and 2D peaks of rGO, respectively [35]. The peaks at 62, 165, and 228 cm⁻¹ correspond to the vibrations mode in the resonance spectrum of Dy₂S₃. The peak at ~480 cm⁻¹ is assigned to the S-S stretchings of Dy₂S₃ thin film observed in **Figure 3.14 (ii and iii)**.

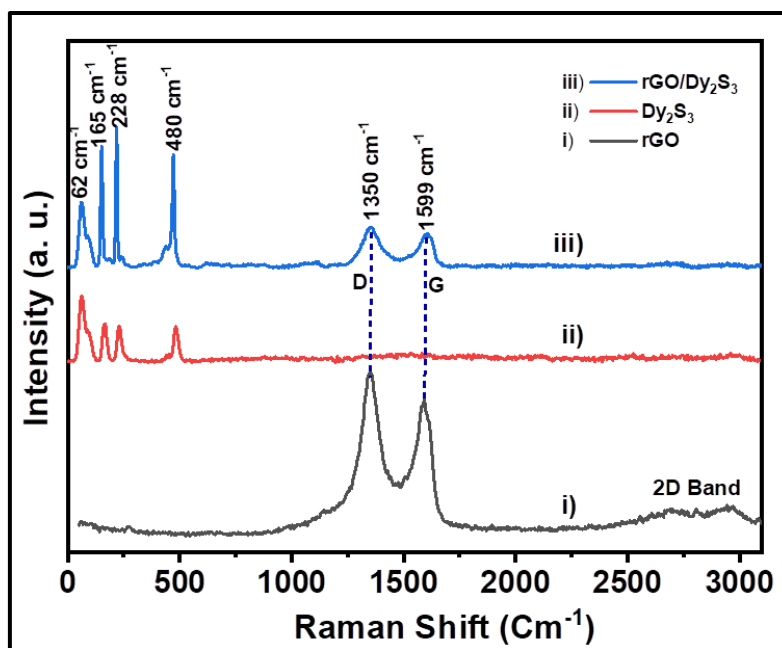


Figure 3.14: The Raman spectra of i) rGO, ii) Dy₂S₃, and iii) rGO/Dy₂S₃ thin films.

In **Figure 3.14 (iii)**, the presence of peaks at 1346 and 1599 cm^{-1} are related to the D and G bands of rGO sheets which confirmed the formation of composite thin film of rGO/Dy₂S₃. The greater D band intensity indicates the relatively large rGO sheet defects, which cause the sp^2 hybridization to be distorted toward the sp^3 . The quantitative examination of rGO sheet is helped by the G peak. The rGO/Dy₂S₃ composite thin-film formation mechanism is indicated by the results of the equation $I(G)/I(2D)$. The electrons have an easy lateral path to conduct due to the stacked rGO sheets with sp^2 hybridization.

3.4A.2.7 Contact Angle Measurement:

The contact angle photographs of rGO/Dy₂S₃ thin film with DDW are shown in **Figure 3.15 (a)**. The contact angle value of 49° for rGO/Dy₂S₃ thin film electrode indicates its hydrophilic nature (**Figure 3.15 (a)**). It is observed that the hydrophilicity of rGO/Dy₂S₃ composite is enhanced to pristine Dy₂S₃. The reduced contact angle is due to the composition with rGO nanosheets which possess various functional groups on its surface. This hydrophilic nature of the thin film surface facilitates intimate contact with the water-based electrolyte. This is essential in order to obtain higher electrochemical performance.

3.4A.2.8 BET Study:

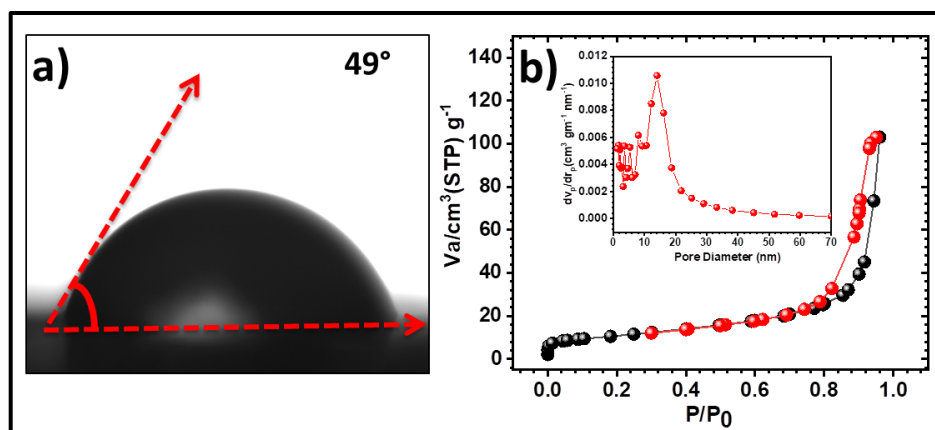


Figure 3.15: a) photograph of water contact angle, b) N₂ sorption isotherms (inset shows the BJH pore size distribution curve) of rGO/Dy₂S₃ thin film.

The BET and BJH techniques were used to measure specific surface area and pore size distribution of thin films. **Figure 3.15 (b)** presented the N₂ adsorption-desorption isotherms of rGO/Dy₂S₃. The rGO/Dy₂S₃ sample has an obtained specific surface area of $36\text{ m}^2\text{ g}^{-1}$. Furthermore, the BJH analysis, inset of (**Figure 3.15 (b)**)

demonstrated a pore size distribution for the rGO/Dy₂S₃ sample, with a mean pore size of 11 nm, suggesting that the thin films have a mesoporous structure.

3.4B Electrochemical characterizations:

3.4B.1 Electrochemical Characterizations of Dy₂S₃ thin Films:

3.4B.1.1 CV Study:

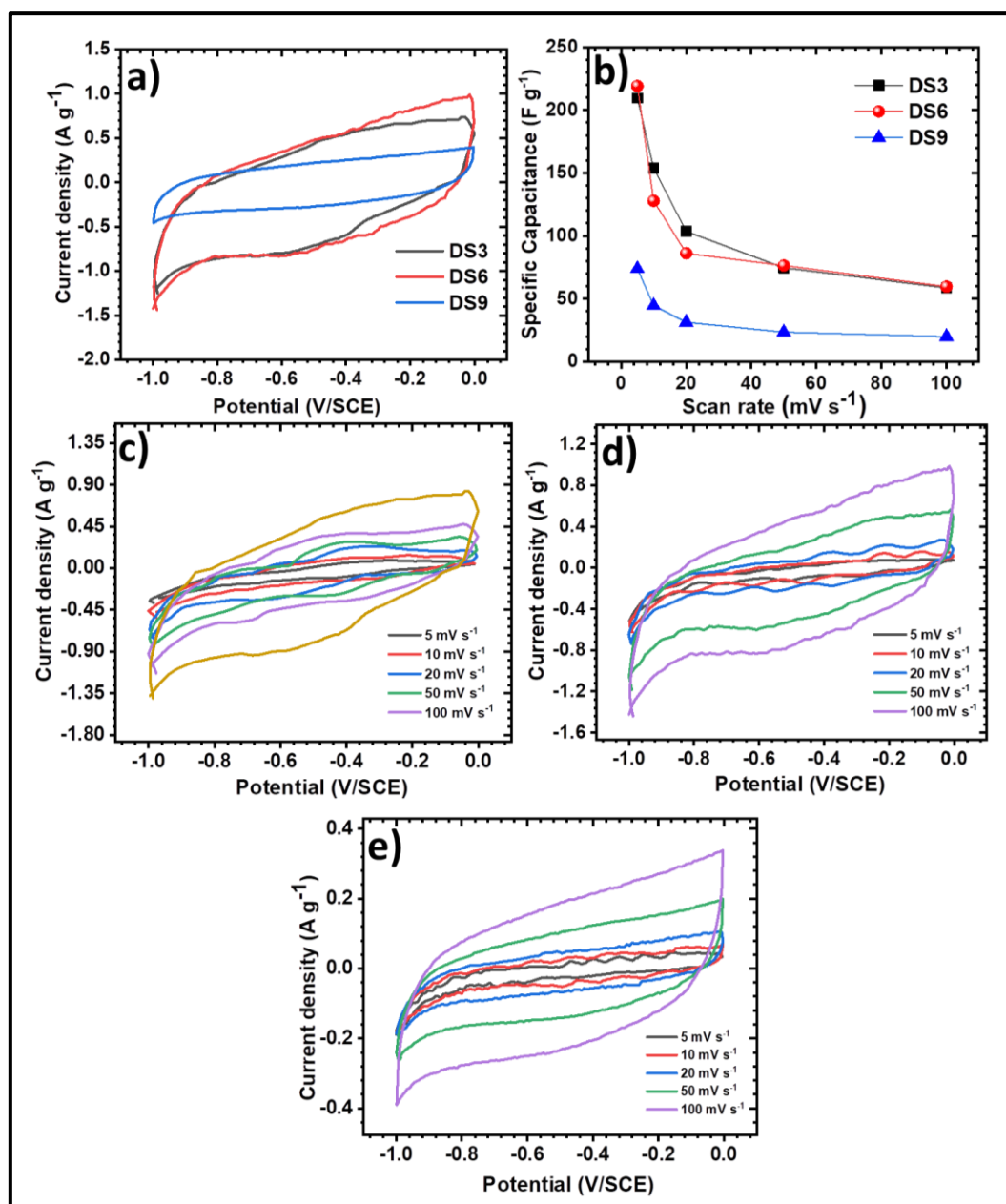


Figure 3.16: a) Comparative CV curves of Dy₂S₃ thin films at a scan rate of 100 mV s⁻¹, b) variation of C_s with the scan rates, and the CV curves at various scan rates from 5-100 mV s⁻¹ of c) DS3, d) DS6, and e) DS9 thin film electrodes.

The electrochemical characterization of Dy₂S₃ thin film was performed in 1 M Na₂SO₄ electrolyte in a working potential window of 0 to -1.0 V SCE. The CV curves of Dy₂S₃ thin films deposited at various deposition times carried out at scan rate of 100 mV s⁻¹ are presented in the **Figure 3.16 (a)**. From the CV plots, its reveal that the area under the CV curve is increased with increasing scan rate and decreasing specific capacitance due to the less time available for electrolyte ions to interact with the electrode at a higher scan rate with decreasing scan rate is enough time for redox reactions [44]. The graph of variation of C_s with scan rate for Dy₂S₃ thin films is presented in **Figure 3.16 (b)**.

Figure 3.16 (c-f) illustrates the CV curves of the thin film electrodes DS3, DS6, and DS9 at various scan rates between 5 and 100 mV s⁻¹. All thin-film electrodes exhibit an increase in current response with scan rate. **Figure 3.16 (d)** shows the area under the CV curves of DS6 film electrode is more than other DS3 and DS9 films, indicating DS6 may facilitate fast electronic and ionic transport. The nontrangular shape of CV curves of Dy₂S₃ film electrodes is indicated typical pseudocapacitive material type. The obtained highest C_s value of DS3, DS6 and DS9 film electrodes at scan rate of 5 mV s⁻¹ are 210, 219, and 74 F g⁻¹, respectively.

3.4B.1.2 GCD Study:

The GCD study of DS3-DS9 electrodes was performed at current density of 3.5 A g⁻¹ over a working potential window of -1.0 to 0.0 V (V/SCE) as shown in **Figure 3. 17 (a)**. The obtained maximum value of the C_s calculated using **Equation 2.12** are 153, 192 and 123 F g⁻¹ for DS3, DS6 and DS9 at the charging current density of 3.5 A g⁻¹. The change in C_s with current densities is presented in **Figure 3.17 (b)**. From GCD plots, its clearly seen that the with increasing current density, the charging and discharging time decrease with decreasing C_s value due to the less time available for interaction of electrolyte ions to interact with the electrode at a higher current density [44]. **Figure 3.17 (c-e)** shows the GCD plots of DS3, DS6 and DS9 electrodes at various current densities (3.5 - 5.5 A g⁻¹). It is suggested by the nontriangular GCD profiles that charge storage is pseudocapacitive in nature. When comparing the DS6 electrode to other electrodes, the highest discharge time is observed, indicating superior electrochemical performance. The surface redox reactions of Dy₂S₃ thin film electrodes are revealed by the nonlinear behavior of the charge and discharge plots [45, 39]. Additionally, good symmetrical features of GCD curves, Dy₂S₃ material

produces excellent electrochemical potential and redox reversibility during charge discharge over the entire potential range. The enhanced electrochemical capacitive performance of the DS6 electrode arises from the high surface area as facilitated by its morphology.

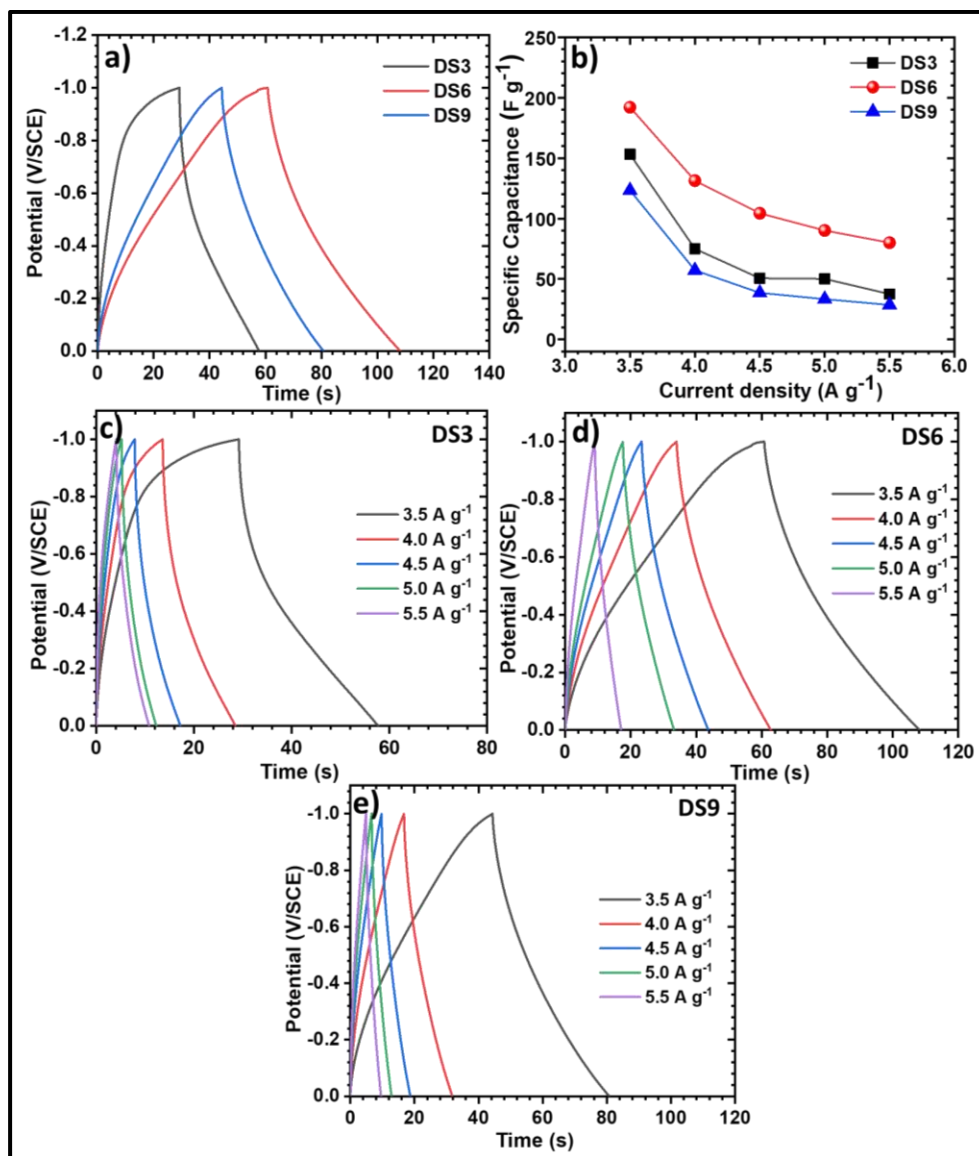


Figure 3.17: a) Comparative GCD curves of Dy₂S₃ thin film electrodes at a current density of 3.5 A g⁻¹, b) variation of C_s with the current densities, and the GCD curves at various current densities from 3.5 - 5.5 A g⁻¹ of c) DS3, d) DS6, and e) DS9 thin film electrodes.

3.4B.1.3 EIS Study:

In the Nyquist plot, there are various EIS parameters such as R_s , R_{ct} and W . The R_s represents the intercept of semicircle on the real axis in high-frequency regions

and the R_{ct} reflects the radius of the semicircle. The W impedance is related to the electrodes diffusion resistance to the electrolyte ions. The W is primarily responsible for the slow ion diffusion process and the resistance to the electrolytes diffusion. For electrochemical performance, appropriate W and CPE values are essential.

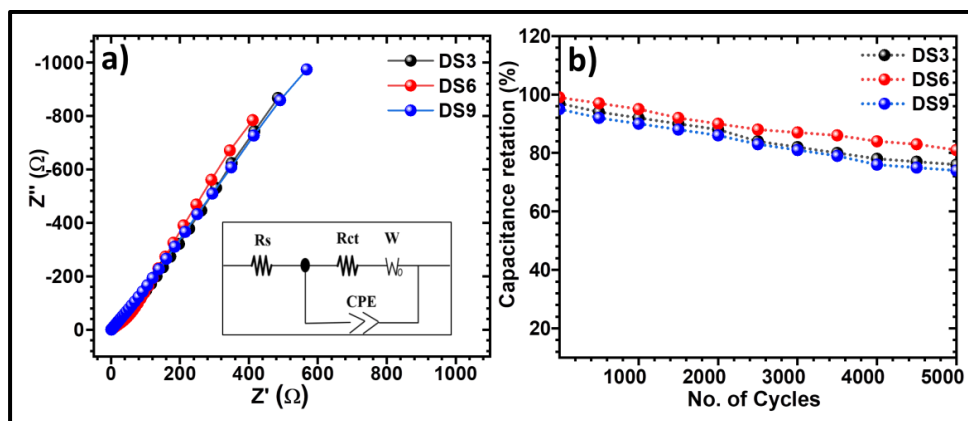


Figure 3.18: a) Nyquist plots, (inset shows the fitted equivalent circuit for the EIS data), and b) the stability curves for Dy_2S_3 thin film electrodes.

The EIS data reveals that DS6 electrode has lower resistance and better electrochemical performance [46, 42]. **Figure 3.18 (a)** depicts the Nyquist plots and the fitted circuits of Dy_2S_3 electrodes conducted in 1 M Na_2SO_4 electrolyte. **Table 3.1** presents the values of the fitted circuit parameters. The best performing DS6 electrode shows fitted values of R_s , R_{ct} , CPE, and W from the equivalent circuit as $1.16 \Omega \text{ cm}^{-2}$, $16.39 \Omega \text{ cm}^{-2}$, 0.54 mF , and 2.1Ω , respectively.

Table 3.1: Electrochemical impedance spectroscopic fitted circuit parameters for Nyquist plots of Dy_2S_3 thin film electrodes.

Sample	R_s ($\Omega \text{ cm}^{-2}$)	R_{ct} ($\Omega \text{ cm}^{-2}$)	CPE (mF)	W (Ω)
DS3	1.57	23.7	0.59	0.30
DS6	1.16	16.39	0.54	2.1
DS9	1.77	47.2	0.12	1.45

3.4B.1.4 Stability Study:

When determining the lifespan of Dy_2S_3 electrode, the stability is crucial. The cyclic electrochemical stability of all Dy_2S_3 electrodes are examined at 4 A g^{-1} current

density over 5,000 cycles and the corresponding capacitive retention plot presented in **Figure 3.18 (b)**. The stability retention of DS3, DS6 and DS9 electrodes is 76, 81, and 71%, respectively. The capacitance value decreases due to the ionic pathway of electrolytic ions diffuses electroactive sites in the bulk electrode. With an increase in the thickness of the film electrode, greater electrochemical stability was observed. However, for the DS9 film electrode, capacitance decreases due to low adherence of the film to the substrate [47].

3.4B.2 Electrochemical Characterizations of rGO and rGO/Dy₂S₃ Thin Films:

3.4B.2.1 Electrochemical Study of rGO Thin Films:

The electrochemical study of rGO thin film was carried out in the potential range of 0 to 1.0 V/SCE in 1M LiClO₄ electrolyte. **Figure 3.19 (a)** presents the CV measurements carried out at various scan rates of 5 to 100 mV s⁻¹. The CV curves show a rectangular shape which indicates EDLC nature. **Figure 3.19 (b)** shows the GCD measurement at various current densities of 3.0, 3.5, 5.0, 6.5, and 8.0 A g⁻¹. The triangular shape of GCD plots indicates the EDLC behaviour of rGO. The rGO electrode exhibits C_s of 96 and 105 F g⁻¹ at 5 mV s⁻¹ scan rate and 3 A g⁻¹ current density, respectively.

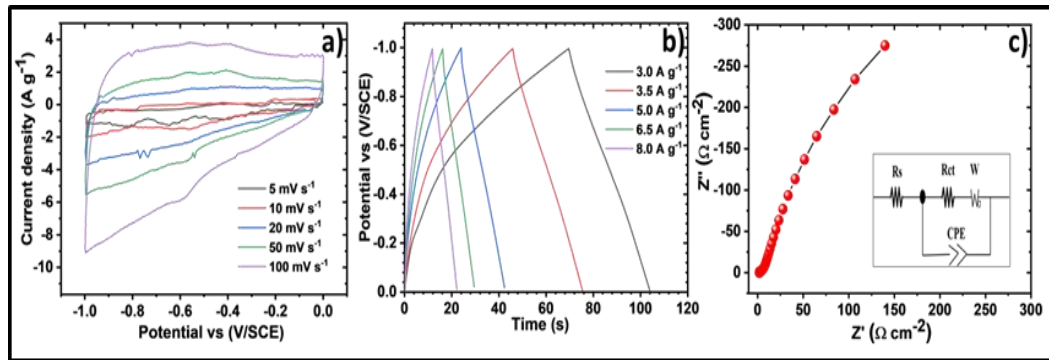


Figure 3.19: a) The CV curves at various scan rates from 5-100 mV s⁻¹, b) the GCD curves at various current densities of 3.0 to 8.0 A g⁻¹, c) Nyquist plot of rGO electrode and simulated equivalent electrical circuit is displayed as an inset image.

Figure 3.19 (c) displays the Nyquist curve of rGO electrode and the inset image shows the simulated equivalent electrical circuit. The observed values of R_s , R_{ct} , CPE, and W are 1.15 Ω cm⁻², 4.5 Ω cm⁻², 0.72 mF, and 0.024 m Ω for rGO. Based on some previous research, the additional planar groups attached to the graphene plane cause the faradaic reactions to take place at rGO [48].

3.4B.2.2 Electrochemical Study of rGO/Dy₂S₃ Thin Films:

3.4B.2.3 CV Study:

The electrochemical study of rGO, Dy₂S₃ and rGO/Dy₂S₃ electrode was carried out within a potential window of -1.0–0.0 V/SCE in 1 M Na₂SO₄ electrolyte. The CV curves of Dy₂S₃ and rGO/Dy₂S₃ thin film electrodes at scan rate of 5 to 100 mV s⁻¹ are shown in **Figure 3.20 (a and b)**, which indicate that there is more current response for rGO/Dy₂S₃ thin film compared with Dy₂S₃ thin film electrodes. The interagated area under the CV curve of Dy₂S₃ was smaller compared to rGO/Dy₂S₃ electrode. The obtained C_s of Dy₂S₃ (219 F g⁻¹) is low as compared to rGO/Dy₂S₃ (392 F g⁻¹) at the scan rate of 5 mV s⁻¹.

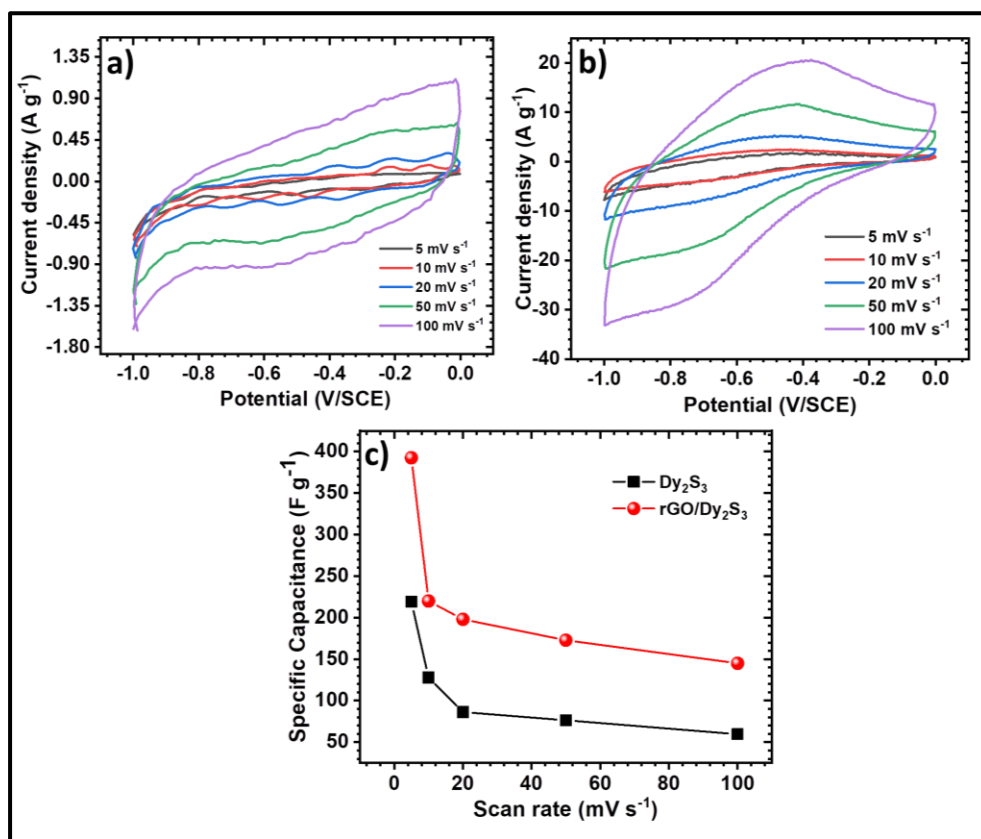


Figure 3.20: The CV curves at various scan rates from 5–100 mV s⁻¹ of a) Dy₂S₃, b) rGO/Dy₂S₃, thin film electrodes and c) variation of C_s with the scan rate.

This indicates that rGO/Dy₂S₃ thin film electrode may enhance rapid electronic and ionic transport, which increase current response capacity of the electrode. The non-rectangular shape observed in the CV curves confirms the existence of a pseudocapacitive charge storage mechanism. The calculated C_s values

of electrodes using **Equation 2.12** at a scan rate of 5 mV s^{-1} are 219 F g^{-1} for Dy_2S_3 , and 392 F g^{-1} for $\text{rGO/Dy}_2\text{S}_3$ thin film electrodes, respectively.

From the CV curves, higher scan rates cause a decrease in C_s because there is less time for reversible redox reactions to occur. At higher scan rates, not all electrolyte ions can undergo reversible redox reactions due to time constraints, leading to a reduction in C_s . The CV curves depicted in **Figure 3.20 (a and b)** illustrate the performance of Dy_2S_3 and $\text{rGO/Dy}_2\text{S}_3$ thin film electrodes across different scan rates ranging from 5 to 100 mV s^{-1} . These CV curves suggest that Dy_2S_3 thin film electrodes exhibit versatility as electrode materials across a range of current ratings. The plots of C_s versus different scan rates for Dy_2S_3 , and $\text{rGO/Dy}_2\text{S}_3$ thin film electrodes are presented in **Figure 3.20 (c)**. The total current response observed in the CV curves is a combination of capacitive and diffusion-controlled charge storage mechanism. The power law is used to study the charge storage kinetics of Dy_2S_3 and $\text{rGO/Dy}_2\text{S}_3$. The approximate charge storage contribution from both mechanisms is determined using power law [49].

$$I_p = av^b \quad (3.1)$$

where I_p , v , and a and b signify the peak current density (A g^{-1}), scan rate (mV s^{-1}), and adjustable parameters, respectively. The b -value is calculated from the slope of the graph of $\log i$ vs $\log v$ as presented in **Figure 3.21 (a)**. There are two classifications of electrode material based on charge storage $b = 0.5$ indicates diffusion assisted charge storage and $b = 1$, where charge storage is mainly owing to the capacitive processes on the surface of the electrode. The estimated b -value for Dy_2S_3 and $\text{rGO/Dy}_2\text{S}_3$ are 0.73 and 0.84, implying that the charge storage is through both diffusions assisted and capacitive processes (**Figure 3.21 (b and c)**). Moreover, the scan rate dependent analysis was performed using the following equation [50].

$$I(v) = k_1v + k_2v^{0.5} = I_{\text{surface}} + I_{\text{bulk}} \quad (3.2)$$

where k_1 is the coefficient for capacitive and k_2 is the coefficients for diffusion assisted processes, respectively. Values of k_1 and k_2 are estimated from the slope (k_1) and Y-axis intercept (k_2) of graph $i/v^{1/2}$ vs $v^{1/2}$. **Figure 3.21 (b and c)** shows the capacitive and diffusion-controlled contributions for Dy_2S_3 and $\text{rGO/Dy}_2\text{S}_3$ electrodes. As the scan rate decreased, capacitive contribution to the total charge was also reduced.

The most charge is stored through capacitive assisted processes at all scan rates leading to a higher value of C_s . The rGO/Dy₂S₃ electrode approximately 90% of charge is stored through the capacitive process at a scan rate of 100 mV s⁻¹ which decreases to just 23% at a scan rate of 5 mV s⁻¹. The charge storage from the capacitive process is 82 and 90% for Dy₂S₃ and rGO/Dy₂S₃ electrodes, and the charge storage from the diffusion-controlled process is 17 and 10%, respectively. Diffusion-controlled charge storage decreases with composition due to EDLC nature of rGO [21].

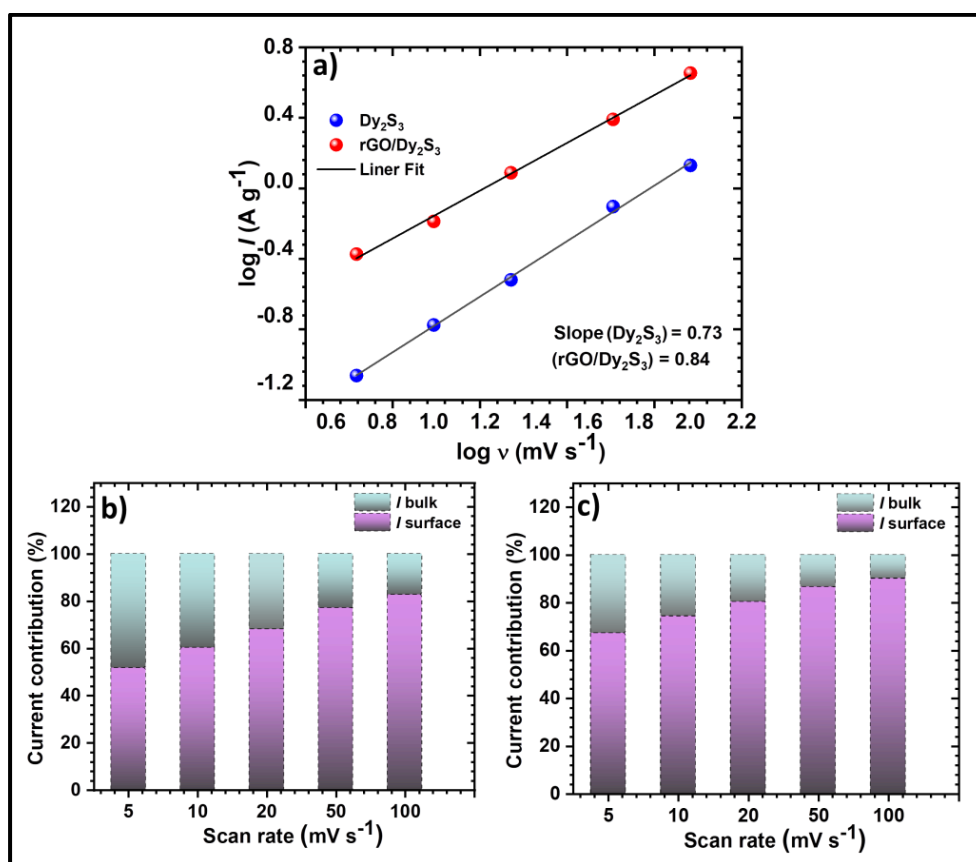


Figure 3.21: a) Plots of $\log I$ versus $\log v$, of Dy₂S₃ and rGO/Dy₂S₃ thin film electrodes, and calculated charge storage by capacitive and diffusion processes for b) Dy₂S₃, and c) rGO/Dy₂S₃ thin film electrodes.

3.4B.2.4 GCD Study:

The GCD curves of Dy₂S₃ and rGO/Dy₂S₃ electrodes at a current densities from 3.5 to 5.5 A g⁻¹ are shown in **Figure 3.22 (a and b)**. At a current density of 3.5 A g⁻¹, the C_s values of Dy₂S₃ and rGO/Dy₂S₃ thin films are 192, and 353 F g⁻¹, respectively. As the applied current density increases, there is a decrease in C_s due to elevated IR and time constraints for the reversible redox reaction [51]. **Figure 3.22 (a**

and b) shows the GCD plots of Dy_2S_3 and $\text{rGO}/\text{Dy}_2\text{S}_3$ electrodes at various current densities. The GCD profile exhibits a nontriangular shape and differs significantly from the GCD profile observed with pristine Dy_2S_3 . This indicates that the charge storage mechanism results from a combination of pseudocapacitive behaviour of Dy_2S_3 and the electric double-layer capacitance (EDLC) characteristic of rGO .

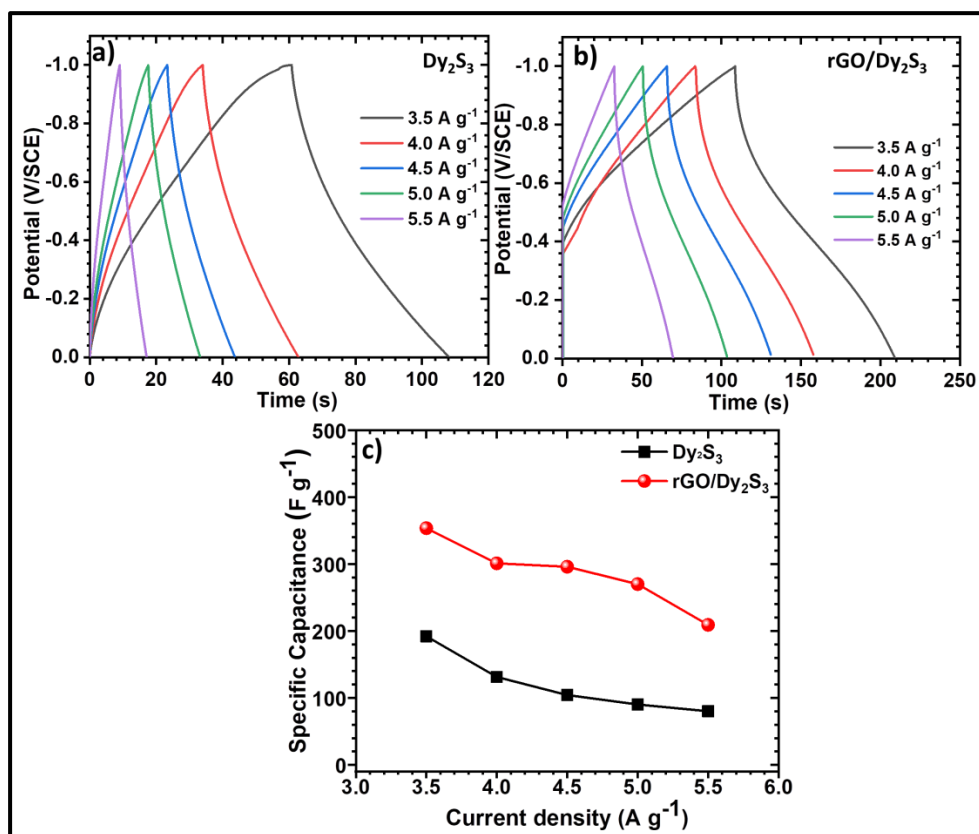


Figure 3.22: The GCD curves at various current densities from 3.5-5.5 A g^{-1} of a) Dy_2S_3 , and b) $\text{rGO}/\text{Dy}_2\text{S}_3$ thin film electrodes, and c) variation of C_s with the current densities.

From **Figure 3.22 (b)**, consistent with CV analysis, the $\text{rGO}/\text{Dy}_2\text{S}_3$ electrode was observed highest discharge time as compared with Dy_2S_3 electrode and demonstrates excellent electrochemical performance. The non-linear (quasi-triangular) nature observed in the charge and discharge curves unveils the intercalation pseudocapacitive characteristic $\text{rGO}/\text{Dy}_2\text{S}_3$ thin film [52]. **Figure 3.22 (c)** illustrates the variation of C_s with current density. The enhanced electrochemical capacitive performance of $\text{rGO}/\text{Dy}_2\text{S}_3$ electrode as compared to pristine Dy_2S_3 , due to optimized concentration of rGO used in the film composition, along with the high surface area facilitated by its porous microsphere-like morphology.

3.4B.2.5 EIS Study:

The EIS technique is used to evaluate resistive parameters of Dy_2S_3 and $\text{rGO/Dy}_2\text{S}_3$ thin film electrodes. **Figure 3.23 (a)** shows the EIS spectra and its fitted data of Dy_2S_3 and $\text{rGO/Dy}_2\text{S}_3$ thin film electrodes. The Dy_2S_3 and $\text{rGO/Dy}_2\text{S}_3$ thin film electrodes have values of $R_s = 1.16$ and $1.04 \Omega \text{ cm}^{-2}$ and $R_{ct} = 16.39$, and $4.18 \Omega \text{ cm}^{-2}$, respectively. The equivalent circuit of best data fitted equivalent circuit is illustrated as an inset of **Figure 3.23 (a)**. The values of R_s , R_{ct} , CPE, and W of Dy_2S_3 and $\text{rGO/Dy}_2\text{S}_3$ electrodes are determined by fitting measured data with the equivalent circuit, as given in **Table 3.2**. The EIS data reveals that $\text{rGO/Dy}_2\text{S}_3$ thin film electrode has lower R_s and R_{ct} values as compared to Dy_2S_3 . Due to the Dy_2S_3 composite with rGO it's enhance the conductivity, surface area and better electrochemical performance [53].

Table 3.2: Electrochemical impedance spectroscopic fitted circuit parameters for Nyquist plots of Dy_2S_3 and $\text{rGO/Dy}_2\text{S}_3$ thin film electrodes.

Sample	$R_s (\Omega \text{ cm}^{-2})$	$R_{ct} (\Omega \text{ cm}^{-2})$	CPE (mF)	$W (\Omega)$
Dy_2S_3	1.16	16.39	0.54	2.1
$\text{rGO/Dy}_2\text{S}_3$	1.04	4.18	0.17	0.90

3.4B.2.6 Electrochemical Stability:

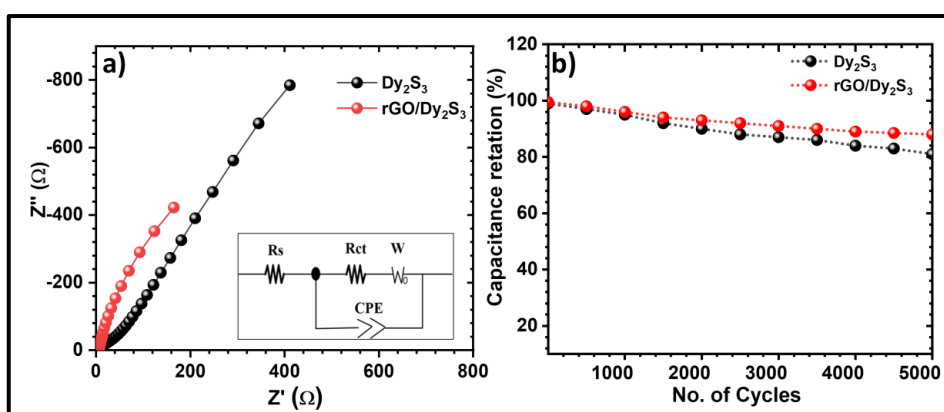


Figure 3.23: a) Nyquist plots of Dy_2S_3 and $\text{rGO/Dy}_2\text{S}_3$ thin films, (inset the fitted equivalent circuit for the EIS data) and b) the stability curves for Dy_2S_3 and $\text{rGO/Dy}_2\text{S}_3$ thin film electrodes.

The electrochemical cyclic stability of Dy_2S_3 and $\text{rGO/Dy}_2\text{S}_3$ thin film electrodes are examined at 4 A g^{-1} over 5,000 GCD cycles as demonstrated in **Figure 3.23 (b)**. The Dy_2S_3 and $\text{rGO/Dy}_2\text{S}_3$ thin film electrodes exhibited capacitance retention of 81 and 88% over 5,000 cycles, respectively. The rGO sheets with porous microsphere-like particles layered architecture of the $\text{rGO/Dy}_2\text{S}_3$ electrodes shows the higher capacitance retention and excellent electrochemical characteristics as compared to Dy_2S_3 . Because, it provided more electroactive sites for electrochemical reactions and randomly distributed vertical paths for electron conduction and ion diffusion.

3.5 Conclusions:

In conclusion, the porous hallow microsphere $\text{rGO/Dy}_2\text{S}_3$ composite thin film electrodes are prepared on SS substrates using the CBD method. rGO composite with Dy_2S_3 exhibited maximum C_s of 392 F g^{-1} in a $1 \text{ M Na}_2\text{SO}_4$ electrolyte at a scan rate of 5 mV s^{-1} . The value of R_s and R_{ct} is decreased for $\text{rGO/Dy}_2\text{S}_3$ electrode compared to pristine Dy_2S_3 electrode. The $\text{rGO/Dy}_2\text{S}_3$ film electrode exhibited more electrochemical cycling stability (88%) in comparison to the Dy_2S_3 film electrode (81%). The electrochemical results concluded that, the introduction of rGO , the electrochemical performance of $\text{rGO/Dy}_2\text{S}_3$ composite is enhanced as compared to Dy_2S_3 . The electrochemical study of $\text{rGO/Dy}_2\text{S}_3$ electrode suggested it as a potential electrode material for SCs in the future.

3.6 References:

- [1] D. Dubal, N. Chodankar, D. Kim, P. Romero, *Chem. Soc. Rev.*, 47, (2018), 2065-2129.
- [2] V. Lokhande, A. Lokhande, C. Lokhande, J. Kim, T. Ji, *J. Alloys Compd.*, 682, (2016), 381-403.
- [3] Y. Wang, X. Wu, Y. Han, T. Li, *Electrochim. Acta*, 42, (2021), 103053-103068.
- [4] Y. Zhang, H. Mei, Y. Cao, X. Yan, J. Yan, H. Gao, H. Luo, S. Wang, X. Jia, L. Kachalova, J. Yang, S. Xue, C. Zhou, L. Wang, Y. Gui, *Coord. Chem. Rev.* 438, (2021), 213910-213940.
- [5] K. Karuppasamy, D. Vikraman, S. Hussain, G. Veerasubramani, P. Santhoshkumar, S. Lee, R. Bose, A. Kathalingam, H. Kim, *J. Chem. Eng.*, 427, (2022), 131535.
- [6] J. Theerthagiri, K. Karuppasamy, G. Durai, A. U. Rana, P. Arunachalam, K. Sangeetha, P. Kuppusami, H. Kim, *J. Nanomater.*, 8, (2018), 256-284.
- [7] M. Barakzahi, M. Montazer, F. Sharif, T. Norby, A. Chatzitakis, *Electrochim. Acta*, 305, (2019), 187–196.
- [8] S. Jayasubramaniyan, S. Balasundari, S. Yeom, N. Naresh, T. Rani, E. Rapaka, N. Satyanarayana, H. Lee, P. Muralidharan, *Electrochim. Acta*, 390, (2021), 138865-138873.
- [9] M. Venkanna, and A. Chakraborty, *AIP Conf. Proc.*, 1591, (2014), 574-576.
- [10] A. González, E. Goikolea, J. Barrena, R. Mysyk, *Renew. Sust. Energ. Rev.*, 58, (2016), 1189-1206.
- [11] Y. Zhao, W. Ran, J. He, Y. Huang, Z. Liu, W. Liu, Y. Tang, L. Zhang, D. Gao, F. Gao, *Small*, 11, (2015), 1310-1319.
- [12] H. Zhang, M. Chhowalla, Z. Liu, *Chem. Soc. Rev.*, 47, (2018), 3015-3017.
- [13] S. Arunachalam, B. Kirubasankar, D. Pan, H. Liu, C. Yan, Z. Guo, S. Angaiah, *Green Energy Environ.*, 5, (2020), 259-273.
- [14] V. Kumbhar, A. Lokhande, N. Gaikwad, C. Lokhande, *Ceram. Int.*, 41, (2015), 5758-5764.

-
- [15] S. Patil, V. Kumbhar, B. Patil, R. Bulakhe, C. Lokhande, J. Alloys Compd., 611, (2014), 191-196.
- [16] S. Ubale, R. Bulakhe, V. Mane, D. Malavekar, S. Ubale, I. In, C. Lokhande, Appl. Nanosci., 10, (2020), 5085-5097.
- [17] P. Bagwade, D. Malavekar, S. Ubale, T. Ghogare, R. Bulakhe, I. In, U. Patil, C. Lokhande, Solid State Sci., 119, (2021), 106693-106699.
- [18] T. Ghogare, R. Pujari, A. Lokhande, C. Lokhande, S Appl. Phys. A., 124, (2018), 248-253.
- [19] S. Ubale S. Kale, V. Mane, P. Bagwade, C. Lokhande, J Solid State Electrochem., 25, (2021), 1753-1764.
- [20] D. Marcano, D. Kosynkin, J. Berlin, A. Sinitskii, Z. Sun, A. Slesarev, L. Alemany, W. Lu, J. Tour, ACS Nano, 4, (2010), 4806–4814.
- [21] D. Malavekar, V. Lokhande, V. Mane, S. Kale, R. Bulakhe, U. Patil, I. In, C. Lokhande, J. Solid State Electrochem., 24, (2020), 2963–2974.
- [22] Z. Jia, X. Shen, H. Zhou, K. Chen, Ceram. Int., 41, (2015), 8710–8716.
- [23] R. Ashwini, V. Dileepkumar, K. Balaji, R. Viswanatha, C. Ravikumar, C. Srivastava, S. Mysore, SI., 2, (2021), 100125-100133.
- [24] H. Naderi, M. Ganjali, A. Dezfali, J. Mater. Sci. Mater. Electron., 29, (2018), 3035–3044.
- [25] S. Khot, D. Malavekar, P. Bagwade, R. Nikam, C. Lokhande, J. Phys. Chem. Solids, 179, (2023), 111419-111431.
- [26] H. Kumar, J. Singh, R. Srivastava, P. Negi, H. Agrawal, K. Asokan, J. Nanosci., 2014, (2014), 1-10.
- [27] E. Westrum, R. Burriel, J. Gruberb, P. Palmer, B. Beaudry, W. Plautz, J. Chem. Phys., 91, (1989), 4838-4848.
- [28] S. Patil and C. Lokhande, Mater. Des. 87, (2015), 939-948.
- [29] R. Bulakhe, S. Sahoo, T. Nguyen, C. Lokhande, C. Roh, Y. Lee, J. Shim, RSC Adv., 6, (2016), 14844-14851.
-

- [30] H. Wang, Y. Wang, X. Cao, M. Feng, G. Lan, J. Raman Spectrosc., 40, (2009), 1791-1796.
- [31] Y. Huang, C. Chang, M. Lin, Phys. Rev. B, 78, (2008), 115422-115431.
- [32] Fesenko, G. Dovbeshko, A. Dementjev, R. Karpicz, T. Kaplas, Y. Svirko, Nanoscale Res. Lett., 10, (2015), 163-170.
- [33] L. Malard, J. Nilsson, D. Elias, J. Brant, F. Plentz, E. Alves, A. Castro Neto, M. Pimenta, Phys. Rev. B, 76, (2007), 201401-201405.
- [34] J. Wu, M. Lin, X. Cong, H. Liu, P. Tan, Chem. Soc. Rev., 47, (2018), 1822-1873.
- [35] N. Hidayah, W. Liu, C. Lai, N. Noriman, C. Khe, U. Hashim, H. Lee, AIP Conf. Proc., 1892, (2017), 150002-150014.
- [36] Y. Yan, J. Zhao, J. Lee, ChemElectroChem, 3, (2016), 1–7.
- [37] S. Manavalan, U. Rajaji, S. Chen, S. Selvin, M. Govindasamy, T. Chen, M. Ali, F. Al-Hemaid, M. Elshikh, Inorg. Chem. Front., 5, (2018), 2885-2892.
- [38] A. Novosselov, E. Talik, A. Pajaczowska, J. Alloys Compd. 351, (2003), 50-53.
- [39] S. Meher, P. Justin, G. Rao, Nanoscale, 3, (2011), 683-693.
- [40] V. Pototskaya, and O. Gichan, Int. J. Electrochem. Sci., 14, (2019), 8195-8205.
- [41] C. Peng, J. Jin, G. Chen, Electrochim. Acta, 53, (2007), 525-537.
- [42] D. Kampouris, X. Ji, E. Randviir, C. Banks, RSC Adv., 5, (2015), 12782-12791.
- [43] A. Khosrozadeh, G. Singh, Q. Wang, G. Luo, M. Xing, J. Mater. Chem. A, 6, (2018), 21064-21077.
- [44] C. Zhang, A. Xie, W. Zhang, J. Chang, C. Liu, L. Gu, X. Duo, F. Pan, S. Luo, J. Energy Storage, 34, (2021), 102181-102192.
- [45] C. Raj, B. Kim, W. Cho, W. Lee, Y. Seo, K. Yu, J. Alloys Compd, 586, (2014), 191-196.
- [46] C. Peng, J. Jin, G. Chen, Electrochim. Acta, 53, (2007), 525-537.
- [47] A. Khosrozadeh, G. Singh, Q. Wang, G. Luo, M. Xing, J. Mater. Chem. A, 6, (2018), 21064-21077.

- [48] A. Galal, H. Hassan, T. Jacob, N. Atta, *Electrochim. Acta.*, 260, (2018), 738–747.
- [49] T. Islam, M. Hasan, S. Shah, M. Karim, F. Al-Mubaddele, M. Zahir, M. Dar, M. Hossain, M. Aziz, A. Ahammad, *J. Energy Storage*, 32, (2020), 101908-101920.
- [50] Y. Hunge, A. Yadav, S. Kang, H. Kim, A. Fujishima, C. Terashima, *J. Hazard. Mater.* 419, (2021), 126453-126465.
- [51] J. Cherusseri and K. Kar, *J. Mater. Chem. A.*, 4, (2016), 9910–9922.
- [52] S. Lehtimäki, A. Railanmaa, J. Keskinen, M. Kujala, S. Tuukkanen, D. Lupo, *Sci. Rep.*, 7, (2017), 460001-460010.
- [53] Y. Ko, D. Shin, B. Koo, S. W. Lee, W. Yoon, J. Cho, *Nano Energy*, 12, (2015), 612-625.

CHAPTER-4

**Dy₂Se₃ and rGO/Dy₂Se₃ Thin Films by
SILAR Method: Characterization and
Electrochemical Performance**

CHAPTER-4

Dy₂Se₃ and rGO/Dy₂Se₃ Thin Films by SILAR Method: Characterization and Electrochemical Performance

Sr. No.	Title		Page No.
4.1	Introduction		107
4.2	Synthesis and Characterizations of Dy ₂ Se ₃ and rGO/Dy ₂ Se ₃ Thin Films		107
	4.2.1	<i>Introduction</i>	107
	4.2.2	<i>Experimental Details</i>	107
		4.2.2.1 <i>Chemicals</i>	107
		4.2.2.2 <i>Preparation of Dy₂Se₃ Thin Films</i>	108
		4.2.2.3 <i>Synthesis of rGO/Dy₂Se₃ Thin Films</i>	108
		4.2.2.4 <i>Material Characterizations</i>	109
4.3	Results and Discussion		110
	4.3.1	<i>Growth Mechanism of Dy₂Se₃ and rGO/Dy₂Se₃ Thin Films</i>	110
	4.3.2	<i>Physico-Chemical Characterizations of rGO, Dy₂Se₃ and rGO/Dy₂Se₃ Thin Films</i>	110
	4.3.3	<i>Electrochemical Characterizations of Dy₂Se₃ and rGO/Dy₂Se₃ Thin Films</i>	117
		4.3.3.1 <i>Electrochemical Study of Dy₂Se₃ and rGO/Dy₂Se₃ Thin Films</i>	117
4.4	Conclusions		122
4.5	References		123

4.1 Introduction:

The composition of pseudocapacitive materials containing modified graphenes (rGO and GO) has been extensively studied due to their remarkable qualities, which include high surface area, moderate electrical conductivity, and good thermal stability [1]. By employing composition, various morphologies can be obtained. Furthermore, the combination of pseudocapacitive materials with EDLC materials is an efficient method of improving electrochemical cycling stability [2]. The carbonaceous materials used in EDLCs have a low S_E [3]. Therefore, the present studies mainly focus on pseudocapacitive materials because of their high S_E . The pseudocapacitive materials composition with rGO modifies surface area, improves electrical conductivity, and exposes more active sites to the electrolyte for redox reactions. Carbon composite also improves ions-diffusion rate and overall cycle life [4-6].

Considering the above viewpoints, dysprosium selenide (Dy_2Se_3) and rGO with Dy_2Se_3 (rGO/ Dy_2Se_3) thin films were synthesized using the SILAR method. The rGO was introduced to enhance electrochemical performance by facilitating electronic transport and improving cyclic stability. The electrochemical performance of Dy_2Se_3 and rGO/ Dy_2Se_3 has been evaluated and configuration of rGO/ Dy_2Se_3 // MnO_2 FSSASCs device was fabricated using MnO_2 as a cathode, a composite electrode (rGO/ Dy_2Se_3) as an anode, and polyvinyl alcohol (PVA)- $LiClO_4$ gel as an electrolyte.

4.2 Synthesis and Characterizations of Dy_2Se_3 and rGO/ Dy_2Se_3 Thin Films:

4.2.1 Introduction:

The electrode material preparation method must be simple and adaptable to large-scale production. From these perspectives, the SILAR method is used to prepare Dy_2Se_3 and rGO/ Dy_2Se_3 thin films at room temperature on flexible SS substrates. Dy_2Se_3 nanoparticles can be composited onto rGO sheets to achieve the porous electrode structure. This section describes the synthesis of thin films of Dy_2Se_3 and rGO/ Dy_2Se_3 .

4.2.2 Experimental Details:

4.2.2.1 Chemicals:

The required chemicals such as analytical grade dysprosium nitrate ($Dy(NO_3)_3$), lithium perchlorate ($LiClO_4$), metallic selenium (Se), and sodium sulfite

(Na₂SO₃) were used as received. A SS sheet measuring 5×1 cm² (304 grade) was used as a substrate and double distilled water (DDW) as a solvent.

4.2.2.2 Preparation of Dy₂Se₃ Thin Films:

For the synthesis of Dy₂Se₃ thin films, analytical grade (AR) chemicals Dy(NO₃)₃, metallic selenium (Se), and sodium sulfite (Na₂SO₃) were used. The SS substrates of thickness 0.4 mm (304 grade) were polished with smooth sandpaper, and cleaned with DDW, followed by ultrasonication for 15 min. After that, the SS substrate dried at room temperature. The source of Se²⁻ ions were synthesized by refluxing 1 g of elemental selenium and 1.26 g Na₂SO₃ in 100 mL of DDW with constant stirring for 10 h at 343 K [7].

The prepared solution was sealed and kept overnight, followed by filtration. For deposition of Dy₂Se₃ thin films, the SILAR method was employed at ambient temperature. Dysprosium nitrate solution (20 mL) of 0.05 M (pH = 4.5±0.1) was used as the cationic precursor and sodium selenosulphate (20 mL), 0.1 M (pH = 10±0.1) was used as an anionic precursor. Ultrasonically cleaned SS substrates were successively immersed in the cationic and anionic precursor for 10 s with in between rinsing in DDW for 15 s. After the reaction, substrates were rinsed in DDW for 15 s to remove non adherent particles on the film. Such 200 SILAR deposition cycles were repeated to obtain optimum film thickness.

4.2.2.3 Synthesis of rGO/Dy₂Se₃ Thin Films:

The GO was synthesized using a modified Hummer's method, employing flakes of graphite bought from Sigma-Aldrich. The previously reported procedures for the chemical reduction of GO were followed [8]. From the **Chapter 3** utilizing the optimized concentration of 1 mg mL⁻¹ rGO suspension, a layer of rGO sheets was deposited onto the SS substrate using the layer-by-layer (LBL) method. The SILAR method was employed to deposit rGO/Dy₂Se₃ on the SS substrate.

The pictorial representation of SILAR method used to deposit rGO/Dy₂Se₃ thin film is shown in **Figure 4.1 (a)**. For the preparation of rGO/Dy₂Se₃ films, 1 mg mL⁻¹ rGO suspension was used as a first beaker, and for 20 s, SS substrate was submerged in rGO suspension and dried for 40 s and followed by a similar process to deposit Dy₂Se₃ as described above in **section 4.2.2.2**. Such 200 cycles result in uniform rGO/Dy₂Se₃ composite thin film. An illustrative representation of the

formation of a layered structure of rGO/Dy₂Se₃ composite is provided in **Figure 4.1 (b)**.

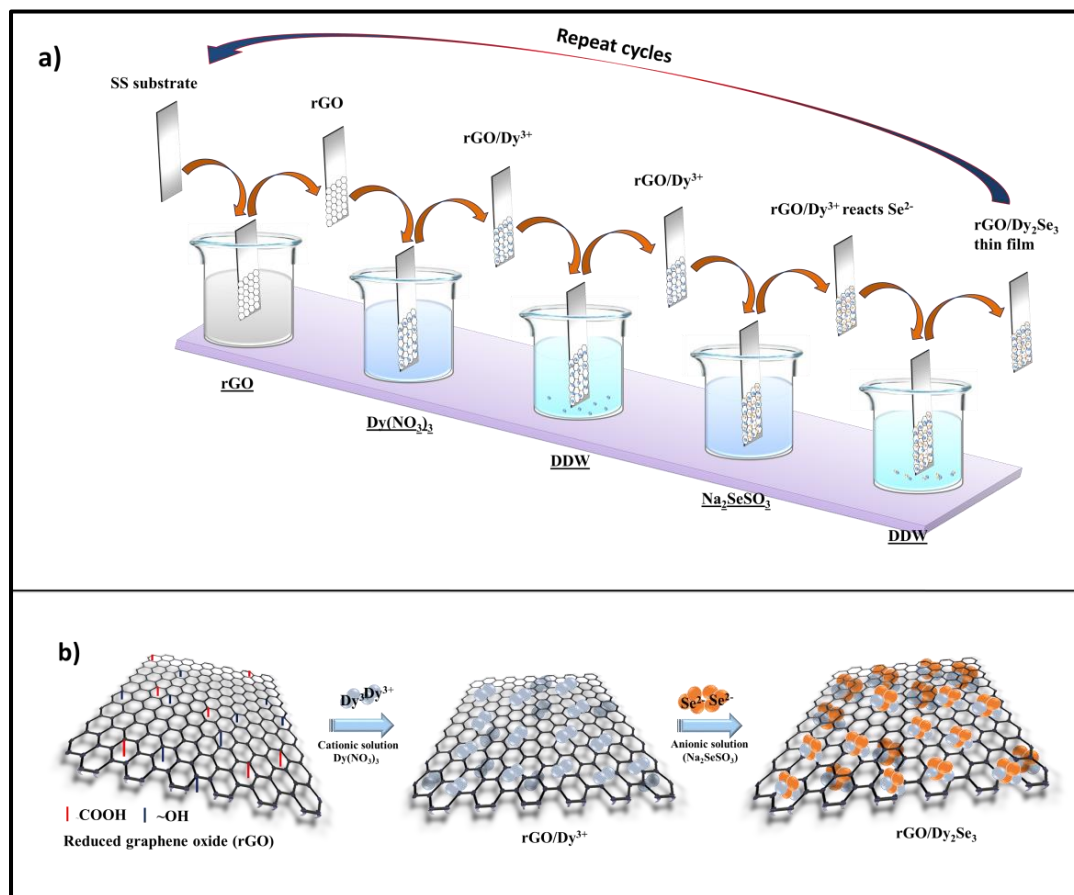


Figure 4.1: a) Schematic of SILAR method for deposition of rGO/Dy₂Se₃ thin film and b) the schematic illustration of the formation of rGO/Dy₂Se₃ composite.

4.2.2.4 Material Characterizations

4.2.2.4A Physico-Chemical Characterizations:

All the physico-chemical characterizations of Dy₂Se₃ and rGO/Dy₂Se₃ thin films were performed as mentioned in **section 3.3.1**.

4.2.2.4B Electrochemical Characterizations:

The electrochemical workstation (ZIVE MP1) was utilized to analyze the electrochemical properties of Dy₂Se₃ and rGO/Dy₂Se₃ thin film electrodes. The typical three-electrode system consists of thin films of Dy₂Se₃ and rGO/Dy₂Se₃ as working electrodes, a saturated calomel electrode (SCE) as a reference, and a platinum sheet as a counter electrode. All electrodes were tested in 1 M LiClO₄ electrolyte at room temperature.

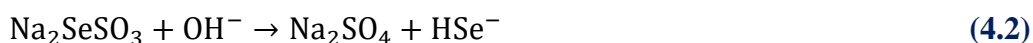
4.3 Results and Discussion:

4.3.1 Growth Mechanism of Dy₂Se₃ and rGO/Dy₂Se₃ Thin Films:

Dy₂Se₃ and rGO/Dy₂Se₃ were deposited on the SS substrate by employing SILAR method. A solid phase of desired material is prepared in a phased manner from water soluble precursors kept in separate containers using SILAR method. For this purpose, a substrate possessing nucleation sites was alternatively immersed in precursor solutions for adsorption and reaction. Ions of dysprosium (Dy³⁺) and selenium (Se²⁻) are produced in (Dy(NO₃)₃) and (Na₂SeSO₃) precursor solutions, respectively owing to dissociation process as,



The selenium ion (Se²⁻) is produced from the sodium selenosulphate (Na₂SeSO₃) solution. The hydrolysis of Na₂SeSO₃ results in the generation of Se²⁻ ions in an alkaline medium as,



In SILAR method, preabsorbed Dy³⁺ ions react with Se²⁻ ions and form insoluble Dy₂Se₃ as,



Multiple SILAR cycles were repeated to get optimized mass loading of Dy₂Se₃ on the substrate [9].

4.3.2 Physico-Chemical Characterizations of rGO, Dy₂Se₃ and rGO/Dy₂Se₃ Thin Films:

4.3.2.1 XRD Study:

A powder XRD technique was used to identify the crystal structure of the pristine and composite materials. **Figure 4.2** shows the XRD patterns of (i) rGO, ii) Dy₂Se₃ and (iii) rGO/Dy₂Se₃ composite thin films. The prominent diffraction peaks from (011) and (302) crystallographic planes of orthorhombic Dy₂Se₃ are observed. The XRD diffraction pattern of rGO/Dy₂Se₃ composite is well indexed to the standard orthorhombic structure of Dy₂Se₃ (JCPDS card no. 00-030-0526). The absence of a diffraction peak for rGO in the composite thin film is due to the small quantity of

rGO. Less ordered stacking of rGO sheets in rGO/Dy₂Se₃ composite may be one of the reasons for the absence of an rGO peak. Due to the effect of composition, an intensity reduction and shift in the peak positions are observed.

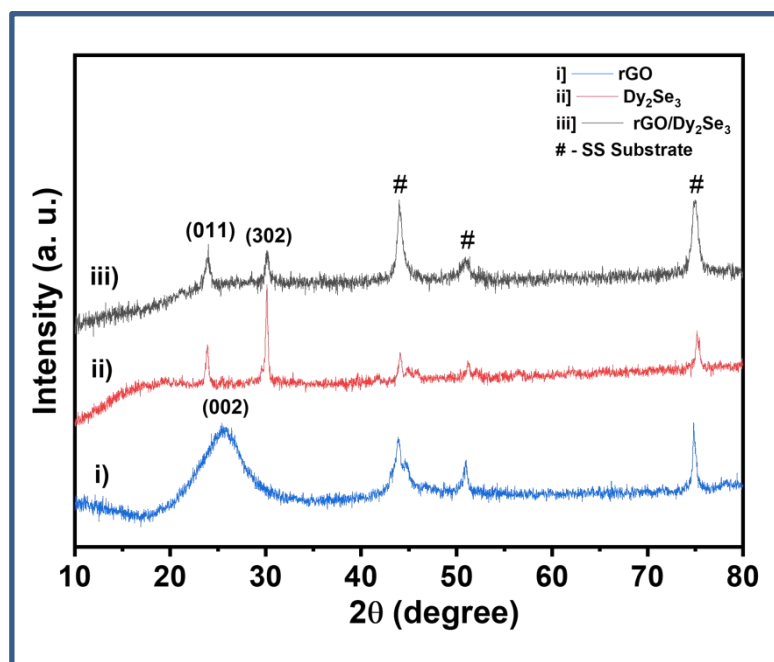


Figure 4.2: The XRD patterns of i) rGO, ii) Dy₂Se₃, and iii) rGO/Dy₂Se₃ thin films

The high intensity peaks suggested a good crystalline structure in the composite. Some research articles also observed a decrease in peak intensity [10, 11]. The diffraction pattern of rGO contains a single peak at 24.61°, which corresponds to the (002) crystal plane of rGO, as presented in **Figure 4.2 (i)** [12]. The XRD study confirmed the formation of Dy₂Se₃ and rGO/Dy₂Se₃ composite film.

4.3.2.2 FTIR Study:

The FT-IR absorption spectra of Dy₂Se₃ and rGO/Dy₂Se₃ thin films in the wavenumber range of 400-4000 cm⁻¹ are shown in **Figure 4.3**. The absorption bands at 419, 569, and 770 cm⁻¹ correspond to Dy-Se bond from Dy₂Se₃ [13]. The bands at 1634 and 1400 cm⁻¹ correspond to -OH symmetric stretching vibrations from adsorbed water molecules [14]. The other absorption bands were observed at 1047 cm⁻¹ (stretching vibration of the alkoxy group), 1351 cm⁻¹ (-C-OH stretching), and 2918 cm⁻¹ (aromatic sp² -C-H stretching) of rGO sheet [15]. The bands at 3120 and 3471 cm⁻¹ are attributed to -OH bending vibrations from water. The FT-IR analysis confirms the formation of Dy₂Se₃ and a composite film of rGO and Dy₂Se₃.

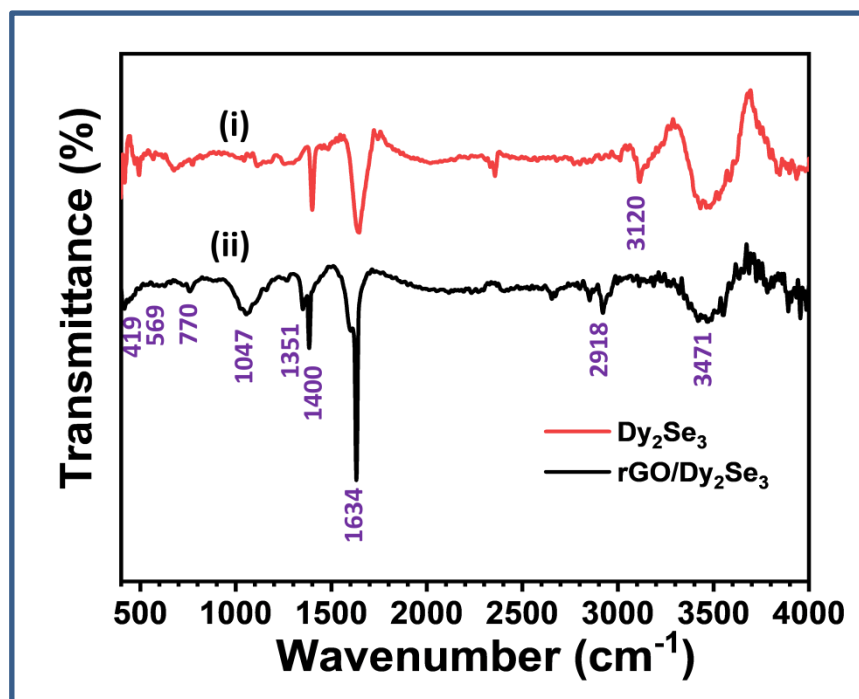


Figure 4.3: The FT-IR spectra of i) Dy_2Se_3 and ii) $\text{rGO}/\text{Dy}_2\text{Se}_3$ composites.

4.3.2.3 FE-SEM Study:

The FE-SEM technique was employed to study surface morphology. The morphology of Dy_2Se_3 and $\text{rGO}/\text{Dy}_2\text{Se}_3$ composite thin films at the magnifications of 10,000X and 50,000X presented in **Figure 4.4 (a-d)**. The morphology of Dy_2Se_3 and $\text{rGO}/\text{Dy}_2\text{Se}_3$ in **Figure 4.4 (a and d)** shows the formation of irregular grains over the SS surface. **Figure 4.4 (a)** shows a sizeable porous structure with multiple voids. The graphene sheets are observed in **Figure 4.4 (d)**. It is observed that Dy_2Se_3 is anchored on rGO sheets. **Figure 4.4 (e and f)** show the morphology of rGO thin films at the magnifications of 10,000X and 20,000X. The FE-SEM images observed the graphene sheets. The $\text{rGO}/\text{Dy}_2\text{Se}_3$ composite thin film formation is confirmed by the FE-SEM images. After the introduction of rGO in the synthesis process, a 2D layered structure is formed, which will facilitate easy ion transport to embedded nanoparticles in the 2D rGO sheets [16, 17].

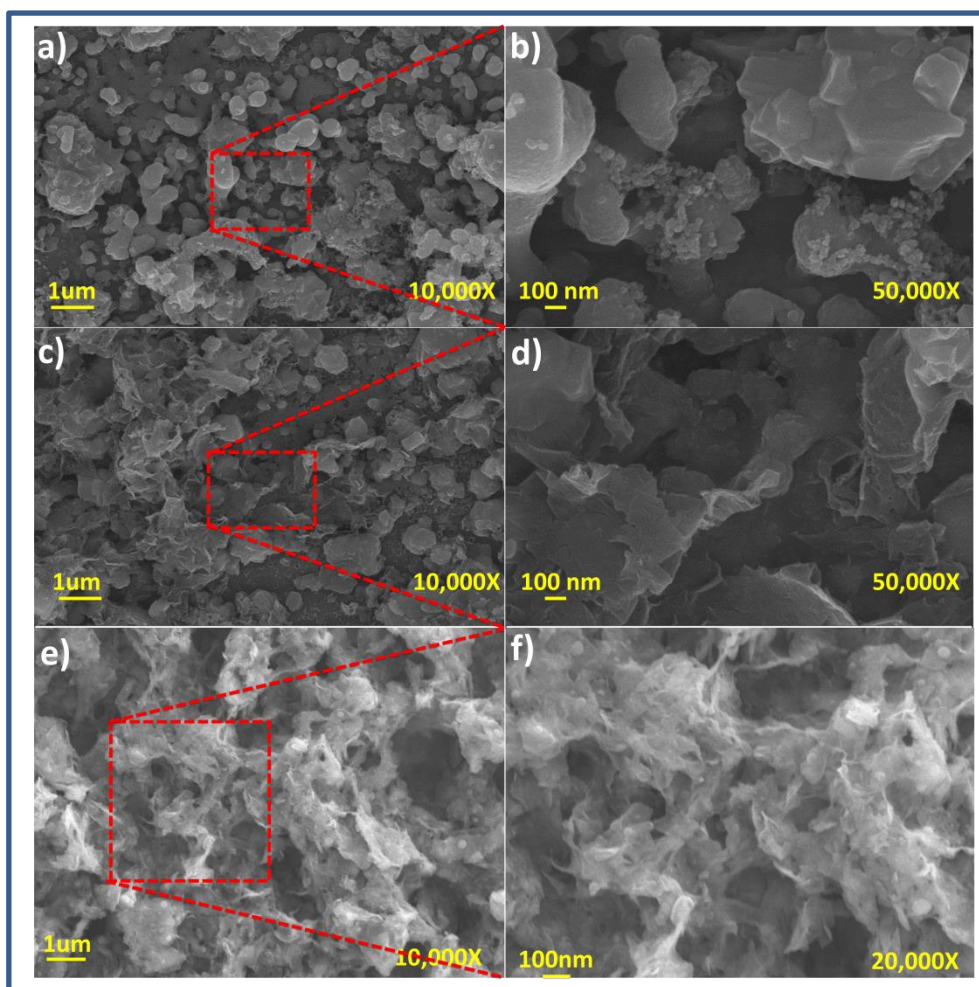


Figure 4.4: The FE-SEM images of **a-b)** Dy_2Se_3 , **c-d)** $\text{rGO}/\text{Dy}_2\text{Se}_3$ at magnifications of 10,000X, and 50,000X, and **e-f)** rGO thin films at magnifications of 10,000X and 20,000X.

4.3.2.4 Raman Study:

FT-Raman spectroscopy is a powerful technique for studying and analyzing samples involving chemical bonds present in pristine or composite materials. **Figure 4.5** shows the Raman spectra of pristine Dy_2Se_3 and $\text{rGO}/\text{Dy}_2\text{Se}_3$ composite thin films. Two broad peaks at 243 and 261 cm^{-1} are ascribed to Dy-Se bonding, and the small peak at 490 cm^{-1} is the overtone of the peak at 243 cm^{-1} [15].

In the Raman spectrum of $\text{rGO}/\text{Dy}_2\text{Se}_3$ sample, D and G peaks at wavenumbers of 1334 and 1604 cm^{-1} confirm the presence of rGO and the formation of a composite thin film. The D and G bands are related to sp^3 and sp^2 -hybridized carbon atoms in the regular honeycomb lattice, respectively. sp^3 hybridized carbon in rGO indicates attachment of functional groups such as $-\text{OH}$, $-\text{COOH}$.

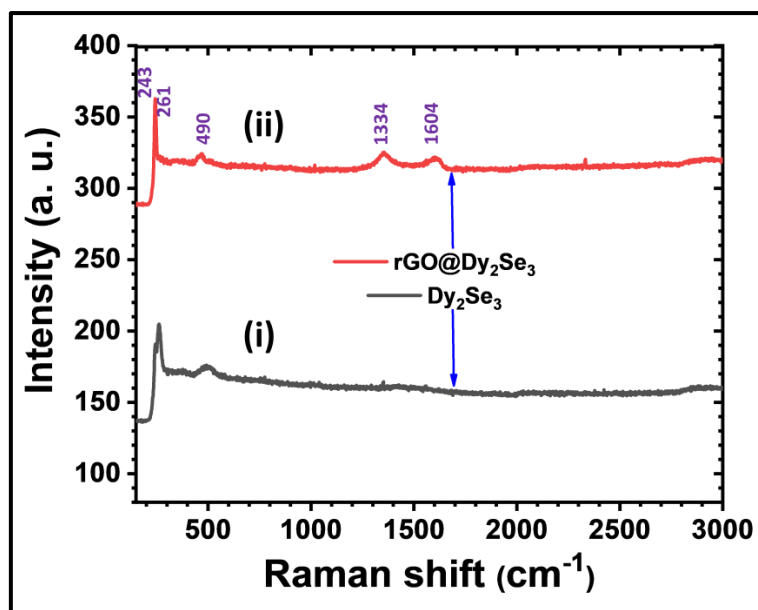


Figure 4.5: The Raman spectra of i) Dy_2Se_3 and ii) $\text{rGO}/\text{Dy}_2\text{Se}_3$ composites.

A key factor in determining the relative abundance of disordered domains in the graphene lattice is the (I_D/I_G) ratio. A higher ratio signifies fewer sp^2 domains and more disorders or defects [18]. In the present work, for $\text{rGO}/\text{Dy}_2\text{Se}_3$, the relative intensity I_D/I_G of 1.27 confirms moderate disorder and the formation of a few layers of rGO stacked between Dy_2Se_3 layers.

4.3.2.5 EDAX Study:

The EDAX spectra for Dy_2Se_3 and $\text{rGO}/\text{Dy}_2\text{Se}_3$ composite film are shown in **Figure 4.6 (a and b)**, respectively. The EDAX spectrum (**Figure 4.6 (a)**) reaffirms the presence of elements Dy and Se in Dy_2Se_3 thin film. Atomic percentages of Se and Dy elements in Dy_2Se_3 film are 64% and 36%, respectively, with Dy: Se atomic ratio of 1:1.77. The elemental ratio diverts from the ideal value (1:1.5) due to excess selenium. **Figure 4.6 (b)** shows the EDAX spectrum of $\text{rGO}/\text{Dy}_2\text{Se}_3$ composite thin film.

The atomic ratio in the composite thin film of $\text{rGO}/\text{Dy}_2\text{Se}_3$ varies from the ideal value (1:2). The atomic percentages of Dy, Se, C, and O are 24.94, 37.56, 28.92, and 8.58%, respectively. The observed atomic percentage of elements determined from the EDAX spectrum, confirm the formation of the Dy_2Se_3 and $\text{rGO}/\text{Dy}_2\text{Se}_3$ composite thin films.

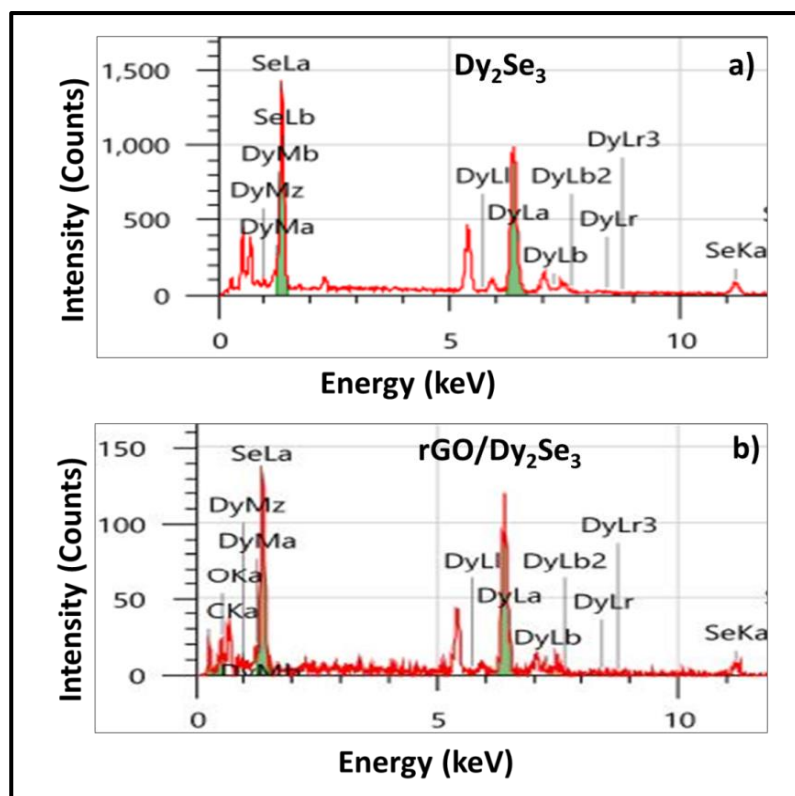


Figure 4.6: The EDAX spectra of a) Dy_2Se_3 , and b) $\text{rGO}/\text{Dy}_2\text{Se}_3$.

4.3.2.6 BET Study:

The BET surface analysis was used to measure the specific surface area and pore size distribution of Dy_2Se_3 and $\text{rGO}/\text{Dy}_2\text{Se}_3$ composite thin films. The N_2 sorption isotherms of Dy_2Se_3 and $\text{rGO}/\text{Dy}_2\text{Se}_3$ composite are of a type-V with H2 hysteresis loop as presented in **Figure 4.7 (a and b)**. The BJH method was used to analyze the electrodes average pore diameter. The results are shown in **Figure 4.7 (c)**. The specific surface areas of Dy_2Se_3 and $\text{rGO}/\text{Dy}_2\text{Se}_3$ are $7 \text{ m}^2 \text{ g}^{-1}$, respectively. These results show that incorporating rGO nanosheets into Dy_2Se_3 thin films effectively increases the surface area [19].

These results suggest that the specific surface area is improved by the combination of pseudocapacitive material and rGO sheets. The observed mean pore diameters of Dy_2Se_3 (58 nm) and $\text{rGO}/\text{Dy}_2\text{Se}_3$ (36 nm) (**Figure 4.7 (c)**) indicate the presence of a mesoporous structure. After composition, the average mean pore diameter of $\text{rGO}/\text{Dy}_2\text{Se}_3$ is smaller than that of Dy_2Se_3 may lead to rise in specific capacitance as compared to Dy_2Se_3 .

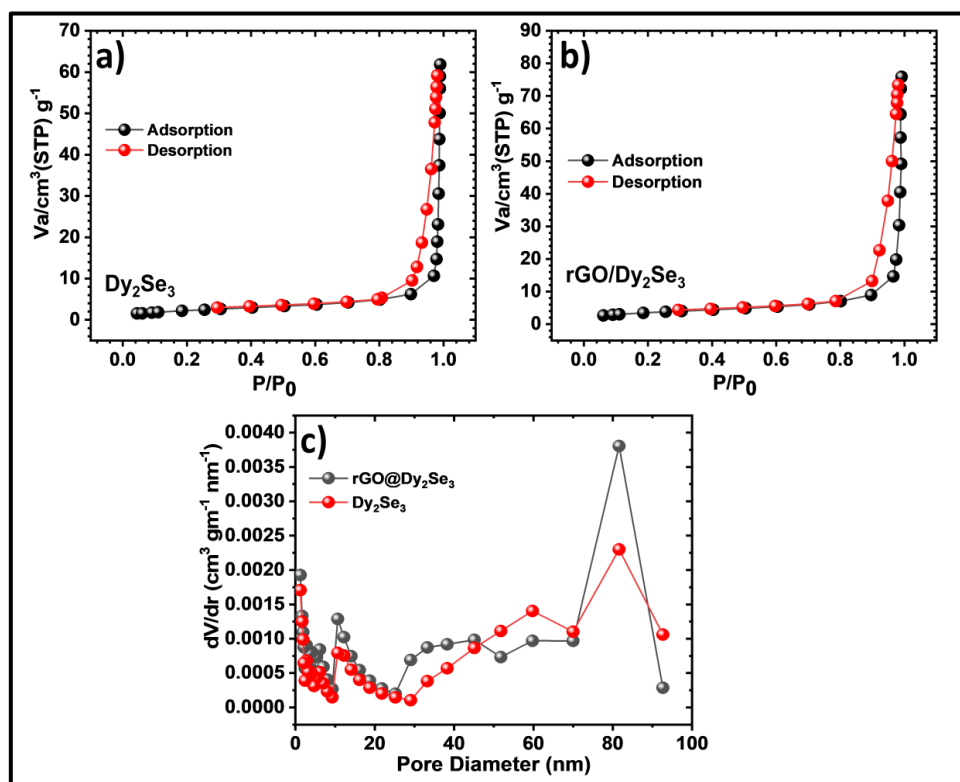


Figure 4.7: The N₂ adsorption–desorption isotherms of a) Dy₂Se₃, and b) rGO/Dy₂Se₃, and c) pore size distributions of Dy₂Se₃, and rGO/Dy₂Se₃.

4.3.2.7 Contact Angle Study:

Contact angle measurement is a simple method to evaluate wettability of solid surfaces. The contact angle depends on the topography of the film. A lower contact angle helps to create intimate contact with aqueous electrolytes. If the surface is hydrophilic, less the contact angle value ($\theta < 90^\circ$).

If the surface is hydrophobic, the contact angle value ($\theta > 90^\circ$). The contact angle images of Dy₂Se₃ and rGO/Dy₂Se₃ thin films are illustrated in **Figure 4.8 (a and b)**. The contact angle values of Dy₂Se₃ and rGO/Dy₂Se₃ composite films are 62° and 46° . The rGO/Dy₂Se₃ composite thin film exhibits more hydrophilic nature as compared to Dy₂Se₃. The hydrophilic nature of the surface is beneficial for high SC performance [20]. Various reports are available on rare earth chalcogenide films for hydrophilic nature, such as Bagwade et al. [21] observed 50° contact angle for Dy₂S₃ electrode synthesized using SILAR method. Ubale et al. [22] reported an angle of 57° for SILAR synthesized Yb₂S₃ film.

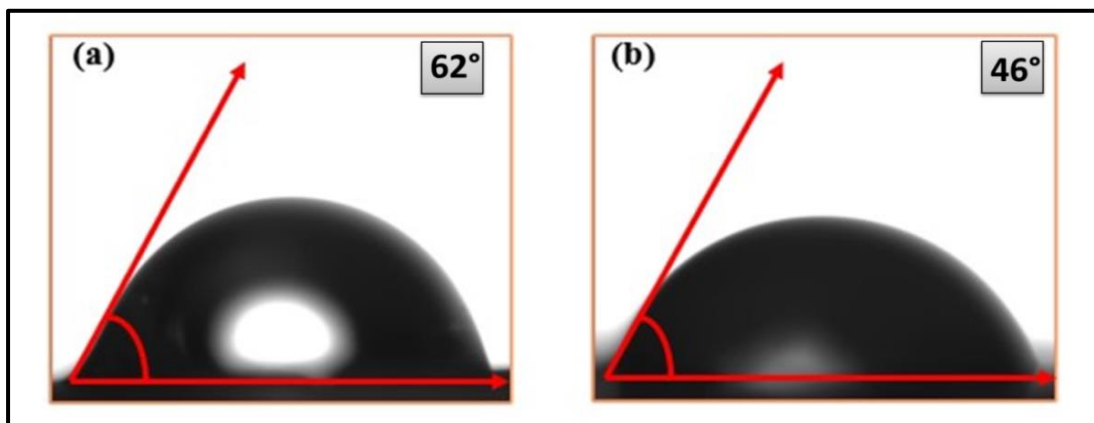


Figure 4.8: Water contact angle photographs of a) Dy_2Se_3 and b) $\text{rGO}/\text{Dy}_2\text{Se}_3$ thin films.

4.3.3 Electrochemical Characterizations of Dy_2Se_3 and $\text{rGO}/\text{Dy}_2\text{Se}_3$ Thin Films:

4.3.3.1 Electrochemical Study of Dy_2Se_3 and $\text{rGO}/\text{Dy}_2\text{Se}_3$ Thin Films:

4.3.3.1A CV Study:

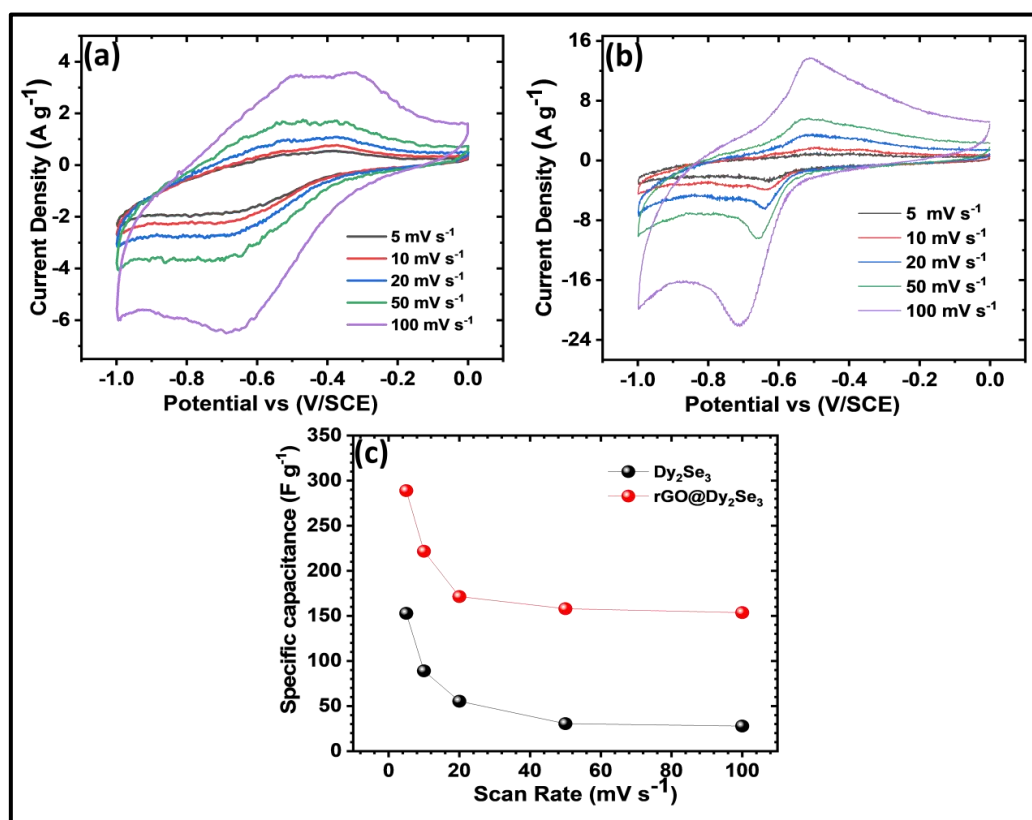


Figure 4.9: The CV curves of a) Dy_2Se_3 , b) $\text{rGO}/\text{Dy}_2\text{Se}_3$ at various scan rates from 5-100 mV s^{-1} , and c) variation of C_s with the scan rate for Dy_2Se_3 and $\text{rGO}/\text{Dy}_2\text{Se}_3$ thin film electrodes.

The CV analysis of Dy₂Se₃, and rGO/Dy₂Se₃ was used to study redox reactions occurring at the electrode/electrolyte interface at different scan rates in a potential window of -1.0 to 0 V/SCE. The CV curves of Dy₂Se₃ and rGO/Dy₂Se₃ composite electrodes at different scan rates (5 to 100 mV s⁻¹) are presented in **Figure 4.9 (a and b)**, respectively. At 5 mV s⁻¹, the *C_s* of the pristine Dy₂Se₃ electrode is 147 F g⁻¹, while that of rGO/Dy₂Se₃ composite electrode is 289 F g⁻¹.

The CV curves show that the integral area is larger than the pure Dy₂Se₃. As the scan rate goes up, the *C_s* of both electrodes decreases due to the less time available for redox reactions at a higher scan rate. Because there was enough time for electrolyte ions to interact with the electrode at the low scan rate, well-defined peaks were observed [23]. Electrochemical characterization of rGO reported in **Chapter 3, section 3.4B.2.1**.

In the case of rGO/Dy₂Se₃ composite electrode, the synergistic effect between Dy₂Se₃ and rGO nanosheets leads to the maximum area under CV curves and a rise in the peak current, which signifies enhanced capacitive performance. A comparative *C_s* value of rGO/Dy₂Se₃ and Dy₂Se₃ electrodes at various sweep rates is presented in **Figure 4.9 (c)**. The total charge stored by the electrode is classified into two types: diffusion-controlled charge storage and surface-controlled charge storage. These mechanisms are associated with the location of redox reactions at or inside the electrode [24]. After the electrolyte ions have been electro-adsorbed onto the electrode surface, surface redox processes take place. The charge storage kinetics of Dy₂Se₃ and rGO/Dy₂Se₃ were determined using power law equation [25],

$$I_p = av^b \quad (4.5)$$

where *I_p* (A g⁻¹) is the current density measured at the potential of -1.0 to 0 V/SCE, *v* (mV s⁻¹) is a scan rate, and *a* and *b* are the adjustable variables. **Figure 4.10 (a)** shows log *I* vs. log *v* graph, which gives *b*-values for Dy₂Se₃ (0.69) and rGO/Dy₂Se₃ (0.89). Capacitive and diffusion-controlled charge storage mechanisms contribute to complete charge storage. The following equation is used to distinguish these two charge storage methods:

$$I(v) = k_1v + k_2v^{0.5} = I_{\text{surface}} + I_{\text{bulk}} \quad (4.6)$$

where *k₁* and *k₂* are constant coefficients. *k₁v* represents the current from the capacitive, and *k₂v^{0.5}* is the current contribution from the diffusion-controlled process.

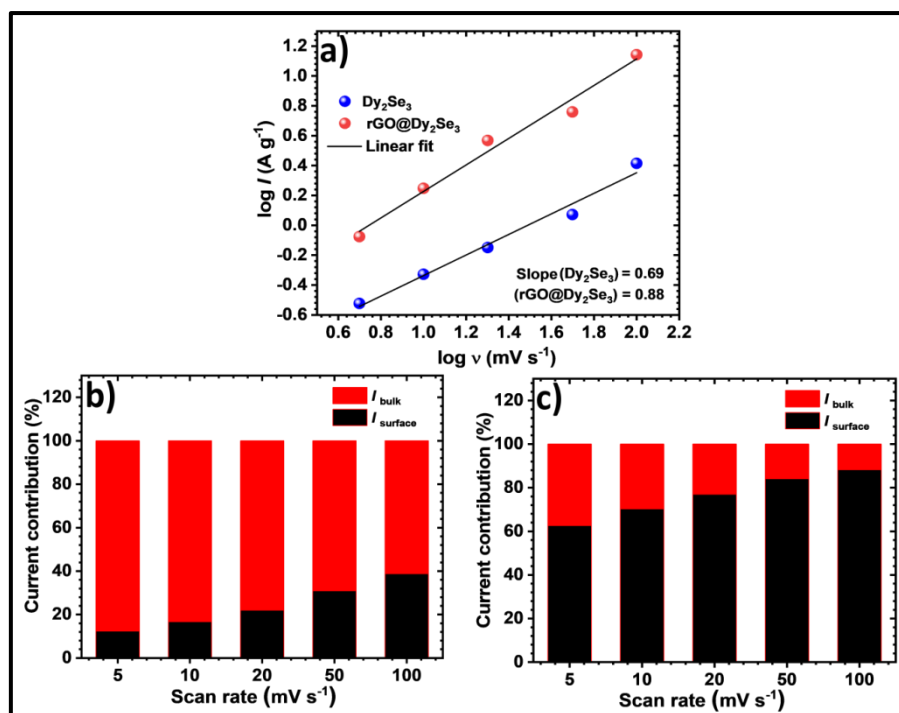


Figure 4.10: a) Plot of $\log I$ vs $\log v$, and contribution of capacitive and diffusion-controlled currents with scan rates of b) Dy_2Se_3 and c) $\text{rGO/Dy}_2\text{Se}_3$ composite electrode.

According to charge storage distribution, the total charge stored by Dy_2Se_3 and $\text{rGO/Dy}_2\text{Se}_3$ electrodes was evaluated using (Equation 4.6). The charge contribution plots of Dy_2Se_3 and $\text{rGO/Dy}_2\text{Se}_3$ at various scan rates are shown in Figure 4.10 (b and c), respectively. For Dy_2Se_3 and $\text{rGO/Dy}_2\text{Se}_3$ electrodes, charge storage from the capacitive process is 39 and 88%, and from the diffusion-controlled process, it is 61 and 12%, respectively. The decrease in diffusion-controlled charge storage with composition is associated with the EDLC nature of rGO. It is observed that the charge contribution of pseudocapacitance increases when the scan rate gradually decreases. The low scan rate benefits the electronic embedding process for energy storage [26].

4.3.3.1B GCD Study:

The GCD analysis was conducted to study the charge-discharge behaviour of Dy_2Se_3 and $\text{rGO/Dy}_2\text{Se}_3$ composite electrodes. Figure 4.11 (a and b) present GCD profiles of Dy_2Se_3 and $\text{rGO/Dy}_2\text{Se}_3$ composite electrodes at different current densities of 4 to 8 A g⁻¹. The obtained C_s of 210 F g⁻¹ at 4 A g⁻¹ current density for $\text{rGO/Dy}_2\text{Se}_3$ composite thin films is larger than C_s of Dy_2Se_3 . The calculated values of C_s for both electrodes from GCD plots at various current densities are displayed in

Figure 4.11 (c). With rising current densities, the C_s of both electrodes showed a decreasing tendency.

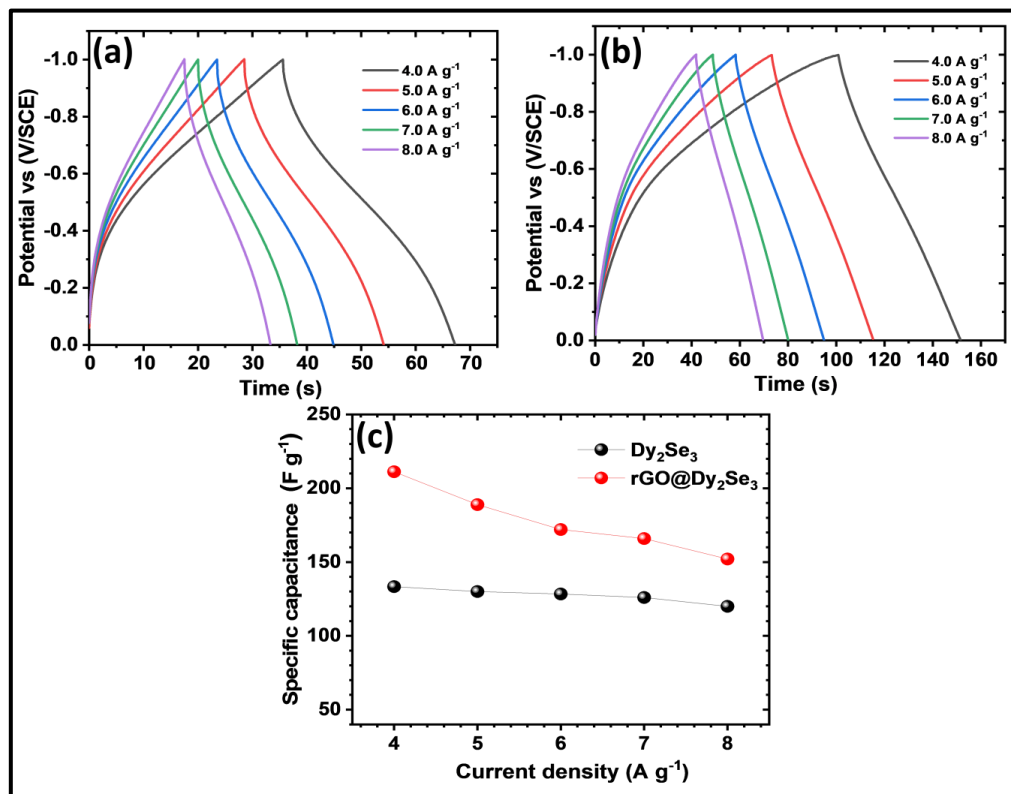


Figure 4.11: The GCD curves of a) Dy_2Se_3 , and b) $\text{rGO/Dy}_2\text{Se}_3$ at different current densities from 4–8 A g^{-1} and c) variation of C_s with charge-discharge current density.

4.3.3.1C EIS Study:

The interface charge transport properties of the electrode materials are analysed using the EIS technique conducted between 0.01 Hz and 0.1 MHz in frequency. **Figure 4.12 (a)** represents Nyquist plots of Dy_2Se_3 and $\text{rGO/Dy}_2\text{Se}_3$ composite electrodes, and **Figure 4.12 (b)** is the enlarged view. The resistance of $\text{rGO/Dy}_2\text{Se}_3$ electrode has been far smaller than that of Dy_2Se_3 . The electrochemical performance of $\text{rGO/Dy}_2\text{Se}_3$ electrode depends on charge transfer resistance (R_{ct}), constant phase element (CPE), and Warburg impedance (W). The Nyquist plots were simulated with Z-View software, and the fitted circuit is shown in **Figure 4.12 (c)**.

The electrical equivalent circuit is composed of four parameters R_s , R_{ct} , CPE, and W [27, 28]. The observed values of R_s , R_{ct} , CPE, and W are $2.49 \Omega \text{ cm}^{-2}$, $178 \Omega \text{ cm}^{-2}$, 0.80 F , and 0.91Ω for Dy_2Se_3 and $1.81 \Omega \text{ cm}^{-2}$, $4.01 \Omega \text{ cm}^{-2}$, 0.93 F , and 0.42Ω respectively, for $\text{rGO/Dy}_2\text{Se}_3$ electrode. Generally, the R_s of the electrode is indicated

by the intersecting points on the real axis at higher-frequency regions. This is the electrochemical contact resistance of the electrode between a current collector and an electrolyte.

The R_{ct} is represented by the semicircle at a high frequency region within the electrode materials. The capacitive performance of the electrode described by CPE is one of the most common circuit elements representing deviations from ideal capacitive behaviour. A linearly inclined line in the Nyquist plot represents W associated with diffusion resistance [29].

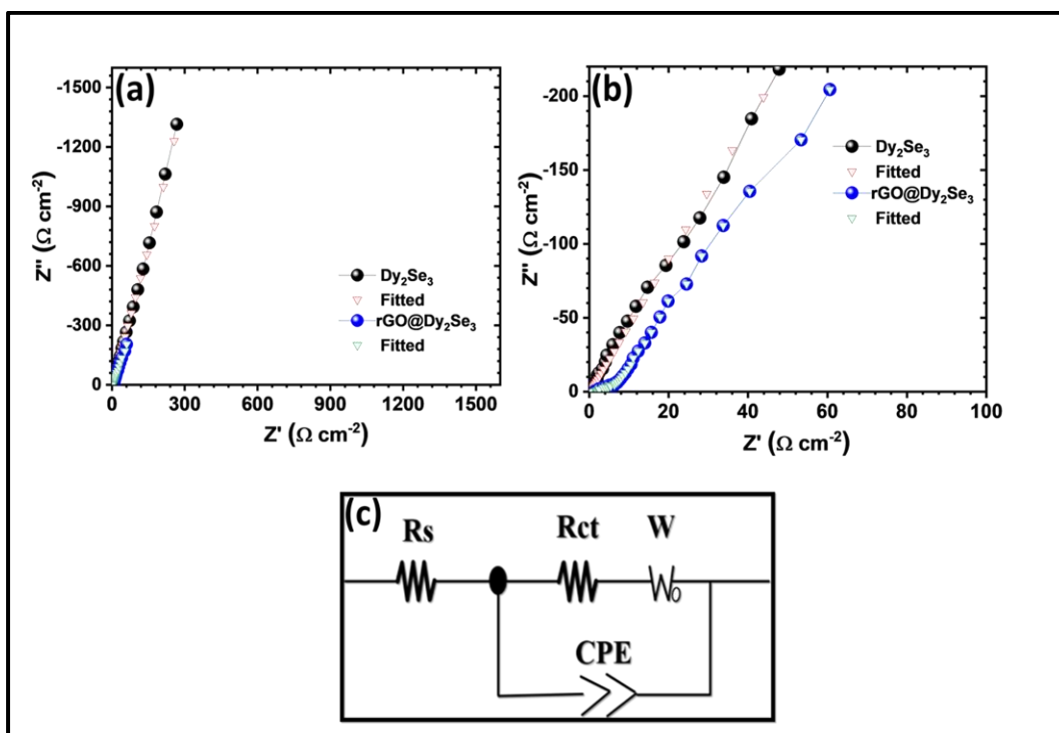


Figure 4.12: Nyquist plots of a) Dy_2Se_3 and $\text{rGO/Dy}_2\text{Se}_3$ electrodes, b) magnified Nyquist plot and c) the fitted equivalent circuit from the EIS data.

Table 4.1: Electrochemical impedance spectroscopic data of Dy_2Se_3 and $\text{rGO/Dy}_2\text{Se}_3$ composite thin films.

Parameters	R_s ($\Omega \text{ cm}^{-2}$)	R_{ct} ($\Omega \text{ cm}^{-2}$)	CPE (F)	W (Ω)
Dy_2Se_3	2.49	178	0.80	0.91
$\text{rGO/Dy}_2\text{Se}_3$	1.81	4.01	0.93	0.42

4.3.3.1D Stability Study:

The cyclability of Dy_2Se_3 and $\text{rGO}/\text{Dy}_2\text{Se}_3$ at the current density of 7 A g^{-1} for 5000 GCD cycles. **Figure 4.13 (a and b)** show the C_s retention and Coulombic efficiency variation with electrochemical cycles of Dy_2Se_3 and $\text{rGO}/\text{Dy}_2\text{Se}_3$ composite electrodes, respectively. It is noted that $\text{rGO}/\text{Dy}_2\text{Se}_3$ composite electrode shows better retention than Dy_2Se_3 . The capacitive retention and Coulombic efficiencies are 84 and 89% for Dy_2Se_3 and 89 and 98% for $\text{rGO}/\text{Dy}_2\text{Se}_3$, respectively.

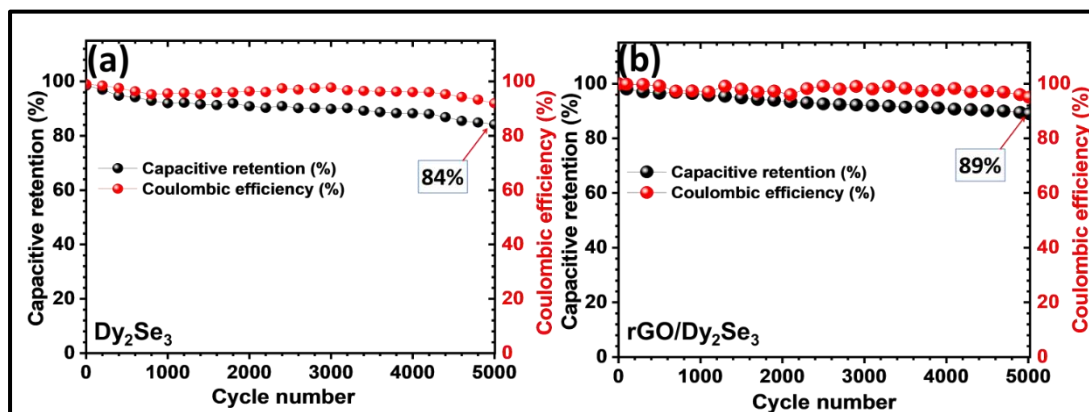


Figure 4.13: Stability curves of a) Dy_2Se_3 and b) $\text{rGO}/\text{Dy}_2\text{Se}_3$ thin film electrodes.

4.4 Conclusions:

In summary, Dy_2Se_3 and $\text{rGO}/\text{Dy}_2\text{Se}_3$ composites were successfully prepared by SILAR method. The capacitance of Dy_2Se_3 was effectively improved due to the composition of rGO nanosheets. This study concludes that the binder less composition of Dy_2Se_3 with rGO affects the structural, morphological, and electrochemical properties of Dy_2Se_3 . The $\text{rGO}/\text{Dy}_2\text{Se}_3$ composite thin film showed orthorhombic crystal structure, hydrophilic nature, and a porous nanoparticle morphology. The composite $\text{rGO}/\text{Dy}_2\text{Se}_3$ electrode exhibited an excellent specific surface area of $18 \text{ m}^2 \text{ g}^{-1}$ compared to that of $9 \text{ m}^2 \text{ g}^{-1}$ for bare Dy_2Se_3 . The Dy_2Se_3 and $\text{rGO}/\text{Dy}_2\text{Se}_3$ composite electrode delivered a C_s of 147 and 289 F g^{-1} , respectively at a 5 mV s^{-1} scan rate. The $\text{rGO}/\text{Dy}_2\text{Se}_3$ composite electrode exhibited remarkable cycling stability of 89% up to 5000 cycles. The enhanced electrochemical activity was due to the synergetic effect between rGO and Dy_2Se_3 electrode. This study highlights the intriguing potentials of the designed $\text{rGO}/\text{Dy}_2\text{Se}_3$ composite as a promising material for manufacturing flexible supercapacitors with high S_E .

4.5 References:

- [1] B. Zhao, D. Chen, X. Xiong, B. Song, R. Hu, Q. Zhang, B. Rainwater, G. Waller, D. Zhen, Y. Ding, Y. Chen, C. Qu, D. Dang, C. Wong, M. Liu, *Energy Storage Mater.*, 7, (2017), 32-39.
- [2] C. Jinga, X. Guo, L. Xia, Y. Chen, X. Wang, X. Liu, B. Dong, F. Dong, S. Li, Y. Zhang, *Chem. Eng. J.*, 379, (2020), 122305-122333.
- [3] R. Nankya, J. Lee, D. Opar, H. Jung, *Appl. Surf. Sci.* 489, (2019), 552–559.
- [4] M. Barakzahi, M. Montazer, F. Sharif, T. Norby, A. Chatzitakis, *Electrochim. Acta*, 305, (2019), 187–196.
- [5] S. Jayasubramaniyan, S. Balasundari, S. Yeom, N. Naresh, T. Rani, E. Rapaka, N. Satyanarayana, H. Lee, P. Muralidharan, *Electrochim. Acta*, 390, (2021), 138865-138873
- [6] M. Venkanna, A. Chakraborty, Synthesis and characterizations of graphene oxide and reduced graphene oxide nanosheets, *AIP Conf. Proc.* 1591, (2014), 574–576.
- [7] S. Samanta, M. Shinde, R. Patil, *J. Nanotechnol. Adv. Mater.* 4, (2016), 53–57.
- [8] D. Malavekar, V. Lokhande, V. Mane, S. Kale, R. Bulakhe, U. Patil, I. In, C. Lokhande, *J. Solid. State Electrochem.*, 24, (2020), 2963–2974.
- [9] U. Patil, K. Gurav, J. Kim, C. Lokhande, S. Jun, *Bull. Mater. Sci.*, 37, (2014), 27–33.
- [10] Z. Jia, X. Shen, H. Zhou, K. Chen, *Ceram. Int.*, 41, (2015), 8710–8716.
- [11] R. Ashwini, V. Dileepkumar, K. Balaji, R. Viswanatha, C. Ravikumar, C. Srivastava, S. Mysore, *SI*, 2, (2021), 100125-100133.
- [12] Y. Shang, D. Zhang, Y. Liu, C. Guo, *Bull. Mater. Sci.*, 38, (2015), 7–12.
- [13] H. Naderi, M. Ganjali, A. Dezfuli, *J. Mater. Sci. Mater. Electron.*, 29, (2018), 3035–3044.
- [14] H. Kumar, J. Singh, R. Srivastava, P. Negi, H. Agrawal, K. Asokan, *J. Nanosci*, 2014, (2014), 1-11.

- [15] S. Ghosh, P. Samanta, N. Murmu, T. Kuila, J. Alloys Compd., 835, (2020), 155432-155444.
- [16] S. Sarkar, P. Howli, B. Das, N. Das, M. Samanta, G. Das, K. Chattopadhyay, ACS Appl. Mater. Interfaces, 9, (2017), 22652–22664.
- [17] M. Choi, S. Ho Lee, D. Ha Kim, K. Hee Shin, C. So Jin, S. Soo Kim, Y. Chang Kang, S. Hwa Yeon, J. Phys. Chem. Solid., 131, (2019), 69–78.
- [18] S. Sadhukhan, T. Ghosh, I. Roy, D. Rana, A. Bhattacharyya, R. Saha, S. Chattopadhyay, S. Khatua, K. Acharya, D. Chattopadhyay, Mater. Sci. Eng. C, 99, (2019), 696–709.
- [19] K. Huang, J. Zhang, Y. Liu, Y. Liu, Int. J. Hydrogen Energy, 40, (2015), 10158–10167.
- [20] R. Sun, A. Nakajima, A. Fujishima, T. Watanabe, K. Hashimoto, J. Phys. Chem. B, 105, (2001), 1984–1990.
- [21] P. Bagwade, D. Malavekar, T. Ghogare, S. Ubale, V. Mane, R. Bulakhe, I. In, C. Lokhande, J. Alloy. Compd. 859, (2021), 157829-157348.
- [22] S. Ubale, R. Bulakhe, V. Mane, D. Malavekar, I. In, C. Lokhande, J. Electroanal. Chem., 897, (2021), 115589-115607.
- [23] S. Karade, and B. Sankapal, J. Electroanal. Chem., 771, (2016), 80–86.
- [24] D. Dubal, N. Chodankar, D. Kim, P. Romero, Chem. Soc. Rev., 47, (2018), 2065–2129.
- [25] D. Malavekar, S. Kale, V. Lokhande, U. Patil, J. Kim, C. Lokhande, J. Phys. Chem. C, 124, (2020), 28395–2840.
- [26] S. Marje, V. Patil, V. Parale, H. Park, P. Shinde, J. Gunjekar, C. Lokhande, U. Patil, J. Chem. Eng., 429, (2022), 132184-132199.
- [27] N. Chodankar, S. Selvaraj, S. Ji, Y. Kwon, D. Kim, Small, 15, (2019), 1803716-1803728.
- [28] B. Pandit, V. Devika, B. Sankapal, J. Alloy. Compd., 726, (2017), 1295–1303.
- [29] R. Drummond, C. Huang, P. Grant, S. Duncan, J. Power Sources, 433, (2019), 126579-126589.

CHAPTER-5

**Dy₂S₃ and rGO/Dy₂S₃ Thin Films By CBD
Method: Characterization and Gas Sensor
Performance**

CHAPTER-5

Dy₂S₃ and rGO/Dy₂S₃ thin films by CBD method: Characterization and Gas Sensor Performance

Sr. No.	Title		Page No.
5.1	Introduction		125
5.2	Synthesis and Characterization of Dy ₂ S ₃ and rGO/Dy ₂ S ₃		126
	5.2.1	Experimental Details	126
		5.2.1.1 Chemicals	126
		5.2.1.2 Synthesis of Dy ₂ S ₃ and rGO/Dy ₂ S ₃	126
		5.2.1.3 Materials Characterization	126
	5.2.2	Results and Discussion	126
		5.2.2.1 XRD Study	126
		5.2.2.2 FE-SEM Study	127
		5.2.2.3 FT-IR Study	128
		5.2.2.4 Raman Study	128
		5.2.2.5 EDAX Study	128
		5.2.2.6 XPS Study	128
		5.2.2.7 BET Study	128
	5.2.3	Experimental Setup for Gas Sensor Studies	128
5.3	NO ₂ Gas Sensor Performance Evaluation of Dy ₂ S ₃ and rGO/Dy ₂ S ₃ Composite Thin Films:		129
	5.3.1	Results and Discussion	129
		5.3.1.1 Effect of Operating Temperature	129
		5.3.1.2 Resistance Stabilization Study	130
		5.3.1.3 Selectivity Study	131
		5.3.1.4 Response and Resistance vs Time Transient Study	132
		5.3.1.5 Sensitivity Study	133
		5.3.1.6 Long-term Stability Study	134
		5.3.1.7 Response and Recovery Time Study	135
		5.3.1.8 Gas Sensing Mechanism	136
5.4	Conclusions		137
5.5	References		138

5.1 Introduction:

Nowadays, the fossil fuel and organic chemical compound consumption has grown significantly due to on-going industrialization, rapid urbanization, and technological advancements that contribute to global ambient air pollution. The atmospheric pollutants that are NO_2 , NO , NH_3 , H_2S , CO , CO_2 , Cl_2 , SO_2 , CH_4 , and volatile organic compounds (VOCs) [1]. These pollutants have affected the human health and the environment when exposure levels are higher than advised. Due this, we need the gas sensors should detect multiple gases simultaneously with excellent sensitivity and selectivity [2, 3]. Among various air pollutants, The World Health Organization (WHO) has widely acknowledged NO_2 emissions in its air pollution guidelines. Wherein higher concentrations of NO_2 is considered as one of the hazardous pollutants [4, 5].

NO_2 is a reddish-brown gas with a strong smell that is produced at high temperatures during nitrogen and oxygen combustion processes [6, 7]. These processes can be found in power plants, vehicle engines, industrial facilities, and residential heating systems. Furthermore, lightning and soil microbial activity naturally release it and toxic to both humans and animals. Inhalation of NO_2 can cause respiratory problems [8]. It also contributes significantly to the formation of secondary particulate matter ($\text{PM}_{2.5}$) and ground-level ozone (O_3). These contaminants lead to the smog formation, reduced visibility, and harmful consequences on the environment and human health.

In general the most of the gas sensors based on the metal oxide semiconductors because of its superior ability to detect a variety of dangerous gases, including CO , H_2S , NO_2 , and NH_3 . However, their long response/recovery times and lack of stability are still significant unsolved drawbacks to the large-scale implementation of these technologies [9]. In this regard, particularly transition-metal sulphides have unique properties that make them attractive for gas sensing applications [10, 11].

This chapter deals with the preparation of hollow microspherical Dy_2S_3 and $\text{rGO/Dy}_2\text{S}_3$ composite thin films via CBD method. Further, the gas sensor fabricated using Dy_2S_3 and $\text{rGO/Dy}_2\text{S}_3$ are evaluated for 423 K and room temperature (RT) (300

K) operated NO₂ sensor respectively. Furthermore, the gas sensing parameters like selectivity, sensitivity, stability, response-recovery are studied.

5.2 Synthesis and Characterization of Dy₂S₃ and rGO/Dy₂S₃:

5.2.1 Experimental Details:

5.2.1.1 Chemicals:

The required chemicals are mentioned earlier in **Chapter-3, section 3.2.2, subsection 3.2.2.2.**

5.2.1.2 Synthesis of Dy₂S₃ and rGO/Dy₂S₃:

The synthesis of Dy₂S₃ and rGO/Dy₂S₃ thin films was carried out using CBD method as illustrated in **Chapter 3, section 3.2.2, subsection 3.2.2.4 and 3.2.2.5.** The 6 h deposited Dy₂S₃ and rGO/Dy₂S₃ composite thin films on glass substrate are carry forwarded to physico-chemical characterizations and gas sensing test.

5.2.1.3 Materials Characterization:

All the physico-chemical characterizations of Dy₂S₃ and rGO/Dy₂S₃ thin films were performed as mentioned in **Chapter 3, section 3.3, and subsection 3.3.1.**

5.2.2 Results and Discussion:

5.2.2.1 XRD Study:

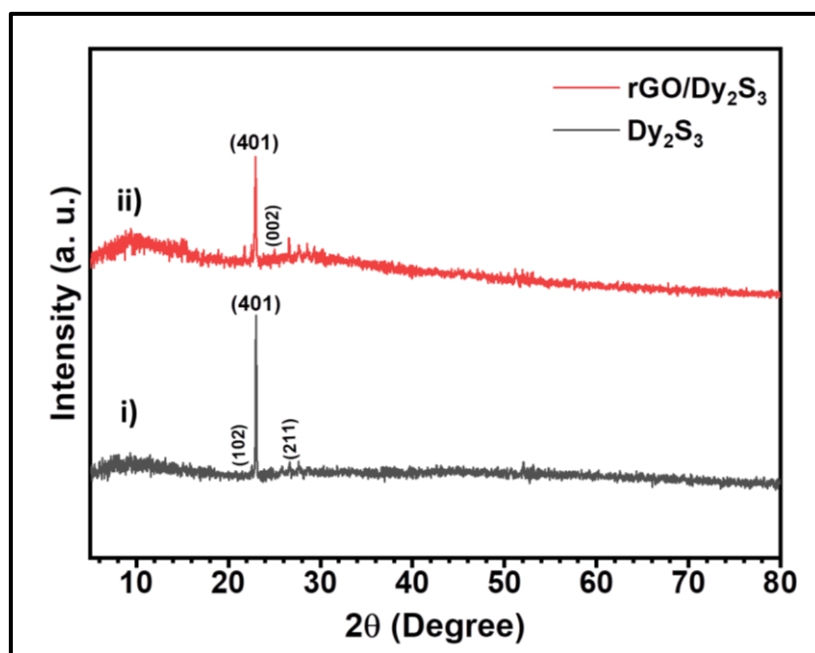


Figure 5.1: The XRD patterns of i) Dy₂S₃, and ii) rGO/Dy₂S₃.

The XRD analysis is used to investigate the crystal structure of the Dy_2S_3 and $\text{rGO}/\text{Dy}_2\text{S}_3$ thin films. **Figure 5.1** displayed the XRD patterns of i) Dy_2S_3 and ii) $\text{rGO}/\text{Dy}_2\text{S}_3$ thin films. **Figure 5.1 (i)** the Dy_2S_3 showed characteristic peak at 2θ of 23.39° , and other peaks at 21.70° , 26.57° , corresponding to planes of (401), (102), and (211). All of the diffraction peaks are correlated with standard JCPDS card no. 00-020-1033 and consistent with the formation of the monoclinic phase of the Dy_2S_3 .

From **Figure 5.1** it is seen that, the diffraction peaks are sharp and intense, which is indicating a high crystalline structure. But in XRD pattern of $\text{rGO}/\text{Dy}_2\text{S}_3$ composite (**Figure 5.1 (ii)**), the intensity of peak is slightly decreased as compared to Dy_2S_3 due to the effect of composition [12]. **Figure 5.1 (ii)** the observed small broader peak for (002) at 24.98° is associated with rGO [13]. According to the XRD analyses confirm the formation of Dy_2S_3 and $\text{rGO}/\text{Dy}_2\text{S}_3$.

5.2.2.2 FE-SEM Study:

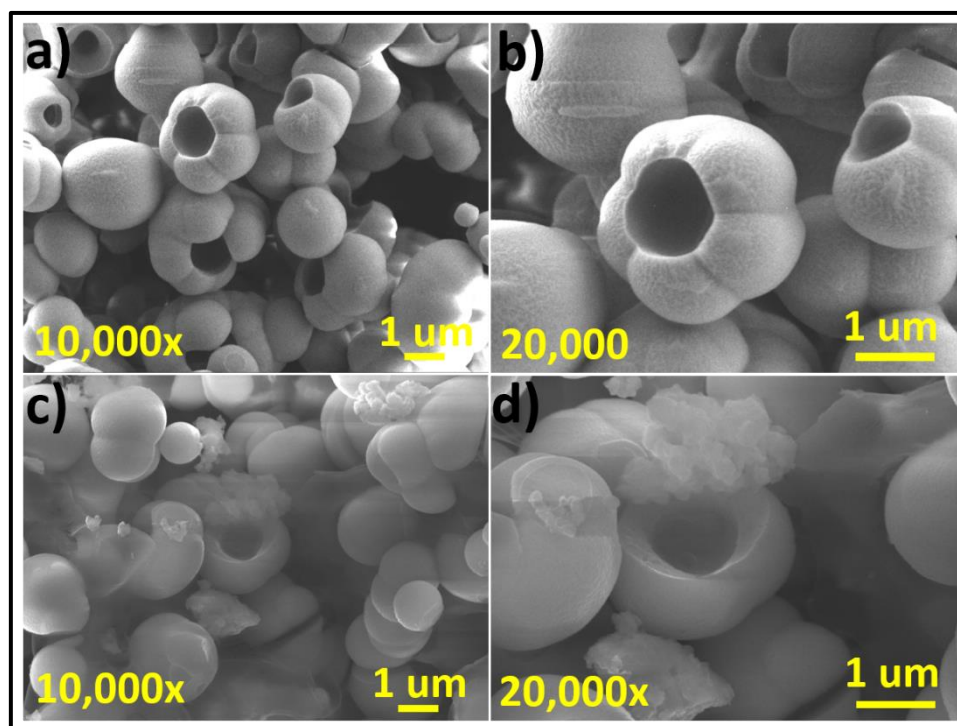


Figure 5.2: FE-SEM images of a) Dy_2S_3 and c) $\text{rGO}/\text{Dy}_2\text{S}_3$ at the magnification of 10,000x and b) Dy_2S_3 and d) $\text{rGO}/\text{Dy}_2\text{S}_3$ at the magnification of 20,000 x.

The surface morphology of pure Dy_2S_3 and $\text{rGO}/\text{Dy}_2\text{S}_3$ composite thin films is analysed using the FE-SEM technique. FE-SEM images of Dy_2S_3 and $\text{rGO}/\text{Dy}_2\text{S}_3$ at varying two magnifications (10,000 and 20,000x) are displayed in **Figure 5.2**. From the figure, it shows that, the Dy_2S_3 hollow microsphere like particles are uniformly

spread over the surface of the glass substrate. In rGO/Dy₂S₃, **Figure 5.2 (c and d)** shows the rGO sheets stacked and intercalated between the Dy₂S₃ hollow microsphere particles. Also, same morphology on SS substrate observed in **Chapter 3, subsection 3.4A.1.4**. There is no change observed in morphology of Dy₂S₃ and rGO/Dy₂S₃ prepared on SS and glass substrate. The detailed discussion given in **section 3.4A.1, subsection 3.4A.1.4**.

5.2.2.3 FT-IR Study:

The FTIR study of Dy₂S₃ and rGO/Dy₂S₃ composite thin films are given in **Chapter 3, subsection 3.4A.2.2**.

5.2.2.4 Raman Study:

The Raman study of Dy₂S₃ and rGO/Dy₂S₃ composite thin films are given in **Chapter 3, subsection 3.4A.2.6**.

5.2.2.5 EDAX Study:

The EDAX study of Dy₂S₃ and rGO/Dy₂S₃ composite thin films are presented in **Chapter 3, subsection 3.4A.2.4**.

5.2.2.6 XPS Study:

The XPS study of Dy₂S₃ and rGO/Dy₂S₃ composite thin films are given in **Chapter 3, subsection 3.4A.2.5**.

5.2.2.7 BET Study:

The BET study of Dy₂S₃ and rGO/Dy₂S₃ composite thin films are given in **Chapter 3, subsection 3.4A.1.7 and 3.4A.2.8**.

5.2.3: Experimental Setup for Gas Sensor Studies:

A schematic illustration of the experimental setup for the gas sensor is provided in **Chapter 2 (Figure 2.17)**. The gas response characteristics of Dy₂S₃ and rGO/Dy₂S₃ composite were measured using a specially designed home built static gas sensing analysis system. The gas detecting system is made up of an airtight stainless steel gas chamber with a gas-swept volume of 315 cm³, provision for gas inlet and outlet, adjustable contact probe for holding sensor with a heating coil connected to a temperature controller. A computer-controlled Keithley 6514 electrometer, integrated

with a data acquisition system, was connected to the external leads of the sensor element to record the resistance response during the entry and exit of the target gas.

All gas sensing measurement tests were conducted at optimised temperature. Two movable contact probes on the sensor holder were used to hold the sensor element placed inside the airtight gas chamber. The silver paste and conducting gold press contact were used to make probe connections on both ends of the sensor element. For each test gas response measurement, the surface area of the gas sensor that comes into contact with the target gas was kept at 1 cm^2 .

To get a steady state of sensor functioning, implanted sensor element a thermo controller warmed the implanted sensor element was preheated at the rated operating temperature through a thermo controller for 30 min. After calibrating the sensor element, the airtight gas chamber was closed, and in the gas sensor assembly the known volume of target gas was injected with it. A Keithley 6514 electrometer connected with computer control was used to record the variation in the resistance of the sensing element over time. After a steady resistance value was achieved, and then the ambient air was evacuated from the gas chamber to retain initial sensor resistance.

The percentage (%) of gas response (S) was determined using the formula provided in **Chapter 2, (Equation 2.22)**, where R_a and R_g represent the sensor's resistance in air and after gas exposure, respectively. The response time is the time required for the sensing element's resistance to change by 90% of its total resistance after the test gas is introduced. Whereas recovery time is the time required for the sensors resistance to restore to 90% of its original value once the test gas is removed [14].

5.3 NO₂ Gas Sensor Performance Evaluation of Dy₂S₃ and rGO/Dy₂S₃ Composite Thin Films:

5.3.1 Results and Discussion:

5.3.1.1 Effect of Operating Temperature:

The gas sensor obtain maximum response, the operating temperature is a vital parameter. Thus, it's necessary to determine the ideal operating temperature of the Dy₂S₃, the performance of Dy₂S₃ gas sensor is investigate to exposed 100 ppm of NO₂ at different operating temperatures (323 to 473 K). The gas response increases with rising operating temperature. The maximum gas response is obtained at 423 K and

after rise in working temperature the gas response decreased by decreasing gas molecule adsorption on the sensor surface [7]. The obtained maximum gas response of Dy_2S_3 is 23.43% at an optimized operating temperature of 423 K. Which are significantly lower than $\text{rGO/Dy}_2\text{S}_3$ (36.08 %) at RT.

In this case, the rate of the chemical reaction limits the sensor response at low temperatures. However, the diffusion rate of gas molecules restricts it at higher temperatures by the low diffusion depth and began to decrease. The maximum sensor response occurs when the rates of the two processes become equal leading at intermediate temperature. Therefore, in this instance, 423 K is selected as the ideal operating temperature for Dy_2S_3 , as that temperature at which the sensor response reaches its maximum value. As a result, it has been identified that 423 K is the ideal operating temperature for Dy_2S_3 sensors [15, 16].

5.3.1.2 Resistance Stabilization Study:

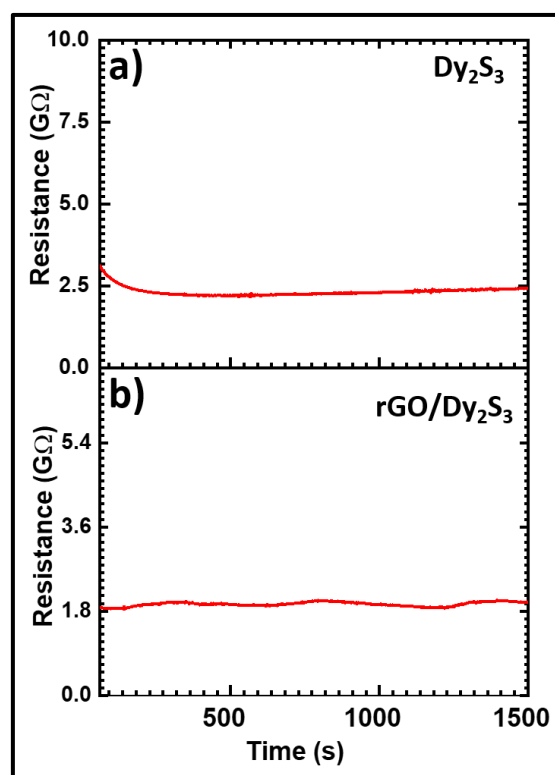


Figure 5.3: Initial resistance stabilization curve of a) Dy_2S_3 and b) $\text{rGO/Dy}_2\text{S}_3$ composite.

To maintain a stable reference resistance level before exposure to the target gas, it is crucial to stabilize sensor element resistance in the ambient atmosphere. Thus, the change in sensor element resistance with time was monitored

before exposure to the target gas. The typical stabilization curves of Dy_2S_3 at 423 K and $\text{rGO/Dy}_2\text{S}_3$ at RT are displayed in **Figure 5.3**. At the beginning of the stabilization period, the resistance of all the sensor elements decreases during the initial 15 min and attain a stable value. The baseline resistances for the Dy_2S_3 at 423 K and $\text{rGO/Dy}_2\text{S}_3$ are 2.5 and 1.8 $\text{G}\Omega$, respectively. Thus, prior to sensing tests, the sensor elements are stabilized for 30 min before exposure to the target gas [17].

5.3.1.3 Selectivity Study:

The Dy_2S_3 and $\text{rGO/Dy}_2\text{S}_3$ sensors are exposed to different gases (NO_2 , SO_2 , Cl_2 , NH_3 , CO , and H_2S for 100 ppm at 423 K and RT to determine the ability to detect specific NO_2 gas. **Figure 5.4** displays the corresponding selectivity responses for different gases. Numerous factors, including operating temperature, the sensors surface catalytic functionality, and the concentration and energy of interference gas, which all influence the selectivity of the sensor.

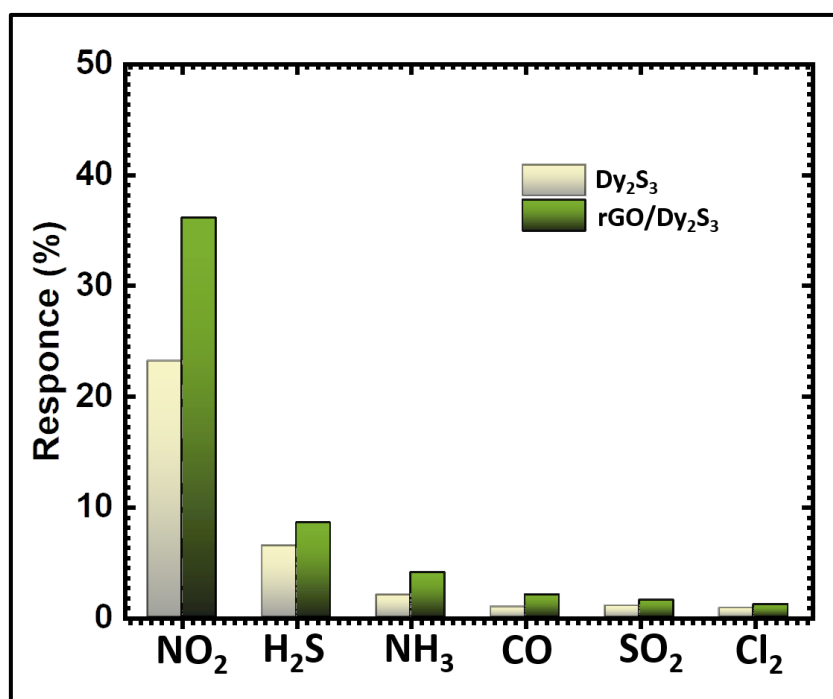


Figure 5.4: The bar chart shows the variation of response of Dy_2S_3 at 423 K, and $\text{rGO/Dy}_2\text{S}_3$ composite sensor at RT for 100 ppm of six different target gases.

The Dy_2S_3 and $\text{rGO/Dy}_2\text{S}_3$ sensors superior selectivity can be attributed to the various interactions that occur between the sensor surface and the adsorbed gas. The $\text{rGO/Dy}_2\text{S}_3$ composite sensor exhibited greater selective response at RT towards NO_2 gas, when compared to the Dy_2S_3 sensor operating at its optimal temperature of 423

K. Furthermore, because of the NO_2 molecules have a stronger electron affinity than other interference gases, they can be easily chemisorbed and accept electrons directly from the sensor surface. This leads to the high selectivity towards NO_2 .

5.3.1.4 Response and Resistance vs Time Transient Study:

As seen in **Figure 5.5 (a and b)**, the resistance vs. time behaviour and gas response transients of Dy_2S_3 at 423 K and $\text{rGO/Dy}_2\text{S}_3$ at RT are examined upon exposure of 100 ppm NO_2 . To determine baseline resistance, the sensor element was maintained at its working temperature for 30 minutes. Subsequently, gaseous NO_2 was systematically injected into the test gas chamber. In the test chamber, NO_2 gas was replaced with air to recover the test sensors baseline resistance.

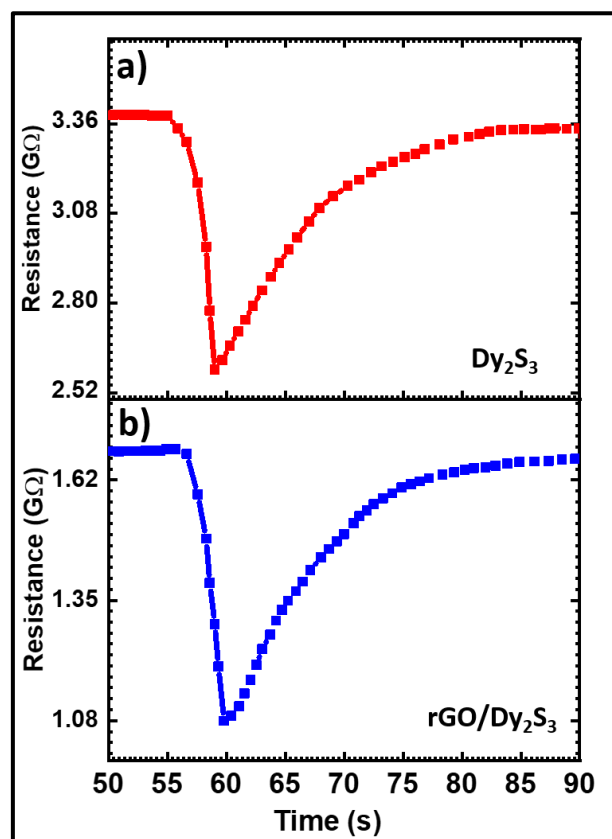


Figure 5.5: Response and resistance vs time transients of a) Dy_2S_3 , and b) $\text{rGO/Dy}_2\text{S}_3$ composite for 100 ppm NO_2 .

When Dy_2S_3 and $\text{rGO/Dy}_2\text{S}_3$ composite sensors are exposed to NO_2 gas, there is an immediate decrease in their resistance. The resistance decreases, which means oxidizing nature of NO_2 gas molecules absorb electrons from the surface [18]. This is confirming the p-type semiconducting behaviour of Dy_2S_3 and $\text{rGO/Dy}_2\text{S}_3$ composite when exposed to NO_2 gas on the gas sensors surface [18, 14]. At RT, $\text{rGO/Dy}_2\text{S}_3$

sensor shows a gas response of 36.08 %, which are significantly higher than Dy₂S₃ sensor (23.43 %).

The higher gas responses of rGO/Dy₂S₃ composite can be attributed to the larger surface area, formation of high surface area mesoporous anchored interconnected rGO sheets morphology which gives enables abundant active gas interaction sites and high adsorption energy mesoporous provide more surface reaction sites to improving NO₂ sensing performance. The decreased Dy₂S₃ gas sensor performance (23.43 %) is attributed to the low specific surface area. The observed gas sensor performances highlight the introduction of optimized concentration of rGO to enhance the as sensor performance of rGO/Dy₂S₃ composite sensor.

5.3.1.5 Sensitivity Study:

The gas responses of Dy₂S₃ and rGO/Dy₂S₃ composite sensors were measured for a range of trace concentrations (1, 10, 50, and 100 ppm) of NO₂ to assess their ability to react minute traces of NO₂. The sensitivity of the sensor is determined using **Equation 2.22 (Chapter 2)** shown in **Figure 5.6 [17]**. In **Figure 5.6 (a and b)**, the Dy₂S₃ and rGO/Dy₂S₃ composite sensors exhibit a significant gas response for different trace concentrations of NO₂. When exposed to varying NO₂ concentrations, the rGO/Dy₂S₃ composite sensors along with pristine Dy₂S₃ exhibit an immediate resistance change, showing a quick response following the introduction of the target analyte and outstanding recovery of sensor resistance after gas removal.

After the removal of NO₂, Dy₂S₃ and rGO/Dy₂S₃ composite sensors exhibit complete recovery of baseline resistance and exhibit linear response behaviour for concentrations between 1 and 100 ppm. The NO₂ gas sensitivity of Dy₂S₃ is increased 2.51 to 23.43% and rGO/Dy₂S₃ is 7.59 to 36.08% as the increasing NO₂ concentration 1.0 to 100 ppm respectively.

The rGO/Dy₂S₃ composite sensors exhibit the largest gas responses at 100 ppm concentration, because the rapid oxidation reaction due to gas molecules covering the more sensor surface at a higher concentration. The higher concentrations over 100 ppm are prevented in the sensor tests because handling higher NO₂ concentrations could lead to occupational hazards.

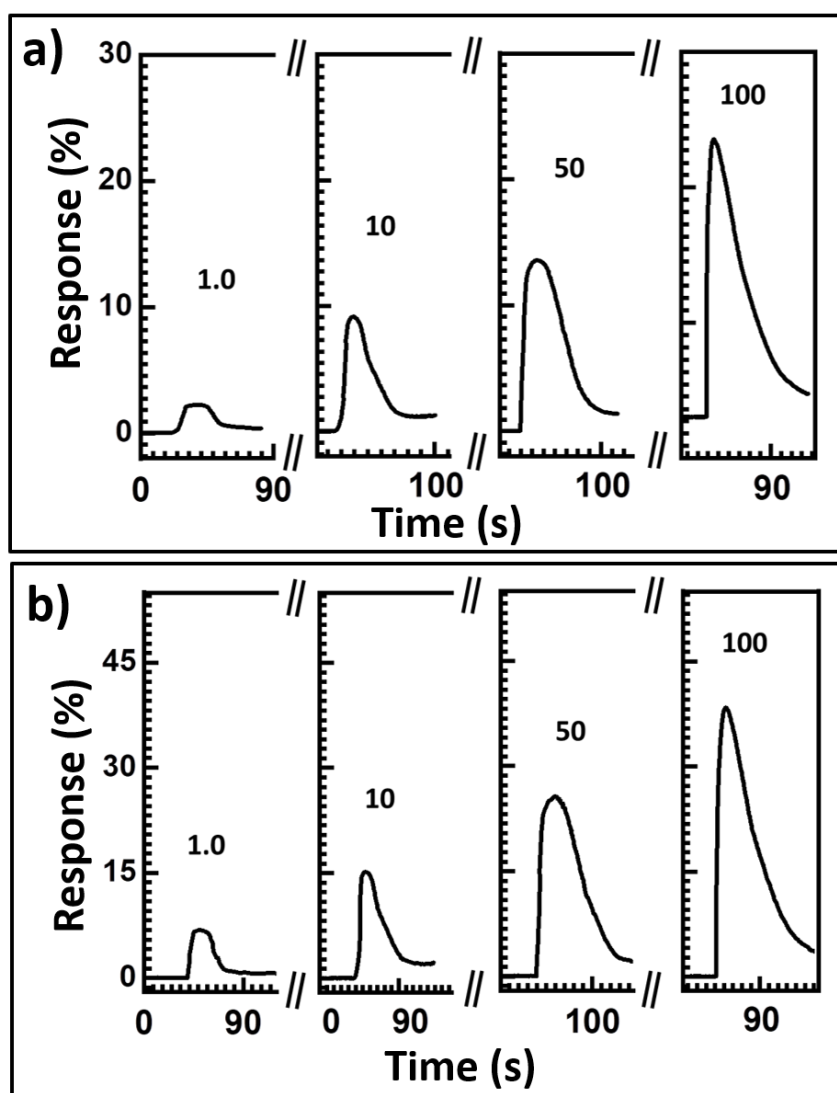


Figure 5.6: The dynamic response curves of a) Dy₂S₃, and b) rGO/Dy₂S₃ composite sensor exposed to various NO₂ concentrations (1.0, 10, 50, and 100 ppm).

5.3.1.6 Long-term Stability Study:

Furthermore, the rGO/Dy₂S₃ composite sensor was kept for an extended period of 40 days to evaluate its long-term stability. The sensors performance was subsequently evaluated after a 10 days interval for exposure to 100 ppm NO₂ as shown in **Figure 5.7**. The rGO/Dy₂S₃ composite sensor shows almost identical responses for the 40 days attributed to its RT operation. After 30 days, the negligible change in sensor performance due to the sensor surface may have become slightly oxidized [19, 20].

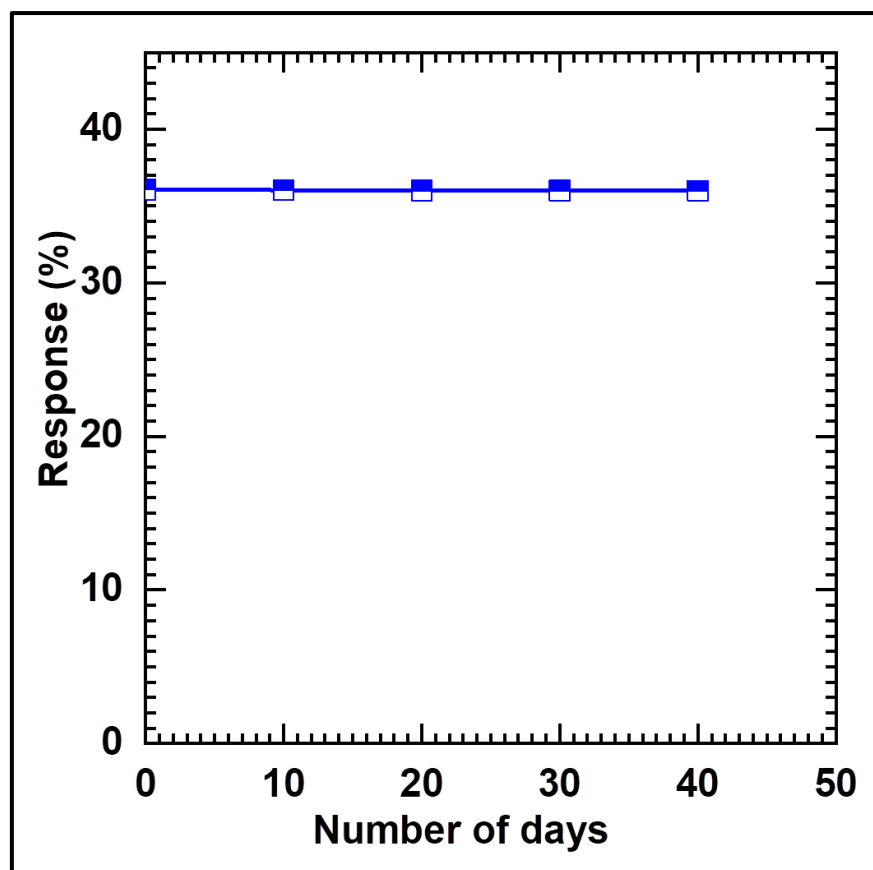


Figure 5.7: Long-term stability of rGO/Dy₂S₃ composite sensor exposed to 100 ppm NO₂ for 40 days (every 10 days).

5.3.1.7 Response and Recovery Time Study:

The rapid sensing capability of Dy₂S₃ and rGO/Dy₂S₃ sensors for detecting NO₂ gas was evaluated by measuring their response and recovery times. The Dy₂S₃ and rGO/Dy₂S₃ composite sensor, interestingly, show response times of less than 20 and 15 s above 1 ppm of NO₂ exposure, indicating their rapid gas sensing capability. The minimal difference in response time of rGO/Dy₂S₃ composite suggests their highly adsorptive nature towards NO₂, attributed to their highly mesoporous, rGO sheet interconnected sheet-like microstructure [21]. Interestingly, the Dy₂S₃ and rGO/Dy₂S₃ composite sensors exhibit complete recovery for all tested concentrations of NO₂, with recovery times under 19 and 17 s for concentrations below 100 ppm.

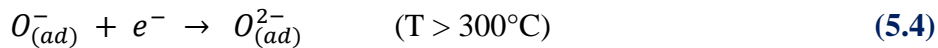
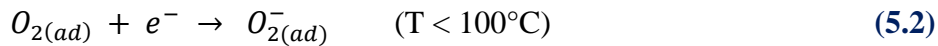
The beneficial effects of rGO intercalation can be observed by the enhanced response of rGO/Dy₂S₃ composite sensor compared to pristine Dy₂S₃. Indicating the NO₂ is adsorbed and desorbs rate on the sensing element surface very quickly. The significantly higher response-recovery characteristic of the rGO/Dy₂S₃ composite

sensor can also be attributed to its abundant chemically interactive mesopores, increased surface area and RT operation.

5.3.1.8 Gas Sensing Mechanism:

The sensing mechanism of chemiresistive sensors depends on the modulation of electrical resistance or resistivity through alterations in charge carrier concentration upon exposure to the target gas. **Figure 5.8** displays a schematic representation of the NO₂ sensing mechanism of rGO/Dy₂S₃ composite sensor. In sensing mechanism, oxygen plays important role. The change in charge carrier concentration is mostly caused by redox reactions between the exposed gas and preadsorbed surface oxygen species or directly on the sensors surface. Typically, these phenomena are temperature-activated processes that require elevated temperatures to occur.

In the case of Dy₂S₃ sensor, the oxygen molecules are adsorbed on the sensor surface at an operating temperature of 423 K and capture the electrons from the semiconductor conduction band, causing its ionosorption in molecules (O_2^-) and atoms (O^- , O^{2-}) forms [22]. The following is an explanation of the adsorption kinematics [23].



Here, the operating temperature is 423 K, Dy₂S₃ sensor is exposed to strong oxidizing NO₂ gas, it reacts with ionosorbed oxygen ions resulting the formation of adsorbed NO₂ (ads) [24] as follows:



In the case of rGO/Dy₂S₃ composite sensor at RT, on the surface of the rGO/Dy₂S₃ composite sensors, O_2^- is the dominant chemisorbed oxygen species and NO₂ sensor reactions as follow:



Above equations, the strongly oxidizing NO_2 gas reacts with $\text{rGO}/\text{Dy}_2\text{S}_3$ sensor surface by trapping electrons from it and reacting either directly with the sensor surface or with chemisorbed oxygen species to form chemisorbed NO_2 species. Consequently, when electron transfer reactions occur, then holes in the p-type $\text{rGO}/\text{Dy}_2\text{S}_3$ sensor increased, leading to raise to an increasing concentration of charge carriers. As a result, $\text{rGO}/\text{Dy}_2\text{S}_3$ sensors resistance drops and its conductivity rises [25-27].

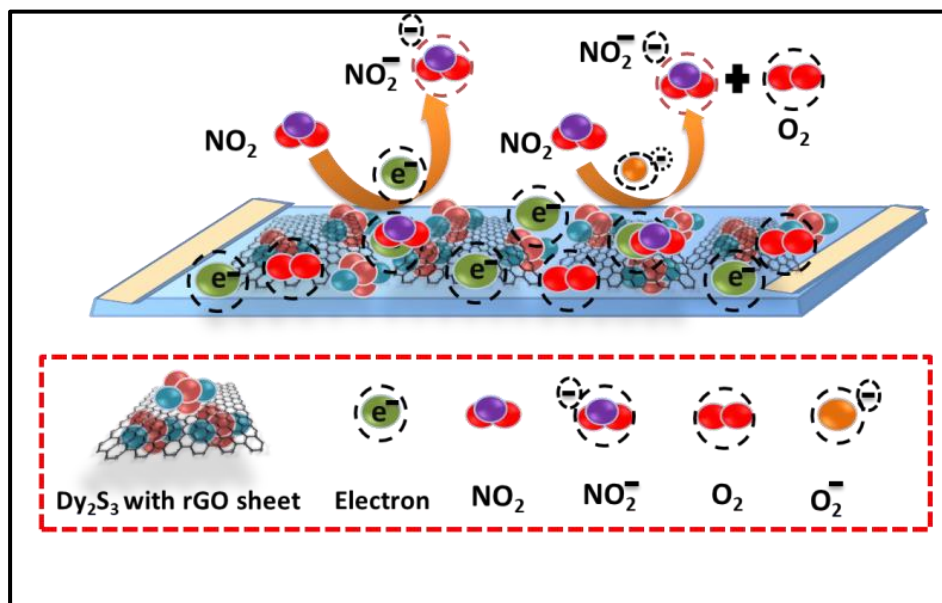


Figure 5.8: Schematic of NO_2 gas sensing mechanism of $\text{rGO}/\text{Dy}_2\text{S}_3$ composite sensors.

5.4 Conclusions:

The simple and cost effective CBD method was employed to successfully synthesized a Dy_2S_3 and $\text{rGO}/\text{Dy}_2\text{S}_3$ composite thin films at 363K with hollow microsphere like structure to sense gaseous NO_2 at 423 K and RT, respectively. The $\text{rGO}/\text{Dy}_2\text{S}_3$ sensor exhibited excellent selectivity (36.08%) towards NO_2 gas amongst the other interfering gases as compared Dy_2S_3 (23.43%) sensor. The rGO composition with Dy_2S_3 significantly affects the NO_2 sensing performance. The introduction of optimized concentration of rGO in Dy_2S_3 it led to increases surface area and hollow microsphere Dy_2S_3 particles with anchored rGO sheets-network morphology which provides plenty of chemically active gas adsorption-desorption sites, superior carrier transportation. These results demonstrate that $\text{rGO}/\text{Dy}_2\text{S}_3$ composite can be used to develop an RT gas sensor with excellent surface adsorptive characteristics for effective NO_2 gas sensing.

5.5 References:

- [1] A. Afroozeh, E. Akbari, P. Yupapin, J. Nanoelectron. Optoe., 14, (2019), 1225-1229.
- [2] S. Feng, F. Farha, Q. Li, Y. Wan, Y. Xu, T. Zhang, H. Ning, Sens., 19, (2019), 3760-3782.
- [3] H. Tang, L. Sacco, S. Vollebregt, H. Ye, X. Fan, G. Zhang, J. Mater. Chem. A, 8, (2020), 24943-24976.
- [4] E. Wongrat, N. Hongstith, D. Wongratanaphisan, A. Gardchareon, S. Choopun, Sens. Actuators B Chem., 172, (2012), 230-237.
- [5] A. Moumen, R. Konar, D. Zappa, E. Teblum, I. Perelshtein, R. Lavi, S. Ruthstein, G. Nessim, E. Comini, ACS Appl. Mater. Interfaces, 13, (2021), 4316-4329.
- [6] <http://www.airqualityontario.com/science/pollutants/nitrogen.php>.
- [7] V. Burungale, R. Devan, S. Pawar, N. Harale, V. Patil, V. Rao, Y. Ma, J. Ae, J. Kim, P. Patil, Mater. Sci.-Pol., 34, (2016), 204-211.
- [8] S. Orzechowska, A. Mazurek, R. Świsłocka, W. Lewandowski, Materials, 13, (2020), 80-100.
- [9] V. Guidia, B. Fabbria, A. Gaiardoa, S. Gherardi, A. Giberti, C. Malagù, G. Zonta, P. Bellutti, Procedia Eng., 120, (2015), 138 -141.
- [10] D. Akinwande, C. Brennan, J. Bunch, P. Egberts, J. Felts, H. Gao, R. Huang, J. Kim, T. Li, Y. Li, K. Liechti, N. Lu, H. Park, E. Reed, P. Wang, B. Yakobson, T. Zhang, Y. Zhang, Y. Zhou, Y. Zhu, Extreme Mech. Lett., 13, (2017), 42-77.
- [11] R. Mas-Balleste, C. Gomez-Navarro, J. Gomez-Herrero, F. Zamora, Nanoscale, 3, (2011), 20-30.
- [12] R. Ashwini, V. Dileepkumar, K. Balaji, R. Viswanatha, C. Ravikumar, C. Srivastava, S. Mysore, SI., 2, (2021), 100125-100133.
- [13] N. Hidayah, W. Liu, C. Lai, N. Noriman, C. Khe, U. Hashim, H. Lee, AIP Conf. Proc., 1892, (2017), 150002-150014.

- [14] S. Navale, A. Mane, G. Khuspe, M. chougule, V. Patil, Synth. Met., 195, (2014), 228-233.
- [15] V. Patil, S. Vanalakar, P. Patil, J. Kim, Sens. Actuators B chem., 239, (2017), 1185-1193.
- [16] S. Bai, K. Zhang, R. Luo, D. Li, A. Chen, C. Liu, J. Mater. Chem., 22, (2012), 12643-12650.
- [17] L. You, Y. Sun, J. Ma, Y. Guan, J. Sun, Y. Du, G. Lu, Sens. Actuators B, 157, (2011), 401-407.
- [18] J. Gunjekar, A. More, C. Lokhande, Sens. Actuators B Chem., 131, (2008), 356-361.
- [19] Y. Qin, L. Wang, X. Wang, Nanotechnology, 29, (2018), 275502-275514.
- [20] J. Kim, J. Lee, Y. Park, J. Kim, A. Mirzaei, H. Kim, S. Kim, Sens. Actuators B 294, (2019), 78-88.
- [21] Y. Qin, R. Zhao, C. Bai, New J. Chem., 44, (2020), 16985-16994.
- [22] J. Lee, J. Gunjekar, Y. Ham, I. Kim, K. Domen, S. Hwang, Chem. Eur. J., 20, (2014), 17004-17010.
- [23] T. Belysheva, L. Bogovtseva, E. Kazachkov, N. Serebryakova, J. Anal. Chem., 58, (2003), 583-587.
- [24] P. Sahay, S. Tewari, S. Jha M. Shamsuddin, J. Mater. Sci., 40, (2005), 4791-4793.
- [25] K. Wetchakun, T. Samerjai, N. Tamaekong, C. Liewhiran, C. Siri Wong, V. Kruefu, A. Wisitsoraat, A. Tuantranontb, S. Phanichphant, Sens. Actuators B, Chem., 160, (2011), 580-591.
- [26] V. Chaudhary and A. Kaur, Polym. Int., 64, (2015), 1475-1481.
- [27] V. Chaudhary and A. Kaur, RSC Adv., 6, (2016), 95349-95357.

CHAPTER-6

**Fabrication and Performance Evaluation of
FSSASCs Devices based on rGO/Dy₂S₃ and
rGO/Dy₂Se₃ Thin Films**

CHAPTER-6

Fabrication and Performance Evaluation of FSSASCs Devices Based on rGO/Dy₂S₃ and rGO/Dy₂Se₃ Thin Films

Sr. No.	Title	Page No.
6.1	Introduction	140
6.2	Experimental Details	141
	6.2.1 Introduction	141
	6.2.2 Electrode Preparation	141
	6.2.3 Preparation of MnO ₂ Electrode	141
	6.2.4 Preparation of Polymer Gel Electrolytes	141
	6.2.5 Fabrication of FSSASCs Devices	142
	6.2.6 Electrochemical Characterizations of FSSASCs Devices	143
6.3	Results and Discussion	143
	6.3.1 Structural and Elemental Analyses of MnO ₂ Thin Film Electrode	143
	6.3.2 Electrochemical Study of MnO ₂ Thin Film Electrode	144
	6.3.3 Electrochemical Characterization of Flexible Solid-State Asymmetric Supercapacitor (FSSASCs) Devices (MnO ₂ /rGO/Dy ₂ S ₃)	145
	6.3.4 Electrochemical Characterization of Flexible Solid-State Asymmetric Supercapacitor (FSSASCs) Devices (MnO ₂ /rGO/Dy ₂ Se ₃)	148
6.4	Conclusions	152
6.5	References	154

6.1 Introduction:

Technological advancement has accelerated energy consumption. As a result, different energy storage devices are required for various instruments in modern technology such as healthcare, intelligent devices, micro-robotics, smartphones, flexible touchscreen displays, electronic skin, implantable medical devices, etc. Because of this, the need for flexible energy storage devices has increased and attracted tremendous research interest [1, 2]. Together with secondary batteries, flexible SCs have received a lot of attention due to their rapid charging, robust mechanical flexibility, long life, light weight, high operating voltage, superior safety, ability to provide required power density in a wide range of temperatures, and nearly constant performance even with mechanical deformation states [3-5]. Considering the above qualities of flexible SCs, the implementation of flexible SCs in wearable and flexible appliances has increased in the recent past. Therefore, the fabrication of flexible SCs has been an attractive research topic in recent years.

In recent years, researchers have developed different materials using rare earth metal chalcogenides (REMC) for electrochemical charge storage. In energy storage systems, the specific capacitance (C_s) of REMC electrode materials is relatively low compared to other transition metal chalcogenides because of their characteristics, such as their lower surface area and larger molecular weight. Therefore, the REMC has been composited with carbonaceous materials to overcome these limitations. The composition with carbon allotropes modifies surface area, improves electrical conductivity, and exposes more active sites to the electrolyte for redox reactions. Carbon composite also improves ions-diffusion rate and overall cycle life. Considering this, flexible supercapacitors have been made with REMC material composites.

The rare earth metals based electrode chalcogenides can be operated in the wide potential window. Therefore, the combination of polymeric gel electrolytes with these electrode materials will be a good contribution to the flexible solid-state asymmetric supercapacitor (FSSASCs) devices. Among transition metal oxides, for a SC, manganese oxide is one of the most durable and robust electrodes which has been found to have good efficiency, high theoretical C_s ($\sim 1371 \text{ F g}^{-1}$), multiple oxidation states, low cost, environmental friendliness, natural abundance, wide potential window, easy to prepare, long term performance, high storage capacity and good

corrosion stability which make it most promising electrode material for fabrication of the FSSASCs device.

In this chapter, the FSSASCs device assembled with configuration rGO/Dy₂S₃//MnO₂ with ionically conducting PVA–LiClO₄ gel as an electrolyte as well as a separator. Thin films of MnO₂ and rGO/Dy₂S₃ with an area of 5×5 cm² were used as positive (cathode) and negative (anode), respectively. Another FSSASCs device is fabricated using thin films of rGO/Dy₂Se₃ and MnO₂ were used as negative (anode) and positive (cathode) electrodes, respectively in rGO/Dy₂Se₃//MnO₂ FSSASCs device with PVA–LiClO₄ as an electrolyte. This chapter deals with the fabrication and electrochemical performance evaluation of FSSASCs devices with configuration rGO/Dy₂S₃//MnO₂ and rGO/Dy₂Se₃//MnO₂.

6.2 Experimental Details:

6.2.1 Introduction:

The present section describes the electrode preparation (MnO₂, rGO/Dy₂S₃, and rGO/Dy₂Se₃), polymer gel electrolyte (PVA–LiClO₄) preparation and fabrication of MnO₂//rGO/Dy₂S₃ and MnO₂//rGO/Dy₂Se₃ FSSASCs devices.

6.2.2 Electrode Preparation:

The CBD method was employed to prepare rGO/Dy₂S₃, and MnO₂ thin films, and SILAR method to prepare rGO/Dy₂Se₃ thin film on flexible SS substrates. The optimized preparative parameters of rGO/Dy₂S₃, and rGO/Dy₂Se₃ thin film electrodes are described in **Chapters III and IV**, respectively.

6.2.3 Preparation of MnO₂ Electrode:

The thin film of MnO₂ required to fabricate an FSSASCs device was deposited according to the procedure reported earlier [6, 7]. In a typical synthesis of MnO₂ thin film, 2.5 mL of methanol was added dropwise into 100 mL of 0.07 M KMnO₄ aqueous solution and were mixed with vigorously magnetic stirring. Then the solution was kept at 4 h at room temperature. After 4 h, the brownish coloured MnO₂ thin film was deposited on the surface of the substrate.

6.2.4 Preparation of Polymer Gel Electrolytes:

The FSSASCs device was assembled using PVA–LiClO₄ gel electrolyte. To prepare PVA based solid-state gel electrolyte, 4 g of PVA was dissolved in 40 mL

DDW at a temperature of 354 ± 05 K with constant stirring for 4 h to form a transparent and viscous solution, followed by gradual addition of 1 M LiClO_4 solution [8]. This solution was constantly stirred for 6 h to form a uniform gel electrolyte and was used for FSSASCs device fabrication.

6.2.5 Fabrication of FSSASCs Devices:

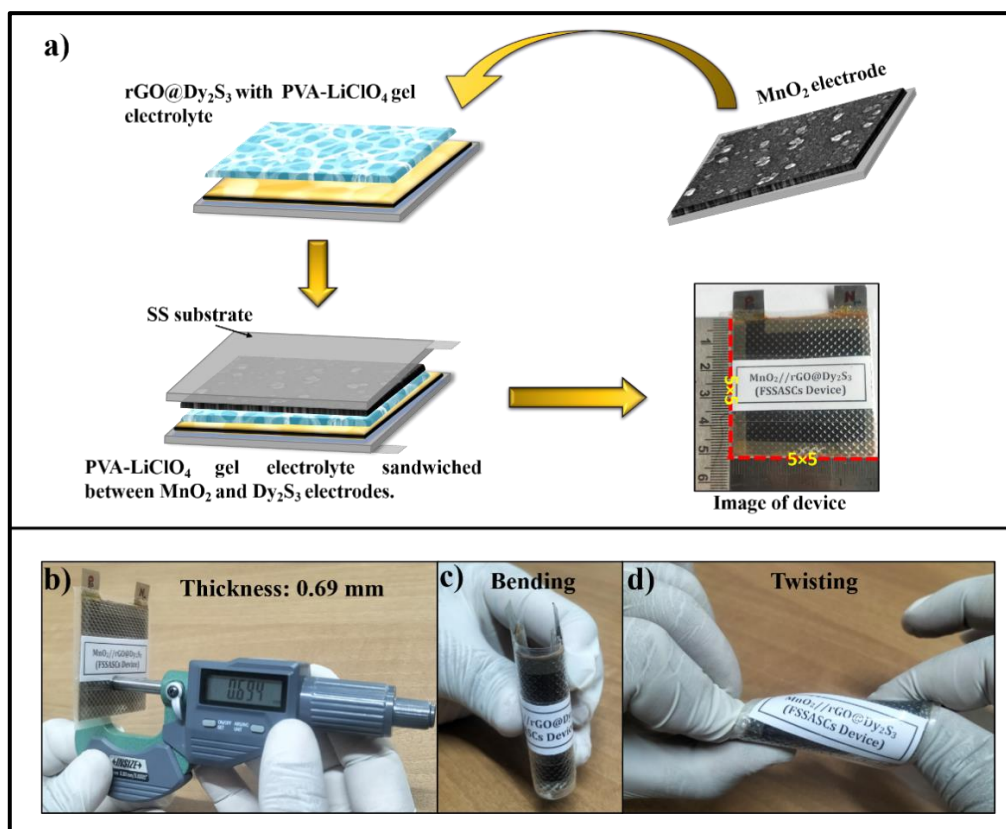


Figure 6.1: a) The schematic of flexible solid state $\text{Dy}_2\text{S}_3//\text{MnO}_2$ FSSASCs device formation, b) the thickness of the FSSASCs device measured by the digital micrometer, c and d) flexibility (physical bending and twisting) of FSSASCs device.

The FSSASCs device assembled with configuration $\text{rGO}/\text{Dy}_2\text{S}_3//\text{MnO}_2$. Thin films of MnO_2 and $\text{rGO}/\text{Dy}_2\text{S}_3$ with an area of $5 \times 5 \text{ cm}^2$ were used as positive (cathode) and negative (anode), respectively. The schematic of FSSASCs device formation is presented in **Figure 6.1 (a)**. The PVA- LiClO_4 gel electrolyte was sandwiched between them. After sealing using a plastic strip, the FSSASCs device was kept under pressure of 0.5 tons for 30 min. An electrolyte in gel form reduces the evaporation rate of the electrolyte, leading to improvement in the life span of the asymmetric device. **Figure 6.1 (b)** shows the thickness of the FSSASCs device (0.69 mm) and **Figure 6.1 (c and d)** shows the flexibility (physical bending and twisting) of

FSSASCs device. A similar process was followed to assemble rGO/Dy₂Se₃//MnO₂ FSSASCs device.

6.2.6 Electrochemical Characterization of FSSASCs Devices:

To optimize operating voltage of FSSASCs devices, CV and GCD studies of FSSASCs devices were carried out at various scan rates and current densities, respectively. The S_E (Wh kg⁻¹) and S_P (W kg⁻¹) of FSSASCs device were calculated from **Equations 1.4 and 1.5**, respectively. To evaluate flexible nature of FSSASCs device, CV curves were repeated at different bending positions. The stability study of FSSASCs devices performed for 5000 cycles using GCD technique.

6.3 Results and Discussion:

6.3.1 Structural and Elemental Analyses of MnO₂ Thin Film Electrode:

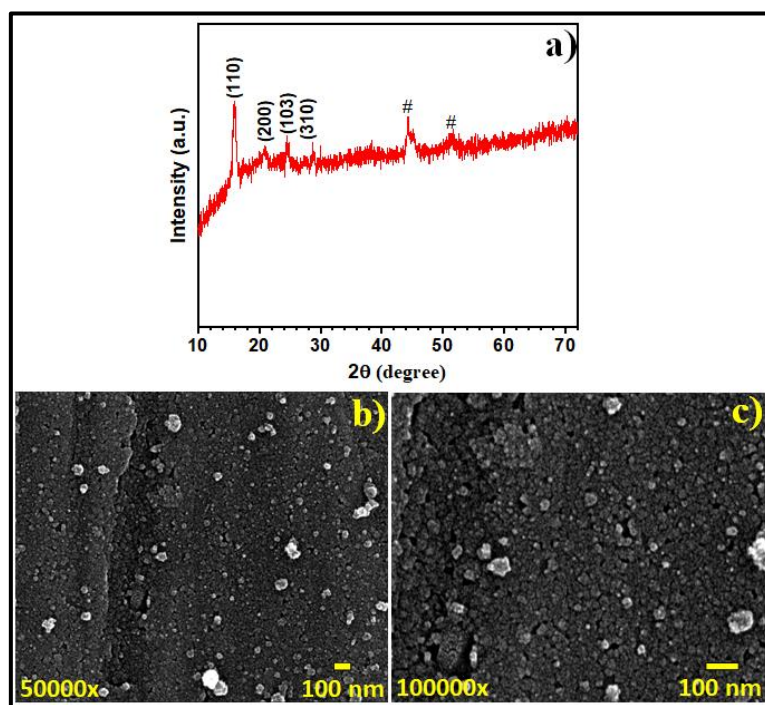


Figure 6.2: a) The XRD pattern, and SEM images at b) 50000x, and c) 100000x magnifications of MnO₂ thin film.

The XRD pattern of MnO₂ thin film material is presented in **Figure 6.2 (a)**. The diffraction peaks correspond to (110), (200), (103), and (310) planes of the tetragonal phase of α -MnO₂ (JCPDS card no. 44-0141) [9]. The lower intensity of diffraction peaks for MnO₂ indicates the nanocrystalline nature. The peaks of SS substrate are marked with symbol #.

In the thin film, specific capacitance (C_s) depends on the surface morphology of the electrode [10]. **Figure 6.2 (b and c)** show SEM images of MnO_2 thin films at a magnification of 50000x and 100000x, respectively. The surface morphology of MnO_2 nanoparticles is interconnected and spread over SS substrate, as depicted in **Figure 6.2 (b and c)**. Such nanoparticles type morphology is helpful to enhance the electrochemical performance [11].

6.3.2 Electrochemical Study of MnO_2 Thin Film Electrode:

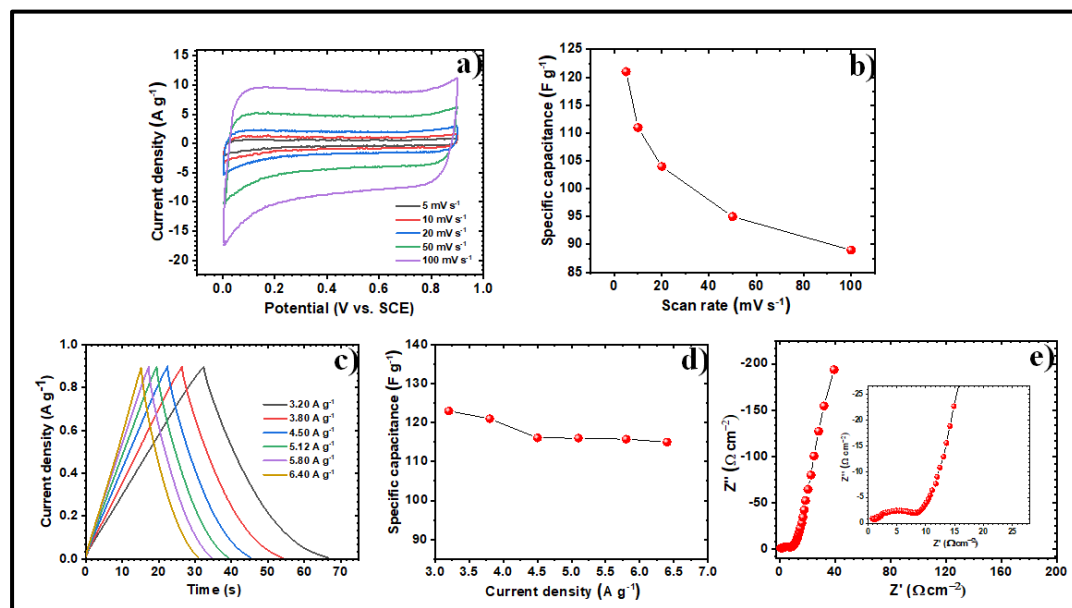


Figure 6.3: a) The CV curves at various scan rates from 5-100 mV s^{-1} , b) plot of specific capacitance at various scan rates, c) the GCD curves at various current densities from 3.20-6.40 A g^{-1} , d) plot of specific capacitance at various current densities, and e) Nyquist plot of MnO_2 electrode in 1 M LiClO_4 electrolyte.

The electrochemical study of MnO_2 electrode was carried out within a potential window of 0 to 0.9 V/SCE in 1 M LiClO_4 electrolyte. The CV curves of MnO_2 electrodes at various scan rates are shown in **Figure 6.3 (a)**. The plot of C_s versus different scan rates is presented in **Figure 6.3 (b)**. The MnO_2 thin film exhibits C_s of 121 F g^{-1} at a scan rate of 5 mV s^{-1} . To determine C_s of MnO_2 thin film, The GCD curves of MnO_2 thin film at different current densities at 3.20-6.40 A g^{-1} are shown in **Figure 6.3 (c)**. The C_s of 123 F g^{-1} is obtained at 3.20 A g^{-1} current density. **Figure 6.3 (d)** shows the variation of C_s with current densities. The Nyquist plot of MnO_2 thin film in the frequency range between 0.01 Hz to 0.1 MHz is depicted in **Figure 6.3 (e)**, and the inset shows an enlarged view at higher frequencies. The

Nyquist plot indicates a tiny semicircle at the high frequency domain, credited to the charge transfer process. The R_s ($0.77 \Omega \text{ cm}^{-2}$) was determined from the X-axis intercept of the Nyquist plot. The charge transfer resistance (R_{ct}) for MnO_2 is $8.2 \Omega \text{ cm}^{-2}$. In the lower frequency range, the straight line nature is attributed to the ion diffusion in the electrolyte as the Warburg resistance.

6.3.3 Electrochemical Characterization of Flexible Solid-State Asymmetric Supercapacitor (FSSASCs) Devices ($\text{MnO}_2/\text{rGO}/\text{Dy}_2\text{S}_3$):

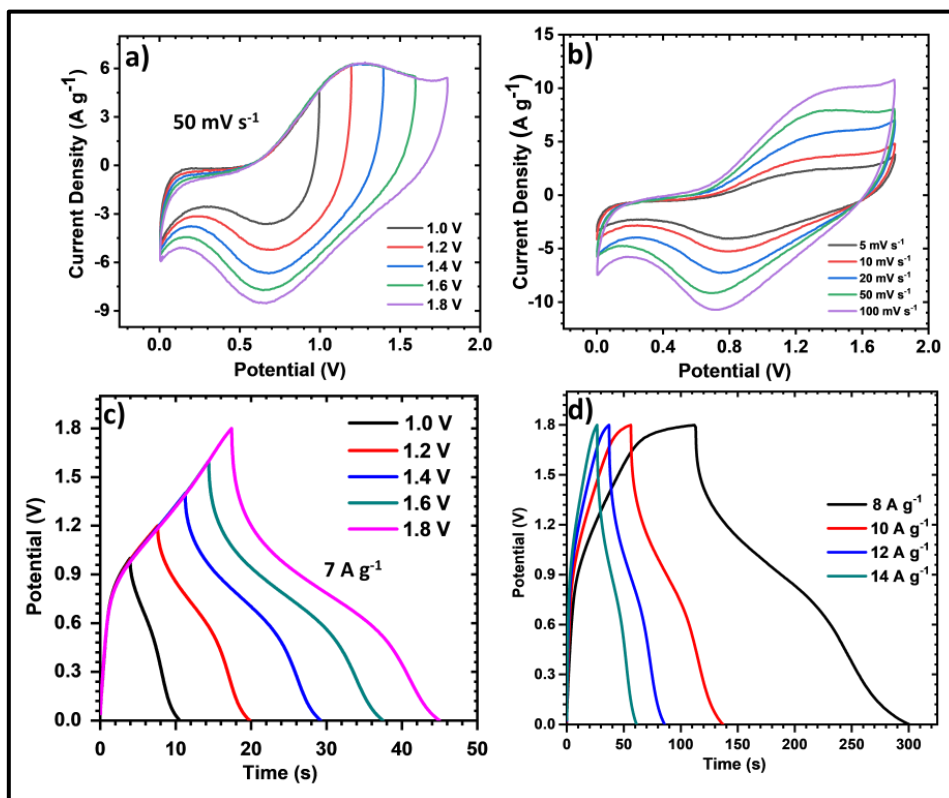


Figure 6.4: a) The CV curves at different potential windows, b) the CV curves at different scan rates, c) the GCD plots at different potential windows and d) the GCD plots at different current densities.

The FSSASCs device was fabricated by employing $\text{rGO}/\text{Dy}_2\text{S}_3$ electrode as an anode and MnO_2 as a cathode (Figure 6.1). To identify the optimal potential voltage of the FSSASCs device, the CV plots in different operating potentials between 0 to +1.8 V are illustrated in Figure 6.4 (a). The value of C_s mainly depends on the operating voltage and area enclosed under the CV curve. The FSSASCs device exhibited good capacitive performance due to the symmetric shape of the CV curves at optimized operating voltage +1.8 V at a scan rate of 50 mV s^{-1} . As no visible water splitting is observed, it can be concluded that FSSASCs device can be charged up to

+1.8 V. The C_s of FSSASCs device calculated from CV profiles was observed 116 F g^{-1} at 5 $mV s^{-1}$ scan rate, respectively. Similarly, the applicable operating potential (0 to +1.8 V) selection of FSSASCs device for GCD carried out from constant charging current density of 7 $A g^{-1}$ is shown in **Figure 6.4 (c)**. CV and GCD plots with nearly symmetric nature indicate good reversibility and charge storage nature of the FSSASCs device.

The plots confirm optimum operating potential is +1.8 V for the FSSASCs device. The CV curves of the FSSASCs device at different sweep rates from 5 to 100 $mV s^{-1}$ are shown in **Figure 6.4 (b)**. The GCD curves of the FSSASCs device at various charging current densities from 8-14 $A g^{-1}$ within the operating potential window of 0 to 1.8 V are illustrated in **Figure 6.4 (d)**. The C_s of FSSASCs device is 91 F g^{-1} at a current density of 8 $A g^{-1}$. As the current density increased, the discharging time (t_d) of FSSASCs device gradually reduced due to insufficient electrode-electrolyte interactions.

The electrochemical cyclic stability for FSSASCs device is examined at 9 $A g^{-1}$ over 5000 cycles as demonstrated in **Figure 6.5 (a)**. The FSSASCs device exhibited capacitance retention of 85% and coulombic efficiency of 95% over 5000 cycles. These cycles retained similar shapes and showed approximately similar discharge times, indicating excellent electrochemical stability of the hybrid device. The EIS is one of the better techniques to evaluate resistive parameters of FSSASCs device. The Nyquist plot and its fitted data of FSSASCs device are presented in **Figure 6.5 (b)**. The starting point and high frequency region of semicircle representing R_s and R_{ct} and observed values of R_s and R_{ct} are 0.9 Ωcm^{-2} and 16.60 Ωcm^{-2} , respectively.

The higher value of R_{ct} is due to the gel form of PVA-LiClO₄ electrolyte, which affects the kinetics of the electrochemical reaction. The lower value of R_s is always beneficial for good electrochemical performance. The equivalent circuit of best data fitted is illustrated as an inset of **Figure 6.5. (b)**. The fitted circuit consists of R_s , R_{ct} , W , and CPE [12, 13]. Correspondingly, the values of W and CPE evaluated from the equivalent circuit are 0.0113 $m\Omega$ and 0.64 F. Performance of the positive and negative electrodes is a key factor for the electrochemical capacitors in commercial applications.

To measure the flexible nature of FSSASCs device, the C_s were measured at various bending angles ranging between 0 to 160°. The FSSASCs device showed 92% capacitive retention at a bending angle of 160°. Measured CV curves at various bending angles are shown as an inset of **Figure 6.5 (c)**. From the CV graphs at various bending angles, the unbroken structural integrity of the FSSASCs device is observed.

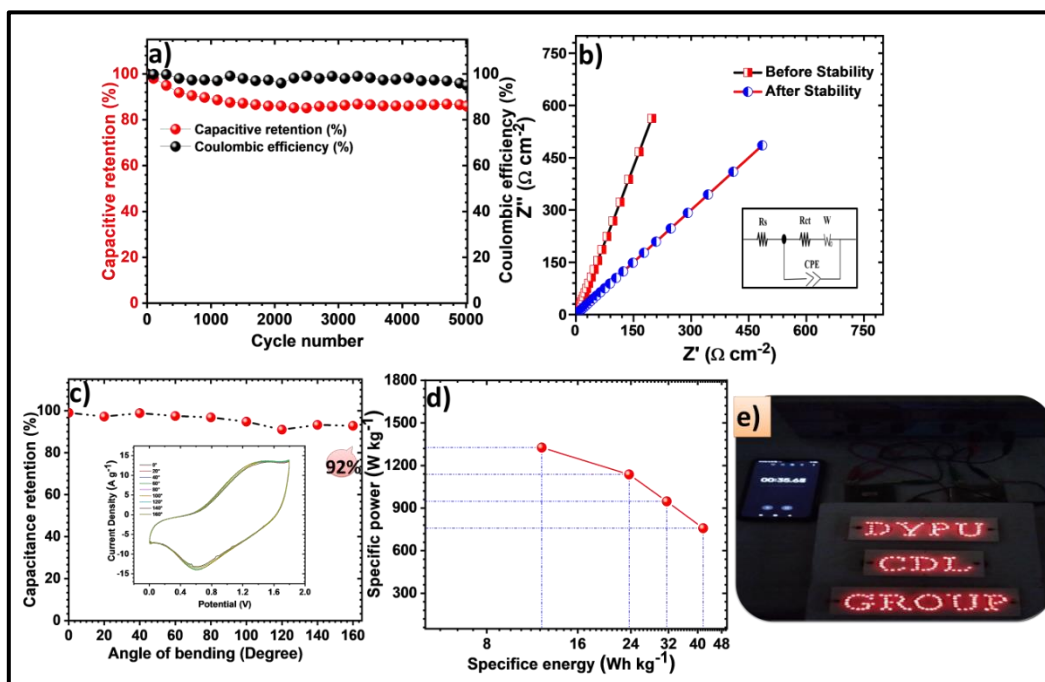


Figure 6.5: a) The specific capacitance retention and Coulombic efficiency of $\text{MnO}_2//\text{rGO}/\text{Dy}_2\text{S}_3$ FSSASCs device, b) the Nyquist plot; before and after stability, (inset image shows the fitted equivalent electrical circuit), c) capacitance retention of the device at different bending angles (inset displays CV curves at varying bending angles), d) Ragone plot of $\text{MnO}_2//\text{rGO}/\text{Dy}_2\text{S}_3$ FSSASCs device, and e) The practical application of two series connected $\text{MnO}_2//\text{rGO}/\text{Dy}_2\text{S}_3$ FSSASCs devices to illuminate 211 red LEDs.

The Ragone plot of $\text{rGO}/\text{Dy}_2\text{S}_3//\text{MnO}_2$ FSSASCs device shown in **Figure 6.5 (d)** indicates that the FSSASCs device can deliver energy at different powers and, hence, have versatile applications. The obtained S_E (40 Wh kg^{-1}) and S_P (1.331 kW kg^{-1}) of $\text{rGO}/\text{Dy}_2\text{S}_3//\text{MnO}_2$ FSSASCs device are comparable to previously reported ASC devices. Furthermore, the performance of two serially connected FSSASCs devices was demonstrated by lighting a panel of 201 red LEDs. After charging for 30 s, these FSSASCs devices can efficiently illuminate the LEDs panel for 60 s

efficiently. The initial power dissipated through $\text{MnO}_2/\text{rGO}/\text{Dy}_2\text{Se}_3$ FSSASCs devices was 0.59 mW cm^{-2} . A photograph of FSSASCs devices while discharging is shown in **Figure 6.5 (e)**. To increase S_E and current output, the assembly of devices can be used according to the requirement.

6.3.4 Electrochemical Characterization of Flexible Solid-State Asymmetric Supercapacitor (FSSASCs) Devices ($\text{MnO}_2/\text{rGO}/\text{Dy}_2\text{Se}_3$):

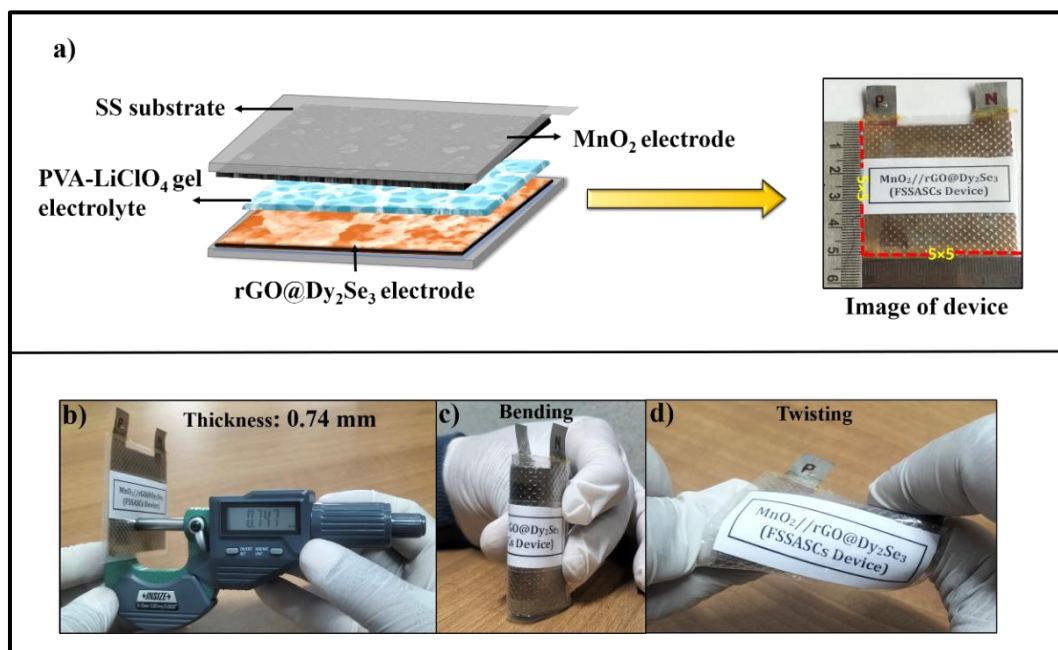


Figure 6.6: The procedure for fabrication of a) $\text{rGO}/\text{Dy}_2\text{Se}_3/\text{MnO}_2$ FSSASCs device, b) the thickness of the FSSASCs device measured by the digital micrometer, c and d) flexibility (physical bending and twisting) of FSSASCs device.

Thin films of $\text{rGO}/\text{Dy}_2\text{Se}_3$ and MnO_2 were used as negative (anode) and positive (cathode) electrodes, respectively in $\text{rGO}/\text{Dy}_2\text{Se}_3/\text{MnO}_2$ FSSASCs device. The electrochemical analysis of two electrode systems, $\text{rGO}/\text{Dy}_2\text{Se}_3/\text{MnO}_2$ FSSASCs device was carried out within the range of 0 to 1.6 V at different scan rates. **Figure 6.6 (a)** shows the procedure for fabricating an FSSASCs device and the thickness of the FSSASCs device, which is 0.74 mm, as shown in **Figure 6.6 (b)** and **Figure 6.6 (c and d)** present the flexibility (physical bending and twisting) of the fabricated FSSASCs device. The balance of charges stored on individual electrodes plays a crucial role in achieving a higher operating voltage range. To identify an appropriate operating potential, the CV plots of FSSASCs device at different operating potentials ranging from 1.1 to 1.6 V were measured (**Figure 6.7 (a)**). The CV plot at 1.6 V

shows a symmetric quasi-rectangular nature due to both EDLC and pseudo-capacitive materials.

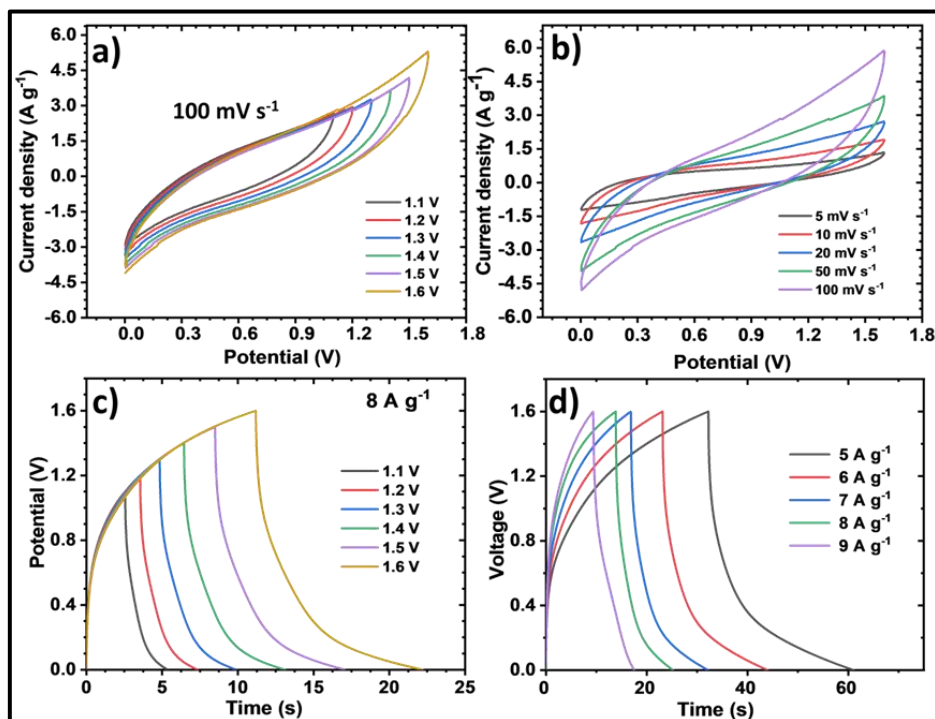


Figure 6.7: Electrochemical characterization of rGO/Dy₂Se₃//MnO₂ FSSASCs device; a) the CV curves at different potentials, b) the CV curves at different scan rates, c) the GCD plots at different potentials, and d) the GCD curves at different current densities.

The GCD profiles of the FSSASCs device measured at various cell potentials from 1.1 to 1.6 V at a current density of 8 A g⁻¹ are shown in **Figure 6.7 (c)**. The maximum time of charge-discharge indicates more charge storage at a potential of 1.6 V, and the symmetric nature of the GCD plot suggests excellent charge storage behaviour of FSSASCs device. The potential of the FSSASCs device was fixed at 1.6 V. The CV curves measured at various scan rates (5 to 100 mV s⁻¹) are shown in **Figure 6.7 (b)**. The similar shape of CV plots at all scan rates suggests good reversibility of the FSSASCs device. The FSSASCs device achieved C_s of 107 F g⁻¹ at a scan rate of 5 mV s⁻¹. **Figure 6.8 (a)** presents calculated C_s values at different scan rates. The GCD analysis of the FSSASCs device was carried out at various current densities from 5 to 9 A g⁻¹ (**Figure 6.7 (d)**). The FSSASCs device exhibits C_s of 102 F g⁻¹ at 5 A g⁻¹ current density. The C_s of the device decreased compared to single electrodes due to ion diffusion restrictions in the gel electrolyte. The variation

in calculated C_s values with the applied current densities (5 to 9 A g^{-1}) is presented in **Figure 6.8 (b)**.

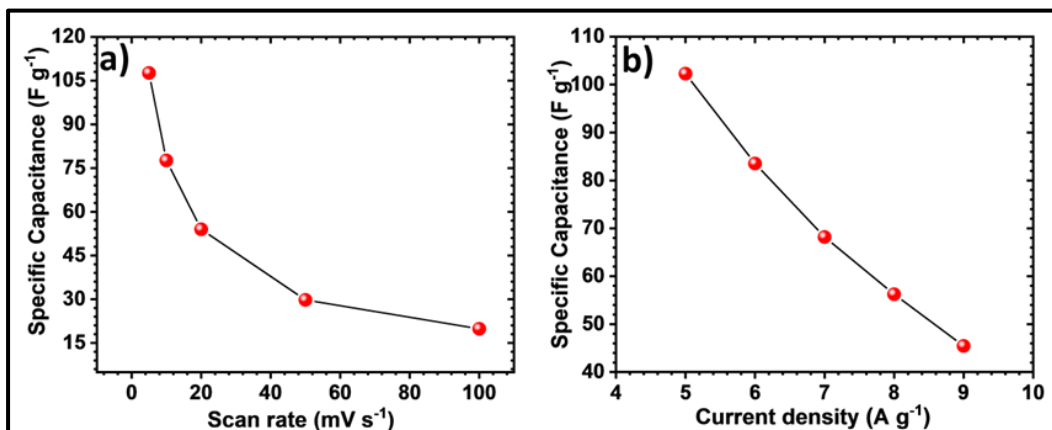


Figure 6.8: The variation of C_s of FSSASCs device a) with different scan rates, b) with different current densities.

Cyclic stability plays a critical role in deciding the applicability of a SC. To evaluate the cyclability of the FSSASCs device, the GCD measurements were conducted over 5000 cycles at a current density of 8 A g^{-1} . The FSSASCs device shows 88 % capacitance retention (**Figure 6.9 (a)**). The better stability of the device under various GCD cycles is attributed to the binder less preparation of the electrodes and rGO composition.

The EIS technique was utilized to analyse charge transport characteristics at the electrode/electrolyte interface of the device. **Figure 6.9 (b)** shows Nyquist plots of the FSSASCs device before and after the stability study. These plots show a similar shape with slightly increased resistance. The simulated equivalent electrical circuit is displayed as an inset image in **Figure 6.9 (b)**. The fitted circuit includes four main components, such as R_s , R_{ct} , CPE, and W , respectively. The observed R_s , R_{ct} , CPE, and W are $0.095 \, \Omega \text{ cm}^{-2}$, $14 \, \Omega \text{ cm}^{-2}$, 0.64 F , and $0.011 \text{ m}\Omega$, respectively. After 5000 cycles, these values changed to $0.099 \, \Omega \text{ cm}^{-2}$ (R_s), $34 \, \Omega \text{ cm}^{-2}$ (R_{ct}), 0.67 F (CPE), and $0.009 \text{ m}\Omega$ (W). The gel form of the electrolyte (PVA- LiClO_4) gives a higher value of R_{ct} [14].

Portable consumer electronics, such as wearable and bendable appliances, are in demand in modern society. Therefore, the flexibility study is more critical for commercial level devices. The FSSASCs device retained 91% capacitive retention after a 160° bending angle, which suggests the better flexibility of the device. The CV

measurements of the FSSASCs device at different bending positions from 20° to 160° are shown in the inset of **Figure 6.9 (c)**. It suggests that when the device is folded in various bending positions, the structural integrity and capacitive performance of the device are maintained. The photographs of FSSASCs device at various bending positions are provided in **Figure 6.10**.

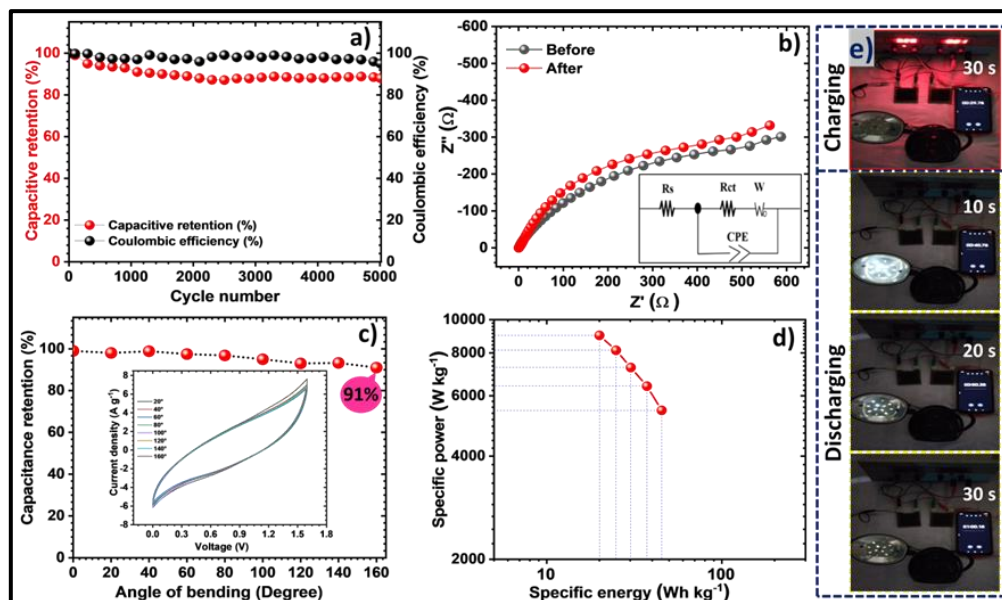


Figure 6.9: a) The specific capacitance retention and Coulombic efficiency of FSSASCs device, b) the Nyquist plot; before and after stability, (inset image shows the fitted equivalent electrical circuit), c) capacitance retention of the device at various bending angles (inset shows CV curves at different bending angles), d) Ragone plot of FSSASCs device, and e) The practical application of two series connected rGO/Dy₂Se₃/MnO₂ FSSASCs devices to illuminate table lamp of 11 white LEDs.

For the FSSASCs device, the specific energy is a crucial factor demonstrating the application of rGO/Dy₂Se₃ composite. **Figure 6.9 (d)** shows the Ragone plot of the FSSASCs device, delivering a maximum S_E of 45 Wh kg^{-1} at the S_P of 9 kW kg^{-1} . The measured S_E and S_P values of the FSSASCs device are compared to those of other previously reported carbon-based supercapacitors. Such as, AC//QC/rGO ASC (5.68 mWh cm^{-3} at 98.8 mW cm^{-3}) [15], SRGO//NiCo₂Se₄/rGO (66.2 Wh kg^{-1} at 1500 W kg^{-1}) [16], CuS//CuSe₂@rGO (28.3 Wh kg^{-1} at 1538 W kg^{-1}) [14], AC//NiO/RGO (32.5 Wh kg^{-1} at 375 W kg^{-1}) [17], (G-SWCNHs)//NiCo₂S₄@rGO (60.9 Wh kg^{-1} at 1.4 kW kg^{-1}) [18], AC//Ni_{1.64}Co_{2.40}S₄/rGO (30.4 Wh kg^{-1} at 10 kW kg^{-1}) [19], rGO//Co₃V₂O₈/rGO (28.36 Wh kg^{-1} at 400 W kg^{-1}) [20]. Among the

reported ASC devices, present FSSASCs device achieved moderate S_E without significant power depletion.

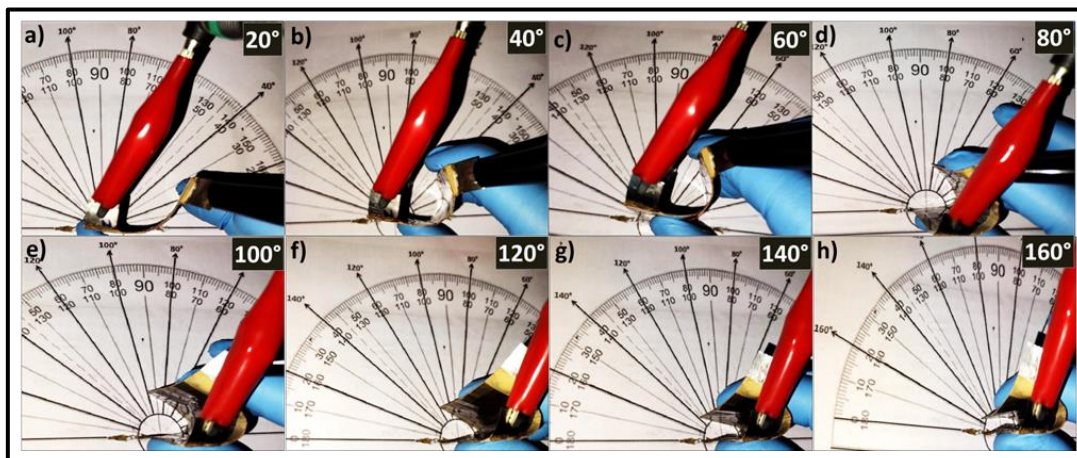


Figure 6.10: The photographs of various bending positions of FSSASCs device a) 20°, b) 40°, c) 60°, d) 80°, e) 100°, f) 120°, g) 140°, and h) 160°.

Furthermore, as a demonstration, two serially connected assembly FSSASCs devices light up a table lamp. After 30 s of charging, two FSSASCs devices can light up the table lamp for 60 s. Initially, the two series connected FSSASCs devices capable of delivering power of 0.41 mW cm^{-2} for 60 s of discharge. The practical application of two series connected $\text{rGO/Dy}_2\text{Se}_3/\text{MnO}_2$ FSSASCs devices to illuminate table lamp of 11 white LEDs shown in **Figure 6.9 (e)**. In this work, low-cost, chemically synthesized electrode materials with diverse energy storage properties have opened the door to extending the features of flexible supercapacitors in a wide range of practical flexible device applications. **Figure 6.10** shows the photographs of various bending positions of FSSASCs device.

6.4 Conclusions:

In summary, $\text{rGO/Dy}_2\text{S}_3/\text{MnO}_2$ FSSASCs device was assembled using anode and cathode electrodes such as $\text{rGO/Dy}_2\text{S}_3$ and MnO_2 with PVA-LiClO_4 gel electrolyte. In the same way, $\text{rGO/Dy}_2\text{Se}_3/\text{PVA-LiClO}_4/\text{MnO}_2$ FSSASCs device was also assembled. The $\text{rGO/Dy}_2\text{S}_3/\text{MnO}_2$ FSSASCs device showed C_s of 116 and 92 F g^{-1} at a scan rate of 5 mV s^{-1} and a current density of 8 A g^{-1} with excellent 85% capacity retention and columbic efficiency of 95% over 5,000 cycles with S_E of 40 Wh kg^{-1} at S_P of 1.33 kW kg^{-1} . The $\text{rGO/Dy}_2\text{Se}_3/\text{MnO}_2$ FSSASCs device observed C_s of 107 and 102 F g^{-1} at scan rate of 5 mV s^{-1} and a current density of 5 A g^{-1} with excellent 88% capacity retention and columbic efficiency of 95% over 5,000 cycles

with S_E of 45 Wh kg⁻¹ at S_P of 9.0 kW kg⁻¹. At a bending angle of 160°, the both FSSASCs devices exhibited excellent flexibility with 91 and 92% of its initial C_s retention, respectively. A couple of series-connected FSSASCs devices light up 201 red LEDs and illuminate table lamp of 11 white LEDs for 60 s. From the results, concluded that the MnO₂/rGO/Dy₂S₃ FSSASCs device shows better performance due to their wide potential window. The present work confirms that the rGO/Dy₂S₃ and rGO/Dy₂Se₃ electrode can be used as a cathode material to fabricate FSSASCs devices.

6.5 References:

- [1] C. Sun, X. Li, Z. Cai, F. Ge, *Electrochim. Acta.*, 296, (2019), 617–626.
- [2] Q. Wang, W. Ren, F. Gao, C. Qiu, Q. Wang, F. Gao, C. Zhao, *ChemElectroChem.*, 6, (2019), 1768–1775.
- [3] J. Sun, X. Du, R. Wu, Y. Zhang, C. Xu, H. Chen, *ACS Appl. Energy Mater.*, 3, (2020), 8026–8037.
- [4] Y. Wang, X. Wu, Y. Han, T. Li, Flexible supercapacitor: overview and outlooks, *J. Energy Storage*, 42, (2021), 103053-103067.
- [5] Y. Zhang, H. Mei, Y. Cao, X. Yan, J. Yan, H. Gao, H. Luo, S. Wang, X. Jia, L. Kachalova, J. Yang, S. Xue, C. Zhou, L. Wang, Y. Gui, *Coord. Chem. Rev.* 438, (2021), 213910-213940.
- [6] D. Malavekar, V. Lokhande, V. Mane, S. Ubale, U. Patil, C. Lokhande, *J. Phys. Chem. Solids*, 141, (2020), 109425-109436.
- [7] V. Mane, D. Malavekar, S. Ubale, R. Bulakhe, I. In, C. Lokhande, *Electrochim. Acta.*, 335, (2020), 135613-135629.
- [8] S. Khot, D. Malavekar, R. Nikam, S. Ubale, P. Bagwade, D. Patil, V. Lokhande, C. Lokhande, *Synth. Met.*, 287, (2022), 117075-117088.
- [9] V. Mane, D. Malavekar, S. Ubale, V. Lokhande, C. Lokhande, *Inorg. Chem. Commun.*, 110, (2020), 107853-107872.
- [10] D. Dubal and R. Holze, *Energy*, 51, (2013), 407-412.
- [11] Y. Hu, H. Zhu, J. Wang, Z. Chen, *J. Alloys Compd.*, 509, (2011), 10234-10240.
- [12] N. Chodankar, S Selvaraj, S. Ji, Y. Kwon, D. Kim, *Small*, 15, (2019), 1803716-1803728.
- [13] B. Pandit, V. Devika, B. Sankapal, *J. Alloys Compd.*, 726, (2017), 1295-1303.
- [14] D. Malavekar, R. Bulakhe, S. Kale, U. Patil, I. In, C. Lokhande, *J. Alloys Compd.*, 869, (2021), 159198-159213.
- [15] S. Sarkar, P. Howli, B. Das, N. Das, M. Samanta, G. Das, K. Chattopadhyay, *ACS Appl. Mater. Interfaces*, 9, (2017), 22652–22664.

- [16] S. Ghosh, P. Samanta, N. Murmu, T. Kuila, J. Alloys Compd., 835, (2020), 155432-155444.
- [17] Q. Li, Q. Wei, L. Xie, C. Chen, C. Lu, F. Yuan, P. Zhou, RSC Adv., 6, (2016), 46548-46557.
- [18] K. Annamalai, L. Liu, Y. Tao, J. Mater. Chem. A, 5, (2017), 9991-9997.
- [19] M. Dong, Z. Wang, J. Wang, H. Guo, X. Li, G. Yan, Front. Mater., 6, (2019), 176-187.
- [20] P. Devi, M. Srivastava, N. Kim, J. Lee, D. Mishra, Compos. B. Eng., 227, (2021), 109384-109398.

CHAPTER-7

Summary and Conclusions

7.1 Conclusions:

The electrochemical energy storage system includes several types, such as batteries, capacitors, and SCs, which have been used in recent years. Batteries, widely utilized in standalone energy storage, portable devices, and electric cars, are known for their high S_E and moderate cycle life. However, they limit their use in portable electronics due to their short service life, safety concerns, and small-scale power. Compared to batteries, SC store charge quickly and has a better power density. SCs are widely used in this field due to their higher power density, stability retention, better S_E , and environmental energy storage, increasing the demand for wearable and portable electronics. Therefore, SC is a fast-emerging technology and an attractive alternative to capacitors and batteries.

Nevertheless, the SCs have several challenges with aqueous electrolytes, including lower metal cation reduction potential and higher metal oxide resistivity. Therefore, investigating novel electrode materials is needed to overcome these drawbacks and enhance SC performance. These best active electrode materials with a combination of supportable electrolytes efficiently increase the FSSASCs devices energy and power capabilities. The previous studies indicate that metal oxides, conducting polymers, and carbon-based materials improve the electrochemical performance of SC devices. However, metal oxides are comparatively less electrically conductive and thermally stable than metal sulfides. Therefore, the development of low-cost, high-performance electrode materials is needed in the REMC materials family.

The global air pollution is driven by industrialization, rapid urbanization, increased vehicle use, fossil fuel consumption, and the emission of organic chemicals. Over the past two decades, the environment has been influenced by the diverse effects of air pollution. Toxic gases, including Cl_2 , SO_2 , NH_3 , NO_2 , and H_2 , contribute to climate change and are harmful to human health. Therefore, highly sensitive gas sensors are crucial for monitoring dangerous and flammable gases, analyzing air quality, and ensuring industry safety. For this reason, the present study is focused on preparing novel dysprosium sulfide by CBD method for developing a gas sensor.

The current work focused on the simple, economical, and binder-free chemical approaches (SILAR and CBD methods) utilized to synthesize dysprosium

chalcogenide (Dy_2S_3 , Dy_2Se_3) and rGO composite dysprosium chalcogenide ($\text{rGO}/\text{Dy}_2\text{S}_3$, $\text{rGO}/\text{Dy}_2\text{Se}_3$) thin films. Optimizing various preparative parameters to result in a high specific surface area with porous surface morphology successfully increases the electrochemical performance of Dy_2S_3 , Dy_2Se_3 , and gas sensor performance of Dy_2S_3 thin films. The rGO composite thin films exhibit better SC performance than Dy_2S_3 , and Dy_2Se_3 thin films. Therefore, the fabrication of the FSSASCs device used composite thin films for their excellent features. Additionally, MnO_2 was chosen as the positive electrode due to its broad potential window. Similarly, in gas sensors, the composite shows better sensitivity than the Dy_2S_3 thin film. The work has been divided into six chapters.

Herein, **Chapter 1** presents the general introduction of SC and gas sensors. It also discusses the significance of Dy_2S_3 and Dy_2Se_3 with their composites for SC and gas sensing research. It explains the simplest energy storage devices, specifically capacitors, batteries, and SCs. Also, it clarifies the requirements and basic working principle of supercapacitors. The classification of SCs and their energy storage capabilities are discussed. Furthermore, the advantages of SCs over standard capacitors and batteries in terms of S_E and S_P are highlighted. The literature survey of rare earth metal chalcogenides includes preparation methods, properties, and supercapacitive parameters. The significance of sensor and classification are discussed. In brief, the types of gas sensors are explained. Furthermore, the literature survey of metal sulphide and their composites for gas sensing applications that have been investigated earlier, and finally, the orientation and purpose of the thesis are described.

With this objective, **Chapter 2** presents the theoretical background, and experimental details of the thin film synthesis using CBD and SILAR methods and characterization techniques. They briefly explain the theoretical background of CBD and SILAR deposition methods with numerous preparative parameters and advantages. Among the physical deposition methods, SILAR and CBD are simple and scalable methods for the deposition of chalcogenide thin films. The physical properties of prepared thin films can be characterized by various physical characterization techniques such as XRD, FTIR, RAMAN, XPS, FE-SEM, EDAX, BET, etc. Their basic principles and working mechanisms are discussed in Chapter 2. Electrochemical characterization techniques such as CV, GCD, and EIS were also

discussed. Similarly, the theory behind the gas sensor measurement, various gas sensor techniques used to evaluate gas sensor performance and theoretical background of the gas sensor mechanism were also studied in Chapter 2.

From this perspective, *Chapter 3* explores the influence of deposition time on the physico-chemical properties and electrochemical performance of dysprosium sulfide. This chapter focused on preparing Dy₂S₃, rGO, and rGO/Dy₂S₃ composite thin films using the CBD method and evaluating their electrochemical performance. Also the synthesis of rGO using a modified Hummer's method is discussed. The effect of optimized rGO concentration on the electrochemical performance of rGO/Dy₂S₃ composite films was evaluated. In the XRD study, the intensity of characteristics peak decreased with the introduction of rGO. The Dy₂S₃ (DS6) thin film obtained the C_s of 219 F g⁻¹ at the scan rate of 5 mV s⁻¹ and stability retention of 81% after 5000 GCD cycles. The introduction of rGO, the surface area of the composite thin films is increased. Due to this, the rGO/Dy₂S₃ composite thin film exhibit maximum C_s of 392 F g⁻¹ at the scan rate of 5 mV s⁻¹ and stability retention of 88% over 5000 GCD cycles. The EIS parameters, R_s , and R_{ct} for DS6 were 1.16 and 16.39 Ω cm⁻², and rGO/Dy₂S₃ composite thin films were 1.04 and 4.18 Ω cm⁻², respectively. Therefore, the appropriate concentration of rGO composite with Dy₂S₃ modifies the structural and morphological properties and, as a result, enhances the specific capacitance. This chapter highlights superiority of rGO/Dy₂S₃ thin film compared to Dy₂S₃ and rGO thin films.

Chapter 4 Contains the synthesis, characterization, and evaluation of the electrochemical performance of SILAR-deposited Dy₂Se₃, and rGO/Dy₂Se₃ composite thin films. The XRD, RAMAN, FT-IR, FE-SEM, and EDAX analyses are used to confirm the formation of the prepared material. The composition of Dy₂Se₃ with rGO is a most efficient strategy to improve the electrochemical performance. The impact on crystal structure, surface morphology, and electrochemical properties with the optimized rGO concentration was studied. The porous nanoparticles of Dy₂Se₃ coated on rGO sheets were observed in rGO/Dy₂Se₃ thin film. The rGO/Dy₂Se₃ composite thin film exhibited a maximum specific surface area of 18 m² g⁻¹ compared to 9 m² g⁻¹ of Dy₂Se₃ thin film. The electrochemical performance of Dy₂Se₃ and rGO/Dy₂Se₃ was analysed by using CV, GCD, electrochemical stability, and EIS study. The non-linear GCD curves indicated the pseudocapacitive behavior of the

Dy₂Se₃ electrode. The Dy₂Se₃ thin film delivered the maximum C_s of 147 F g⁻¹ at a scan rate of 5 mV s⁻¹, which is lower than rGO/Dy₂Se₃ composite thin films obtained C_s of 289 F g⁻¹ at a scan rate of 5 mV s⁻¹. The rGO/Dy₂Se₃ composite electrode shows remarkable cycling stability of 89 % up to 5000 GCD cycles. The values of R_s and R_{ct} for Dy₂Se₃ thin film were 2.49 and 178 Ω cm⁻², and that of rGO/Dy₂Se₃ were 1.81 and 4.01 Ω cm⁻², respectively. In conclusion, the highest specific surface area and enhanced electrochemical activity were due to the synergetic effect between rGO and Dy₂Se₃ thin film.

Chapter 5 deals with the preparation of Dy₂S₃ and rGO/Dy₂S₃ composite by CBD method, physicochemical characterizations, and NO₂ gas sensing study. The XRD, FE-SEM, RAMAN, FTIR, and XPS confirm the formation of composite thin film. The analysis of the surface morphology reveals that the formation of hollow microspherical Dy₂S₃ intercalated between rGO sheets morphology. The rGO/Dy₂S₃ composite displayed expanded surface area (36.08 m² g⁻¹), mesoporous anchored hollow microspherical Dy₂S₃ particles with intimate coupling between rGO sheets. The Dy₂S₃ and rGO/Dy₂S₃ composite sensors are studied for oxidizing (NO₂, SO₂, and Cl₂) and reducing (H₂S, CO, and NH₃) gases at 423 K and room temperature (RT) 300 K, respectively. The rGO/Dy₂S₃ composite displayed excellent selectivity towards NO₂ gas amongst the other interfering gases. The rGO/Dy₂S₃ composite shows excellent NO₂ sensing performance with high NO₂ response (36.08%), fast response time (3 s), and recovery time (17 s) for the NO₂ gas at RT as compared to Dy₂S₃ sensor NO₂ response (23.43%) at 423 K. Further, rGO/Dy₂S₃ composite demonstrated almost identical responses for long-term stability (40 days).

Chapter 6 includes the fabrication and electrochemical performance evaluation of asymmetric MnO₂//rGO/Dy₂S₃ and MnO₂//rGO/Dy₂Se₃ FSSASCs devices. MnO₂ is used as high performance positive electrode material for ASC device fabrication. Furthermore, this chapter explain the preparation of electrodes (rGO/Dy₂S₃, MnO₂ (CBD method), and rGO/Dy₂Se₃ (SILAR method)), solid-state polymer gel electrolyte (PVA-LiClO₄), and fabrication of FSSASCs devices. Due to the different operating potentials of MnO₂ and rGO/Dy₂S₃ electrodes, the MnO₂//rGO/Dy₂S₃ FSSASCs device can be charged up to +1.8 V. The FSSASCs device obtained excellent C_s of 116 F g⁻¹ with a capacitance retention of 85% after 5000 GCD cycles. The device shows the superior S_E of 40 Wh kg⁻¹ at the S_p of 1.33

kW kg^{-1} and robust mechanical flexibility by retaining 92% capacitance at a bending angle of 160° .

Also, this chapter explain the supercapacitive performance evaluated for $\text{MnO}_2//\text{rGO}/\text{Dy}_2\text{Se}_3$ FSSASCs device. The FSSASCs device operating at 1.4 V achieved the C_s of 107 F g^{-1} at a 5 mV s^{-1} scan rate. The FSSASCs device shows remarkable S_E (45 Wh kg^{-1}) and S_P (9.0 kW kg^{-1}), highlighting its potential use in practical applications.

$\text{MnO}_2//\text{rGO}/\text{Dy}_2\text{Se}_3$ FSSASCs device delivered capacitance retention of 88% over 5000 GCD cycles with excellent flexibility of 91% of its initial C_s retention. Finally, for practical applicability, the couple of FSSASCs devices connected in series were able to light up 201 red LEDs and a table lamp of 11 white LEDs efficiently. The initial power dissipated through $\text{MnO}_2//\text{rGO}/\text{Dy}_2\text{S}_3$ and $\text{MnO}_2//\text{rGO}/\text{Dy}_2\text{Se}_3$ FSSASCs devices was 0.59 mW cm^{-2} and 0.41 mW cm^{-2} .

In *Chapter 7*, includes the results and conclusions from the above chapters. **Table 7.1** highlights the electrochemical parameters of Dy_2S_3 , $\text{rGO}/\text{Dy}_2\text{S}_3$, Dy_2Se_3 , and $\text{rGO}/\text{Dy}_2\text{Se}_3$ composite thin films. This table includes the method of material preparation, surface morphology, electrolytes, C_s , R_s , R_{ct} , and cycle stability of the electrodes.

Table 7.2 illustrates the electrochemical characteristics of the $\text{MnO}_2//\text{rGO}/\text{Dy}_2\text{S}_3$ and $\text{MnO}_2//\text{rGO}/\text{Dy}_2\text{Se}_3$ FSSASCs devices. Finally, the observed results conclude that the dysprosium chalcogenide-based FSSASCs devices can power up small electronic equipment that requires power in the range of 0.01 mW to 0.1 mW.

In gas sensor, the comparative gas sensor performance of Dy_2S_3 and $\text{rGO}/\text{Dy}_2\text{S}_3$ composite are summarised in **Table 7.3**. By the examination of **Table 7.3**, it is concluded that $\text{rGO}/\text{Dy}_2\text{S}_3$ exhibited the maximum sensitivity (36.08 %) towards NO_2 at RT with the rapid response (3 s) and recovery (17 s) of the resistance. Also, it exhibits a highly stable NO_2 sensing response for 40 days of continuous operation, indicating its good stability. Thus, the conclusion is drawn that the tested Dy_2S_3 , the $\text{rGO}/\text{Dy}_2\text{S}_3$ composite, is superior for the RT operated gas sensor and may be useful for the commercial gas sensor.

Table 7.1: The electrochemical parameters of Dy₂S₃, rGO/Dy₂S₃, Dy₂Se₃, and rGO/Dy₂Se₃ thin film electrodes deposited using CBD and SILAR methods in three electrode system.

Material	Surface morphology	Method	Electrolyte	C _s (F g ⁻¹)	R _s (Ω cm ⁻²)	R _{ct} (Ω cm ⁻²)	Stability (%) (5000 cycles)
DS3	Hollow microsphere	CBD	1 M Na ₂ SO ₄	210	1.57	23.7	76
DS6	Hollow microsphere			219	1.16	16.39	81
DS9	Hollow microsphere			74	1.77	47.2	71
rGO/Dy ₂ S ₃	Hollow microsphere			392	1.04	4.18	88
Dy ₂ Se ₃	Nanoparticles	SILAR	1 M LiClO ₄	147	2.49	178	84
rGO/Dy ₂ Se ₃	Spherical nanoparticles on sheet-like structure			289	1.81	4.01	89

Table 7.2: The electrochemical parameters of FSSASCs devices evaluated using two electrode system.

Configuration of FSSASCs device	C _s (F g ⁻¹)	Specific energy (Wh kg ⁻¹) at specific power (kW kg ⁻¹)	R _s (Ω cm ⁻²)	R _{ct} (Ω cm ⁻²)	Stability (%) (cycles)	Flexibility (%) at 165°
MnO ₂ //rGO/Dy ₂ S ₃	116 at 5 mV s ⁻¹	40 at 1.33	0.9	16.60	85 (5000)	92
MnO ₂ //rGO/Dy ₂ Se ₃	107 at 5 mV s ⁻¹	45 at 9.0	0.095	14	88 (5000)	91

Table 7.3: Comparative gas sensor performance of Dy₂S₃ and rGO/Dy₂S₃ composite sensor.

Sr. No	Sensor	Target gas	Operating temperature (K)	Sensitivity (%)	Response/Recovery time (s)	Long Term stability (days)
1	Dy ₂ S ₃	NO ₂	423	23.43	6/19	40
2	rGO/Dy ₂ S ₃	NO ₂	RT (300)	36.08	3/17	40

CHAPTER-8

80_Recommendations

8.1 Recommendations:

The present study employed the CBD and SILAR approach to prepare thin films of dysprosium chalcogenides, specifically dysprosium sulfide and dysprosium selenide. The increased surface area and porous morphology of thin films improved their charge storage capacity. To accomplish this, the dysprosium chalcogenide composite with rGO using CBD and SILAR methods. The goal of preparing composite electrodes was to make the material more stable and have a higher specific capacitance than pristine materials.

Finally, it is recommended that, at 6h CBD deposited Dy_2S_3 thin film shows best electrochemical performance and 200 SILAR cycles of Dy_2Se_3 . To get the best electrochemical performance, the optimized concentration of rGO is 1.0 mg mL^{-1} . Due to the simplicity and scalable nature of the deposition method, it can be potentially translated at the industrial level with minimum modification. In gas sensors, the CBD synthesized Dy_2S_3 and rGO/ Dy_2S_3 composites are used as sensor elements to sense various gases. The rGO/ Dy_2S_3 composite displayed excellent gas-sensing performance for the NO_2 at RT ($27 \pm 2^\circ\text{C}$) with a sensitivity of 36.08 % and possesses fast response and recovery periods and long term stability over 40 days. Thus, rGO is recommended as the best to improve the sensing performance of rGO/ Dy_2S_3 .

8.2 Future Findings:

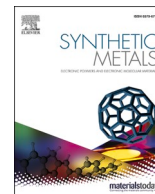
In the present study, a dysprosium chalcogenide thin films and its composite with a highly conducting carbon structure rGO was systematically synthesized using CBD and SILAR methods by controlled experiments and used for supercapacitor and gas sensing applications. The composition of rGO improves electrical conductivity, specific surface area, and overall electrochemical and gas sensing performance (sensitivity, response time, recovery time) of pristine material. Thus, the present research work also opens up possibilities to further enhance dysprosium chalcogenide thin films electrochemical and gas sensor performance.

There is potential to replace rGO with other carbon allotropes, such as fullerene, CNTs, MWCNTs, carbon aerogel, and carbon foam, can be used for the composition with dysprosium chalcogenide thin films. Additionally, incorporating other transition metals (Cu, Mn, Ni, Co) to form bimetallic compounds could further

enhance the electrochemical energy storage and gas sensing properties of the electrode material.

The future work is proposed to prepare Dy_2Se_3 and $\text{rGO}/\text{Dy}_2\text{Se}_3$ composites electrodes using CBD method and utilized in supercapacitor and gas sensing applications. Understanding the process of energy storage in dysprosium chalcogenide based compounds, and analyzing the change in structural, morphological and chemical composition the physical characterization must be done using XRD, FE-SEM, TEM, and XPS techniques. Moreover, a better understanding of the processes involved in charge storage may also be possible by in situ characterization of symmetric and asymmetric devices utilizing TEM and NMR analyses.

PUBLICATIONS



SILAR synthesized dysprosium selenide (Dy_2Se_3) thin films for hybrid electrochemical capacitors

S.D. Khot^a, D.B. Malavekar^a, R.P. Nikam^a, S.B. Ubale^a, P.P. Bagwade^a, D.J. Patil^a,
V.C. Lokhande^b, C.D. Lokhande^{a,*}

^a Centre for Interdisciplinary Research, D.Y. Patil Education Society, Kolhapur 416006, India

^b Department of Electronics and Computer Engineering, Chonnam National University, Gwangju 61186, South Korea

ARTICLE INFO

Keywords:

Dysprosium selenide
Flexible hybrid electrochemical capacitor
Successive ionic layer adsorption and reaction (SILAR) method
Thin film

ABSTRACT

As the necessity of energy storage is continuously increasing, new materials have been investigated for electrochemical energy storage, especially for electrochemical capacitors. These storage devices are rapidly convertible as well as air pollution free. Therefore, a number of materials have been explored as electrode materials for supercapacitors to fulfill different requirements of electrochemical energy storage. Herewith, dysprosium selenide (Dy_2Se_3) films were prepared using the simple successive ionic layer adsorption and reaction (SILAR) method and characterized using different physico-chemical techniques. The specific capacitance (C_s) of 92 F g^{-1} was obtained at the current density of 2.85 A g^{-1} in 1 M LiClO_4 electrolyte with a retention of 85% over 5000 galvanostatic charge-discharge (GCD) cycles performed at a current density of 4 A g^{-1} . The flexible solid-state hybrid electrochemical capacitor of configuration $\text{Dy}_2\text{Se}_3/\text{LiClO}_4\text{-PVA/MnO}_2$ showed C_s of 83 F g^{-1} and specific energy of 18 Wh kg^{-1} at a specific power of 2.7 kW kg^{-1} . This hybrid device retained 92% of capacitance at a device bending angle of 160° . These results demonstrate the facile synthesis of Dy_2Se_3 and its possible use in electrochemical energy storage applications.

1. Introduction

In everyday life, advancing technology has made the most significant impact on the working nature of people. Therefore, it is essential to develop cheap and sophisticated technologies in the electronics, automobile industry, home appliances, biomedical field, etc., to uplift the quality of the human lifestyle. For this, a sustainable, green, and high-performance energy storage system is required which will play a vital role in our modern society [1]. There are different energy storage systems, but batteries, capacitors, and electrochemical capacitors (EC) are most promising. Among these, the charge accumulation mechanism is dissimilar for each of them. Currently, batteries have high energy density but possess disadvantages like low power density, finite cycle life, high cost of manufacturing, and several hours of charging time. The use of ECs can reduce those disadvantages due to their ability to deliver energy at a high rate, fast charging and discharging, efficient fabrication process, and long cycle life and hence gained significant attention in recent time [2,3].

The types of ECs materials mainly depend on the charge storage

mechanism. They are broadly listed into three categories, i.e. electric double-layer capacitors (EDLC), pseudocapacitors and battery-type ECs. Charge accumulation in EDLCs is due to electrostatic mechanism across the electrode and electrolyte interface. The carbon derivatives and MXenes are of EDLCs type materials. In pseudocapacitors, redox reactions occurring on the surface and interior of the electrodes are responsible for charge accumulation. Metal oxides, chalcogenides as well as conducting polymers are the pseudocapacitive electrode materials. The battery-type ECs obey the faradic mechanism of charge storage [4,5]. Mostly nickel and iron oxides and phosphates are used as battery-type materials.

Due to their excellent redox activity, metal chalcogenides and conducting polymers show excellent pseudocapacitive behavior with high specific capacitance (C_s) than EDLCs [6]. The electrode material structure plays an important role by providing access to the electrolyte ions to electrode material for interaction. Many factors affect the electrode's charge storage, i.e., type of crystal structure, surface morphology, elemental composition, electrical resistivity, deposited mass of the electrode, and chemical composition [7]. The method of preparation

* Corresponding author.

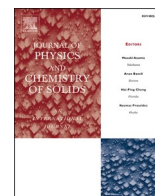
E-mail address: l.chandrakant@yahoo.com (C.D. Lokhande).

<https://doi.org/10.1016/j.synthmet.2022.117075>

Received 18 January 2022; Received in revised form 19 March 2022; Accepted 28 March 2022

Available online 1 April 2022

0379-6779/© 2022 Elsevier B.V. All rights reserved.



Synthesis of reduced graphene oxide (rGO)/dysprosium selenide (Dy_2Se_3) composite electrode for energy storage; flexible asymmetric supercapacitor

S.D. Khot^a, D.B. Malavekar^b, P.P. Bagwade^a, R.P. Nikam^a, C.D. Lokhande^{a,*}

^a Centre for Interdisciplinary Research, D. Y. Patil Education Society, Kolhapur, 416 006, India

^b School of Materials Science and Engineering, Chonnam National University, Gwangju, 500757, South Korea

ARTICLE INFO

Keywords:

Composite electrodes
Dysprosium selenide
Flexible electrochemical supercapacitor
Reduced graphene oxide
Successive ionic layer adsorption and reaction
Thin film

ABSTRACT

In recent years, the requirement for flexible electrode materials has attracted scientific attention for developing flexible supercapacitors. The present work reports the porous reduced graphene oxide/dysprosium selenide (rGO/ Dy_2Se_3) composite thin films preparation, employing successive ionic layer adsorption and reaction (SILAR) method. This work offers thorough information about the structure, morphology, and elemental analysis of prepared rGO/ Dy_2Se_3 composite, as well as its electrochemical properties such as specific capacitance (C_s), charge transfer resistance, electrochemical stability, etc. The rGO/ Dy_2Se_3 composite electrode achieved a C_s of 289 F g^{-1} at a 5 mV s^{-1} scan rate with 89% retention up to 5000 galvanostatic charge-discharge (GCD) cycles due to synergy between properties of Dy_2Se_3 and rGO. A flexible solid-state asymmetric supercapacitor (FSSAS) rGO- $\text{Dy}_2\text{Se}_3/\text{LiClO}_4\text{-PVA/MnO}_2$ device delivered C_s of 107 F g^{-1} at a 5 mV s^{-1} and a specific energy of 45 Wh kg^{-1} at a power of 9 kW kg^{-1} . The FSSAS device retained 91% of its capacitance at a 160° bending angle. These findings show that Dy_2Se_3 anchored on rGO using SILAR method is a promising candidate for supercapacitors.

1. Introduction

Technological advancement has accelerated energy consumption. As a result, different energy storage devices are required for various instruments in modern technology, such as healthcare, intelligent devices, micro-robotics, smartphones, flexible touchscreen displays, electronic skin, implantable medical devices, etc. Because of this, the need for flexible energy storage devices has increased and attracted tremendous research interest [1,2]. Together with secondary batteries, flexible supercapacitors have received a lot of attention due to their rapid charging, robust mechanical flexibility, long life, light weight, high operating voltage, superior safety, ability to provide required power density in a wide range of temperatures, and nearly constant performance even with mechanical deformation states [3–5]. Considering the above qualities of flexible supercapacitors, the implementation of flexible supercapacitors in wearable and flexible appliances has increased in the recent past. Therefore, the fabrication of flexible supercapacitors has been an attractive research topic in recent years.

One of the effective strategies to fabricate flexible SCs is to incorporate essential components like flexible and lightweight substrates, suitable electroactive materials, and electrolytes. The flexible substrates

used so far are cellulose papers, textiles, paper, elastomeric polymers, cable-type matrices, stainless steel (SS), carbon sponge, and carbon-based papers (e.g., carbon cloth). However, the low conductivity, negative electrochemical activity, and low mechanical strength of some of these current collectors made obtaining desirable specific energy difficult. In this context, the SS substrate is the most favorable owing to its various benefits like low cost, high flexibility with mechanical strength, lightweight, ease of surface modification, and environment compatibility [6,7].

The electric double-layer capacitor (EDLC) and pseudocapacitive types of electrode materials are used in supercapacitors. The carbonaceous materials used in EDLCs have a low energy density [8]. Therefore, the present studies mainly focus on pseudocapacitive materials because of their high specific energy. Pseudocapacitive materials consist of transition metal oxides, chalcogenides, phosphates, nitrides, tungstate, and rare earth metal chalcogenides (REMC). The REMC possesses great potential as a pseudocapacitive material. The distinctive characteristics of REMC include 4f vacant orbital, high mechanical stability, rapid charge transfer, and high ionic conductivity at the electrode-electrolyte interaction [9,10]. Due to this, REMC materials are now widely utilized in a variety of applications like magnetic, catalysts, optical, and energy

* Corresponding author.

E-mail address: l.chandrakant@yahoo.com (C.D. Lokhande).

<https://doi.org/10.1016/j.jpcs.2023.111419>

Received 15 February 2023; Received in revised form 29 March 2023; Accepted 30 April 2023

Available online 5 May 2023

0022-3697/© 2023 Elsevier Ltd. All rights reserved.



Review

Doping of rare earth elements: Towards enhancing the electrochemical performance of pseudocapacitive materials

D.B. Malavekar ^{a,b}, V.V. Magdum ^a, S.D. Khot ^a, J.H. Kim ^{b,*}, C.D. Lokhande ^{a,*}^a Centre for Interdisciplinary Research, D. Y. Patil Education Society, Kolhapur 416 006, India^b Optoelectronic Convergence Research Center, Department of Materials Science and Engineering, Chonnam National University, Gwangju 61186, South Korea

ARTICLE INFO

Article history:

Received 1 March 2023

Received in revised form 29 April 2023

Accepted 15 May 2023

Available online 16 May 2023

Keywords:

Doping

Electrochemistry

Electrode materials

Rare earth elements

Supercapacitor

ABSTRACT

The emerging challenges of global warming have instigated people to produce and store renewable energy. Among various energy storage devices, the supercapacitor is an advanced energy storage device that has been used in many crucial applications to provide the necessary power. As a result, in the last couple of decades, pseudocapacitive materials such as metal oxides and conducting polymer-based electrode materials have shown remarkable electrochemical performance. However, the performance of bare pseudocapacitive materials is hindered due to their limitations, such as low conductivity, low surface area, poor electrochemical activity, etc. These limitations can be addressed by doping as it is an effective way of altering various physicochemical properties, such as crystal structure, surface morphology, specific surface area, electronic conductivity, and chemical stability of the host material, which ultimately enhances the electrochemical performance of the doped material. Therefore, in this review, we have discussed the effect of rare earth element doping in pseudocapacitive material. The doping strategy altered the crystallographic parameters, surface morphology, specific capacitance, and cyclability. In addition, various methods employed for doping rare earth elements in pseudocapacitive materials are summarized. Finally, the prospects of rare earth element doped electrode materials in current supercapacitor development are discussed.

© 2023 Elsevier B.V. All rights reserved.

Contents

1. Introduction	2
2. Factors affecting supercapacitor performance	3
2.1. Chemical composition of the material	3
2.2. Electrolyte	3
2.3. Temperature	3
2.4. Crystal structure and crystallinity	3
2.5. Morphology	4
2.6. Pore structure and specific surface area	4
2.7. Thickness of the electrode	4
3. Role of doping in the enhancement of electrochemical properties of host material	4
4. Various REE-doped pseudocapacitive materials for supercapacitor application	5
4.1. Ce-doped pseudocapacitive materials	5
4.2. La-doped pseudocapacitive materials	11

Abbreviations: AC, activated carbon; CBD, chemical bath deposition; CCGN, CeO₂/Co₃O₄/rGO; Ce, cerium; CNTs, carbon nanotubes; CV, cyclic voltammetry; DFT, density functional theory; Dy, dysprosium; EDLC, electric double-layer capacitors; EDS, energy-dispersive X-ray spectroscopy; Eu, europium; GCD, galvanostatic charge-discharge; Gd, gadolinium; GNS, graphene nanosheets; GO, graphene oxide; HRTEM, high-resolution transmission electron microscopy; HSC, hybrid supercapacitor; La, lanthanum; LED, light-emitting diode; Lu, lutetium; MWCNT, multiwalled carbon nanotubes; Nd, neodymium; NiHN, nickel hydroxide nitrate; OAB, oxide acetylene black; PANI, polyaniline; PL, photoluminescence; PLD, pulsed laser deposition; REEs, rare earth elements; rGO, reduced graphene oxide; Sc, scandium; SEAD, selected area diffraction; SEM, scanning electron microscope; SILAR, successive ionic layer adsorption and reaction; Sm, samarium; XRD, X-ray diffraction; Y, Yttrium; Yb, Ytterbium

* Corresponding authors.

E-mail addresses: jinhyeok@chonnam.ac.kr (J.H. Kim), l_chandrakant@yahoo.com (C.D. Lokhande).



Performance of solid-state symmetric supercapacitors based on Dy₂S₃ electrodes

P.P. Bagwade^a, R.P. Nikam^a, R.P. Bhosale^b, S.D. Khot^a, C.D. Lokhande^{a,*}

^a Centre for Interdisciplinary Research, D. Y. Patil Education Society, Kolhapur 416 006, India

^b Department of Physics, D. P. Bhosale College, Koregaon, Satara 415516, India

ARTICLE INFO

Keywords:

Dysprosium sulfide
Energy storage
Rare earth
Solid state symmetric supercapacitor
Thin film

ABSTRACT

Rare earth metal sulfides show good capacitance retention and better charge discharge performance. Dysprosium based materials could be a promising candidate for the utilization in supercapacitors due to its multiple transition states. The dysprosium sulfide (Dy₂S₃) thin films were deposited on stainless steel (SS) substrate using facile successive ionic layer adsorption and reaction (SILAR) method. The films exhibit orthorhombic crystal structure and spherical nanoparticles morphology. The electrochemical supercapacitive performance of Dy₂S₃ film showed maximum specific capacitance (C_s) of 273 F g⁻¹ at a scan rate of 5 mV s⁻¹ with excellent (83 %) cycling performance over 2000 cycles in 1 M Na₂SO₄ electrolyte. The industrial application of SILAR deposited Dy₂S₃ thin film was examined by fabricating flexible solid-state symmetric supercapacitor (FSS-SSC) device with configuration Dy₂S₃/PVA-Na₂SO₄/Dy₂S₃. It exhibited C_s of 26 F g⁻¹ with specific energy of 17 Wh kg⁻¹ and specific power of 520 W kg⁻¹. A good cyclic stability was observed with capacitive retention of 79 % at the scan rate of 100 mV s⁻¹ after 5000 cyclic voltammetry (CV) cycles. This study highlights the potential application of Dy₂S₃ for supercapacitor application.

Introduction

Large energy shortages and renewable energy sources have inspired the overall efforts for research to expand the use of energy saving devices that are beneficial and environmentally friendly. Hence, various energy storage devices are under investigation [1,2]. A battery-powered energy storage system has a shorter life cycle and requires more space for the system. Supercapacitors (SCs), on the other hand, have emerged as potential competitors for remarkable features, such as high charging-discharging rates, excellent life cycles and reversibility. The SCs are energy storage devices having capacitance greater than common capacitors [3,4]. SCs are categorized as electrical double layer capacitors (EDLCs) and pseudocapacitors based on the charge storage mechanism [5]. The EDLC (carbon-based substances) possesses greater surface area and extensive life span. The charge storage mechanism in pseudocapacitors are based on reversible faradic redox reactions. Metal sulfides, oxides, and polymers are some of the pseudocapacitive materials [6,7].

Recently, transition metal sulfides have emerged as potential pseudocapacitive materials [8]. Of these, compounds based on rare earth metals owing to their excellent electrical conductivity and abundance,

attracting significant research attention. Dysprosium is a promising rare earth metal which exhibits various oxidation states (Dy⁺³, Dy⁺², Dy⁺¹) useful for pseudocapacitive performance. As of now, many researchers have employed rare earth compounds for the SC application [9]. Ghogare et al. [10] reported hydrothermal method for lanthanum sulfide (La₂S₃) thin film with specific capacitance (C_s) of 121.4 F g⁻¹. Pujari et al. [11] and Patil et al. [12] synthesized ytterbium sulfide (Yb₂S₃) and lanthanum telluride (La₂Te₃) and obtained C_s of 270 and 469 F g⁻¹, respectively. Arunachalam et al. [13] using chemical precipitation process produced neodymium hydroxide (Nd(OH)₃) thin films with C_s of 871 F g⁻¹.

Though various methods are useful for the deposition of thin films on different substrates, SILAR method comes out as an effective approach by providing direct deposition on any kind of substrate without having to use binder for the adhesion purpose. It gives access to control the film thickness by means of varying deposition cycles. In addition, one can have large area deposition using SILAR method which is applicable at industrial scale [6]. As a result, SILAR is being widely used for the deposition of many materials for various applications [10].

In continuation to our previous work [14], this report highlights a direct deposition of Dy₂S₃ thin film and evaluation of its supercapacitive

* Corresponding author.

E-mail address: l.chandrakant@yahoo.com (C.D. Lokhande).

<https://doi.org/10.1016/j.apsadv.2023.100529>

Received 30 September 2023; Received in revised form 27 November 2023; Accepted 27 November 2023

Available online 5 December 2023

2666-5239/© 2023 The Authors. Published by Elsevier B.V. This is an open access article under the CC BY-NC-ND license (<http://creativecommons.org/licenses/by-nc-nd/4.0/>).

Available online at www.sciencedirect.com

ScienceDirect

journal homepage: www.elsevier.com/locate/he

Nanocrystalline cobalt tungstate thin films prepared by SILAR method for electrocatalytic oxygen evolution reaction

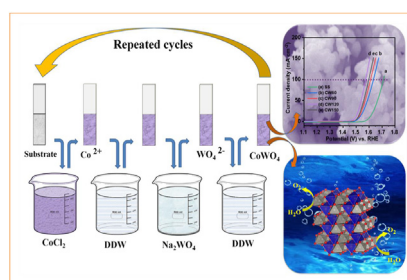
P.P. Bagwade, D.B. Malavekar, V.V. Magdum, S.D. Khot, R.P. Nikam, D.J. Patil, U.M. Patil, C.D. Lokhande*

Centre for Interdisciplinary Research, D. Y. Patil Education Society, Kolhapur 416 006, India

HIGHLIGHTS

- CoWO₄ thin film electrocatalysts prepared by SILAR method was employed for oxygen evolution reaction.
- The CoWO₄ material exhibited porous morphology with specific surface area of 49.3 m² g⁻¹.
- CoWO₄ electrode exhibited excellent OER functioning with overpotential of 330 mV at a current density of 100 mA cm⁻².
- CoWO₄ thin film electrode exhibited remarkable stability (97%) after 24 h in 1 M KOH.

GRAPHICAL ABSTRACT



ARTICLE INFO

Article history:

Received 7 July 2022

Received in revised form

30 September 2022

Accepted 9 November 2022

Available online xxx

Keywords:

Cobalt tungstate

Thin film

Electrocatalyst

Oxygen evolution reaction

Successive ionic layer adsorption and reaction (SILAR)

ABSTRACT

This study highlights on the application of nanocrystalline cobalt tungstate (CoWO₄) thin films as an electrocatalyst for oxygen evolution reaction (OER) prepared using successive ionic layer adsorption and reaction (SILAR) method. The X-ray diffraction, scanning electron microscopy, X-ray photoelectron spectroscopy, Fourier transform infrared spectroscopy etc. were employed for the characterization of CoWO₄ thin films, revealing the formation of crystalline CoWO₄ with spherical morphology. Furthermore, CoWO₄ showed excellent electrochemical performance with the overpotential of 330 mV and Tafel slope of 153 mV dec⁻¹ with retaining 97% of electrochemical stability after 24 h of OER. The study confirmed the structural maintenance of CoWO₄ thin films after stability study.

© 2022 Hydrogen Energy Publications LLC. Published by Elsevier Ltd. All rights reserved.

* Corresponding author.

E-mail address: l_chandrakant@yahoo.com (C.D. Lokhande).

<https://doi.org/10.1016/j.ijhydene.2022.11.090>

0360-3199/© 2022 Hydrogen Energy Publications LLC. Published by Elsevier Ltd. All rights reserved.

Binder-Free Synthesis of Mesoporous Nickel Tungstate for Aqueous Asymmetric Supercapacitor Applications: Effect of Film Thickness

Dilip J. Patil, Dhanaji B. Malavekar, Vaibhav C. Lokhande, Prity P. Bagwade, Sambhaji D. Khot, Taeksoo Ji, and Chandrakant D. Lokhande*

Nickel tungstate thin films of different thicknesses are synthesized using the binder-free successive ionic layer adsorption and reaction (SILAR) method at ambient temperature and subsequent calcination at a temperature of 727 K. The physicochemical characterizations of NiWO_4 thin films are carried out using different techniques. The electrochemical performances of NiWO_4 films are evaluated in 2 M KOH electrolyte using a standard three electrode system. The specific capacitance of 1536 F g^{-1} at the current density of 2 A g^{-1} is obtained for the NiWO_4 film. The film exhibits excellent electrochemical stability of 87% after 5000 galvanostatic charge–discharge (GCD) cycles at the current density of 3 A g^{-1} . This study highlights use of SILAR-deposited NiWO_4 thin films as a cathode in aqueous asymmetric supercapacitors (ASCs). The ASC device $\text{NiWO}_4/\text{KOH}/\text{Fe}_2\text{O}_3$ exhibits a specific capacitance of 115 F g^{-1} at 2 A g^{-1} and specific energy of 23 Wh kg^{-1} at specific power of 1.2 kW kg^{-1} . The device shows remarkable electrochemical cycling stability (78% capacitance retention after 5000 GCD cycles). The SILAR-deposited NiWO_4 thin films are expected to emerge as a potential candidate for supercapacitors.

However, the cost and the energy stored by these devices vary with the design, chemistry, and materials used to fabricate. The specific energy for batteries is comparatively more than the SCs and capacitors.^[1,2] Due to outstanding cycle stability, greater power density, and rapid charge–discharge rate, SCs are some of the better optimistic contenders.^[3,4] A significant drawback of SCs is that they are deficient in specific energy to fulfill the growing energy requirements for new-age energy storage equipment.^[5,6] Nowadays, more research activities have been concentrated to enhance the specific energy of SCs without losing their specific power and cyclability.^[7,8] The specific energy ($E = 0.5CV^2$) can be raised by improving capacitance (C) and operating potential window (V). Different electroactive materials with ranges of capacitance values have been used to fabricate SCs.^[9–11] Hence, the preparation of

1. Introduction

In the present era, environmental pollution originating from burning of hydrocarbon fuels is affecting human health along with the surrounding nature. So, the shifting of energy generation and usage habits became the need of an hour. Renewable energy generation/conversion is convincing path for the pollution-free environment. The major challenge faced by these sources is storage of energy because of abruptness in the generation. The capacitors, batteries, and supercapacitors (SCs) have been used for electrochemical energy storage from a long time.

novel electrode materials possessing high specific capacitance and fabrication of asymmetric supercapacitors (ASCs) to overcome the issue of low cell potential can result in enhanced specific energy.^[12,13]

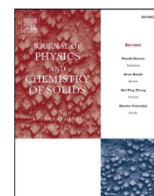
Metal tungstates have the general formula AWO_4 , where A is a divalent cation ($\text{A}^{2+} = \text{Ni, Fe, Mn, Cu, Co}$) that acts as a network modifier. The monoclinic crystal structure of metal tungstates (shown in Figure 1a,b) resembles with the crystal structure of metal sulfates.^[14] Crystal structure formed by tungstate ion with bivalent metal ion forms tetrahedral coordination. However, due to the smaller radius of bivalent cations like nickel having ionic radius of less than 0.77 \AA will perform well for the supercapacitors. In addition to this, the bimetallic nature of the metal tungstates helps to improve the energy storage capacity of materials compared to a single metal compound like NiO and WO_3 . Compared to nickel oxide and hydroxide, NiWO_4 have higher molecular mass, leading to lower theoretical capacitance. Higher cost of preparation due to addition of W in synthesis process can be considered a disadvantage. Metal oxides, including tungsten oxide and metal tungstates, show several advantages over other materials, such as low toxicity, low synthetic cost, high resistance against photocorrosion, and compatibility with up-scale. Normally, metal tungstate materials were tested for SC applications,^[15] Li-ion battery,^[16] electrocatalysis,^[17] gas

D. J. Patil, D. B. Malavekar, P. P. Bagwade, S. D. Khot, C. D. Lokhande
Centre for Interdisciplinary Research
D. Y. Patil Education Society
Kolhapur 416006, India
E-mail: l_chandrakant@yahoo.com

V. C. Lokhande, T. Ji
Department of Electronics and Computer Engineering
Chonnam National University
Gwangju 61186, South Korea

The ORCID identification number(s) for the author(s) of this article can be found under <https://doi.org/10.1002/ente.202200295>.

DOI: 10.1002/ente.202200295



Pseudocapacitive performance of amorphous ruthenium oxide deposited by successive ionic layer adsorption and reaction (SILAR): Effect of thickness

A.G. Bagde^a, D.B. Malavekar^b, D.C. Pawar^a, S.D. Khot^a, C.D. Lokhande^{a,*}

^a Centre for Interdisciplinary Research, D. Y. Patil Education Society, Kolhapur, 416 006, India

^b School of Materials Science and Engineering, Chonnam National University, Gwangju, 500757, South Korea

ARTICLE INFO

Keywords:

Ruthenium oxide
Successive ionic layer adsorption and reaction (SILAR)
Supercapacitor
Thin film

ABSTRACT

Developing and fabricating effective, affordable electrode materials for supercapacitors is still a challenge. Electrical conductivity, a large surface area, dynamic faster electron transport, and other customizable qualities are present in metal oxide materials while being inexpensive to manufacture. In this work, successive ionic layer adsorption and reaction (SILAR) method was employed for deposition of amorphous ruthenium oxide (RuO₂) thin films of different thicknesses on a stainless steel substrate. At 1.56 mg cm⁻² thickness amorphous RuO₂ achieved a maximum specific capacitance (C_s) of 1146 F g⁻¹ at a scan rate of 5 mV s⁻¹ with 87% capacitance retention up to 5000 cycles. These findings bolster the idea of cost effective deposition of amorphous RuO₂ material for supercapacitor applications.

1. Introduction

Enhancing the capacity of energy storage systems has certainly been the subject of significant study worldwide because of growing need for large-capacity power storage for use in hybrid electric cars, armed forces gears, lightweight and versatile digital devices, and designate biomedical gear [1–4]. However, the more accomplished energy that is sustainable is not suitable to meet the energy storage demands. Hence, this energy storage transformation is important for research as well as industries. Supercapacitor (SC) signifies a rising energy storage system category that has drawn interest because it offers a greater energy density than conventional capacitors. The SCs possess a higher capacity for rapid charging and discharging and longer cycle life than rechargeable batteries [5]. The electrode material is crucial in the design of SC. It is effectively tuneable for the crucial electrochemical performances of the SC. The taxonomy of SCs is classified in three kinds, such as electric double layer capacitor (EDLC), pseudocapacitor, and hybrid capacitor, based on their charge storage techniques. In EDLCs, energy storage mechanisms arise from electronic and ionic charge processes that are separated at the interfaces between electrode and electrolyte. The EDLC-type behaviour has been shown by carbon-based materials, like activated carbon, carbon nanotubes, graphene, diamond, carbon aerogel, etc. [6]. On the other hand, metal oxides/sulfides and conducting polymers store charge mostly by a quick, reversible redox process that

results in pseudocapacitance [7–9]. Here, electron transport takes place chemically, producing the excess pseudocapacitance at a certain potential. Here, charge storage is carried out by bulk of material, enhancing the specific energy density and device capacitance [10]. Both methods of charge storage reveal both beneficial and undesirable electrochemical qualities. The efficiency of a single-charge storage method is insufficient to compete with batteries. In this sense, the deployment of a performance-oriented energy storage system requires the development of a hybrid strategy. Both types of charge storage methods are included in the hybrid strategy. The capacitive method increases device stability and electronic conductivity by having a large surface area and an efficient charge transportation path [11].

Ruthenium oxide (RuO₂), one of the most popular metal oxide has been extensively researched due to its enormous surface area, excellent reversibility, and relatively high capacitance [12]. Recently, it has also been revealed that RuO₂ has excellent electrocatalytic activity in a wide range of electrochemical processes [13]. The stable RuO₂ mainly adopts the “rutile structure” of RuO₂, even though it is observed in other variations with respect to liquid hydrate. Its molecular orbital theory effectively explained the thermodynamic stability and large isotropic charge transportation characteristics of RuO₂. Additionally, RuO₂ has a long cycle life with tunable-metallic conductivity, multiple oxidation states, and durable stability across a broad potential range. In fact, these characteristics have greatly aided SC research. However, a few

* Corresponding author.

E-mail address: lchandrakant@yahoo.com (C.D. Lokhande).

<https://doi.org/10.1016/j.jpcs.2023.111386>

Received 15 February 2023; Received in revised form 6 April 2023; Accepted 17 April 2023

Available online 17 April 2023

0022-3697/© 2023 Elsevier Ltd. All rights reserved.



Performance of chemically synthesized polyaniline film based asymmetric supercapacitor: Effect of reaction bath temperature

D.C. Pawar^a, D.B. Malavekar^b, S.D. Khot^a, A.G. Bagde^a, C.D. Lokhande^{a,*}

^a Centre for Interdisciplinary Research, D.Y. Patil Education Society, Kolhapur 416 006, India

^b School of Materials Science and Engineering, Chonnam National University, Gwangju 500757, South Korea

ARTICLE INFO

Keywords:

Asymmetric supercapacitor
Chemical bath deposition
Hybrid supercapacitor
Polyaniline
Tungsten oxide

ABSTRACT

Polyaniline (PANI) electrodes were prepared using chemical bath deposition method at various reaction bath temperatures ranging from 263 to 323 K. The specific surface area and wettability of films are significantly impacted by the polymerization temperature, which influences the electrochemical performance of electrodes. The electrode synthesized at 303 K showed a maximum specific surface area of $25 \text{ m}^2 \text{ g}^{-1}$, specific capacitance (C_s) of 816 F g^{-1} (0.11 F cm^{-2}) at a scan rate of 0.005 V s^{-1} , and 89% capacitive retention after 1,000 cyclic voltammetry (CV) cycles. An aqueous asymmetric supercapacitor device was fabricated using PANI as a cathode and tungsten oxide (WO_3) as an anode in $1 \text{ M H}_2\text{SO}_4$ electrolyte. The fabricated PANI/ H_2SO_4 / WO_3 device achieved a maximum C_s of 43 F g^{-1} with an energy density of 12 Wh kg^{-1} at a power density of 0.88 kW kg^{-1} and 72 % capacitive retention after 10,000 CV cycles.

1. Introduction:

In response to the fast growth of the global economy, the depletion of fossil fuels, and the degradation of ecosystems, there is a critical need to improve extremely effective, inexhaustible, and environment friendly methods for the conversion and storage of energy. This has animated advances in converting renewable energy through greenways and innovations related to electrochemical energy storage, i.e., supercapacitors and batteries [1,2]. Because of their inherent electrochemical properties, such as fast charge–discharge, long cycle stability, greater energy density compared to capacitors, and larger power density than ordinary batteries, supercapacitors have been explored as key enabler for the next generation energy storage device. Supercapacitor materials are split into three groups based on charge storage mechanisms: electric double-layer capacitors (EDLC), pseudocapacitors, and battery-type supercapacitors [3].

In EDLC capacitors, charge storage is caused by an electrostatic process at the electrode/electrolyte interface. EDLC materials are carbon-based, such as carbon nanotubes (CNT), activated carbon, and carbon aerogel, etc. [4–6]. The pseudocapacitor charge-storage system essentially depends on exchanging charge through the electrolyte and electrode surface redox reactions. Pseudocapacitor materials include transition metal chalcogenides and conducting polymers such as

polyaniline (PANI) [7], polypyrrole (Ppy), and polythiophene (PT) [8,9]. The charge storage mechanism is based on strongly electrochemical redox reactions in battery-type materials, like Ni-based materials. Conducting polymers have unique and important properties, such as high electrical conductivity like metals and the capability to transition between redox states. PANI is an excellent material among conducting polymers and has been studied recently due to its easy synthesis process, low price, and interesting redox properties applicable in supercapacitor devices [10].

A convenient method for significant deposition on many substrates is the chemical bath deposition (CBD) method. It is quite an easy and cheap method compared to other methods. The development of nucleation is essential for the formation of precipitates. The result of nucleation in solution is that the molecular clusters produced quickly decompose, and particles combine to grow the film to a particular thickness. The controlled precipitation of the desired compound from a solution of its constituents is the fundamental principle of the CBD method [11,12].

The reaction temperature is more important in thin film preparation since it impacts the rate of reaction, morphology, thickness, surface wettability, and pore size, which determine the ions transport kinetics [13]. However, a complete understanding of its impact on electrode electrochemical activity is still lacking. The specific surface area of the

* Corresponding author.

E-mail address: l.chandrakant@yahoo.com (C.D. Lokhande).

<https://doi.org/10.1016/j.mseb.2023.116432>

Received 22 December 2022; Received in revised form 22 February 2023; Accepted 5 March 2023

Available online 14 March 2023

0921-5107/© 2023 Elsevier B.V. All rights reserved.



Flexible solid-state asymmetric supercapacitor based on reduced graphene oxide (rGO)/ruthenium oxide (RuO₂) composite electrode

A.G. Bagde^a, D.B. Malavekar^b, A.C. Lokhande^c, S.D. Khot^a, C.D. Lokhande^{a,*}

^a Centre for Interdisciplinary Research, D. Y. Patil Education Society, Kolhapur 416003, India

^b Optoelectronic Convergence Research Center, Department of Materials Science and Engineering, Chonnam National University, Gwangju 61186, South Korea

^c Applied Quantum Materials Laboratory (AQML), Department of Physics, Khalifa University of Science and Technology, P.O. Box 127788, Abu Dhabi, United Arab Emirates

ARTICLE INFO

Keywords:

Asymmetric supercapacitor
Composite material, Reduced graphene oxide
Ruthenium oxide
Successive ionic layer adsorption and reaction (SILAR)

ABSTRACT

Energy storage in flexible supercapacitor devices extensively depends on electrode design with good electrochemical as well as mechanical properties. Here, a cost-effective and scalable method is proposed for the synthesis of a reduced graphene oxide/ruthenium oxide (rGO/RuO₂) composite thin film for flexible supercapacitor. The successive ionic layer adsorption and reaction (SILAR) method used to synthesize rGO/RuO₂ composite electrode allowed the synthesis of amorphous RuO₂ with optimized rGO composition. The morphological structure of rGO/RuO₂ composite examined using a scanning electron microscope showed compact spherical microparticles coated on rGO sheets. The electrochemical measurements of rGO/RuO₂ composite electrode revealed that the composite material achieved a specific capacitance of 1371 F g⁻¹ at a scan rate of 5 mV s⁻¹. Due to the combined impact of rGO and RuO₂, a flexible solid-state asymmetric supercapacitor (FSS-ASC) of configuration rGO/RuO₂/PVA-H₂SO₄/WO₃ exhibited C_s of 114 F g⁻¹ at 5 mV s⁻¹ with 88% of capacitance retention after 5000 galvanostatic charge-discharge (GCD) cycles. The FSS-ASC provided a remarkable specific energy of 23 Wh kg⁻¹ and a specific power of 613 W kg⁻¹. The electrochemical features of rGO/RuO₂ composite show a promising way to fabricate flexible supercapacitors.

1. Introduction

The exponential growth in energy use has resulted in a shortage of energy resources, leading to a surge in prices. The aforementioned demand has resulted in increased utilization of nonrenewable energy sources and the advancement of renewable energy technology. Renewable energy technologies such as wind and solar need energy storage systems [1,2]. Furthermore, the progress in electronic devices has resulted in a significant increase in demand for electrical energy storage devices. Currently, a battery and a supercapacitor are commonly used energy storage devices. Although they have distinct energy storage mechanisms, they complement each other in storage systems [3,4]. Innovative and affordable energy storage technologies have been attracting researchers owing to increased reliance on electronic devices. In the last few years, the development of flexible supercapacitors has drawn a lot of interest because of their rapid charging-discharging ability, longer durability, lightweight nature, wide operation voltage, robust mechanical flexibility, and safer operation with excellent power

density [5]. Due to these advantages, flexible supercapacitors are extensively utilized in many electronic devices like memory backups, electric vehicles, and electronic gadgets, as well as in certain energy conversion systems in combination with fuel cells or batteries.

Supercapacitive materials have been classified into two primary categories: electric double-layer capacitors (EDLCs) and pseudocapacitors [6]. In general, carbon allotropes with dimensions ranging from one to three dimensions, like carbon quantum dots (CQDs), carbon nanotubes (CNTs), and foams, exhibit characteristics of electric double-layer capacitors (EDLCs). Carbon electrodes are widely used in various electrochemical applications, including electrochemical double-layer capacitors (EDLCs), electrolysis, and certain types of batteries. These electrodes are made from carbon-based materials and are valued for their unique properties, which include high electrical conductivity, stability, and a variety of available structures. The ability to store charge at the interface between the electrode and electrolyte. The electrochemical reactions that occur at the carbon electrode/electrolyte interface in EDLCs involve the physical adsorption and desorption of ions on

* Corresponding author.

E-mail address: l.chandrakant@yahoo.com (C.D. Lokhande).

<https://doi.org/10.1016/j.jalcom.2024.173591>

Received 27 October 2023; Received in revised form 10 January 2024; Accepted 17 January 2024

Available online 19 January 2024

0925-8388/© 2024 Elsevier B.V. All rights reserved.



Effect of post annealing on chemisynthesized cadmium selenide (CdSe) thin films: physicochemical and photoelectrochemical properties

R. P. Nikam¹ , V. C. Lokhande², S. D. Khot¹, P. P. Bagwade¹, J. L. Gunjekar¹, and C. D. Lokhande^{1,*}

¹ Centre for Interdisciplinary Research, D. Y. Patil Education Society (Deemed to be University), Kolhapur 416 006, India

² Department of Electrical, Electronic Communication and Computer Engineering, Chonnam National University, Yongbong-Dong, Puk-Gu, Gwangju 500 757, South Korea

Received: 19 February 2023

Accepted: 9 September 2023

Published online:

4 October 2023

© The Author(s), under exclusive licence to Springer Science+Business Media, LLC, part of Springer Nature, 2023

ABSTRACT

The utilization of solar energy is an essential aspect in order to sustain in the energy crisis situation. Semiconductor based photoelectrochemical (PEC) cells are used for it. Herein, a binder free approach was employed for the synthesis of CdSe thin films on stainless steel substrate and effect of post annealing (350–500 K) on physicochemical as well as photoelectrochemical properties were investigated. The characterization showed that CdSe thin films crystallized in cubic crystal structure with spherical granular morphology with optical band gap of 1.76 eV. The effect of post annealing on CdSe thin films is further tested by examining their PEC properties. Thin film CdSe electrode annealed at temperature 400 K showed highest fill factor (*FF*) and efficiency (η) of 0.32 and 1.54%, respectively. In addition, electrochemical impedance spectroscopy (EIS) study showed superior charge transfer properties.

1 Introduction

In recent days, the global energy need is rising day by day due to overpopulation and worldwide technoeconomic growth. The progress of humans and nation is depending on the utilization of energy. In order to have rapid development, adequate energy is a key requisite. At present, mainly fossil fuels viz. petrol, diesel, coal, etc., are used to fulfill the energy requirement of the world. However, due to limited availability, environmental pollution, and overutilization of fossil fuels,

mankind is going through a drastic energy crisis situation. In order to resolve this energy crisis scientists are looking forward for pollution free, eco-friendly, affordable, secure, and sustainable sources of energy [1].

To reduce dependency on fossil fuels and quench energy requirement, researchers are gregariously paying interest in renewable energy sources (RES) including solar, nuclear, wind, tidal, geothermal, etc. Among them, solar energy is one of the best options. It is a clean and green energy source, as it does not generate any pollutants or byproducts hazardous

Address correspondence to E-mail: l_chandrakant@yahoo.com



Chemical synthesis and photoelectrochemical study of CdS/rGO nanocomposite films

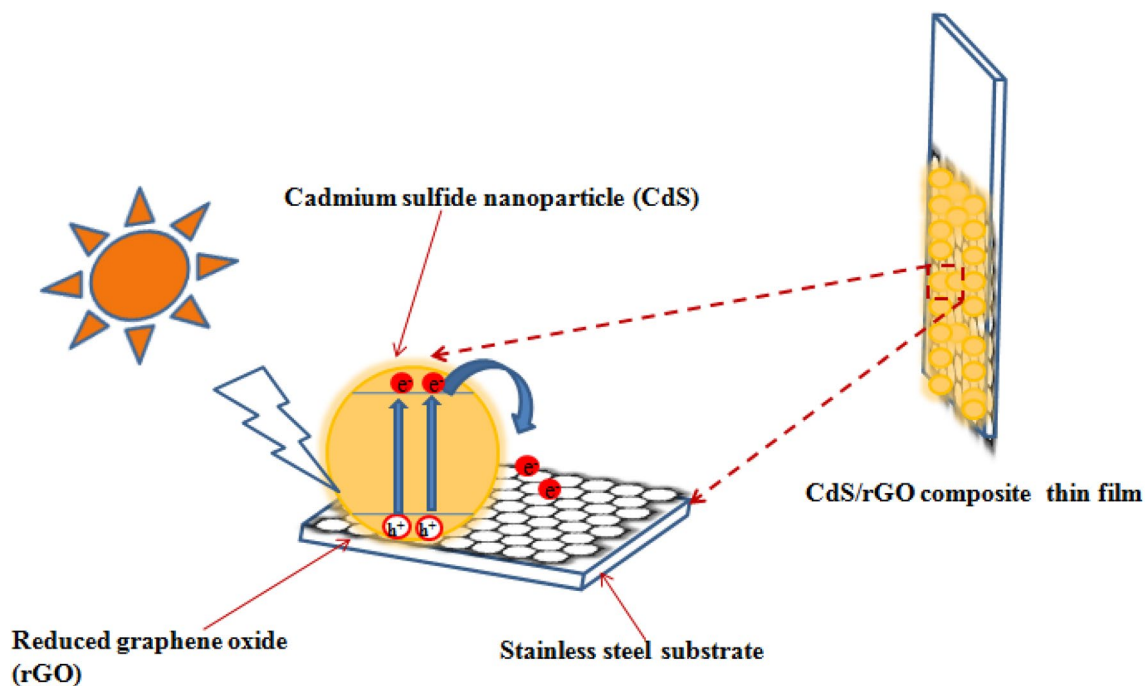
Ranjit P. Nikam¹ · Abhishekh C. Lokhande² · Sambhaji D. Khot¹ · Vikas J. Mane¹ · Chandrakant D. Lokhande¹

Received: 24 March 2022 / Revised: 6 October 2022 / Accepted: 19 October 2022
© The Korean Ceramic Society 2022

Abstract

The cadmium sulfide/reduced graphene oxide (CdS/rGO) composite thin films were synthesized on stainless steel (SS) substrates using the successive ionic layer adsorption and reaction (SILAR) method. The physico-chemical properties of CdS/rGO films were studied. The X-ray diffraction (XRD) revealed the growth of nanocrystalline CdS/rGO films with a cubic crystal structure. The field-emission scanning electron microscopy (FE-SEM) images of CdS/rGO-80 composite thin films showed compact spherical nanoparticles and an optical band gap found to be 2.27 eV. The CdS/rGO-80 composite thin film displayed hydrophilic nature with a water contact angle of 33°. The photoelectrochemical (PEC) studies of CdS/rGO thin film in dark and under light exhibited n-type of electrical conductivity with an improved photoactivity over bare CdS in 1 M polysulfide ($\text{NaOH} + \text{Na}_2\text{S} + \text{S}$) electrolyte. It is observed that rGO composited CdS thin film enhances the conversion efficiency (η) from 0.09 to 0.31% than bare CdS films. The electrical transport properties were investigated by electrochemical impedance spectroscopy (EIS) study in dark and under illumination conditions and corresponding equivalent circuit of the impedance model is developed.


Graphical Abstract



Extended author information available on the last page of the article



Synthesis and characterization of crystalline cristobalite alpha low silicon dioxide nanoparticles: a cost-effective anode for lithium-ion battery

Sohan Thombare¹ , Rohan Patil², Ranjit Humane³, Bharat Kale^{4,6}, Ramchandra Kalubarme³, Dhanaji Malavekar⁵, Sambhaji Khot¹, Manisha Phadatare^{2,*}, and Chandrakant Lokhande^{1,*}

¹ Centre for Interdisciplinary, Research, D. Y. Patil Education Society (Deemed To Be University), Kolhapur 416006, India

² Departments of Engineering, Mathematics and Subject Didactics (IMD), Mid Sweden University, 85170 Sundsvall, SE, Sweden

³ Centre for Materials for Electronics Technology, Panchawati, Off. Pashan Road, Pune 411008, India

⁴ Centre for Materials for Electronics Technology (C-MET), Government of India, Pune, Maharashtra 411007, India

⁵ Optoelectronics Convergence Research Center, Department of Materials Science and Engineering, Chonnam National University, Gwangju 61186, South Korea

⁶ Material Science (COE) Research and Development, MIT World Peace University (MIT-WPU) Kothrud Pune, Pune, Maharashtra 411038, India

Received: 24 January 2024

Accepted: 30 June 2024

© The Author(s), 2024

ABSTRACT

Silicon dioxide (SiO₂ or Silica) is one of the most prevalent substances in the crust of the Earth. The main varieties of crystalline silica are quartz, cristobalite, and tridymite. When applied as a material for energy, it is affordable and eco-friendly. The SiO₂ is considered as electrochemically inactive toward lithium. The SiO₂ exhibits low activity for diffusion and inadequate electrical conductivity. As the particle size of SiO₂ decreases, the diffusion pathway of Li-ions shortens, and the electrochemical activity is promoted. In investigation, Cost-effective synthesis approach was employed to produce crystalline cristobalite alpha low silicon dioxide nanoparticles (CCαL SiO₂ NPs) derived from *Oryza sativa* (rice) husk using a solvent extraction modification technique. The objective was to fabricate an cost-effective future anode nanomaterial that could reduce the significant volume expansion growth, pulverization, and increase electrical conductivity of CCαL SiO₂ NPs anode and develop high specific capacity for Lithium-ion battery (LiB). To study the phase and purity of the SiO₂, a variety of characterization methods, including X-Ray Diffraction, Fourier Infra-Red Spectroscopy, Surface area analysis, Raman Shift analysis, Field Emission Scanning Electron Microscopy and Energy Dispersive X-Ray Spectroscopy, Contact angle measurement, Post-mortem X-ray diffraction, and Post-mortem field emission scanning electron microscopy were employed. This cost-effective synthesis of CCαL SiO₂ NPs anode was first reported in this work.

Address correspondence to E-mail: Manisha.Phadatare@miun.se; l_chandrakant@yahoo.com

PATENTS



INTELLECTUAL
PROPERTY INDIA

PATENTS | DESIGNS | TRADE MARKS
GEOGRAPHICAL INDICATIONS



सत्यमेव जयते

भारत सरकार
GOVERNMENT OF INDIA

पेटेंट कार्यालय
THE PATENT OFFICE

पेटेंट प्रमाणपत्र
PATENT CERTIFICATE
(Rule 74 of The Patents Rules)

क्रमांक : 022124564
SL No :



पेटेंट सं. / Patent No. : 433033
आवेदन सं. / Application No. : 202221021506
फाइल करने की तारीख / Date of Filing : 11/04/2022
पेटेंटी / Patentee : D.Y.PATIL EDUCATION SOCIETY (DEEMED TO BE UNIVERSITY)
आविष्कारक (जहां लागू हो) / Inventor(s) : 1.PROF.CHANDRAKANT DNYANDEV LOKHANDE
2.MR.SAMBHAJI DINKAR KHOT 3.MR.RANJIT PANDURANG NIKAM 4.MS.PRITY PRAKASH BAGWADE
5.MR.DHANAJI BALASO MALAVEKAR

प्रमाणित किया जाता है कि पेटेंटी को, उपरोक्त आवेदन में यथाप्रकटित CHEMICAL SYNTHESIS OF REDUCED GRAPHENE OXIDE - DYSPROSIUM SELENIDE COMPOSITE THIN FILMS FOR ENERGY STORAGE नामक आविष्कार के लिए, पेटेंट अधिनियम, 1970 के उपबंधों के अनुसार आज तारीख अप्रैल 2022 के ग्यारहवें दिन से बीस वर्ष की अवधि के लिए पेटेंट अनुदत्त किया गया है।

It is hereby certified that a patent has been granted to the patentee for an invention entitled CHEMICAL SYNTHESIS OF REDUCED GRAPHENE OXIDE - DYSPROSIUM SELENIDE COMPOSITE THIN FILMS FOR ENERGY STORAGE as disclosed in the above mentioned application for the term of 20 years from the 11th day of April 2022 in accordance with the provisions of the Patents Act, 1970.



अनुदान की तारीख : 29/05/2023
Date of Grant :

पेटेंट नियंत्रक
Controller of Patent

टिप्पणी - इस पेटेंट के नवीकरण के लिए फीस, यदि इसे बनाए रखा जाना है, अप्रैल 2024 के ग्यारहवें दिन को और उसके पश्चात प्रत्येक वर्ष में उसी दिन देय होगी।

Note. - The fees for renewal of this patent, if it is to be maintained will fall / has fallen due on 11th day of April 2024 and on the same day in every year thereafter.



सत्यमेव जयते



पेटेंट कार्यालय, भारत सरकार

The Patent Office, Government Of India

पेटेंट प्रमाण पत्र

Patent Certificate

(पेटेंट नियमावली का नियम 74)

(Rule 74 of The Patents Rules)

पेटेंट सं. / Patent No.

519511

आवेदन सं. / Application No.

202321020957

फाइल करने की तारीख / Date of Filing

24/03/2023

पेटेंटी / Patentee

D.Y.PATIL EDUCATION SOCIETY (DEEMED TO BE UNIVERSITY)

आविष्कारकों का नाम / Name of Inventor(s)

1.PROF.CHANDRAKANT DNYANDEV LOKHANDE
2.MR.SAMBHAJI DINKAR KHOT 3.DR.VAIBHAV CHANDRAKANT LOKHANDE

प्रमाणित किया जाता है कि पेटेंटी को, उपरोक्त आवेदन में यथाप्रकरित "CHEMICAL SYNTHESIS OF DYSPROSIUM SULPHIDE COATING FOR ENERGY STORAGE". नामक आविष्कार के लिए, पेटेंट अधिनियम, 1970 के उपबंधों के अनुसार आज तारीख मार्च 2023 के चौबीसवें दिन से बीस वर्ष की अवधि के लिए पेटेंट अनुदत्त किया गया है।

It is hereby certified that a patent has been granted to the patentee for an invention entitled "CHEMICAL SYNTHESIS OF DYSPROSIUM SULPHIDE COATING FOR ENERGY STORAGE", as disclosed in the above mentioned application for the term of 20 years from the 24th day of March 2023 in accordance with the provisions of the Patents Act, 1970.



इकांत की दंडित

अनुदान की तारीख : 05/03/2024

पेटेंट नियंत्रक

Controller of Patents

टिप्पणी - इस पेटेंट के नवीकरण के लिए फीस, यदि इसे बनाए रखा जाना है, मार्च 2025 के चौबीसवें दिन को और उसके पश्चात प्रत्येक वर्ष में उसी दिन देय होगी।

Note. - The fees for renewal of this patent, if it is to be maintained, will fall / has fallen due on 24th day of March 2025 and on the same day in every year thereafter.



सत्यमेव जयते

The Patent Office, Government Of India

Patent Certificate

(Rule 74 of The Patents Rules)

473475

202121062097

31/12/2021

D.Y.PATIL EDUCATION SOCIETY(DEEMED TO BE UNIVERSITY).KASAB BAWADA,KOLHAPUR

1.PROF.CHANDRAKANT DYANDEV LOKHANDE 2.MR.RANJIT
PANDURANG NIKAM 3.MR.SAMBHAJI DINKAR KHOT
4.MISS.PRITY PRAKASH BAGWADE 5.MR.DILIP JAGANNATH
PATIL

It is hereby certified that a patent has been granted to the patentee for an invention entitled "**CHEMICAL SYNTHESIS OF CADMIUM SELENIDE/REDUCED GRAPHENE OXIDE COMPOSITE THIN FILM AND PHOTOELECTROCHEMICAL CELL APPLICATION.**" as disclosed in the above mentioned application for the term of 20 years from the 31st day of December 2021 in accordance with the provisions of the Patents Act, 1970.

Act, 1970. **బౌద్ధిక సంపత్తి కార్యాలయము, భారత ప్రభుత్వము, హైదరాబాద్.**

[illegible]

00 12062020, बौद्धिक संपदा का कार्यालय, भारत सरकार, नई दिल्ली, भारत।
பகுதி 1, 2020, பௌத்த பாரம்பரியம், இந்திய அரசு, புதுச்சேரி, இந்தியா.

[illegible]

अनुदान की तारीख: 28/11/2023

Date of Grant : 28/11/2023

टिप्पणी - इस पेटेंट के नवीकरण के लिए फीस, यदि इसे बनाए रखा जाना है, दिसम्बर 2023 के इक्कीसवें दिन को और उसके पश्चात प्रत्येक वर्ष में उसी दिन देय होगी।

Note. - The fees for renewal of this patent, if it is to be maintained, will fall / has fallen due on 31st day of December 2023 and on the

same day in every year thereafter. गौद्धिक संपदा दफ्तर, भारत सरकार, वौद्धिक सम्पदा कार्यालय, भारत सरकार, बंगलूरु ५६०००१, भारत
संपत्ती कार्यालय, भारत सरकार, वौद्धिक सम्पदा कार्यालय, भारत सरकार, बंगलूरु ५६०००१, भारत

[illegible]



क्रम सं/SL No :022126821

पेटेंट कार्यालय, भारत सरकार

The Patent Office, Government Of India

पेटेंट प्रमाण पत्र

Patent Certificate

(पेटेंट नियमावली का नियम 74)

(Rule 74 of The Patents Rules)

पेटेंट सं. / Patent No.

445967

आवेदन सं. / Application No.

202221029730

फाइल करने की तारीख / Date of Filing

24/05/2022

पेटेंटी / Patentee

D.Y.PATIL EDUCATION SOCIETY (DEEMED TO BE UNIVERSITY)

आविष्कारकों का नाम / Name of Inventor(s)

1.PROF.CHANDRAKANT DNYANDEV LOKHANDE
2.MS.PRITY PRAKASH BAGWADE 3.MR.DHANAJI BALASO
MALAVEKAR 4.MR.SAMBHAJI DINKAR KHOT 5.MR.RANJIT
PANDURANG NIKAM

प्रमाणित किया जाता है कि पेटेंटी को, उपरोक्त आवेदन में यथाप्रकटित **ELECTROCHEMICAL SUPERCAPACITOR DEVICE** नामक आविष्कार के लिए, पेटेंट अधिनियम, 1970 के उपबंधों के अनुसार आज तारीख मई 2022 के चौबीसवें दिन से बीस वर्ष की अवधि के लिए पेटेंट अनुदत्त किया गया है।

It is hereby certified that a patent has been granted to the patentee for an invention entitled **ELECTROCHEMICAL SUPERCAPACITOR DEVICE** as disclosed in the above mentioned application for the term of 20 years from the 24th day of May 2022 in accordance with the provisions of the Patents Act, 1970.



(Signature)

पेटेंट नियंत्रक
Controller of Patents

अनुदान की तारीख : 21/08/2023
Date of Grant :

टिप्पणी - इस पेटेंट के नवीकरण के लिए फीस, यदि इसे बनाए रखा जाना है, मई 2024 के चौबीसवें दिन को और उसके पश्चात प्रत्येक वर्ष में उसी दिन देय होगी।

Note. - The fees for renewal of this patent, if it is to be maintained, will fall / has fallen due on 24th day of May 2024 and on the same day in every year thereafter.

क्रम सं/SL No :022132650



INTELLECTUAL
PROPERTY INDIA
PATENTS | DESIGNS | TRADE MARKS
GEOGRAPHICAL INDICATIONS



सत्यमेव जयते



पेटेंट कार्यालय, भारत सरकार

The Patent Office, Government Of India

पेटेंट प्रमाण पत्र

Patent Certificate

(पेटेंट नियमावली का नियम 74)

(Rule 74 of The Patents Rules)

पेटेंट सं. / Patent No. 479403

आवेदन सं. / Application No. 202221039656

फाइल करने की तारीख / Date of Filing 11/07/2022

पेटेंटी / Patentee

D.Y.PATIL EDUCATION SOCIETY (DEEMED TO BE UNIVERSITY), KASABA BAWADA, KOLHAPUR

आविष्कारकों का नाम / Name of Inventor(s)

1.PROF.CHANDRAKANT DNYANDEV LOKHANDE 2.MR.DILIP JAGANNATH PATIL 3.DR.DHANAJI BALASO MALAVEKAR 4.MR.SAMBHAJI DINKAR KHOT 5.MR.RANJIT PANDURANG NIKAM

प्रमाणित किया जाता है कि पेटेंटी को, उपरोक्त आवेदन में यथाप्रकटित A METHOD OF SYNTHESIZING COMPOSITE OF REDUCED GRAPHENE OXIDE AND NICKEL TUNGSTATE FOR ENERGY STORAGE नामक आविष्कार के लिए, पेटेंट अधिनियम, 1970 के उपबंधों के अनुसार आज तारीख जुलाई 2022 के ग्यारहवें दिन से बीस वर्ष की अवधि के लिए पेटेंट अनुदत्त किया गया है।

It is hereby certified that a patent has been granted to the patentee for an invention entitled A METHOD OF SYNTHESIZING COMPOSITE OF REDUCED GRAPHENE OXIDE AND NICKEL TUNGSTATE FOR ENERGY STORAGE as disclosed in the above mentioned application for the term of 20 years from the 11th day of July 2022 in accordance with the provisions of the Patents Act, 1970.

अनुदान की तारीख : 08/12/2023

Date of Grant :



पेटेंट नियंत्रक
Controller of Patents

टिप्पणी - इस पेटेंट के नवीकरण के लिए फीस, यदि इसे बनाए रखा जाना है, जुलाई 2024 के ग्यारहवें दिन को और उसके पश्चात प्रत्येक वर्ष में उसी दिन देय होगी।

Note. - The fees for renewal of this patent, if it is to be maintained, will fall / has fallen due on 11th day of July 2024 and on the same day

in every year thereafter.

CONFERENCES



2nd Asian e-Conference on Engineered Science



CERTIFICATE

Sambhaji Khot

This is to certify that Miss/Mr/Mrs/Dr

has Presented a Paper in 2nd Asian e-Conference on Engineered Science jointly organized by Prof. C. D. Lokhande Endowment Charitable Trust and Engineered Science Publisher, USA held during 5-6 December 2021.

Prin. Dr. J. D. Desai
President, Prof. CDLET, Pune



Prof. John Zhanhu Guo,
ES Publisher, USA



‘Social Transformation Through Dynamic Education’

Bharati Vidyapeeth's

Dr. Patangrao Kadam Mahavidyalaya, Sangli

Affiliated to Shivaji University, Kolhapur



Fourth National Conference on

Recent Trends in Pure and Applied Sciences (RTPAS-2022)

organized by

Internal Quality Assurance Cell

CERTIFICATE

This is to certify that **Mr. Sambhaji Dinkar Khot** of **D. Y. Patil Education Society, Kolhapur, India 416 006** has participated and presented paper titled *‘Synthesis and Characterization of Dysprosium Selenide (DY2SE3) Thin Films by Using Simple Successive Ionic Layer Adsorption and Reaction SILAR Method’* in the Fourth National Conference on “Recent Trends in Pure and Applied Sciences” held on 21st and 22nd January, 2022.

(Dr. Dada P. Nade)
Secretary, RTPAS 2022

(Dr. A. B. Awale)
Convenor, RTPAS 2022

(Dr. A. R. Supale)
Coordinator, IQAC

(Prin. Dr. D. G. Kanase)
Member, Management Council
Shivaji University, Kolhapur



Estd. 1884

Deccan Education Society's

Certificate No. 95

WILLINGDON COLLEGE, SANGLI

Maharashtra- 416 415

One Day International Conference on

“Recent Trends in Science and Technology”

CERTIFICATE

This is to certify that, **Sambhaji Khot of Centre for Interdisciplinary Research, D. Y. Patil Education Society, Kolhapur** has participated in **One Day International Conference on “Recent Trends in Science and Technology”** and presented a paper titled *“Chemical synthesis of dysprosium sulphide thin films for supercapacitor application”* held on 29th June 2022 at Willingdon College, Sangli .

Dr. S.G. Kulkarni

Organizing Secretary

Dr. N.T. Padal

Coordinator

Dr. B.V. Tamhankar

Principal

Willingdon College, Sangli

"Education through self-help is our motto" - Karmaveer



Rayat Shikshan Sanstha's

RAJARSHI CHHATRAPATI SHAHU COLLEGE, KOLHAPUR

(Reaccredited by NAAC (3rd Cycle) with A grade (CGPA 3.07) affiliated to Shivaji University, Kolhapur



DEPARTMENT OF CHEMISTRY and IQAC

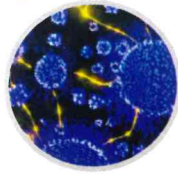
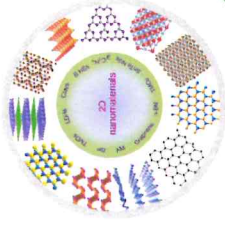
With Knowledge Partner

D.Y. PATIL EDUCATION SOCIETY, KOLHAPUR

Organizes

Two days National Conference on

"Emerging Trends in Chemical Sciences and Nanomaterials (ETCSN-23)"



Certificate

This is to certify that, Dr./Prof./Mr./Ms./Mrs. Khot Sambhaji Ainkae of _____

D.Y. Patil University, Kolhapur

has participated/worked as Resource Person
/Chairperson/Organizing Committee Member in Two days National Conference on "Emerging Trends in
Chemical Sciences and Nanomaterials" (ETCSN-23) held on 24th & 25th February, 2023. He/She has presented a

Paper/Poster titled Chemically Synthesized Dysprosium Sulfide for Supercapacitor



Dr. S. P. Pawar
Coordinator



Dr. K. V. Gaikwad
Convener



Prof. Dr. Mrs. P. B. Piste
Organizing Secretary



Prin. Dr. L. D. Kadam
Chairman



Department of Chemistry
organizes
Two day National Seminar on
'Recent Scenario in
Chemical Sciences
and Material Sciences'
(RSCSMS-2023)
On 3rd & 4th March, 2023
Sponsored by
Shivaji University,
Kolhapur

Shri Shahu Shikshan Prasarak Seva Mandal's

Shri Vijaysinha Yadav College

Peth Vadgaon, Dist. Kolhapur

Re-Accredited with Grade: A+ (CGPA: 3.41) by NAAC, Bangalore

(Affiliated to Shivaji University, Kolhapur)

CERTIFICATE

This is to certify that, Mr./Miss/Dr. Sambhaji Pinkar Khot of D.Y. Patil University, Kolhapur has participated / worked as a resource person / chaired a session / worked as an organizing committee member in Two - Day National Seminar on "**Recent Scenario in Chemical Sciences and Material Sciences**" (**RSCSMS-2023**) organized by **Dept. of Chemistry** on 3rd and 4th March, 2023. He / She has presented a paper entitled Chemical Synthesis of dysprosium sulphide thin films for supercapacitor application in the Oral / Poster session of the Seminar. We appreciate and congratulate the participant for enthusiastic performance.



Mr. Dattatraya B. Patil
Treasurer

Dr. Chandrakant B. Mane
Organizing Secretary

Mrs. Renuka A. Pawar
Coordinator

Dr. Vijaya R. Chavan
Convenor / Principal



D. Y. PATIL EDUCATION SOCIETY,
(Deemed to be University) Kolhapur
Accredited NAAC with 'A' Grade

Certificate

DNYANSHODH -2023
(Search For Knowledge)

This is to certify that

Mr/Ms. Sambhaji Dinkar Khot

has presented a Poster on 9th March 2023, in Dnyanshodh -2023,
organized by Centre for Interdisciplinary Research (CIR), D. Y. Patil Education Society
(Deemed to be University), Kolhapur - 416006.

Chairman
Prof. (Dr.) C. D. Lokhande
Dean,
Centre for Interdisciplinary Research

Convenor
Dr. Arpita Pandey -Tiwari
Associate Professor,
Department of Medical Biotechnology.



"Education through self-help is our motto." - Karmaveer

Rayat Shikshan Sanstha's

RAJARSHI CHHATRAPATI SHAHU COLLEGE, KOLHAPUR

(Reaccredited 3rd Cycle by NAAC at 'A' Grade with CGPA 3.07)



DEPARTMENT OF PHYSICS and IQAC

Organizes Under G20 University Connect Program

One Day International Conference on



"Recent Trends in Fabrication of Nanomaterials and Their Applications (ICRTFNA-2023) "

Certificate

This is to certify that, Dr. /Prof./Mr./Ms./Mrs. Sambhaji D. Khot of

D.Y. Patil university kolhapur

has participated /worked as Resource

~~Person/Chairperson~~ / Organizing committee member in One Day International Conference on 'Recent Trends in Fabrication of Nanomaterials and Their Applications (ICRTFNA-2023) ' Organized by Department of Physics and IQAC held on March 15, 2023. He/She has presented paper entitled High performance Flexible

Solid state asymmetric supercapacitor device based on $\text{rGO}/\text{Dy}_2\text{Se}_3$ and

MnO_2 electrodes

Dr. A. R. Patil

Coordinator

Dr. V. V. Killedar

Organizing secretary

Dr. L. D. Kadam

Principal



D. Y. PATIL EDUCATION SOCIETY
(Deemed to be University), KOLHAPUR
NAAC 'A+' Grade in 3rd Cycle



DNYANSHODH-2024

Certificate

This is to certify that **Mr./Ms. Sambhaji B. Khot** of **CIR AYPES, Kolhapur** has participated and presented poster in poster presentation competition (Ph.D. category) in **DNYANSHODH-2024 (Search for Knowledge)** on 28th February 2024 organized by Centre for Interdisciplinary Research, D. Y. Patil Education Society (Deemed to be University), Kolhapur, Maharashtra, India. His/Her contribution in the event is highly appreciated.

Pravin P. Pawar

Convener

Dr. Pravin P. Pawar

Chandrakant D. Lokhande

Chairman

Prof. Chandrakant D. Lokhande



Rayat Shikshan Sanstha's

SADGURU GADAGE MAHARAJ COLLEGE, KARAD

(AN AUTONOMOUS COLLEGE - Affiliated to Shivaji University, Kolhapur)

Accredited 'A+' with CGPA 3.63 by NAAC • ISO 9001 : 2015 Certified & NAAC Designed Mentor College



Department of Physics

A TWO DAY INTERNATIONAL CONFERENCE ON

Innovation in Smart & Technomaterials (ICISTM-2023)



Sponsored by

RASHTRIYA UCHCHATAR SHIKSHA ABHIYAN (RUSA)

CERTIFICATE

This is to certify that, Prof./Dr./Mr./Ms. Sambhaji Linkar Khot has Participated/Presented a Paper of D.Y. Patil University, Kolhapur (Oral/Poster) entitled STLAR Synthesized Dysprosium sulfide thin film for supercapacitor. in **International Conference on Innovation in Smart & Technomaterials (ICISTM-2023)** organized by Dept. of Physics, Sadguru Gadage Maharaj College, Karad on 16th and 17th January 2023.


Dr. I. A. Dhole
Co-convenor


Dr. N. S. Harale
Convener


Dr. S. H. Pisal
Coordinator


Prof. Dr. J. B. Thorat
Organizing Secretary


Prin. Dr. M. M. Rajmane
S.G.M. College, Karad



D. Y. PATIL EDUCATION SOCIETY
(Institution Deemed to be University), Kolhapur
Re-Accredited by NAAC with 'A' Grade

Workshop on **CERTIFICATE** **GOOD LABORATORY PRACTICES**

Successfully attended by **Sambhaji Khot**
on Saturday 06 February 2021

Organized By

Department of Stem Cell and Regenerative Medicine and Department of
Medical Physics, Centre for Interdisciplinary Research

Prof. Dr. C. D. Lokhande
Chairman

Prof. Dr. S. Mohan Karuppayil
Convener

Dr Shivaji Kashte
Organising Secretary

Made for free with Certify'em



SHIVAJI UNIVERSITY, KOLHAPUR

SOPHISTICATED ANALYTICAL INSTRUMENT FACILITY (SAIF) – COMMON FACILITY CENTRE (CFC)

WORKSHOP & HANDS-ON TRAINING ON XRD ORGANISED

BY SAIF-CFC UNDER STRIDE PROGRAMME

Certificate of Participation

This is certify that Mr. Khot Sambhaji D. has successfully participated in the workshop & hands-on training on XRD organised by SAIF (CFC), Shivaji University, Kolhapur held during 11-12 Nov, 2021 under the STRIDE (Scheme for Trans-disciplinary Research for India's Developing Economy) programme.

A handwritten signature in blue ink, reading 'R. G. Sonkawade'.

Prof. R. G. Sonkawade
Co-ordinator : SAIF, Head (i/c) : CFC
Shivaji University, Kolhapur.
Chairman



SANJAY GHODAWAT UNIVERSITY Kolhapur
Empowering Lives Globally !

(Approved by UGC & Govt.of Maharashtra)

Certificate

This is to certify that

Prof. / Dr. / Mr. / Ms. **Sambhaji Khot Ph.D Scholar**
of **DY Patil Deemed University Kolhapur** has participated in National Seminar on

“Emerging Nano Materials for Renewable Energy”

held on Monday, 26th December, 2022 and organized by Sanjay Ghodawat University, Kolhapur.

Dr. Sambhaji M. Pawar
Convener

Dr. Pallavi D. Bhangre
Convener

Dr. Sarita P. Patil
Co-ordinator

Prof. Dr. Arun S. Patil
Vice-Chancellor

e-Certificate of Participation

This is to certify that, **Mr. Sambhaji Dinkar Khot** of **D.Y.Patil deemed to be university kolhapur** participated in the **National Level One Day Online Workshop on "Intellectual Property Rights"** under **National IPR Awareness Mission** organized by Research Committee, IPR Cell in Association with IQAC, D. P. Bhosale College, Koregaon, Dist- Satara and Collaboration with Office of Controller General of Patents & Design Office, Mumbai, Govt. of India on 12-08-2022.



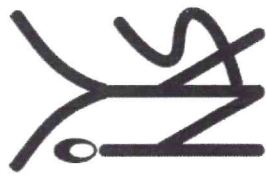
Dr. V. S. Jamadade
Convener



Dr. B. S. Lokde
IQAC Coordinator



Dr. V. S. Sawant
Principal



INYAS SCIENCE CAMP-2022

CERTIFICATE

This is to certify that

Mr./Mrs.

Sambhaji Khot

has served as a volunteer in the “INYAS Science Camp -2022” organized by
D. Y. Patil Education Society (Institution Deemed to be University), Kolhapur,
Indian National Young Academy of Science (INYAS),
Indian National Science Academy (INSA) and D. Y. Patil Knowledge Campus, Salokhenagar,
Kolhapur
at D. Y. Patil Vidyaniketan School, Salokhenagar, Kolhapur during 16 - 17 December 2022.

Penjaka

Dr. J. L. Gunjekar
DYPES, INYAS Member

Dr. V. V. Parkar

Dr. V. V. Parkar
BARC, INYAS Member

Prof. C. D. Lokhande

Prof. C. D. Lokhande
Dean CIR, DYPES



DYP
SALOKHE NAGAR